Mechanical & Aerospace Engineering Theses & Dissertations

Mechanical & Aerospace Engineering

Summer 1995

Numerical Investigation of Shock-Induced Combustion Past Blunt Projectiles

Jagjit K. Ahuja
Old Dominion University

Follow this and additional works at: https://digitalcommons.odu.edu/mae_etds

Part of the Aerospace Engineering Commons, and the Heat Transfer, Combustion Commons

NUMERICAL INVESTIGATION OF SHOCK-INDUCED COMBUSTION PAST BLUNT PROJECTILES

by

Jagjit K. Ahuja

A Dissertation submitted to the Faculty of
Old Dominion University in Partial Fulfillment of the
Requirement for the Degree of

DOCTOR OF PHILOSOPHY

MECHANICAL ENGINEERING

OLD DOMINION UNIVERSITY
August, 1995

Approved by:

Surendra N. Tiwari (Director)

Ajay Kumar (Co–Director)

Sushil K. Chaturvedi

Arthur Taylor

ABSTRACT

NUMERICAL INVESTIGATION OF SHOCK-INDUCED COMBUSTION PAST BLUNT PROJECTILES

Jagjit K. Ahuja

Department of Mechanical Engineering

Old Dominion University

Director: Dr. Surendra N. Tiwari

Co-Director: Dr. Ajay Kumar

A numerical study is conducted to simulate shock-induced combustion in premixed hydrogen-air mixtures at various free-stream conditions and parameters. Two-dimensional axisymmetric, reacting viscous flow over blunt projectiles is computed to study shock-induced combustion at Mach 5.11 and Mach 6.46 in hydrogen-air mixture. A seven-species, seven reactions finite rate hydrogen-air chemical reaction mechanism is used combined with a finite-difference, shock-fitting method to solve the complete set of Navier-Stokes and species conservation equations. In this approach, the bow shock represents a boundary of the computational domain and is treated as a discontinuity across which Rankine-Hugoniot conditions are applied. All interior details of the flow such as compression waves, reaction front, and the wall boundary layer are captured automatically in the solution. Since shock-fitting approach reduces the amount of artificial dissipation, all the intricate details of the flow are captured much more clearly than has been possible with the shock-capturing approach. This has allowed an improved understanding of the

physics of shock-induced combustion over blunt projectiles and the numerical results can now be explained more readily with one-dimensional wave-interaction model than before. For Mach 5.11 the flow field is found to be unsteady with regular periodic oscillations of the reaction front. There is a progression of higher frequency and lower amplitude oscillations as the Mach number is increased with a steady flow observed at some point above the C-J velocity. Numerical results show good qualitative agreement with the ballistic range shadowgraphs. In addition, the frequency of oscillations, determined by using the Fourier power spectrum is found to be in good agreement with the experiment.

Various parameters for the triggering of the instabilities have been identified. Projectile diameter is one of the parameter and an unstable reaction front can be made stable by choosing an appropriate small diameter projectile. The other parameter is the heat release rate which, in turn, depends upon the free-stream pressure. A number of simulations of shock-induced combustion past blunt projectiles in regular and large-disturbance regimes are also made at a Mach number of approximately 5 and pressures in the range of 0.1 to 0.5 atm. For a free-stream pressure of 0.1 atm, the reaction front is steady; at a pressure of 0.25 atm, the reaction front develops regular, periodic oscillations. As the pressure is increased to 0.5 atm, the oscillations become highly pronounced and irregular. Combustion with periodic oscillations has been classified as a *regular regime* and combustion with large, irregular oscillations has been classified as a *large-disturbance regime*. These calculations are in agreement with the experimental observations from ballistic-range tests. The transition from steady reaction front to regular, periodic oscillations, and then to large-disturbance regime is explained by a one-dimensional wave-interaction model.

ACKNOWLEDGMENTS

I would like to express my sincere thanks to various people who have been responsible for the completion of this dissertation. First, I am grateful to Dr. Ajay Kumar of NASA Langley Research Center for his consistent encouragement and support during the course of this study. I would like to thank my advisor, Dr. Surendra N. Tiwari for his guidance, support and aboveall his patience with me during this research work. Many of his suggestions have made this a quality work. Special thanks are due to Dr. D. J. Singh of Analytical Services and Materials Inc. for his valuable technical insights and suggestions throughout this work. I am also thankful to my other committee members Dr Sushil K. Chaturvedi and Dr. Arthur Taylor for providing valuable feedbacks.

My sincere thanks are to Dr. H. F. Lehr for providing the original photographs from his Ph.D. work, and to NASA Langley Library and Photographic Laboratory for providing me and helping to develop the original photographs of Ruegg and Dorsey's experimental work.

My special thanks go to my family members who have always encouraged and supported me. My wife Dr. Anuradha Sarkar, despite her being in Medical profession, has given new engineering artistic ideas to present this work in a professional manner. She has always been very patient and supportive in this endeavor. Finally I thank God for giving me energy and enthusiasm for the enhancement of this knowledge.

Program through NASA grant NAG-1–363. This grant was provided by the Office of Education, NASA Langley Research Center, Hampton, Virginia.

TABLE OF CONTENTS

LIST OF TABLES

LIST OF FIGURES

x

LIST OF SYMBOLS

A_j	reaction-rate constant for the jth reaction
C_i	concentration of ith species
C_{pi}	constant pressure-specific heat of ith species
D_{ij}	binary diffusion coefficient of ith and jth species
E	total (internal and kinetic) energy
f_i	mass fraction of species i
F,G	flux vectors
H	source vectors
h_i^R	base enthalpy of ith species
$\vec{i}_r$	unit vector tangential to the body
J	Jacobian
k	thermal conductivity
M_i	molecular weight of ith species
N_s	number of chemical reactions
$\vec{n}$	unit vector normal to the shock
p	pressure
R_i	gas constant of ith species
r_n	nose radius
r_{s_t}	radial shock velocity
$\vec{s}$	unit vector tangential to the shock
t	time
T	temperature
U	dependent variable vector
u	x-component of the velocity
u_∞	velocity tangential to the body
U_s	local shock velocity
$\tilde{u}_i$	x-component of the diffusion velocity of the ith component
v	y-component of the velocity

xi

Symbol	Definition
v_∞	velocity normal to the body
$\tilde{v}_i$	y-component of diffusion velocity of ith species
X_i	mole fraction of ith species
x	streamwise coordinate in the physical domain
y	normal coordinate in the physical domain
α_j	temperature coefficient in reaction rate expression for jth reaction
ΔG_{Rj}	Gibbs free energy change for the jth reaction
Δn_j	molar change for the jth reaction
ϵ_j	activation energy of jth reaction
η	normal coordinate in the computational domain
θ	angle the radius makes with the x-axis i.e., body angle
κ_{bj}	backward rate constant for jth reaction
κ_{eqj}	equilibrium constant for jth reaction
κ_{fj}	forward rate constant for jth reaction
λ	second viscosity coefficient
μ	dynamic viscosity
ν'_{ji}	stoichiometric coefficient of reactant corresponding to ith species and jth reaction
ν''_{ji}	stoichiometric coefficient of product corresponding to ith species and jth reaction
ξ	streamwise coordinate in the computational domain
ρ	density
σ_x	normal stress in the x direction
σ_y	normal stress in the y direction
τ_{xy}	shear stress in the xy plane
$\dot{\omega}_i$	production rate of ith species

Chapter 1

INTRODUCTION

1.1 Importance of Overall Research

The national commitment to the National Aerospace Plane (NASP) program and other hypersonic vehicles such as Trans-Atmospheric Vehicle (TAV) and Aero-assisted Orbital Transfer Vehicle (AOTV) have generated renewed interest in hypersonic flows. Since these vehicles will rely on air-breathing propulsion, hypersonic propulsion is one of the key areas being actively researched. For a successful design of the propulsion system to be used for NASP, it is essential to have a clear understanding of the physics of mixing and combustion at supersonic speeds in order to develop efficient engines. The phenomenon of shock-induced combustion/detonation around bodies travelling at hypersonic speeds into combustible mixtures is of great theoretical interest because of the need to understand the basic mechanism of combustion instability. These chemical instabilities are triggered and sustained via a close coupling between the gas dynamics and chemical kinetics and are characterized by a periodic density variation behind the shock. It also has a practical application in the development of hypersonic airbreathing engines in which supersonic flow is maintained throughout the engine to avoid the losses associated with slowing down the fluid. In supersonic combustion ramjet (SCRAMJET) engines, strong shocks will most likely occur in local regions of the flow. The presence of combustible mixture and shocks create conditions where detonation waves can be formed. Thus, it is essential to study the instabilities associated with such conditions to have a properly designed engine. The term detonation is applied to the process where a

1

shock and reaction front follow each other very closely and are pressure coupled, while shock-induced combustion implies that the shock wave and reaction front are decoupled, i.e. the reaction front does not influence the shock directly. In this sense, detonation is a limiting case of the shock-induced combustion for the types of flow field considered in the present investigations.

Because of the limited experimental data available in this field, computational fluid dynamics (CFD) proves to be a viable tool to better understand the physics of supersonic combustion and high-speed flows. The present research will be a good validation tool for the numerical codes for high-speed chemically reacting flows.

1.2 Applications and Motivation

Conventional ramjets are shown in Figs. 1a and 1b. Figure 1a shows a supersonic ramjet with subsonic combustion. In this conventional ramjet engine, free-stream air at high supersonic speeds is compressed to a subsonic Mach number at the entrance to the combustor. There are three principal components of the ramjet: (i) the diffuser, through which air is admitted to the engine and in which the velocity is reduced and ram pressure developed; (ii) the fuel injection system, with which fuel is introduced, vaporized and distributed; and (iii) the combustor, which includes a flameholder, the combustion zone where heat is released, and a nozzle through which the burned gases are ejected rearward at high velocity. Fuel is injected into the combustor, and burning takes place in a subsonic stream. It is advantageous over the standard gas turbines in the Mach number range of 2 to 5, but is disadvantageous at hypersonic speeds. Figure 1b shows a hypersonic ramjet with subsonic combustion. In this ramjet free-stream air at hypersonic speeds is compressed to a subsonic speed. Slowing from hypersonic to subsonic speeds will result in large pressure losses and will cause very high temperature of air entering the combustor inlet (much higher than the adiabatic fuel/air flame temperature), resulting

2
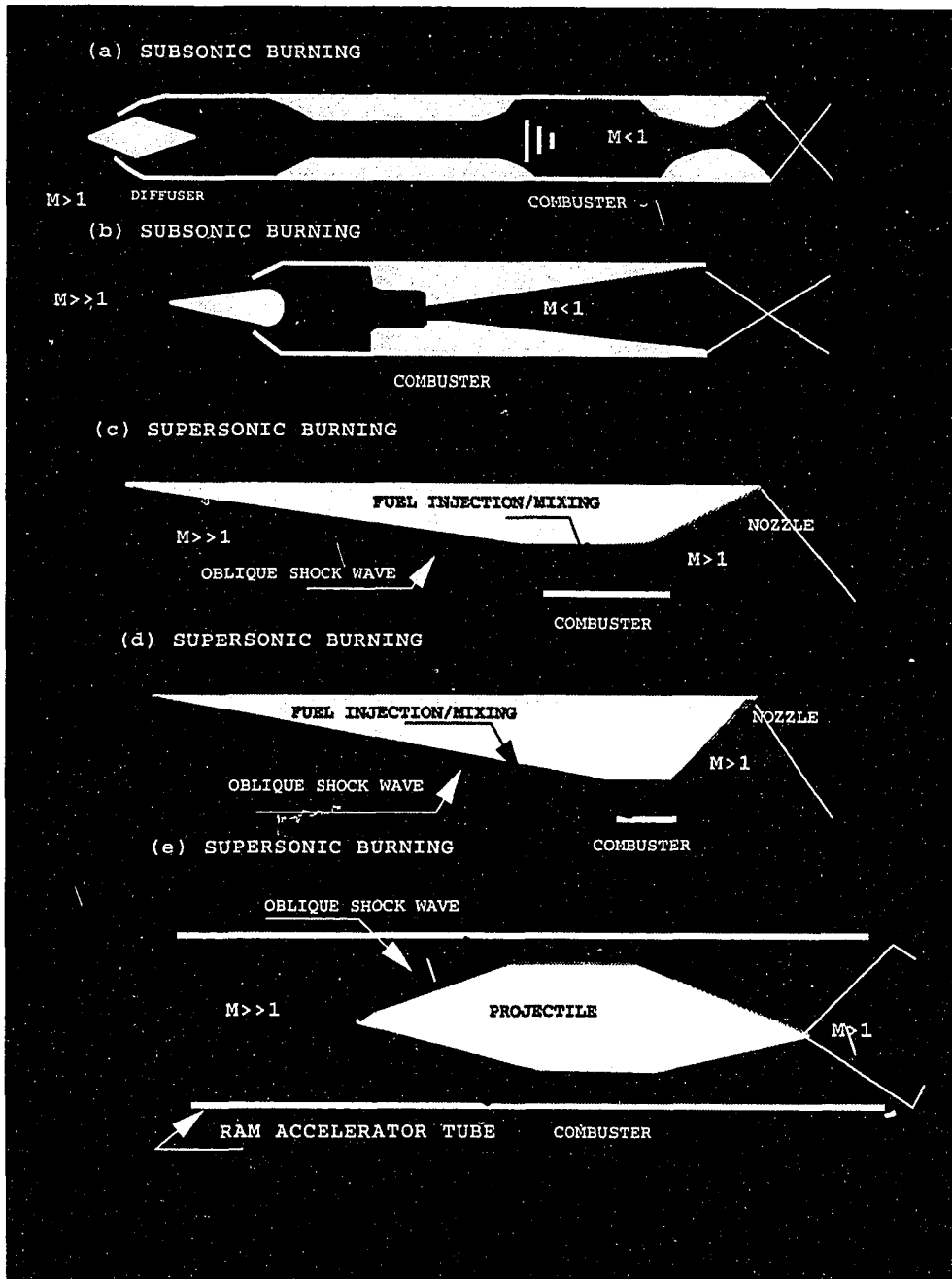
Figure 1   Schematics of some ramjet configurations: (a) Supersonic ramjet with
subsonic combustion; (b) hypersonic ramjet with subsonic combustion;
(c) hypersonic ramjet with supersonic combustion (Scramjet);
(d) oblique wave detonation engine where the fuel burns by the
oblique shocks; and (e) ram accelerator or ramjet in a tube concept.

3

in decomposition of the fuel rather than burning. Therefore, the engine will be a drag device rather than a thrust device.

For an efficient propulsion system at hypersonic speeds, the combustion must take place at supersonic speeds, for which two modes of propulsion are being proposed; namely, the *Scramjet* (supersonic combustion ramjet) and *Shramjet* (shock-induced combustion ramjet). The Scramjet ([1]–[2]) is an integrated airframe-propulsion concept for a hypersonic airplane. A schematic of scramjet is shown in Fig. 1c. The entire under surface of the vehicle is part of the scramjet engine. Initial compression of the air takes place through the bow shock from the nose of the aircraft. Further compression takes place inside a series of modules near the rear of the aircraft, thus increasing its pressure and temperature. In the combustor, fuel (usually hydrogen) is injected into the hot air by a series of parallel and perpendicular injectors where mixing and combustion takes place at supersonic speeds. The expansion of burned gases is partially realized through nozzles in the engine modules but mainly over the bottom rear surface of the aircraft. At high Mach numbers, the fuel and air do not have enough time for mixing and, therefore, the combustion efficiency decreases. Thus, in order to get the desired mixing, the length of the combustor has to be long. Since the highest pressure and temperature in the engine occur in the combustor, it has to be very strong; combined with the long length, it increases the weight and the drag of the vehicle.

In order to reduce the size of the combustor, shock-induced combustion (Shramjet [3]) has been proposed, where, a shock is employed to increase the temperature of premixed fuel and air to a point where chemical reaction will start. Figure 1d shows the schematic of Shramjet engine. In Shramjet, fuel is injected well upstream of the combustor where temperatures are relatively low and this improves the fuel air mixing. Apparent advantages of the Shramjet over the Scramjet engine includes very short-length

4

combustors and simple engine geometries. The Shramjet's ability to operate at lower combustor inlet pressures will allow the vehicle to operate at a lower dynamic pressure which lessens the heating loads on the airframe. Shramjet is expected to perform better than scramjet in the Mach 12 to 15 range. In another concept which is called the ram accelerator or ramjet-in-tube [4], a shaped projectile is fired into a tube filled with a premixed gaseous fuel/oxidizer mixture. Figure 1e shows such a concept. There is no propellant on board the projectile. Ignition of the fuel/oxidizer mixture is achieved by means of a series of shock waves that increase its temperature until the ignition temperature is reached. The resulting energy release develops high pressure behind the projectile and this accelerates the projectile to high velocities. The ram accelerator concept has the potential for a number of applications, such as hypervelocity impact studies and as a mass launcher system.

1.3. Literature Survey

In the 1950s the major research effort was directed toward understanding the initiation, structure, and instability mechanism of the detonation wave. However, most of the studies were concerned with the propagation of Chapman-Jouget type detonation in tubes filled with combustible mixtures. The main characteristics of these flows is the presence of two distinct fronts; the bow shock and the reaction front. These two fronts are separated from each other by a distance equal to the induction length. Another interesting feature of these flows is the oscillatory behavior of the flow field; the entire flow field pulsates in a periodic manner with a characteristic frequency.

The Chapman-Jouget (CJ) velocity of a mixture (velocity with which a normal detonation propagates in the mixture) is an important parameter and is a characteristic of the mixture. If the projectile is travelling at a velocity lower than the CJ velocity, the flow field is observed to be highly unsteady and the free-stream velocity is referred to as

5

underdriven, while if the projectile velocity is higher than the CJ velocity of the mixture, the flow field appears steady and the free-stream velocity is referred to as overdriven.

In the past, many researchers have conducted ballistic range experiments to study supersonic combustion/detonation. In these experiments, projectiles were fired in different fuel-air mixtures, and detonation structures around the projectiles were recorded. Zeldivich and Shlyapintokh [5] suggested in 1960 that combustion can be stabilized by the shock wave produced by bodies moving at supersonic speeds in combustible mixtures. This technique was widely used to study combustion in ballistic range facilities by firing projectiles at supersonic speeds into quiescent combustible gas mixtures. In these experiments, projectiles were fired in different premixed fuel air mixtures and detonation structures around the projectiles were recorded. If the projectile is flying above the C-J velocity of the gas mixture, the detonation or reaction front structure shows a coupled shock-deflagration system near the stagnation line of the body. These two fronts separate from each other as one moves away from the stagnation line. The separation between the two fronts occurs as soon as the velocity component normal to the bow shock is equal to the detonation velocity. The separation between the bow shock and the reaction front is called the induction zone.

In 1961 Ruegg and Dorsey [6] investigated the problem and effects of stabilizing combustion on 20 mm diameter spherical projectiles flying through a quiescent combustible mixture. Combustion produced detectable effects on the shape and positions of shock wave at Mach numbers between 4 and 6.5 and above a pressure of one-tenth atmosphere. Ignition delay was observed behind the bow shock, thus causing a separation between the bow shock and the reaction front. Strong combustion driven oscillations were also observed with frequencies up to one-tenth megacycles per second.

Behran et al. [7] conducted similar ballistic experiments by firing 9 mm plastic

6

spheres into hydrogen-air and hydrogen-oxygen mixtures at 1500–3000 m s^{-1}. They also observed that at velocities higher than C-J velocities a steady combustion front is established, while at lower velocities unstable forms of oscillations appear. The period of oscillations was found to be equal to the induction time for self-ignition.

Toong and his associates [8–10] conducted a series of experiments using conical and spherical projectiles to study the initiation and decay of chemical instabilities. Projectiles were fired into lean acetylene-oxygen and stoichiometric hydrogen-air mixtures. They proposed the wave interaction model to explain the instabilities in the structure of the detonation wave. Their model explains how compression waves can be formed when a new reaction front develops in the induction zone between the normal segment of the bow shock and the original reaction front. These compression waves lead to a cyclic process which is compatible with most of the observed features of the flow. However, the strength of the compression waves remained unresolved in their wave-interaction model, which is an important factor in determining if such a model is physically possible. Alpert and Toong [9] included the effect of the strength of the compression waves and proposed a modified form of the wave-interaction model.

Alpert and Toong [9] investigated detonation-wave structures by firing a spherical projectile with a diameter of 12.7 mm at 200 torr initial pressure in a hydrogen-oxygen mixture. They proposed that the periodic density variations appear in two main types (or regimes) of flow. In the regular regime, the widespread density variations are highly regular. The second regime, which is the large-disturbance regime, is characterized both by density variations that are less regular but far more pronounced than those of the first regime and by distortions of the bow shock. The regular regime has high frequency, low amplitude periodic oscillations, while the large-disturbance regime is characterized by low frequency, high amplitude oscillations. Alpert and Toong concentrated most of their

7

attention on the large-disturbance regime and proposed a modified form of the wave-interaction model to explain the large-disturbance-regime case.

In 1972 Lehr [11] conducted a detailed experimental study to extend the database for a wide range of projectile shapes and combustible mixtures. The projectile shapes tested included not only spheres but cones, bi-cones, and flat-nose projectiles. The mixtures included hydrogen-air, hydrogen-oxygen, methane-air, and methane-oxygen. The results were in general agrement with the previous studies. The shadowgraphs also revealed for the first time some three dimensional structure of the flow.

Oppenheim et al. [12] published an excellent review of detonation research. They concentrated on the development of the detonation wave, its stability, and its structure. They emphasized that a change to any of the parameters, such as the composition of the mixture, its initial pressure, or the diameter of the tube, causes a variation in the amplitude of the oscillations of the detonation wave. This variation progressively increases as the limits of the detonation are approached in the composition, initial pressure, or diameter. Consequently, the wave can possibly become quite unstable.

Several researchers [13–18] have recently attempted to numerically simulate Lehr's ballistic range experiments [11], but have met with limited success. Youngster et al. [13] and Lee et al. [14] simulated Lehr's experimental data for Mach 4.18, 5.11, and 6.46. They used Euler equations coupled with species equations to capture the shock and the reaction front. The reaction model used was hydrogen-air mixture of six species and an inert gas such as Argon or Nitrogen and eight reactions. The flow field was found to be steady in contrast to the experimental evidence that the flow field is, indeed, unsteady. For the test conditions of stoichiometric hydrogen-air mixture, the detonation wave speed of the mixture is Mach 5.11. Experimentally, it has been demonstrated in Lehr's work that Mach 5.11 and 4.18 show structural instabilities of the detonation wave which

8

disappear if the flight Mach number is increased beyond Mach 5.11. Further, the flow field was not well resolved. They used 32×32 and 57×41 size grids, respectively, in their blunt body calculations. These grids were not sufficient to resolve the flow field correctly.

Wilson et al. [15] conducted a detailed numerical investigation of the shock-induced combustion phenomena. They used Euler equations and a 13–species and 33–reactions chemistry model. They showed the validity of the reaction models and the importance of grid resolution needed to properly model the flow physics. They did highly resolved calculations for Lehr's Mach 5.11 and Mach 6.46 cases with adaptive grid. The calculations were not time accurate, so that the unsteady behavior was not captured. However, for cases lower than Mach 5.11, they could successfully capture the instabilities.

Sussman et al. [16]–[17] also studied the instabilities in the reaction front for a Mach number of 4.79. They also used Euler equations and a 13–species and 33–reactions chemistry model. They have proposed a new formulation based on logarithmic transformation. It greatly reduces the number of grid points needed to properly resolve the reaction front. They successfully simulated the unsteady case. However, the frequency was slightly underpredicted.

Matsuo and Fujiwara [18]–[19] have studied the instabilities of shock-induced combustion around an axisymmetric blunt body. They used Euler equations and a simplified two-step chemistry model. They investigated the growth of periodic instabilities by a series of simulations with various tip radii and showed that these periodic instabilities are related to shock-standoff distance and induction length. They proposed a new model based on McVey and Toong's model [8]. The instabilities in the reaction front were explained by their model.

The key parameters for the triggering of instabilities has been identified by various parametric studies [20]-[22]. Matsuo and Fujiwara [20] and Ahuja and Tiwari [21]

9

showed that an underdriven case, which shows instabilities in the reaction front, can be made stable by having an appropriately small size projectile and an overdriven case can be made unstable by having a large size projectile. Kumar and Singh [22] concluded that the key parameters for triggering these instabilities were projectile velocity, activation temperature, projectile nose radius, reaction rate constant, and heat release.

Tivanov and Rom [23] conducted an analytical study based on an energy equation and a chemical rate equation for the flow of a detonable gas mixture over a blunt body. They evaluated the conditions for the stability of the detonation process and the appearance of the oscillations. The frequency of oscillations matched very well with the experimental data.

Matsuo et al. [24] simulated the regular and large disturbance regime cases of Ruegg and Dorsey [6] using two-step chemistry model. With a series of simulations the large disturbance regime was explained with a new one-dimensional wave-interaction model. Their results revealed that the intensity of heat release was a key parameter in determining the regime of the unsteady flow. Flow features of the unsteady combustion with low-frequency and high-amplitude oscillation, known as large-disturbance regimes, are reproduced when the concentration of the heat release is very high. For moderately high heat release, a high-frequency, low-amplitude periodic unsteadiness that belongs to regular regimes was observed.

Ahuja et al. [25]-[29] used the Navier-Stokes equations with a nine-species and eighteen-reactions and seven-species and seven-reaction H_2-air reaction model to simulate Lehr's Mach 5.11 and 6.46 cases. They used both shock-capturing and shock-fitting method to resolve the flow field for the above two cases. Shock-fitting method gave much better results with all the intricate flow features very well resolved. The Mach 5.11 case was found to be unsteady while the Mach 6.46 case was macroscopically stable.

10

The frequency of oscillations was found to be in good agreement with the experimental frequency. Ahuja et al. [30] also simulated Ruegg and Dorsey's [6] regular and large-disturbance cases and tied their numerical results with Matsuo and Fujiwara's [24] one-dimensional wave-interaction model to explain the large-disturbance regime.

All the investigations considered so far dealt with ballistic range experiments and their simulations. The primary focus was on blunt bodies, i.e., detached detonation waves. Attention will now be diverted to attached detonation waves, i.e., flow fields involving sharp nosed bodies. The experimental evidence of attached detonation waves is very sketchy, and even the experiments themselves are controversial.

Gross et al. [31] conducted a series of experiments involving shock-induced combustion/detonation in a H_2-air mixture. The experiments were conducted in a Mach 3-plus flow of H_2-air mixture at total temperature of 833 K. They claimed to have obtained a steady, planer and reproducible attached detonation wave. Pratt et al. [32] re-examined their results and concluded that what had been interpreted as an attached oblique detonation wave was in fact a non-reacting strong oblique shock formed due to shock-induced combustion downstream of the test section, off camera, which increased the back pressure and, thus, supported the strong shock wave.

Adelman et al. [33] designed a proof-of principle experiment to be conducted at the NASA Ames Research Center. But, they incorrectly identified the C-J turning angle as the maximum stabilization angle of the oblique detonation wave.

In the last few years, a large number of numerical computations involving attached detonation wave have appeared in the literature. Fort et al. [34] studied the shock induced combustion of premixed H_2-air over a ramp using the RPLUS code. The chemistry was modelled by an 18-step model. The simulations were carried out for various wedge angles for both viscous and inviscid flows, and it was concluded that any study of attached

11

oblique detonation wave that ignores viscous effects is incomplete, if not in error. Their results also showed an ignition hysteresis phenomena.

Singh et al. [35] conducted a numerical study to address the structural stability of an oblique detonation wave. They used Navier-Stokes equations coupled with a seven-species and seven-reaction H_2-air model. The viscous effects were included to account for the elliptic influence of the viscosity in the near lip region. All the calculations were time accurate. They concluded that an oblique detonation wave is a stable phenomenon as long as a sufficient amount of overdrive is present.

Li et al. [36] studied combustion mechanisms applicable to ram accelerators using numerical simulations. Their study showed that it is possible to generate steady detonation waves over wedge surfaces under appropriate flow and mixture conditions. They used the Flux-Corrected Transport (FCT) algorithm to solve mass, momentum, energy and species density equations. The chemical reactions were simulated by using a two step reaction model. In addition, all diffusive transport processes were neglected.

The instability in the structure of the reaction front originates in the induction zone which separates the bow shock and the exothermic reaction front in the nose region of the flow field and then spreads outwards. In order to capture the physical instabilities, the calculations must be carried out for long times to ensure that all relevant time scales are being captured. Since all numerical schemes have some numerical diffusion, which is dependent on the grid resolution, a coarse grid may damp these oscillations. Further, the numerical damping added to the scheme in the vicinity of the reaction front may damp or alter the instability modes. The objective of this study is to investigate, in detail, the shock-induced combustion phenomena for the premixed stoichiometric H_2-air mixture flow at hypersonic speeds. The analysis is carried out using the axisymmetric version of the SPARK2D code [37], which incorporates a 7-species, 7-reactions combustion

12

model for hydrogen-air mixture. The code also incorporates a 9-species and 18-reactions

hydrogen-air model. The code has both shock-capturing and shock-fitting capabilities.

13

Chapter 2

PHYSICAL PROBLEMS AND CONCEPTS

In this chapter we shall be explaining some of the shadowgraphs of Lehr [11] and

Ruegg and Dorsey [6]. Later in the chapter some of the concepts of shock-induced

combustion shall be discussed followed by various models to explain some of the

phenomenon in shock-induced combustion.

To help explain the experimental shadowgraphs, a schematic of shock-induced

combustion is shown in Fig. 2.1. The figure depicts a supersonic, one-dimensional

flow of combustible gas which encounters a stationary normal shock. The temperature

upstream of the shock is too low for combustion but the temperature behind the shock

is high enough to induce combustion. As the gas passes through the shock, the rise in

temperature initiates the chemical reactions which leads to burning. Because it takes

time for the gas to reach the ignition temperature, the gas during that time shall travel

downstream before ignition can occur if the fluid motion is relatively fast. This cause a

separation between the bow shock and the energy release front. This separation between

the bow shock and the energy release front is referred to as the induction zone. The

induction zone is characterized by an almost constant values for the fluid quantities

such as temperature, density, and pressure after the shock. The length of the ignition

zone is determined by the ignition time at the post-shock conditions and the fluid speed

downstream of the shock. The pressure across the energy release front is nearly constant,

the temperature rises, and the density drops. After the energy release front, pressure rises,

while temperature and density relatively remains constant. What we observed in a tube

14
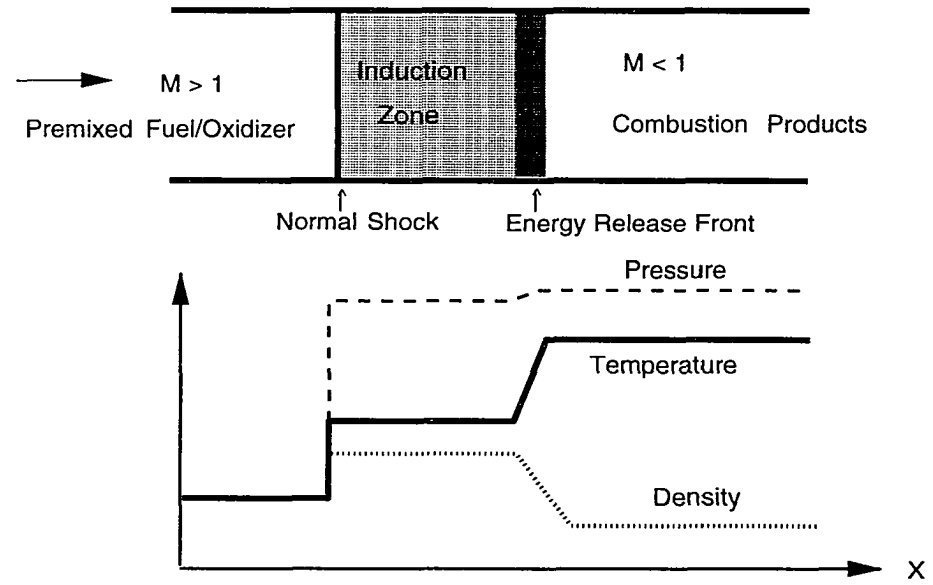
Figure 2.1   Schematic of shock-induced combustion.

filled with combustible gas mixture can also take place in external flows where a blunt projectile is fired in a combustible gas mixture.

2.1 Experimental Work of H. F. Lehr

In 1972 Lehr [11] conducted a detailed experimental study for a wide range of projectile shapes and combustible mixtures. The experimental shadowgraphs of Lehr were chosen to support the numerical simulations presented in this work. This is because the quality of the shadowgraph available is excellent and therefore numerical results can be more clearly tied to the experimental results. In Lehr's work spherical nosed projectiles of 15 mm diameter were fired in stoichiometric hydrogen-air mixtures for a range of Mach numbers so that both steady and unsteady flow phenomenon are represented. In unsteady cases only regular regimes are included in his work. Table 2.1 at the end of the chapter describes the various free-stream conditions used in Lehr's work and the corresponding frequencies of oscillations. In the current numerical simulations we have chosen two cases from the spectrum of cases of Lehr's work. These are Mach 5.11 and 6.46 cases. Reason we choose Mach 5.11, because it is the most controvercial case. Experimentally it has been observed that Mach 5.11 shows instabilities in the reaction front whereas numerically no researcher has ever been able to show these instabilities. Though for lower than Mach 5.11, earliar researchers have successfully simulated the instabilities. Mach 6.46 is the superdetonative case where the instabilities disapperas.

Ballistic range shadowgraph pictures for Mach 5.11 and Mach 6.46 from Lehr's experiments are shown in Figs. 2.2 and 2.3, respectively. In both cases, a free-stream temperature of 292 K and a pressure of 42663.2 N/m^2 (320 mm of Hg) is used along with a stoichiometric mixture of hydrogen-air. The projectile diameter was 15 mm. At these conditions the C-J Mach number of the mixture is 5.11.

Figure 2.2 shows two discontinuities separated from each other. The outer front

17
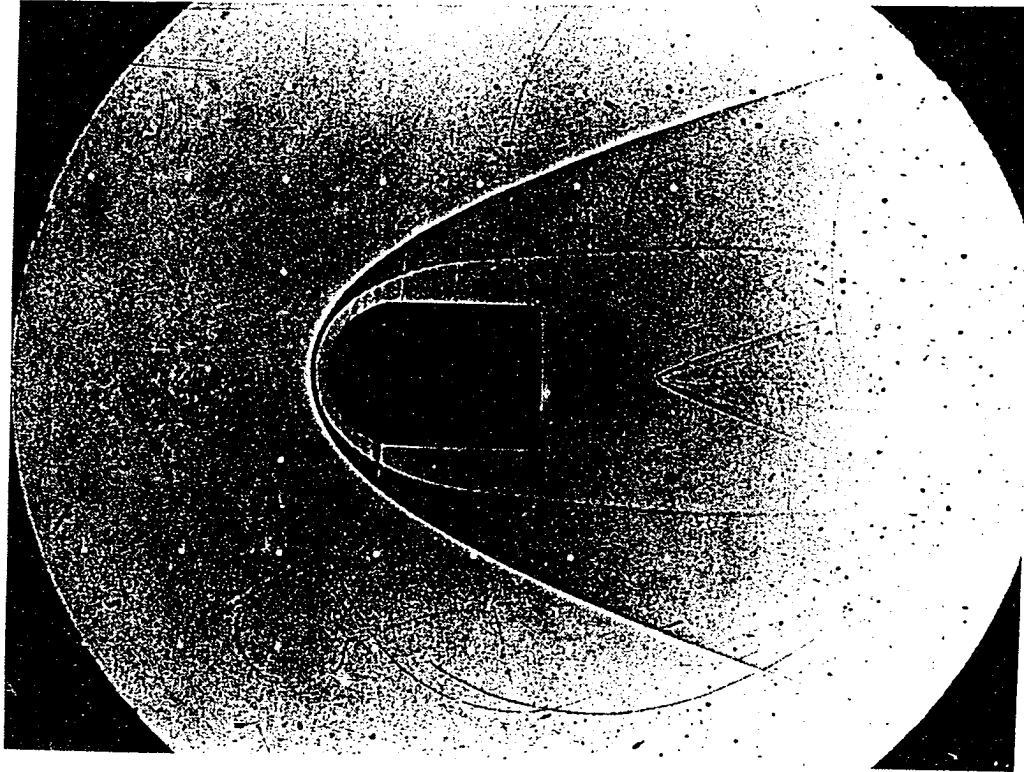
Figure 2.2   Shadowgraph of a spherical nose projectile moving at Mach 5.11 into a premixed stoichiometric hydrogen-air mixture (Courtesy of Dr. H. F. Lehr).

18
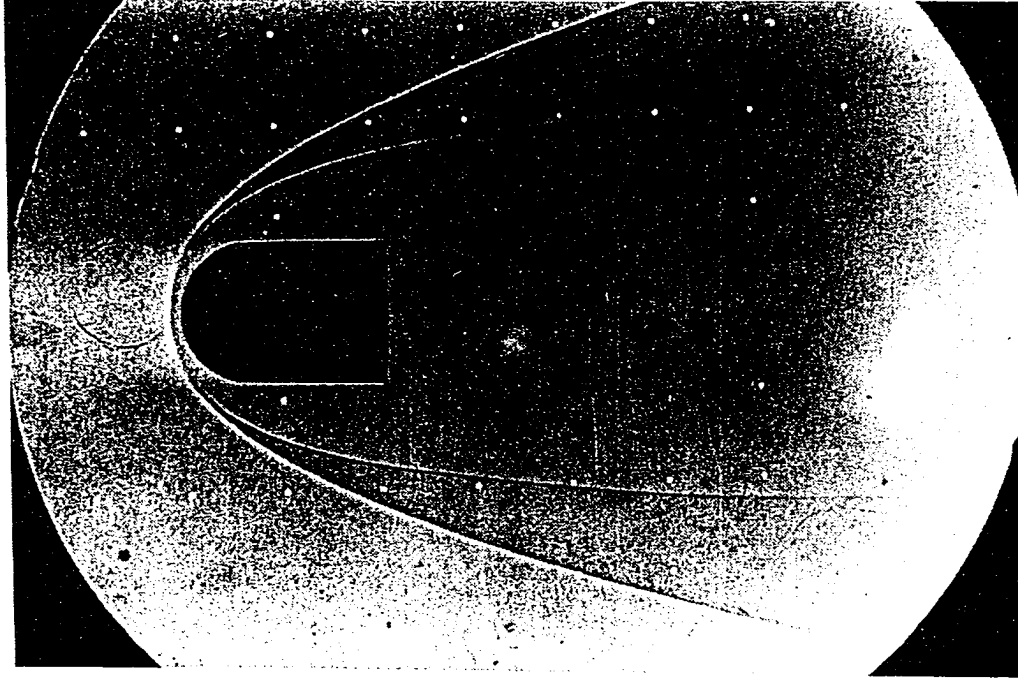
Figure 2.3 Shadowgraph of a spherical nose projectile moving at Mach 6.46 into a premixed stoichiometric hydrogen-air mixture (Courtesy of Dr. H. F. Lehr).

is the bow shock and the inner front is the reaction front produced by ignition of the heated H_2-air mixture. The separation between the shock front and the reaction front is called an induction zone. The separation between the two is minimum near the stagnation point and increases as the shock curves around the body, due to increase in induction distance (decrease in post shock temperature) away from the stagnation zone. In general, the ignition time is inversely related to the temperature because the chemical reactions proceed faster (and the separation becomes smaller) with increasing temperature. A close examination of the shadowgraphs reveals that as the flow crosses the bow shock, the color changes from light to dark, indicating an increase in density. But, as the flow crosses the reaction front, the color changes from dark to light, indicating a decrease in density across the reaction front. This is due to a large release of energy across the reaction front, causing an increase in the temperature; since the pressure remains relatively constant, the density must decrease. Another interesting feature is the presence of corrugation in the reaction front. These corrugations are caused by the pulsation of the reaction front. The frequency of this pulsation was determined to be 1.96 MHz [11, 38].

Figure 2.3 is for the Mach 6.46 case, and it is seen that the reaction front is coupled with the shock near the stagnation line and up to about 60–65 degree body angle from the stagnation line. This is because of a very high post-shock temperature at Mach 6.46 that causes the induction zone to become so narrow that it appears that the two fronts are merged with each other. Decoupling begins further downstream from the stagnation line when the post-shock temperature starts decreasing and, therefore, the induction distance increases. Further, both the bow shock and the reaction fronts are smooth without any visible instabilities. Thus for an overdriven case of Mach 6.46, the instabilities have disappeared. References [11, 38] show other underdriven cases where it has been shown that the instabilities in the reaction front become more pronounced as we reduce the

19

projectile velocity lower than the C-J velocity of the mixture. In all these cases the projectile diameter was fixed as 15 mm.

2.2 Experimental Work of Ruegg and Dorsey

Depending upon the magnitude of various parameters, the detonation wave can be stable or unstable. Further, the instabilities in the detonation-wave structure can be highly periodic; these instabilities are termed as "regular regime". The instabilities can also be highly pronounced and irregular with large-amplitude oscillations and a distorted bow shock. These oscillations have been classified in the literature as the "large-disturbance regime". Ruegg and Dorsey [6] fired a projectile with a diameter of 20 mm in a stoichiometric hydrogen-air mixture at various free-stream pressures and Mach numbers. Tests were made at pressures from 0.026 to 1 atm (absolute) and at Mach numbers up to 6.5. The effects of combustion on the wave shape and position were detected at pressures of 0.1 atm and higher and for a range of Mach numbers from 4 to 6.5. Results between pressures of 0.5 and 1 atm were qualitatively similar. When the Mach number was kept approximately constant in the range of 4.8 to 5 and only the free-stream pressure was changed from 0.1 to 0.25 atm, the reaction front changed from a stable to a periodic unstable front. For the same Mach-number range, the reaction front instabilities became highly pronounced (with large amplitudes) and irregular when the pressure was increased to 0.5 atm. The bow shock was completely distorted by the reaction front, and the period of oscillation became much higher than the regular periodic case.

In the present study, some of the cases of Ruegg and Dorsey's [6] experimental work have been simulated numerically to demonstrate the transition from steady regime to regular unsteady regime to large-disturbance unsteady regime as the free-stream pressure is changed from 0.1 to 0.25 to 0.5 atm (the free-stream Mach number is kept approximately constant around 5). Table 2.2 at the end of this chapter describes the

20
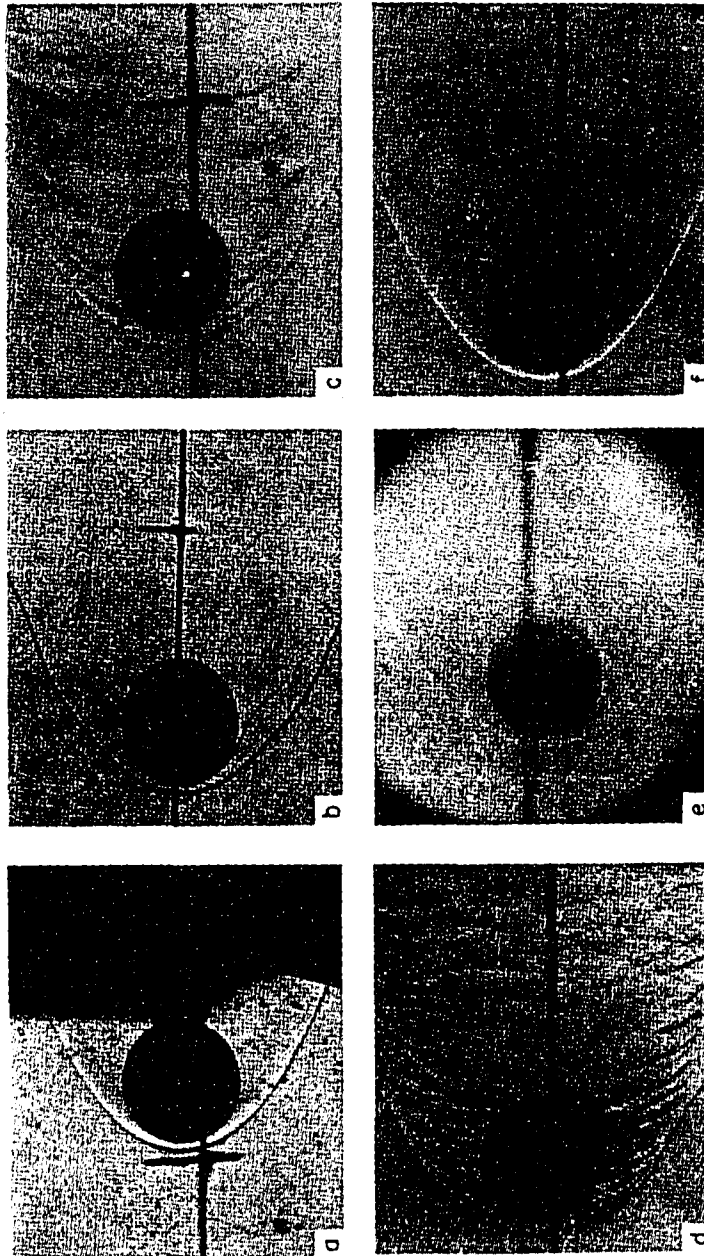
Figure 2.4 Ruegg and Dorsey's ballistic experiments shadowgraphs (a) M=5.4; p=0.5 atm; Air (b) M=4.3; p=0.5 atm, (c) M=4.8; p=0.5 atm (d) M=5.5; p=0.5 atm (e) M=6.3; p=0.5 atm and (f) M=5.0; p=0.1 atm.

21
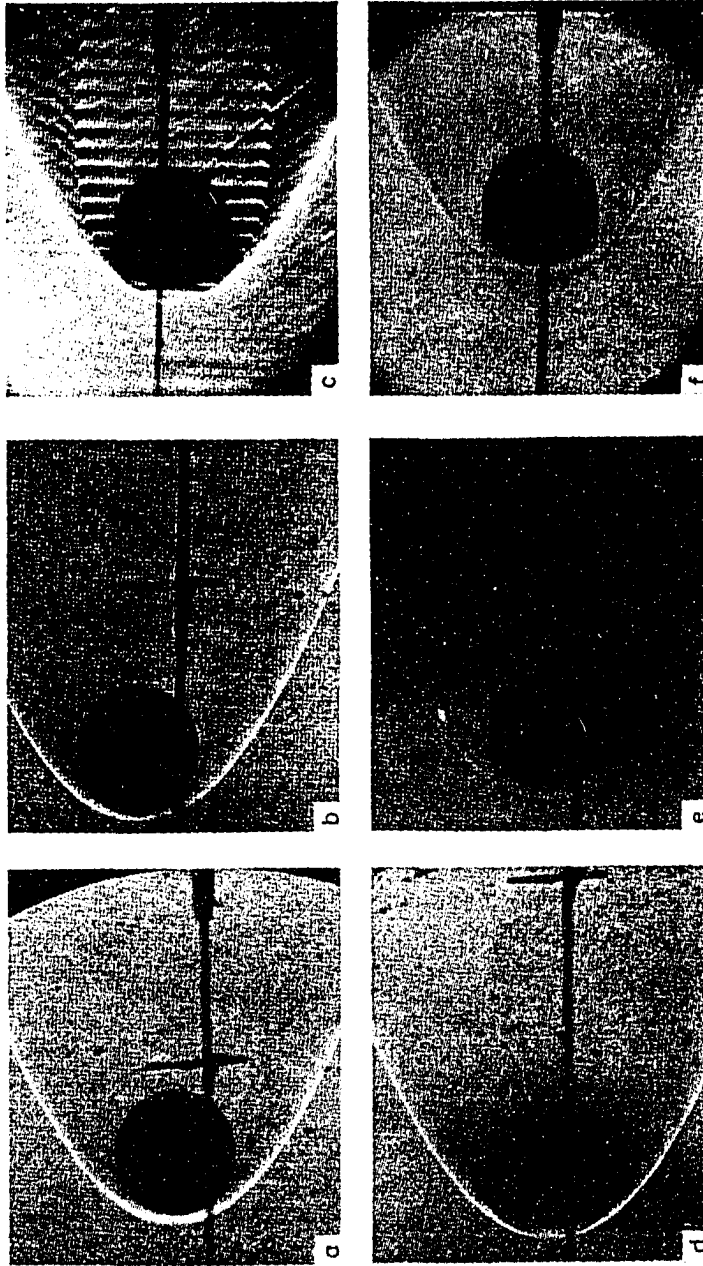
Figure 2.5 Ruegg and Dorsey's ballistic experiments shadowgraphs for p=0.25 atm (a) M=4.4; .3H$_2$ + .7N$_2$ (b) M=4.5 (c) M=4.9 (d) M=5.1 (e) M=5.9 and (f) M=6.5.

22
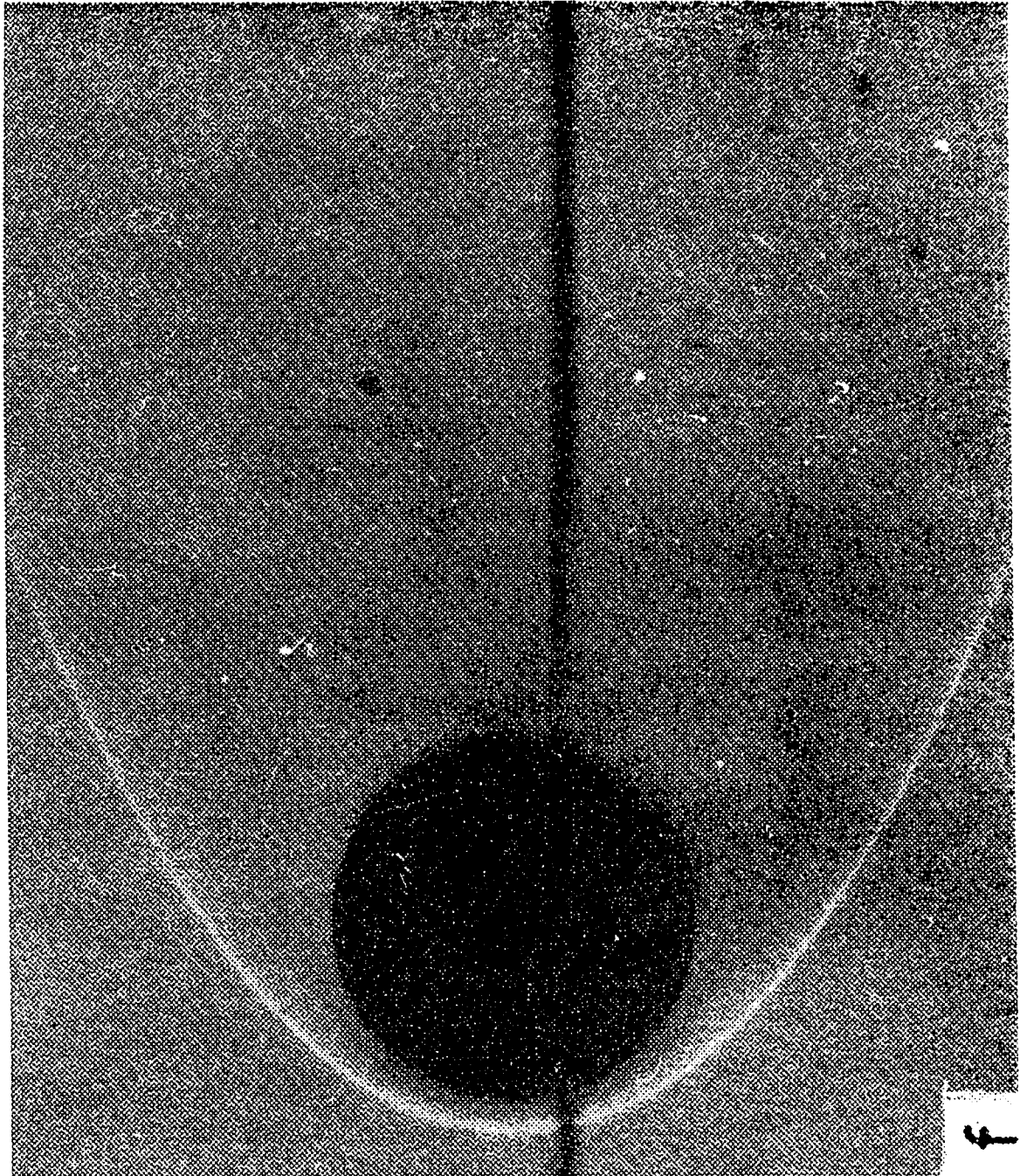
Figure 2.6 Enlarged experimental shadowgraph for M=5.0; p=0.1 atm.

23
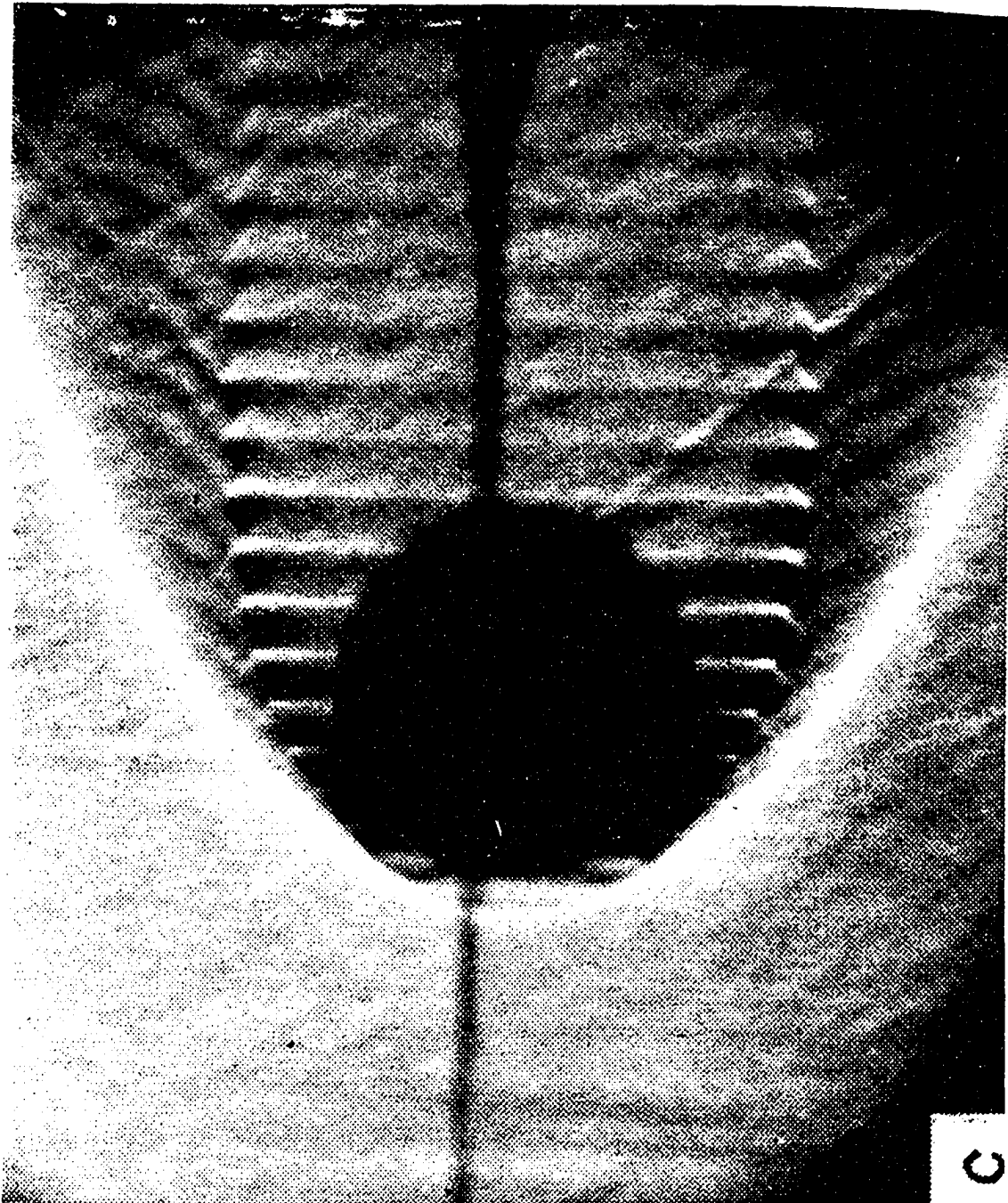
Figure 2.7 Enlarged experimental shadowgraph for M=4.9; p=0.25 atm.

24
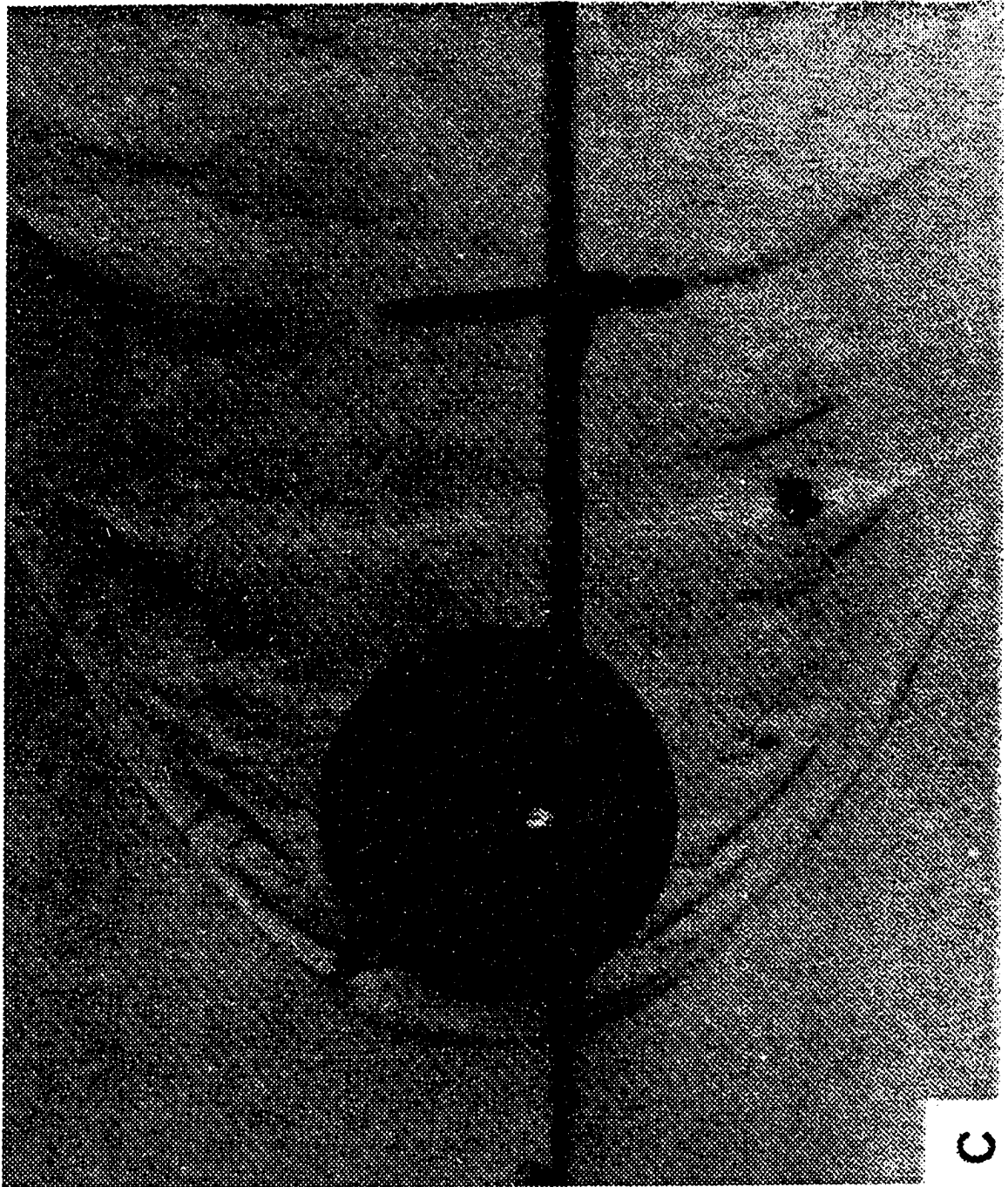
Figure 2.8 Enlarged experimental shadowgraph for M=4.8; p=0.5 atm.

25

various free-stream conditions used in Ruegg and Dorsey's work. Figures 2.4 and 2.5 show schlieren shadowgraphs of a series of experiments done by Ruegg and Dorsey [6] under various free-stream Mach-number and pressure conditions. Figure 2.4a is the schlieren shadowgraph of the missile in air; Fig. 2.5a is the shadowgraph for the same missile fired in a mixture of nitrogen and hydrogen. These results are presented here for comparison with those in the combustible gas. Figures 2.4 and 2.5 show additional results for the stoichiometric mixture of H_2 and air. At M = 4.3 and p = 0.5 atm, Fig. 2.4b shows a discrete region of reaction front that surrounds the sphere. A smooth bow shock is also visible. As the Mach number is increased, the reaction front and shock front merge to give smooth and continuous discontinuities at M = 6.3, as shown in Fig. 2.4e. However, at a pressure of 0.5 atm and M = 4.8 as shown in Fig. 2.4c and at M = 5.5 as shown in Fig. 2.4d, the bow shock and the reaction fronts are completely distorted. The oscillations in the reaction front become pronounced due to high heat-release rates. Figure 2.4f shows the results for M = 5.0 and p = 0.1 atm. At this low pressure, the bow shock and the reaction front are both smooth and are separated from each other by a large induction region.

When p = 0.25 atm (Figs. 2.5b-2.5f), a dark combustion wave is clearly visible. For M = 4.5 and p = 0.25 atm, Fig. 2.5b clearly shows the smooth bow shock and the reaction front separated near the stagnation region; this separation increases as we move away from the stagnation region. The key point to emphasize here is that both the bow shock and the reaction front are smooth, with no visible oscillations. An increase in Mach number to 4.9, as shown in Fig. 2.5c, triggers periodic instabilities. The bow shock is nearly smooth; however, the reaction front appears highly periodic. A further increase in Mach number from M = 4.9 (Fig. 2.5c) to M = 5.1 (Fig. 2.5d) to M = 6.5 (Fig. 2.5f), causes these instabilities to disappear. Consequently, a smooth reaction front

26

evolves, which merges with the bow shock. The separation between the bow shock and the reaction front (i.e., the induction zone) decreases continuously in Figs. 2.5d through 2.5f as the Mach number increases. This decrease results from the high post-shock temperature, which causes the two fronts to nearly merge.

In the present study, we simulate three cases. The first case corresponds to Fig. 2.4f at Mach number of 5 and pressure of 0.1 atm. This case is steady; the reaction and shock fronts are smooth. The second case corresponds to Fig. 2.4c at M = 4.8 and p = 0.5 atm. This case is a large-disturbance regime case; it shows a distorted bow shock and large-amplitude nonperiodic oscillations of the reaction front. The last case is shown in Fig. 2.5c; here, p = 0.25 atm and M = 4.9. In this case, the bow shock is separated from the reaction front by an induction zone. The bow shock is quite smooth, but the reaction front shows periodic oscillations. This case is a regular-regime case. Figures 2.4f, 2.5c, and 2.4c are enlarged for clarity in Figs. 2.6, 2.7 and 2.8 respectively. Wave-detachment distances for the shock wave and the combustion wave are compared with experimental and analytical results. The results are interpreted with the concepts developed by Oppenheim et al. [12] and the model developed by Matsuo et al. [24]. Simulations are carried out with the shock-fitting technique.

2.3 McVey and Toong's One-Dimensional Wave-Interaction Model

In order to explain the instabilities in the reaction front both in Lehr's Mach 5.11 case and Ruegg and Dorsey's regular regime case, McVey and Toong proposed a one-dimensional wave interaction model. An x-t diagram of the complete cycle of events for the postulated instability model is shown in Fig. 2.9. The figure contains the features along the stagnation streamline in time. The steps referred to in the following are designated in the figure. The cycle of events starts at a time when the contact discontinuity approaches the original reaction front. At Step 2 the hot gases behind the contact discontinuity begins

27

28
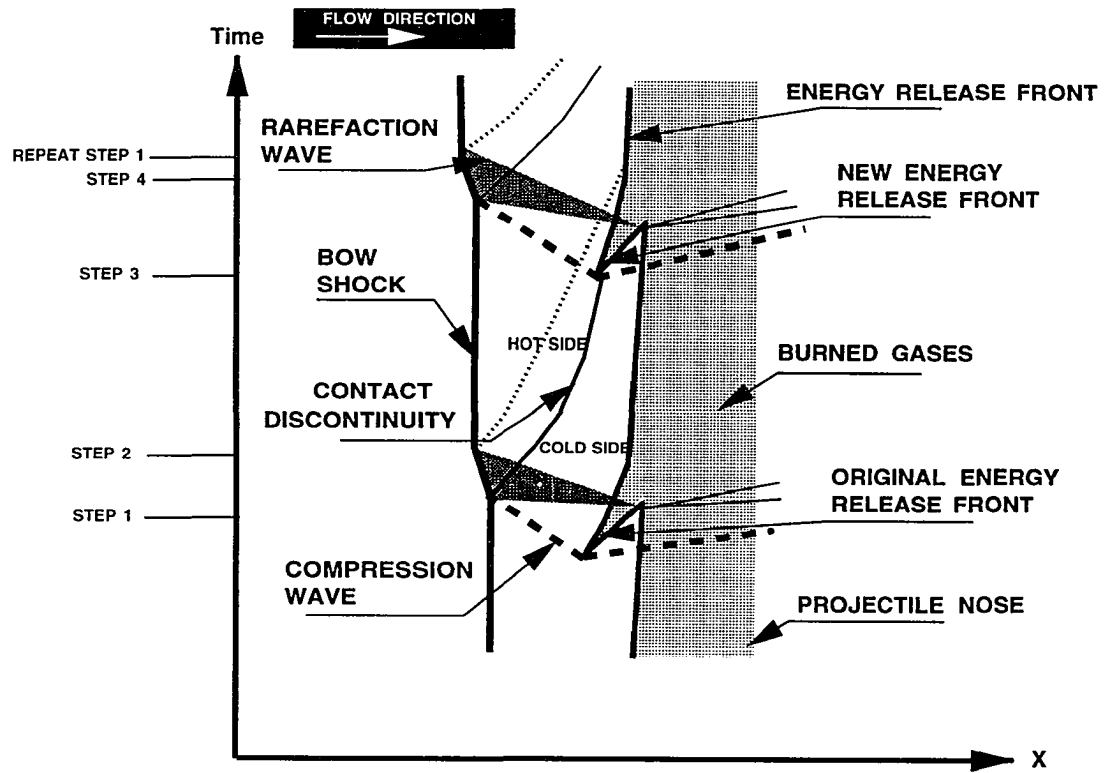
Figure 2.9   McVey and Toong's one-dimensional wave-interaction model.

to react, generating compression waves which propagates upstream and downstream. At a somewhat later time (Step 3), the contact discontinuity reaches the position of the original reaction front, extinguishing the reaction at this point and generating rarefaction waves. The reaction front begins to recede because of the increasing induction time of the colder fluid within the entropy zone. At a later time (Step 4), the compression wave generated earlier at the new reaction front interacts with the bow shock, thus strengthening it, reflecting a weak rarefaction, and producing another contact discontinuity. The incident rarefaction generated by the extinguishing of the original reaction front penetrates the bow shock, thus weakening it, and generating a zone of decreasing entropy. The cycle of events is completed as the contact discontinuity followed by the zone of decreasing entropy approaches the receded reaction front (Step 1).

McVey and Toong described how the compression waves and contact discontinuities present in the interaction model can explain the various features observed in experimental shadowgraphs.

The interaction model of the Alpert and toong added more complexity to the model of McVey and Toong by accounting for the strength of the compression waves created by the exothermic reactions in the new energy-release front. Accounting for such effects was deemed necessary to investigate the large-disturbance regime because it had been observed that the oscillations in this regime were more likely to occur when the Damköhlar parameter (the ratio of chemical energy released to the sensible energy present before reaction) was large. The Alpert and Toong mechanism theorizes that four periods of a type similar to the model by McVey and Toong occur within each large-disturbance period. Each of the McVey and Toong type of interactions are slightly different and occur in such a way that one of them is re-enforced and effects the flow much more than the others. This could cause the irregular behavior observed in the large-disturbance case.

29

Because of the complexity of the Alpert and Toong mechanism we shall not discuss this method here. Instead we shall be using another simple model developed by Matsuo and Fujiwara [24] to explain the large-disturbance regime case.

2.4 Matsuo and Fujiwara's One-Dimensional Wave-Interaction Model

The wave interaction in the regular regime case of Lehr or Ruegg and Dorsey showed a completely different structure from that of the large-disturbance regime of Ruegg and Dorsey. The regular corrugated structure of regular regime disappears in the large-disturbance regime case and is replaced by a non-periodic oscillations of large amplitude. The oscillations become much more pronounced with low frequency and high amplitude. Further the period of oscillations for large-disturbance regime is 4–5 times that of the regular regime case. The mechanism of the large disturbance regime is also dominated by the wave interactions but the role of wave and interactions change from those of the regular regime.

The most important point of the mechanism of the regular regime is different induction time before and behind the contact discontinuity. On the other hand, the large-disturbance regime shows a new feature of periodicity. The extremely strong exothermicity occurs on the reaction front, and causes the strong reaction shock toward the bow shock and the body surface. The reaction shock is so strong that the gas behind the reaction shock is compressed very much, and the exothermic reaction follows and accelerates the reaction front. The phenomenon is considered to be onset of " explosion within an explosion", producing two strong shock waves in opposite directions. The forward shock is referred to as "superdetonation" and moves into unburned gas. In the opposite direction a shock moves into the burned gas and is known as "retonation". The mechanism is usually observed as a typical example of deflagration-to-detonation transition (DDT).

30
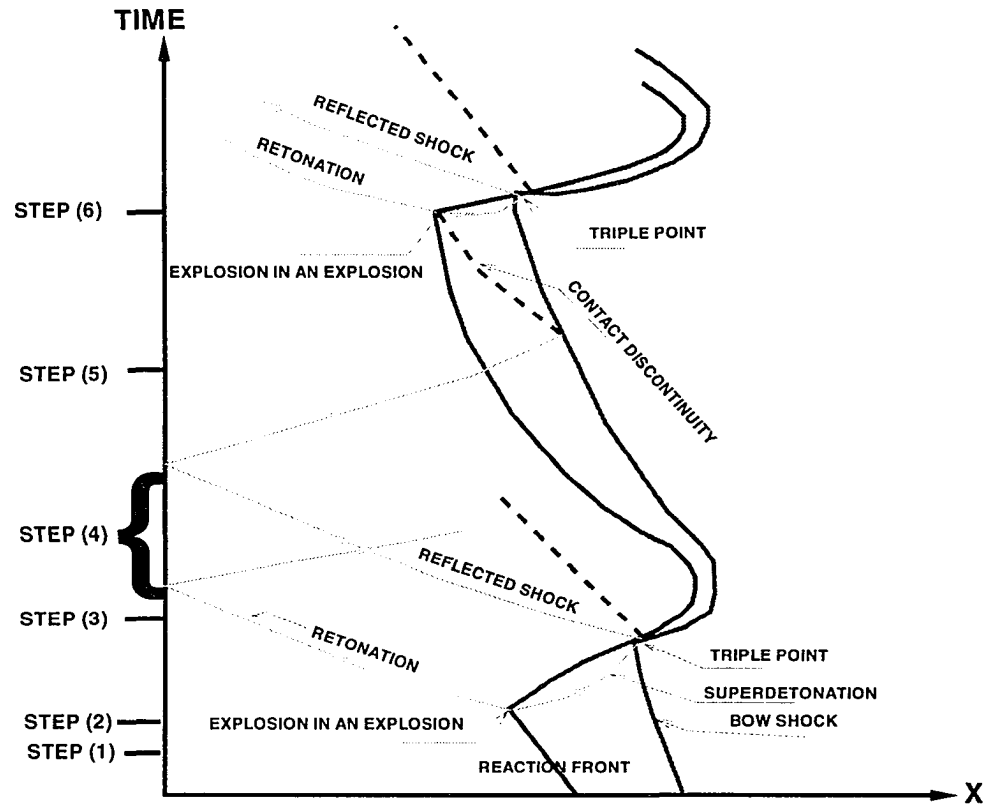
Figure 2.10 Matsuo and Fujiwara's one-dimensional wave-interaction model.

The detonation wave in the unburned gas behind the bow shock overtakes and penetrates the bow shock, then the reflected shock and the contact discontinuity are generated. The intersection point of the bow shock, the detonation wave and the reflected shock is called the triple point which is usually observed in the detonation wave structure. After the penetration, the detonation wave cannot develop the self sustained detonation in front of the projectile body. Eventually the bow shock wave accelerated by the penetration of the detonation wave with respect to the projectile body is decelerated, and the transition from detonation to shock-deflagration system, which is the ordinary shock-induced combustion appears.

Figure 2.10 is the model proposed by Matsuo and Fujiwara to explain the large-disturbance regime. The steps to be referred in the following are indicated by the bracketed numbers in the left hand margins of Fig. 2.10. The beginning of the cycle is shown at Step 1, when "explosion within an explosion" occurs on the reaction front, and then the reaction shocks propagate upstream and downstream. The forward shock referred to as "superdetonation" moves into the unburned gas, and the backward shock referred to "retonation" moves into the burned gas. The superdetonation speed is much faster than the retonation speed due to acceleration by the following reaction front. At Step 2, the detonation wave overtakes and penetrates the bow shock. Then the bow shock and the detonation wave creates a triple point and generates a reflected shock and a contact discontinuity. The bow shock is accelerated by the penetration, and the gas behind the bow shock is much compressed. At Step 3, the bow shock is decelerated and the bow shock and the reaction front becomes separated. At Step 4, the retonation wave and the reflected shock reach the body surface and the reflected compression waves go to the bow shock. The reflected compression wave interacts with the bow shock at Step 5, and the contact discontinuity is created. The temperature behind the contact discontinuity

32

is higher than that before it, so that the induction time becomes shorter. At Step 6, the contact discontinuity reaches the original reaction front, and the "explosion within an explosion" occurs on it and the cycle of events is completed.

Table 2.1 H. F. Lehr's Experimental Ballistic-Range Data

Projectile diameter = 15 mm

Free-stream pressure = 0.42 atm. (320 mm of Hg)

Free-stream temperature = 292°K

Combustible gas: stoichiometric hydrogen-air mixture

$$2H_2 + O_2 + 3.76N_2 \rightarrow 2H_2O + 3.76N_2$$
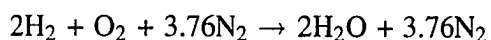
Mach No.	Free-stream velocity, u (m/sec)	$\frac{\text{Free-stream velocity (u)}}{\text{Detonation velocity (D)}} \left(\frac{m}{sec}\right)$	Frequency f(MHz)
6.46	2605	1.27	- - - -
5.11	2058	1.00	1.96
5.04	2029	0.99	1.04
4.79	1931	0.94	0.72
4.18	1685	0.82	0.15

Table 2.2 Free-Stream Conditions for Ruegg and Dorsey's Data

Projectile diameter = 20 mm

Combustible gas: stoichiometric hydrogen-air mixture

$$2H_2 + O_2 + 3.76N_2 \rightarrow 2H_2O + 3.76N_2$$
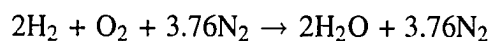
Mach No.	p_∞, atm	T_∞, ° K	Case
5.0	0.1	300	Steady Regime
4.9	0.25	300	Regular Unsteady Regime
4.8	0.5	300	Large-Disturbance Unsteady Regime

34

Chapter 3

GOVERNING EQUATIONS AND METHOD OF SOLUTION

In this chapter we shall be describing the basic governing equations used to numerical simulate the physical problem for the chemically reacting flows. Also detailed chemistry and thermodynamics models used shall be discussed. Finally, to include the effects of diffusion of momentum, energy and mass, kinetic theory based diffusion transport models are incorporated into the program. Details of the models shall be discussed.

3.1. Basic Governing Equations

The physical model for analyzing the flow field is described by the Navier-Stokes and species continuity equations. For two-dimensional planar or axisymmetric flows, these equations are expressed in physical coordinates as

$$\frac{\partial U}{\partial t} + \frac{\partial F}{\partial x} + \frac{\partial G}{\partial y} = H \qquad (3.1)$$

where vectors U, F, G, and H are written as

$$U = \begin{bmatrix} \rho \\ \rho u \\ \rho v \\ \rho E \\ \rho f_i \\ \cdot \\ \cdot \end{bmatrix}$$

$$F = \begin{bmatrix} \rho u \\ \rho u^2 - \sigma_x \\ \rho u v - \tau_{xy} \\ (\rho E - \sigma_x)u - \tau_{xy}v + q_x \\ \rho f_i(u + \tilde{u}_i) \\ \cdot \\ \cdot \end{bmatrix}$$

35

$$G = \begin{bmatrix} \rho v \\ \rho u v - \tau_{xy} \\ \rho v^2 - \sigma_y \\ (\rho E - \sigma_y)v - \tau_{xy}u + q_y \\ \rho f_i(v + \tilde{v}_i) \\ \cdot \\ \cdot \end{bmatrix}$$

For axisymmetric flow,

$$H = \frac{1}{y} \begin{bmatrix} \rho v \\ (\rho v u + \tau_{xy}) \\ \rho v^2 + \tau_{yy} - \tau_{\theta\theta} \\ (\rho E + p + \tau_{yy})v + \tau_{xy}u + q_y \\ \omega_i \\ \cdot \\ \cdot \end{bmatrix}$$

and for planar flow

$$H = \frac{1}{y} \begin{bmatrix} 0 \\ 0 \\ 0 \\ 0 \\ \dot{\omega}_i \\ \cdot \\ \cdot \end{bmatrix}$$

The other terms that appear in the vectors **F**, **G**, and **H** are defined as

$$\sigma_x = -p + 2\mu \frac{\partial u}{\partial x} + \lambda \nabla . u \tag{3.2}$$

$$\sigma_y = -p + 2\mu \frac{\partial v}{\partial y} + \lambda \nabla . u \tag{3.3}$$

$$\tau_{xy} = \mu \left(\frac{\partial u}{\partial y} + \frac{\partial v}{\partial x} \right) \tag{3.4}$$

$$\tau_{yy} = -\frac{2}{3}\mu \left(2\frac{\partial v}{\partial y} - \frac{v}{y} - \frac{\partial v}{\partial x} \right) \tag{3.5}$$

36

$$\tau_{\theta\theta} = -\frac{2}{3}\mu\left(2\frac{v}{y} - \frac{\partial v}{\partial y} - \frac{\partial u}{\partial x}\right) \tag{3.6}$$

$$q_x = -k\frac{\partial T}{\partial x} + \rho\sum_{i=1}^{N_s} h_i f_i \tilde{u}_i \tag{3.7}$$

$$q_y = -k\frac{\partial T}{\partial y} + \rho\sum_{i=1}^{N_s} h_i f_i \tilde{v}_i \tag{3.8}$$

$$p = \rho R_u T \sum_{i=1}^{N_s} \frac{f_i}{M_i} \tag{3.9}$$

$$E = \sum_{i=1}^{N_s} h_i f_i - \frac{p}{\rho} + \frac{u^2 + v^2}{2} \tag{3.10}$$

In Eq. (3.1), only (N_s-1) species equations must be considered in the formulation because the mass fraction of the species is prescribed by satisfying the constraint equation

$$\sum_{i=1}^{N_s} f_i = 1 \tag{3.11}$$

The binary diffusion equation for the diffusion velocity of the i th species

$$\tilde{u}_i = \tilde{u}_i i + \tilde{u}_j j \tag{3.12}$$

is

$$\nabla X_i = \sum_{j=1}^{N_s}\left(\frac{X_i X_j}{D_{ij}}\right)(\tilde{u}_j - \tilde{u}_i) + (f_i - X_i)\left(\frac{\nabla p}{p}\right) \tag{3.13}$$

Note that this equation must be applied only to (N_s-1) species. The diffusion velocity for the remaining species is prescribed by satisfying the constraint equation $\sum_{i=1}^{N_s} f_i \tilde{u}_i = 0$, which ensures consistency. In Eq. (3.13), we assume that the body-force vector per unit

37

mass is negligible. In addition, thermal diffusion is assumed considered to be negligible in comparison with the binary diffusion coefficient.

3.2. Thermodynamic Model

In order to calculate the thermodynamic quantities, the specific heat for each species is first calculated by a fourth-order polynomial in temperature:

$$\frac{C_{p_i}}{R_i} = A_i + B_i T + C_i T^2 + D_i T^3 + E_i T^4 \tag{3.14}$$

The coefficients A_i, B_i, C_i, D_i, and E_i for each species are found by a curve fit of the data tabulated in Ref. 39. Once we know the specific heat of each species, the enthalpy of each species can then be found from

$$h_i = h_i^R + \int_{T^R}^{T} C_{p_i} dT \tag{3.15}$$

and then the total internal energy can be calculated from Eq. (3.10). In order to determine the equilibrium constant (which we shall be needing in the next section) for each chemical reaction being considered, we need the information about the Gibbs energy of each species. For a constant pressure process, C_p/R from the above Eq. (3.14) is first integrated over temperature to define the entropy of the species, and the resulting expression is integrated again over temperature to obtain the following fifth-order polynomial in temperature for the Gibbs energy of each species:

$$\frac{g_i}{R_i} = A_i T(1 - \ln T) - \left(\frac{B_i}{2}\right) T^2 - \left(\frac{C_i}{6}\right) T^3 - \left(\frac{D_i}{12}\right) T^4 - \left(\frac{E_i}{20}\right) T^5 + F_i - G_i T \quad (i = 1, \dots N_s) \tag{3.16}$$

Coefficients F_i and G_i are defined in Ref. 39. The Gibbs energy of reaction can then be calculated as the difference between the Gibbs energy of product species and reactant species.

$$\Delta G_{R_j} = \sum_{i=1}^{N_s} \nu_{ji}'' g_i - \sum_{i=1}^{N_s} \nu_{ji}' g_i \quad (j = 1, \dots N_r) \tag{3.17}$$

38

The equilibrium constant for each reaction is then found from

$$\kappa_{eq_j} = \left(\frac{1}{R_u T}\right)^{\Delta n_j} \exp\left(\frac{-\Delta G_{R_j}}{R_u T}\right) \qquad (j = 1, \dots N_r) \qquad (3.18)$$

where

$$\Delta n_j = \sum_{i=1}^{N_s} \nu_{ji}'' - \sum_{i=1}^{N_s} \nu_{ji}' \qquad (j = 1, \dots N_r) \qquad (3.19)$$

and is the change in the number of moles when going from reactants to products.

3.3 Chemistry Model

In the current simulations, a finite-rate chemical reaction of gaseous hydrogen fuel and air has been used. That reaction is modeled by two different ways. The reactions are first modeled by 9–species, 18–reaction. Next the reactions are modeled by 7–species and 7–reactions. Both the models are shortened versions of the Jachimowski's original 13–species and 33 reactions hydrogen-air model. In the nine species model eight of the chemical species (H_2, O_2, H_2O, OH, H, O, HO_2, H_2O_2) are active, and the ninth (N_2) is assumed inert.

Chemical-reaction-rate expressions are usually determined by summing the contributions from each relevant reaction path to obtain the total rate of change of each species. Each path is governed by a law-of-mass-action expression in which the rate constants can be determined from a temperature-dependent Arrhenius expression. The forward rate for each reaction j is determined from the modified Arrhenius law

$$\kappa_{f_j} = A_j T^{\alpha_j} \exp\left(\frac{-\epsilon_j}{R_u T}\right) \qquad (j = 1, \dots N_r) \qquad (3.20)$$

The appropriate constants A_j, α_j, and ϵ_j for the H_2-air reaction system can be found in Table 4.1. Knowing the forward rate, and using the equilibrium constant determined in the previous section, the backward rate can be defined by

$$\kappa_{b_j} = \frac{\kappa_{f_j}}{\kappa_{eq_j}} \qquad (j = 1, \dots N_r) \qquad (3.21)$$

39

Once we have determined the forward and reverse reaction rates, the production rates of the eight species (for 9-species and eighteen reaction model) or 6 species (for 7-species and 7-reaction model) can be found from the law of mass action. For the general N_r-step chemical reaction

$$\sum_{i=1}^{N_s} \nu'_{ji} S_i \rightleftharpoons \sum_{i=1}^{N_s} \nu''_{ji} S_i \quad (j = 1, \ldots N_r) \tag{3.22}$$

the law of mass action states that the rate of change of concentration of species i by reaction j is given by

$$\dot{C}_i = (\nu''_{ji} - \nu'_{ji}) \left(\kappa_{f_j} \prod_{m=1}^{N_s} C_m^{\nu'_{jm}} - \kappa_{b_j} \prod_{m=1}^{N_s} C_m^{\nu''_{jm}} \right) \tag{3.23}$$

All third-body efficiencies are assumed to be equal to 1.0. The net rate of change in concentration of species i by reaction j is then found by summing the contributions from each reaction,

$$\dot{C}_i = \sum_{j=1}^{N_r} \left(\dot{C}_i \right)_j \tag{3.24}$$

Finally, in the vector $\mathbf{H}$, in Eq. (3.1) the term ω_i represents the net rate of production of species i in all chemical reactions and is given by

$$\dot{\omega}_i = \dot{C}_i M_i \tag{3.25}$$

3.4 Diffusion Models

Models for the coefficients governing the diffusion of momentum, energy, and mass are now determined. The individual species viscosities are computed from Sutherland's law,

$$\frac{\mu}{\mu_0} = \left(\frac{T}{T_0} \right)^{3/2} \frac{T_0 + S}{T + S} \tag{3.26}$$

40

where μ_0 and T_0 are reference values and S is the Sutherland constant. All three values are tabulated for the species in Refs. 40 and 41. Once the viscosity of each species has been determined, the mixture viscosity is determined by Wilke's law (Ref. 42)

$$\mu_m = \sum_{i=1}^{N_s} \frac{\mu_i}{1 + \frac{1}{X_i} \sum_{j=1}^{N_s} X_j \phi_{ij}}$$ (3.27)

where

$$\phi_{ij} = \frac{\left\{1 + \left[\left(\frac{\mu_i}{\mu_j}\right)\left(\frac{\rho_j}{\rho_i}\right)\right]^{1/2}\left(\frac{M_i}{M_j}\right)^{1/4}\right\}^2}{\left(\frac{4}{\sqrt{2}}\right)\left[1 + \left(\frac{M_i}{M_j}\right)\right]^{1/2}}$$ (3.28)

The species thermal conductivities are also computed from Sutherland's law

$$\frac{k}{k_0} = \left(\frac{T}{T_0'}\right)^{3/2} \frac{T_0' + S'}{T + S'}$$ (3.29)

but with different values of the reference values k_0 and T'_0, and the Sutherland's constant S'. These values are also taken from Refs. 40 and 41. The mixture thermal conductivity is computed by using conductivity values for the individual species and Wassiljewa's formula (Ref. 43),

$$k_m = \sum_{i=1}^{N_s} \frac{k_i}{1 + \frac{1}{X_i} \sum_{j=1}^{N_s} X_j \phi'_{ij}}$$ (3.30)

where $\phi'_{ij} = 1.065\phi_{ij}$ and ϕ_{ij} is taken from Eq. 3.28.

For dilute gases, Chapman and Cowling used kinetic theory to drive the following expression for the binary diffusion coefficient D_{ij} between species i and j (Ref. 40):

$$D_{ij} = \frac{0.00185 8 T^{3/2} \left[\frac{(M_i + M_j)}{M_i M_j}\right]^{1/2}}{p\sigma_{ij}^2 \Omega_D}$$

Here, the diffusion collision integral Ω_D is approximated by

$$\Omega_D = T^{*-0.145} + (T^* + 0.5)^{-2}$$

41

where

$$T^* = \frac{T}{T_{\epsilon_{ij}}}$$

Values of the effective temperature T_ϵ and effective collision diameter σ are taken to be averages of the separate molecular properties of each species, giving (Ref. 40)

$$\sigma_{ij} = \frac{1}{2}(\sigma_i + \sigma_j)$$

and

$$T_{\epsilon_{ij}} = \left(T_{\epsilon_i} T_{\epsilon_j}\right)^{1/2}$$

Once the binary diffusion coefficients for all species combinations are known, the diffusion velocities of each species can be computed from Eq. (3.13). The diffusion velocity of each species is the species velocity due to all diffusion processes algebraically added to the convection velocity. When computing the diffusion velocities, it is assumed as suggested in Ref. 44, that the thermal diffusion coefficient D_T is negligible compared with the binary diffusion coefficient. The solution of Eq. (3.13) requires solving a simultaneous equation system, with the number of equations equivalent to the number of species present for each component of diffusion velocity.

42

Chapter 4

THE COMBUSTION PROCESS OF HYDROGEN-AIR SYSTEM

The combustion process involves the oxidation of constituents in the fuel that are capable of being oxidized, and can therefore be represented by a chemical equation. During a combustion process the mass of each element remains the same. Thus, writing chemical equation and solving problems involving quantities of the various constituents basically involves the conservation of mass of each element. A brief review of this subject, particularly as it applies to the combustion of hydrogen-air system is presented in this chapter.

4.1 Hydrogen-Air Reaction Mechanism

In hydrogen-air combustion, hydrogen is oxidized by oxygen and chemical energy is released and water is formed as product of the reaction. It should be pointed out that in the combustion process there are many intermediates products formed during the chemical reaction. An elementary chemical reaction is one that takes place in a single step. For example, a dissociation reaction such as

$$O_2 + M \rightarrow 2O + M \qquad (4.1)$$

is an elementary reaction because it literally takes place by a collision of an O_2 molecule with another collision partner, yielding directly two oxygen atoms. On the other hand, the reaction

$$2H_2 + O_2 \rightarrow 2H_2O \qquad (4.2)$$

43

is not an elementary reaction. Two hydrogen molecules don't come together with one oxygen molecule to directly yield two water molecules. Instead Eq. (4.2) is a statement of an overall reaction that actually takes place through a series of elementary steps.

$$H_2 \rightarrow 2H \tag{4.3a}$$

$$O_2 \rightarrow 2O \tag{4.3b}$$

$$H + O_2 \rightarrow OH + O \tag{4.3c}$$

$$O + H_2 \rightarrow OH + H \tag{4.3d}$$

$$OH + H_2 \rightarrow H_2O + H \tag{4.3e}$$

Equations (4.3 a-e) constitutes the reaction mechanism for the overall reaction given by Eq. (4.2). Each of Eqs. (4.3a-e) is an elementary reaction.

The assumption that air is 21.0 per cent oxygen and 79.0 percent nitrogen by volume leads to the conclusions that for each mole of oxygen, 79.0/21.0 = 3.76 moles of nitrogen are involved. Therefore, when the oxygen for the combustion of hydrogen is supplied as air, the overall reaction can be written as

$$2H_2 + O_2 + 3.76N_2 \rightarrow 2H_2O + 3.76N_2 \tag{4.4}$$
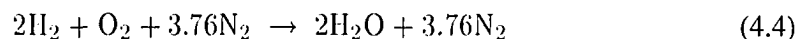
The minimum amount of air that supplies sufficient oxygen for the complete combustion of all the hydrogen, is called the "theoretical air" or "stoichiometric air" and the combustion mixture is called "stoichiometric hydrogen-air mixture". The nitrogen acts as an inert gas or a diluent.

There is a broad category of reaction mechanisms that involves homolysis of covalent bonds with the production of intermediates posessing unpaired electron called radicals (or free radicals).

$$A:B \rightarrow A. + B.$$

44
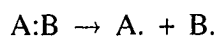
Almost all small radicals are short-lived, highly reactive species. When they collide with other moleculles they tend to react in a way that leads to pairing of their unpaired electrons. One way they can do this is by extracting an atom from another molecule. For example in the reaction $N_2 + O \rightarrow NO + N$, the nitrogen radical extracts an oxygen atom from oxygen molecule and gives another radical of oxygen. This behavior is charecteristic of radical reaction and consists of three basic steps. The first step is called the *chain-initiating step*. In this step radicals are created. The second step is called *chain-propagating step*. In chain-propagating step one radical generates another. The third step is the *chain-terminating step*. This last step occurs less frequently but occurs often enough to use up one or both of the reactive intermediates. These intermediate process can have time scales similar to the fluid time scales, therefore, fluid dynamic simulations requiring finite rate chemistry must account for this. Further it is important that all pertinent reactions that may affect the rate process must be included. Values of the rate constants for high-temperature hydrogen-air mixture are readily available in the literature. But there is always some uncertainty in the published rate constants; they are difficult to measure experimentally, and very difficult to calculate accurately. Thus the ideal way to create a reaction mechanism is to assemble the important species in the hydrogen-air reaction. The most important species in the hydrogen-air reaction mechanism are the eight species (N_2, O_2, H_2, OH, HO_2, H_2O, O, H). These species form the core of hydrogen air combustion mechanism.

4.2 Hydrogen-Air Reaction Model

The hydrogen-air combustion mechanism used in this work is based on the Jachimowski hydrogen-air model [45], which use 13–species and 33–reactions and is given in Table 4.1. The values of reaction-rate constant, temperature coefficient in reaction rate expression and activation energy for the various reactions are also tabulated. The current

45

numerical work uses a modified form of this model by using only the most important species. We have used both 9-species 18-reactions and 7-species 7-reactions models, both of which are tabulated in Tables 4.3 and 4.4 respectively. There is no significant difference in the results by these two models. Thus it saves considerably in computational time by using the shortened model.

4.3 Third Body Reactions

When simple radicals recombine to form a product the energy liberated in the process is sufficiently great to cause the product to decompose into the original radicals.

A + B $\rightleftharpoons$ C + D + energy
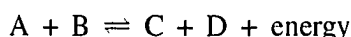
This energy must be removed by a third body M in order to stop recombination. If the molecule formed (like C and D above) in a recombination process has a large number of internal (generally vibrational) degrees of freedom, it can redistribute the energy of formation among these degrees and a third body is not necessary.

In the above Table 4.3 for 18 reactions model, reactions (6), (7), (8) and (18) needs a third body. In some cases the recombination process can be stabilized by the formed molecules radiately dissipating some energy or colliding with a surface and dissipating energy in this manner.

Now let us consider the third body reaction

$$A + B + M_i \underset{K_{b_i}}{\overset{K_{f_i}}{\rightleftharpoons}} C + M_i \qquad (4.4)$$
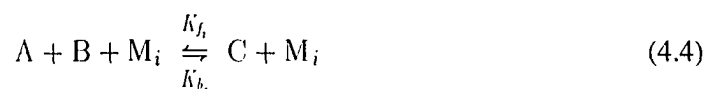
where M_i can be any species present in the fluid. Here M_i plays the role of a catalyst and as a result the forward and backward reaction rates will depend on which species is involved as the third body.

Rate of formation of species C is

$$\frac{\partial C_C}{\partial t} = K_{f_i} C_A C_B C_{M_i} \qquad (4.5)$$

46

Rate of consumption of species C is

$$\frac{\partial C_C}{\partial t} = K_{b_i} C_C C_{M_i} \tag{4.6}$$

Therefore, net rate of formation of species C is

$$\frac{\partial C_C}{\partial t} = K_{f_i} C_A C_B C_{M_i} - K_{b_i} C_C C_{M_i} \tag{4.7}$$

At equilibrium we have

$$\frac{\partial C_C}{\partial t} = 0 \tag{4.8}$$

and Eq. (4.7) becomes

$$K_{f_i}(C_A)_e (C_B)_e (C_{M_i})_e = K_{b_i}(C_C)_e (C_{M_i})_e$$

or

$$K_e = \frac{K_{f_i}}{K_{b_i}} = \frac{(C_C)_e}{(C_A)_e (C_B)_e}$$

where subscript e stands for equilibrium and K_e is the equilibrium constant. Note that this is independent of the catalyst species M_i. We can rewrite Eq. (4.7) as

$$\frac{\partial C_C}{\partial t} = K_{f_i} C_{M_i} \left[C_A C_B - \frac{1}{K_e} C_C \right] \tag{4.9}$$

Now since M_i could be any species, so Eq. (4.9) actually represents N reactions (one for each of the N species present in the fluid). Total production of species C is the sum of the production of C from all of the reactions.

Therefore,

$$\frac{\partial C_C}{\partial t} = \sum_{i=1}^{N} \left[K_{f_i} C_{M_i} \left(C_A C_B - \frac{1}{K_e} C_C \right) \right]$$

$$\frac{\partial C_C}{\partial t} = \left[\sum_{i=1}^{N} (K_{f_i} C_{M_i}) \right] \left(C_A C_B - \frac{1}{K_e} C_C \right) \tag{4.10}$$

47

4.4 Third Body Efficiencies

We can relate the reaction rate co-efficients, K_{f_i} corresponding to the various species acting as third bodies to the reaction rate of one of the species acting as a third body. For example, if we choose nitrogen as the third body we can write

$$\eta_i = \frac{K_{f_i}}{\left(K_f\right)_{N_2}}$$

where η_i is the third body efficiency of the ith species. In the above equation i could be any species and in the denominator instead of nitrogen it could be any particular species as reference.

Therefore, we can write Eq. (4.10) as

$$\frac{\partial C_C}{\partial t} = \left(K_f\right)_{N_2} \left(C_A C_B - \frac{1}{K_c} C_C\right) \left(\sum_{i=1}^{N} \eta_i C_{M_i}\right) \tag{4.11}$$

Table 4.2 shows some third body efficiencies for several reactions where H_2 and H_2O are the third bodies, i.e., the collision partner denoted by M in some of the chemical equations.

48

Table 4.1 Jachimowski's Hydrogen-Air Model

j	Reaction	A_j	α_j	c_j
1	$H_2 + O_2 = OH + OH$	1.7E13	0.	48000.
2	$OH + H_2 = H_2O + H$	2.2E13	0.	5150.
3	$H + O_2 = OH + O$	2.20E14	0.	16800.
4	$O + H_2 = OH + H$	1.80E10	1.	8900.
5	$OH + OH = H_2O + O$	6.3E12	0.	1090.
6	$H + OH = H_2O + M$	2.20E22	-2.	0.
7	$H + O = OH + M$	6.00E16	-0.6	0.
8	$H + H = H_2 + M$	6.40E17	-1.	0.
9	$H + O_2 = HO_2 + M$	1.70E15	0.	-1000.
10	$HO_2 + H = H_2 + O_2$	1.30E13	0.	0.
11	$HO_2 + H = OH + OH$	1.40E14	0.	1080.
12	$HO_2 + O = OH + O_2$	1.50E13	0.	950.
13	$HO_2 + OH = H_2O + O_2$	8.00E12	0.	0.
14	$HO_2 + HO_2 = H_2O_2 + O_2$	2.00E12	0.	0.
15	$H + H_2O_2 = H_2 + HO_2$	1.40E12	0.	3600.
16	$O + H_2O_2 = OH + HO_2$	1.40E13	0.	6400.
17	$OH + H_2O_2 = H_2O + HO_2$	6.10E12	0.	1430.
18	$M + H_2O_2 = 2OH + M$	1.20E17	0.	45500.
19	$O + O = O_2 + M$	6.00E13	0.	-1000.
20	$N + N = N_2 + M$	2.80E17	-0.75	0.
21	$N + O_2 = NO + O$	6.40E9	1.0	6300.
22	$N + NO = N_2 + O$	1.60E13	0.	0.
23	$N + OH = NO + H$	6.30E11	0.5	0.
24	$H + NO = HNO + M$	5.40E15	0.	-600.
25	$H + HNO = NO + H_2$	4.80E12	0.	0.
26	$O + HNO = NO + OH$	5.00E11	0.5	0.
27	$OH + HNO = NO + H_2O$	3.60E13	0.	0.
28	$HO_2 + HNO = NO + H_2O_2$	2.00E12	0.	0.
29	$HO_2 + NO = NO_2 + OH$	3.43E12	0.	-260.
30	$H + NO_2 = NO + OH$	3.50E14	0.	1500.
31	$O + NO_2 = NO + O_2$	1.00E13	0.	600.
32	$M + NO_2 = NO + O$	1.16E16	0.	66000.

49

Table 4.2 Third Body Efficiencies

Reaction	Third Body Efficiencies[1]
$H + OH + M = H_2O + M$	H_2 1.0 H_2O 6.0
$H + O\ M = OH + M$	H_2 1.0 H_2O 5.0
$H + H + M = H_2 + M$	H_2 1.0 H_2O 6.0
$H + O_2 + M = HO_2 + M$	H_2 2.0 H_2O 16.0
$M + H_2O_2 = 2OH + M$	H_2 1.0 H_2O 15.0

Table 4.3 9–Species and 18–Reactions Hydrogen-Air Model

Species are H_2, O_2, H_2O, OH, H, O, HO_2, H_2O_2 and N_2.

j	Reaction
1	$H_2 + O_2 = OH + OH$
2	$OH + H_2 = H_2O + H$
3	$H + O_2 = OH + O$
4	$O + H_2 = OH + H$
5	$OH + OH = H_2O + O$
6	$H + OH = H_2O + M$
7	$H + H = H_2 + M$
8	$H + O_2 = HO_2 + M$
9	$HO_2 + H = H_2 + O_2$
10	$HO_2 + H = OH + OH$
11	$HO_2 + O = OH + O_2$
12	$HO_2 + H_2 = H_2\ O_2 + H$
13	$HO_2 + OH = H_2O + O_2$
14	$HO_2 + HO_2 = H_2O_2 + O_2$
15	$H + H_2O_2 = H_2O + HO$
16	$O + H_2O_2 = OH + HO_2$
17	$OH + H_2O_2 = H_2O + HO_2$
18	$M + H_2O_2 = 2OH + M$

---

[1]   All other third bodies have efficiency of 1.0

50

Table 4.4 7–Species and 7–Reactions Hydrogen-Air Model

The species are N_2, O_2, H_2, OH, H_2O, O, and H.

j	Reaction
1	$O_2 + H_2 \rightleftharpoons OH + OH$
2	$O_2 + H \rightleftharpoons OH + O$
3	$H_2 + OH \rightleftharpoons H_2O + H$
4	$H_2 + O \rightleftharpoons OH + H$
5	$OH + OH \rightleftharpoons H_2O + O$
6	$OH + H + M \rightleftharpoons H_2O + M$
7	$H + H + M \rightleftharpoons H_2 + M$

Chapter 5

METHOD OF SOLUTION USING SHOCK CAPTURING

This chapter deals with the solution procedure using *shock capturing* method. In this work we used both shock capturing method as well as shock fitting method. Shock-fitting will be discussed in the next chapter. In both the methods the standard MacCormick's central difference algorithm was used.

5.1 Shock Capturing Method

In shock capturing the outer boundary of the coordinate system is outside the bow shock wave. Here, the shock comes naturally out of the finite-difference calculations, showing up as a rapid change of flow properties across several grid points. It is not treated explicitly as a discontinuity, and the oblique shock relations are not used. Once the thermodynamic properties, diffusion coefficients and chemical production rates have been defined, the governing equations can be solved numerically. The finite difference solution procedure is discussed in the next section.

5.2 Finite-Difference Solution Method

To solve the governing equations 3.1 with the finite-difference scheme, the equations must first be transformed from the physical domain (x,y) in which they are written to an appropriate computational domain (ξ,η). The grid is kept uniform in both x and y directions.

To transform the governing equations from the physical to the computational domain, fluxes $\mathbf{F}$ and $\mathbf{G}$ are first written in functional form and differentiated with respect to the

52

computational coordinates. Therefore, given $F = F(x,y)$ and $G = G(x,y)$, and we have

$$F_\xi = F_x x_\xi + F_y y_\xi \tag{5.1}$$

$$F_\eta = F_x x_\eta + F_y y_\eta \tag{5.2}$$

Then, substituting F_y from Eq. (5.2) into Eq. (5.1) and simplifying gives

$$F_x = \frac{F_\xi y_\eta - F_\eta y_\xi}{J} \tag{5.3}$$

where

$$J = x_\xi y_\eta - y_\xi x_\eta \tag{5.4}$$

is the Jacobian of the transformation.

Proceeding in the same manner for G gives

$$G_y = \frac{G_\eta x_\xi - G_\xi x_\eta}{J} \tag{5.5}$$

Finally, substituting Eqs. (5.3) and (5.5) into Eq. (3.1) gives the governing equations in the computational domain

$$\frac{\partial \widehat{U}}{\partial t} + \frac{\partial \widehat{F}}{\partial \xi} + \frac{\partial \widehat{G}}{\partial \eta} = \widehat{H} \tag{5.6}$$

where,

$$\widehat{U} = JU, \qquad \widehat{H} = JH$$

$$\widehat{F} = y_\eta F - x_\eta G \tag{5.7}$$

$$\widehat{G} = x_\xi G - y_\xi F \tag{5.8}$$

Here $(x_\xi, x_\eta, y_\xi, y_\eta)$ are the transformations metrics that form the inverse Jacobian metrics, and J is the Jacobian of the transformation. The metrics can be computed numerically once the physical coordinate grid has been prescribed.

53

5.3 MacCormack's Implicit (Partial) Method

The MacCormack's [48] finite-difference method is a predictor-corrector scheme of the Lax Wendroff type. The scheme is second-order accurate in time and space, which results in a spatially and temporally discrete simultaneous system of equations at each grid points. To solve the governing chemically reacting flows equations, the *spatial* derivatives must first be discretized, and then an approximate *temporal* discretization must be chosen to advance the equation ahead in time. The temporal scheme must be chosen carefully because the system of partial differential equations describing chemically reacting flows can be *stiff* because of the highly disparate time scales that exist among the equations.

The governing equations can be stiff because of the *kinetic source terms* contained in the vector **H** and because of the diffusive terms in the vectors **F** and **G**. Only the kinetic terms introduce stiffness in this work; spatial stiffness is controlled by the choice of the grid. To deal with the stiff system, the kinetic term is computed *implicitly*. Since it is only partial implicit so only the **U** vector and source term vector **H** are advanced in time level $n+1$. Thus in temporally discrete form we have

$$\frac{\widehat{U}_{i,j}^{n+1} - \widehat{U}_{i,j}^{n}}{\Delta t} = -\left[\left(\frac{\partial \widehat{F}}{\partial \xi}\right)_{i,j}^{n} - \left(\frac{\partial \widehat{G}}{\partial \eta}\right)_{i,j}^{n}\right] + \widehat{H}^{n+1} \tag{5.9}$$

Therefore,

$$\widehat{U}_{i,j}^{n+1} = \widehat{U}_{i,j}^{n} - \Delta t\left[\left(\frac{\partial \widehat{F}}{\partial \xi}\right)_{i,j}^{n} + \left(\frac{\partial \widehat{G}}{\partial \eta}\right)_{i,j}^{n} - \widehat{H}_{i,j}^{n+1}\right] \tag{5.10}$$

Equation (5.10) above is non-linear and so a linearization procedure must be followed. A linearization procedure based on Taylor series expansion is used. Thus **H** is linearized by expanding it in a Taylor series in time. All flux vectors are expressed in terms of the flux vector **U**. Thus **H** is linearized by Taylor series as

$$H_{i,j}^{n+1} = H_{i,j}^{n} + \frac{\partial H}{\partial t}\Delta t + \vartheta(\Delta t)^2 \tag{5.11}$$

54

In order to rewrite $\frac{\partial H}{\partial t}$ in terms of the gradients of the flux vector U we know that

$$H = f(U, \xi_t, \xi_x, \xi_y)$$

The chain rule of differentiation yields the following relation

$$\frac{\partial \widehat{H}}{\partial t} = \frac{\partial \widehat{H}}{\partial \widehat{U}}\frac{\partial \widehat{U}}{\partial t} + \frac{\partial \widehat{H}}{\partial \xi_t}\frac{\partial \xi_t}{\partial t} + \frac{\partial \widehat{H}}{\partial \xi_x}\frac{\partial \xi_x}{\partial t} + \frac{\partial \widehat{H}}{\partial \xi_y}\frac{\partial \xi_y}{\partial t} \qquad (5.12)$$

For many applications the grid is independent of time. Therefore the above equation reduces to

$$\frac{\partial \widehat{H}}{\partial t} = \frac{\partial \widehat{H}}{\partial \widehat{U}}\frac{\partial \widehat{U}}{\partial t} \qquad (5.13)$$

Therefore, substituting this in Eq. (5.11) gives

$$\widehat{H}_{i,j}^{n+1} = \widehat{H}_{i,j}^{n} + \frac{\partial \widehat{H}}{\partial \widehat{U}}\frac{\partial \widehat{U}}{\partial t}\Delta t + \vartheta(\Delta t)^2 \qquad (5.14)$$

The partial derivative $\frac{\partial U}{\partial t}$ is approximated by a first order forward difference expression as

$$\frac{\partial \widehat{U}}{\partial t} = \frac{\widehat{U}^{n+1} - \widehat{U}^n}{\Delta t} + \vartheta(\Delta t) = \frac{\Delta \widehat{U}}{\Delta t} + \vartheta(\Delta t) \qquad (5.15)$$

Substituting the preceding Eq. (5.15) in Eq. (5.14) gives

$$\widehat{H}_{i,j}^{n+1} = H_{i,j}^{n} + \frac{\partial H}{\partial U}\Delta U + \vartheta(\Delta t)^2 \qquad (5.16)$$

Terms like $\frac{\partial H}{\partial U}$ are called Jacobian metrics. In Eq. (5.15) above, the term $\Delta \widehat{U}^{n+1} = \widehat{U}^{n+1} - \widehat{U}^n$ is the change in flow properties per time step. The finite difference equations shall be formulated in terms of ΔU which is referred to as the *delta formulation*.

Next the linearized Eq. (5.16) is substituted in Eq. (5.10) to yield

$$\widehat{U}_{i,j}^{n+1} = \widehat{U}_{i,j}^{n} - \Delta t\left[\left(\frac{\partial \widehat{F}}{\partial \xi}\right)_{i,j}^{n} + \left(\frac{\partial \widehat{G}}{\partial \eta}\right)_{i,j}^{n} - \widehat{H}_{i,j}^{n} - \frac{\partial \widehat{H}}{\partial U}\Delta U\right] \qquad (5.17)$$

This gives

$$\frac{\Delta U}{\Delta t} + \left(\frac{\partial \widehat{F}}{\partial \xi}\right)_{i,j}^{n} + \left(\frac{\partial \widehat{G}}{\partial \eta}\right)_{i,j}^{n} = \widehat{H}_{i,j}^{n} + \frac{\partial \widehat{H}}{\partial U}\Delta U \qquad (5.18)$$

55

Let $\left(\frac{\partial H}{\partial U}\right)^n = K^n$ equals the Jacobian metric of H with respect to U.

Also $\left(\frac{\partial \widehat{F}}{\partial \xi}\right)^n_{i,j} + \left(\frac{\partial \widehat{G}}{\partial \eta}\right)^n_{i,j} - \widehat{H}^n_{i,j} = \widehat{R}^n_{i,j}$ equals the steady state residuals. Therefore Eq. (5.18) reduces to

$$\frac{\Delta \widehat{U}^{n+1}}{\Delta t} + \widehat{R}^n - K^n \Delta \widehat{U}^{n+1} = 0$$

$$\Delta \widehat{U}^{n+1} + \Delta t \widehat{R}^n - K^n \Delta t \Delta \widehat{U}^{n+1} = 0$$

$$\Delta \widehat{U}^{n+1}[I - \Delta t K^n] = -\Delta t \widehat{R}^n \qquad (5.19)$$

where I is the identity metrix. Once the temporal discretization has been used to construct Eq. (5.19), the resulting equations are spatially differenced by using unsplit MacCormack's scheme. The modified MacCormack's technique becomes

5.3.1. Predictor Step

The predictor step is given by

$$[I - \Delta t K^n_{i,j}] \Delta U^{\overline{n+1}}_{i,j} = -\Delta t R^n_{i,j} \qquad (5.20)$$

where, $R^n_{i,j}$ represents a forward spatial difference of R. Also $\Delta U^{\overline{n+1}}_{i,j} = U^{\overline{n+1}}_{i,j} - U^n_{i,j}$ where $\overline{n+1}$ is the temporary advanced level of time. For the second step (corrector) a backward differencing for spatial is used for R.

5.3.2. Corrector Step

The corrector step is given by

$$\left[I - \Delta t K^{\overline{n+1}}_{i,j}\right] \Delta U^{n+1}_{i,j} = -\Delta t R^{\overline{n+1}}_{i,j} \qquad (5.21)$$

where this time a backward spatial differencing for R is used. Because,

$$U^{n+1} - U^n = \Delta U^{n+1}$$

Therefore,

$$\Delta U^{n+1} - \frac{1}{2} \Delta U^{n+1} = \frac{1}{2} \Delta U^{\overline{n+1}}$$

56

This gives,

$$\frac{1}{2}\Delta U^{n+1} = \frac{1}{2}\Delta \overline{U^{n+1}}$$

or,

$$\Delta U^{n+1} = \Delta \overline{U^{n+1}}$$

Hence, we get

$$U^{n+1}_{i,j} = U^n + \frac{1}{2}\left[\Delta \overline{U^{n+1}} + \Delta U^{n+1}\right] \qquad (5.22)$$

This completes the corrector step. Therefore solving for $\Delta U^{n+1}_{i,j}$ we get

$$U^{n+1}_{i,j} = U^n_{i,j} + \frac{1}{2}\left[\underbrace{\Delta \overline{U^{n+1}_{i,j}}}_{\text{fromEq.(5.20)}} + \underbrace{\Delta U^{n+1}_{i,j}}_{\text{fromEq.(5.21)}}\right]$$

Equations (5.20) and (5.21) are used to advance solution from time n to time $n+1$ and this process is continued until a desired integration time has been reached. The magnitude of the time step in Eqs. (5.20) and (5.21) is chosen based on the physical time scales present at any given time in the solution. The fluid-dynamic time step Δt_f can be shown to be limited by the Courant or viscous stability limit of the governing equations. The chemical relaxation time for a species i is given by

$$t_c = \frac{\rho f_i}{\dot{\omega}_i}$$

Changes in this relaxation time are then given by

$$\Delta t_c = \frac{\Delta(\rho f_i)}{\dot{\omega}_i}$$

since $\dot{\omega}_i$ remains nearly constant over a time step. For accuracy, it is required that the chemical time step be chosen such that no change in mass fraction greater than 0.01 occurs over that time step. The computational time step Δt is then chosen to be the minimum over all grid points of the fluid and chemical time steps.

57

5.4 Boundary and Initial Conditions

The governing Eqs. (3.1) require boundary conditions along all the three boundaries. For the problem to be considered the inflow boundary is always supersonic, so the velocity, static temperature and pressure, and species are specified and fixed there. At the supersonic outflow boundary, all flow quantities are extrapolated from interior grid points. Although full Navier-Stokes (N-S) equations are used, the slip conditions are used to numerically simulate the inviscid flow. A flow tangency or slip boundary condition is implied on solid wall. The wall temperature and pressure are extrapolated from interior grid points. Initial conditions are obtained by specifying free-stream conditions throughout the flow field.

5.5 Artificial Viscosity

The Lax-Wendroff type schemes are inherently unstable and, hence, higher-order numerical dissipation terms are often necessary to get a stable solution. For a non-reacting flow field, an artificial viscosity based on temperature and /or pressure is traditionally used, but in chemically reacting flows, in addition to temperature and pressure gradients, one can also have very strong species concentration gradients. To suppress the numerical oscillations in the induction zone where the gradients in the concentration of reactants and products are very strong, additional artificial viscosity based on water mass fraction is used similar to the one used by Singh et al. [35]

58

Chapter 6

METHOD OF SOLUTION USING SHOCK-FITTING TECHNIQUE

The bow shock generated by an object in a supersonic/hypersonic flow field may be selected as the outer boundary of the domain and determined as a part of the overall solution. This procedure is known as the shock-fitting method. In problems like shock-induced combustion where physical instabilities are present, the shock capturing methods will smear some of the instabilities. Thus shock-capturing methods, when used in complicated problems of practical interest, would not reproduce many intricate flow features. On the other hand, in the shock-fitting approach, one knows the precise location of the discontinuity which acts as one of the boundaries of the flow field, across which Rankine-Hugoniot conditions are applied. This approach avoids taking differences across the shock and the smearing of the shock that occurs in the shock-capturing method. There are some obvious advantages of shock fitting over shock capturing. Shock fitting requires far less grid points compared to shock capturing. In shock capturing the bow shock becomes a smeared shock surface and, requires more grid points for the extension of the grid in the free-stream region. This adds to the savings in computational time in shock fitting as compared to shock capturing. Since very small dissipation is needed in shock fitting, the intricate details of the flow can be reproduced, as the dissipation does not smear the important flow features. This chapter deals in details the solution procedure used with shock-fitting method.

6.1 Time-Dependent Navier-Stokes Equations in Strong Conservation Law Form

Navier Stokes equations in vector form given by Eq. (3.1) and repeated here for

59

convenience is

$$U_t + F_x + G_y = H \tag{6.1}$$

The governing equations of motion are transformed from physical space (x,y) to the computational space (ξ, η) by the following relations:

$$\tau = t \tag{6.2}$$

$$\xi = \xi(t, x, y) \tag{6.3}$$

$$\eta = \eta(t, x, y) \tag{6.4}$$

Applying the chain rule of partial differential equation gives the following expressions for the cartessian derivatives.

$$\frac{\partial}{\partial t} = \frac{\partial}{\partial \tau} + \xi_t \frac{\partial}{\partial \xi} + \eta_t \frac{\partial}{\partial \eta} \tag{6.5}$$

$$\frac{\partial}{\partial x} = \xi_x \frac{\partial}{\partial \xi} + \eta_x \frac{\partial}{\partial \eta} \tag{6.6}$$

$$\frac{\partial}{\partial y} = \xi_y \frac{\partial}{\partial \xi} + \eta_y \frac{\partial}{\partial \eta} \tag{6.7}$$

Therefore Eq. (6.1) reduces to

$$U_\tau + \xi_t U_\xi + \eta_t U_\eta + \xi_x F_\xi + \eta_x F_\eta + \xi_y G_\xi + \eta_y G_\eta = H \tag{6.8}$$

6.2 Computation of Metrics $\xi_t, \eta_t, \xi_x, \eta_x, \xi_y, \eta_y$

From Eqs. (6.5)-(6.7) it is obvious that the value of the metrics $\xi_t, \eta_t, \xi_x, \eta_x, \xi_y, \eta_y$ must be provided in some fashion. In most cases the analytical determination of the metrics is not possible and must be computed numerically. Since the step sizes in the computational domain are equally spaced x_ξ, x_η etc can be computed by various finite difference approximation. Thus, if the metrics appearing in Eqs. (6.3)-(6.5) can

60

be expressed in terms of these derivatives, the numerical computation of metrics is completed. To obtain such relation, the following differential expression is considered

$$dt = \frac{\partial t}{\partial \tau} + \frac{\partial t}{\partial \xi}d\xi + \frac{\partial t}{\partial \eta}d\eta$$

But according to Eq. (6.2)

$$\frac{\partial t}{\partial \tau} = 1$$

and

$$\frac{\partial t}{\partial \xi} = \frac{\partial t}{\partial \eta} = 0$$

Therefore,

$$dt = d\tau \tag{6.9}$$

$$dx = x_\tau d\tau + x_\xi d\xi + x_\eta d\eta \tag{6.10}$$

$$dy = y_\tau d\tau + y_\xi d\xi + y_\eta d\eta \tag{6.11}$$

Writing Eqs. (6.9)-(6.11) in matrix form we have

$$\begin{bmatrix} dt \\ dx \\ dy \end{bmatrix} = \begin{bmatrix} 1 & 0 & 0 \\ x_\tau & x_\xi & x_\eta \\ y_\tau & y_\xi & y_\eta \end{bmatrix} \begin{bmatrix} d\tau \\ d\xi \\ d\eta \end{bmatrix} \tag{6.12}$$

Reversing the role of independent variables, we can write

$$d\tau = dt \tag{6.13}$$

$$d\xi = \xi_t dt + \xi_x dx + \xi_y dy \tag{6.14}$$

$$d\eta = \eta_t dt + \eta_x dx + \eta_y dy \tag{6.15}$$

Therefore,

$$\begin{bmatrix} d\tau \\ d\xi \\ d\eta \end{bmatrix} = \begin{bmatrix} 1 & 0 & 0 \\ \xi_t & \xi_x & \xi_y \\ \eta_t & \eta_x & \eta_y \end{bmatrix} \begin{bmatrix} dt \\ dx \\ dy \end{bmatrix} \tag{6.16}$$

61

Comparing Eqs. (6.12) and (6.16) we have

$$
\begin{bmatrix} 1 & 0 & 0 \\ \xi_t & \xi_x & \xi_y \\ \eta_t & \eta_x & \eta_y \end{bmatrix} = \begin{bmatrix} 1 & 0 & 0 \\ x_\tau & x_\xi & x_\eta \\ y_\tau & y_\xi & y_\eta \end{bmatrix}^{-1}
$$

$$
= \frac{[\mathbf{X}]}{\det |\text{denominator}|}
$$

where

$$
[\mathbf{X}] = \begin{bmatrix} -\begin{bmatrix} x_\xi & x_\eta \\ y_\xi & y_\eta \end{bmatrix} & -\begin{bmatrix} 0 & 0 \\ y_\xi & y_\eta \end{bmatrix} & \begin{bmatrix} 0 & 0 \\ x_\xi & x_\eta \end{bmatrix} \\ -\begin{bmatrix} x_\tau & x_\eta \\ y_\tau & y_\eta \end{bmatrix} & \begin{bmatrix} 1 & 0 \\ y_\tau & y_\eta \end{bmatrix} & -\begin{bmatrix} 1 & 0 \\ x_\tau & x_\eta \end{bmatrix} \\ \begin{bmatrix} x_\tau & x_\xi \\ y_\tau & y_\xi \end{bmatrix} & -\begin{bmatrix} 1 & 0 \\ y_\tau & y_\xi \end{bmatrix} & \begin{bmatrix} 1 & 0 \\ x_\tau & x_\xi \end{bmatrix} \end{bmatrix}
$$

Let

$$
J = \frac{1}{\det |\text{denominator}|}
$$

Therefore,

$$
\xi_x = J y_\eta
$$

$$
\xi_y = -J x_\eta
$$

$$
\xi_t = -J(x_\tau y_\eta - x_\eta y_\tau)
$$

$$
\eta_x = -J y_\xi
$$

$$
\eta_y = J x_\xi
$$

$$
\eta_t = J(x_\tau y_\xi - x_\xi y_\tau)
$$

In the evaluation of Eq. (6.8) many terms which adds to zero analytically but numerically are not zero (known as GCL terms) have been neglected. Now we evaluate those terms and add it to the source term H. We can write

$$
\mathbf{U}_t = \frac{\partial \mathbf{U}}{\partial \tau} + \xi_t \frac{\partial \mathbf{U}}{\partial \xi} + \eta_t \frac{\partial \mathbf{U}}{\partial \eta}
$$

$$
= \frac{\partial \mathbf{U}}{\partial \tau} + \left\{ [\mathbf{U}\xi_t]_\xi - \mathbf{U}(\xi_t)_\xi \right\} + \left\{ [\mathbf{U}\eta_t]_\eta - \mathbf{U}(\eta_t)_\eta \right\}
$$

62

Also,

$$\mathbf{F}_x = \xi_x \mathbf{F}_\xi + \eta_x \mathbf{F}_\eta$$

$$= (\mathbf{F}\xi_x)_\xi - \mathbf{F}(\xi_x)_\xi + (\mathbf{F}\eta_x)_\eta - \mathbf{F}(\eta_x)_\eta$$

$$= (\mathbf{F}\xi_x)_\xi + (\mathbf{F}\eta_x)_\eta - \left[\mathbf{F}(\xi_x)_\xi + \mathbf{F}(\eta_x)_\eta\right]$$

similarly,

$$\mathbf{G}_y = (\mathbf{G}\xi_y)_\xi + \mathbf{G}(\eta_y)_\eta - \mathbf{G}\left[(\xi_y)_\xi + (\eta_y)_\eta\right]$$

Substituting the values of $\mathbf{U}_t$, $\mathbf{F}_x$, and $\mathbf{G}_y$ in Eq. (6.1) gives

$$\frac{\partial \mathbf{U}}{\partial \tau} + [\mathbf{U}\xi_t + \mathbf{F}\xi_x + \mathbf{G}\xi_y]_\xi + [\mathbf{U}\eta_t + \mathbf{F}\eta_x + \mathbf{G}\eta_y]_\eta$$

$$\overbrace{\qquad\qquad\qquad\qquad\qquad\qquad\qquad\qquad\qquad}^{\text{GCL TERMS}} \tag{6.17}$$

$$= \mathbf{H} + \left[\mathbf{U}(\xi_t)_\xi + \mathbf{U}(\eta_t)_\eta\right] + \left[\mathbf{F}(\xi_x)_\xi + \mathbf{F}(\eta_x)_\eta\right] + \left[\mathbf{G}(\xi_y)_\xi + \mathbf{G}(\eta_y)_\eta\right]$$

Dividing Eq. (6.17) through the Jacobian of the transformation and substituting the values

of $\xi_x, \xi_y, \xi_t, \eta_x, \eta_y,$ and η_t and rearranging terms we have

$$\left(\overbrace{\underbrace{J^{-1}\mathbf{U}}_{}}^{\hat{\mathbf{U}}}\right)_\tau + \left(\overbrace{[\{-x_\tau y_\eta + x_\eta y_\tau\}\mathbf{U} + y_\eta\mathbf{F} - x_\eta\mathbf{G}]}^{\hat{\mathbf{F}}}\right)_\xi + \left(\overbrace{[\{x_\tau y_\xi + x_\xi y_\tau\}\mathbf{U} - y_\xi\mathbf{F} + x_\xi\mathbf{G}]}^{\hat{\mathbf{G}}}\right)_\eta$$

$$\overbrace{\underbrace{\qquad\qquad\qquad\qquad\qquad\qquad\qquad\qquad\qquad\qquad\qquad\qquad\qquad\qquad\qquad\qquad\qquad}_{\hat{\mathbf{H}}}}^{}$$

$$\overbrace{\qquad\qquad\qquad\qquad\qquad\qquad\qquad\qquad\qquad\qquad\qquad\qquad\qquad\qquad}^{\text{GCL TERMS}}$$

$$= J^{-1}\mathbf{H} + \left[\mathbf{U}\{-x_\tau y_\eta + x_\eta y_\tau\}_\xi + \mathbf{U}\{x_\tau y_\xi - x_\xi y_\tau\}_\eta\right] + \left[\mathbf{F}(y_\eta)_\xi - \mathbf{F}(y_\xi)_\eta - \mathbf{G}(x_\eta)_\xi + \mathbf{G}(x_\xi)_\eta\right]$$

$$\tag{6.18}$$

Therefore, the final form of the governing equation in the computational domain with

time-dependent terms is given by

$$\frac{\partial \hat{\mathbf{U}}}{\partial t} + \frac{\partial \hat{\mathbf{F}}}{\partial \xi} + \frac{\partial \hat{\mathbf{G}}}{\partial \eta} = \hat{\mathbf{H}}$$

In Eq. (6.18), the terms that add to zero analytically but numerically are not zero are

referred to as geometric conservation law (GCL) correction terms.

63

6.3 Shock Conditions

The flow conditions along the leftmost boundary are those conditions which exist immediately downstream of the bow shock as determined by Rankine-Hugoniot relations. Therefore, this boundary is allowed to move with the bow shock as the later moves towards the steady state position. Figure 6.1 shows the coordinate transformation used in shock fitting procedure in which the following notations are employed.

Let θ equals the angle the radius makes with the horizontal (i.e. body angle).

α equals the angle the radius makes with respect to body (i.e. tangent to the shock makes w.r.t. tangent to the body).

Taking projections of unit vectors $\vec{i_r}$, $\vec{i_\theta}$ on $\vec{n}$ and $\vec{s}$ we have,

$$\vec{s} = \vec{i_\theta}\cos\alpha + \vec{i_r}\sin\alpha$$

$$\vec{n} = \vec{i_r}\cos\alpha - \vec{i_\theta}\sin\alpha$$

Let $\Delta\theta$ is the small increment in the body angle.

$$\tan\alpha = \frac{\Delta r_s}{r_s\Delta\theta} = \frac{1}{r_s} \times \frac{dr_s}{d\theta} = \frac{r_{s\theta}}{r_s}$$

$$\cos\alpha = \frac{1}{\sqrt{1+(\frac{r_{s\theta}}{r_s})^2}}$$

$$\sin\alpha = \frac{\frac{r_{s\theta}}{r_s}}{\sqrt{1+(\frac{r_{s\theta}}{r_s})^2}}$$

Let $\vec{V_1}$ represent the vector component of the fluid velocity normal to and measured with respect to the moving shock.

Therefore, one may express the following:

$$\vec{V_1} = \left\{\left[\vec{V_\infty} - \vec{U_s}\right]\cdot\vec{n}\right\}\vec{n} = \left\{\left(v_\infty\vec{i_r}\cdot\vec{n} + u_\infty\vec{i_\theta}\cdot\vec{n} - \vec{U_s}\cdot\vec{n}\right)\cdot\vec{n}\right\} \tag{6.19}$$

Now $\vec{i_r}\cdot\vec{n} = \left|\vec{i_r}\right|\left|\vec{n}\right|\cos\alpha$

Let

$$\beta = \sqrt{1 + \left(\frac{r_{s\theta}}{r_s}\right)^2} \tag{6.20}$$

64
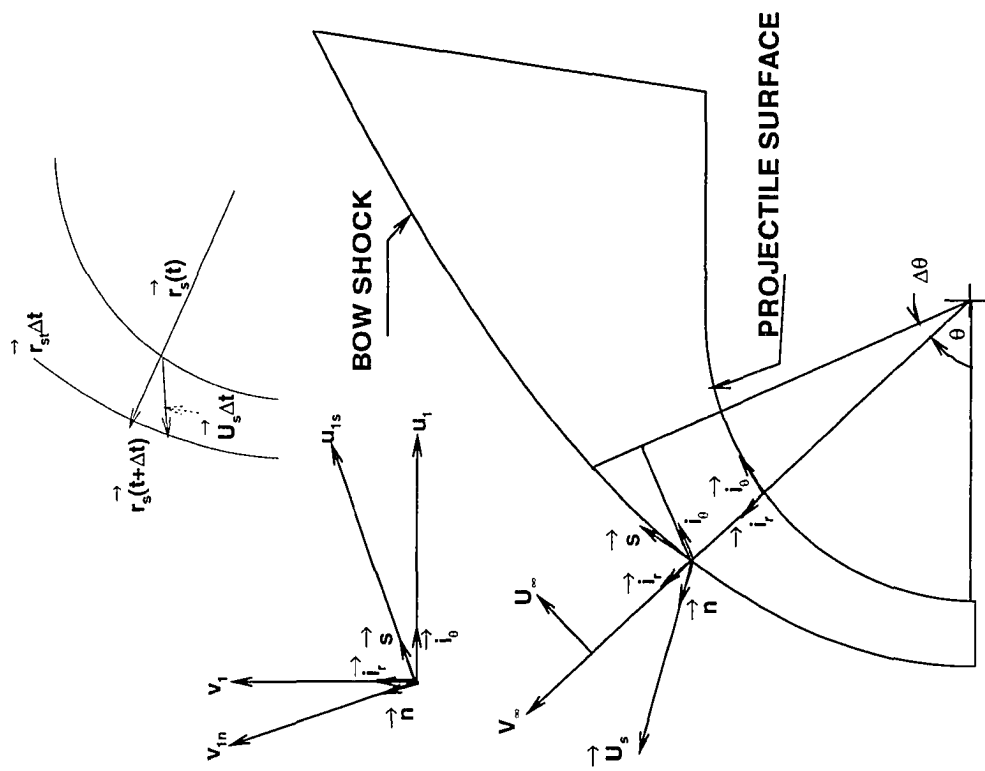
Figure 6.1 Notation and coordinate system used in shock-fitting.

65

Therefore, $\sin \alpha = \frac{r_{s_\theta}}{\frac{r_s}{\beta}}$ and $\cos \alpha = \frac{1}{\beta}$

$$\vec{i}_r \cdot \vec{n} = \frac{1}{\beta}$$

and

$$\vec{i}_\theta \cdot \vec{n} = -\left|\vec{i}_\theta\right|\left|\vec{n}\right|\cos\left(90 - \alpha\right) = -\sin\alpha = \frac{r_{s_\theta}/r_s}{\beta} \tag{6.21}$$

Equation (6.19) reduces to

$$V_1\vec{n} = \left[\frac{v_\infty}{\beta} - \frac{r_{s_\theta}/r_s}{\beta}U_\infty - \vec{U}_\infty \cdot \vec{n}\right]\vec{n} \tag{6.22}$$

Let r_{s_t} equals the radial shock velocity.

Therefore, magnitude of the shock velocity in the direction normal to the body (i.e. along the radius) is given by

$$r_{s_t} = \frac{\partial r_s}{\partial t} = \frac{U_s}{\cos\alpha} = U_s\beta$$

Hence, Eq. (6.22) reduces to

$$r_{s_t} = V_1\left[1 + \left(\frac{r_{s_\theta}}{r_s}\right)^2\right]^{1/2} + v_\infty - u_\infty\left(\frac{r_{s_\theta}}{r_s}\right) \tag{6.23}$$

The derivative $r_{s_\theta}^n$ that appears in Eq. (6.23) is evaluated by using the second-order central difference formula

$$r_{s_{\theta(j)}}^n = \frac{\left(r_{s_{\theta(j+1)}}^n - r_{s_{\theta(j-1)}}^n\right)}{2\Delta\theta} \qquad (2 \leq j \leq nny - 1)$$

At the beginning of the predictor step, the shock wave radial distance is computed from the Euler predictor equation

$$r_{s_{(t+\Delta t)}} = r_{s_{(t)}} + \Delta t \frac{\partial r_s}{\partial t}$$

or,

$$r_s^{\overline{n+1}} = r_s^n + \Delta t\, r_{s_t}^n \tag{6.24}$$

66

Therefore,

$$\vec{V_1} = V_1 \cdot \vec{n}$$

$$= V_1 \left[\vec{i_r} \cos\alpha - \vec{i_\theta} \sin\alpha \right]$$

$$= [V_1 \cos\alpha]\vec{i_r} + [-V_1 \sin\alpha]\vec{i_\theta}$$

$$= v_1 \vec{i_r} + u_1 \vec{i_\theta}$$

where, v_1 equals the component of fluid velocity V_1 normal to the body (*i.e.* along $\vec{i_r}$ direction), and u_1 equals the component of the fluid velocity V_1 tangential to the body (i.e. along $\vec{i_\theta}$) direction. Therefore,

$$u_1 = -\frac{\left(\frac{r_{s_\theta}}{r_s}\right)}{\left[1 + \left(\frac{r_{s_\theta}}{r_s}\right)^2\right]} \left[r_{s_t} - v_\infty + u_\infty \left(\frac{r_{s_\theta}}{r_s}\right) \right]$$

and

$$v_1 = V_1 \cos\alpha = \left[r_{s_t} - v_\infty + u_\infty \left(\frac{r_{s_\theta}}{r_s}\right) \right] \frac{1}{\sqrt{1 + \left(\frac{r_{s_\theta}}{r_s}\right)^2}}$$

Let u_{1s} equal the velocity component tangent to the shock (i.e in $\vec{s}$ direction) and v_{1n} equals the velocity component normal to the shock (i.e. in $\vec{n}$ direction).

Then by applying the shock jump conditions we have

$$\rho_1 v_{1n} = \rho_2 v_{2n}$$

Because tangential velocity is preserved, therefore

$$u_{2s} = u_{1s}$$

Let $\vec{V_2}$ equals the resultant velocity after the shock with respect to shock coordinates.

Therefore, $\vec{V_2} = v_{2n}\vec{n} + u_{2s}\vec{s}$

The component of $\vec{V_2}$ along $\vec{i_\theta}$ (i.e tangent to the body) is given by

$$u_2 = \vec{V_2} \cdot \vec{i_\theta} = v_{2n}\vec{n} \cdot \vec{i_\theta} + u_{2s}\vec{s} \cdot \vec{i_\theta} = -v_{2n}\sin\alpha + u_{2s}\cos\alpha \qquad (6.25)$$

67

Similarly, the component of $\vec{V_2}$ along $\vec{i_r}$ (i.e normal to the body) is given by

$$v_2 = \vec{V_2} \cdot \vec{i_r} = (v_{2n}\vec{n} + u_{2s}\vec{s}) \cdot \vec{i_r} = v_{2n}\cos\alpha + u_{2s}\sin\alpha \qquad (6.26)$$

Hence,

$$u_{1s} = \left[v_\infty \vec{i_r} + u_\infty \vec{i_\theta} - \vec{u_s} \right] \cdot \vec{s}$$

$$= v_\infty \vec{i_r} \cdot \vec{s} + u_\infty \vec{i_\theta} \cdot \vec{s} - \vec{u_s} \cdot \vec{s}$$

$$= v_\infty \sin\alpha + u_\infty \cos\alpha$$

$$= u_{2s}$$

(Because $\vec{U_s} \cdot \vec{s} = 0$; $\vec{i_r} \cdot \vec{s} = \sin\alpha$; $\vec{i_\theta} \cdot \vec{s} = \cos\alpha$)

Therefore,

$$u_{1s} = u_{2s} = \frac{v_\infty \left(\frac{r_{s_\theta}}{r_s} \right) + U_\infty}{\sqrt{1 + \left(\frac{r_{s_\theta}}{r_s} \right)^2}} \qquad (6.27)$$

From Eq. (6.25) we have,

$$u_2 = -\frac{\rho_1}{\rho_2} v_{1n} \sin\alpha + u_{1s}\cos\alpha$$

$$= -\frac{\rho_1}{\rho_2} \sin\alpha \left[\frac{v_\infty}{\beta} - \frac{r_{s_\theta}}{\beta} U_\infty - \frac{r_{s_t}}{\beta} \right] + \frac{\cos\alpha}{\beta} \left[v_\infty \left(\frac{r_{s_\theta}}{r_s} \right) + U_\infty \right]$$

Rearranging terms we have,

Tangential component of the fluid velocity after the shock with respect to body is given by

$$u_2 = U_\infty - \left(1 - \frac{\rho_1}{\rho_2} \right) \times \frac{\left[r_{s_t} - v_\infty + U_\infty \left(\frac{r_{s_\theta}}{r_s} \right) \right] \left(\frac{r_{s_\theta}}{r_s} \right)}{\left[1 + \left(\frac{r_{s_\theta}}{r_s} \right)^2 \right]} \qquad (6.28)$$

Similarly, normal component of fluid velocity after the shock with respect to body coordinates is given by

$$v_2 = v_{2n} \cos\alpha + u_{2s} \sin\alpha$$

68

Substituting values and rearranging terms, we have

$$v_2 = v_\infty + \left(1 - \frac{\rho_1}{\rho_2}\right) \times \frac{\left[r_{s_t} - v_\infty + U_\infty \left(\frac{r_{s_\theta}}{r_s}\right)\right]}{\left[1 + \left(\frac{r_{s_\theta}}{r_s}\right)^2\right]} \tag{6.29}$$

Pressure behind the shock is obtained from the MacCormick's scheme at the predictor level. Once the pressure is known behind the shock, the normal component of the flow velocity ahead of the shock (measured w.r.t. shock) can be related to the pressure behind the shock by manipulating the oblique shock relations, which are

$$\rho_1 v_1 = \rho_2 v_2 \tag{6.30}$$

$$p_1 + \rho_1 v_1^2 = p_2 + \rho_2 v_2^2 \tag{6.31}$$

$$u_1 = u_2 \tag{6.32}$$

$$h_1 + \frac{V_1^2}{2} = h_2 + \frac{V_2^2}{2} \tag{6.33}$$

where V_1 and V_2 are resultant velocities.

From Eq. (6.31) we have

$$\rho_1 v_1^2 - \rho_2 v_2^2 = p_2 - p_1$$

From Eq. (6.30) we have

$$\frac{\rho_1}{\rho_2} = \frac{v_2}{v_1}$$

$$p_2 - p_1 = \rho_1 v_1^2 \left[1 - \frac{\rho_2 v_2^2}{\rho_1 v_1^2}\right] = \rho_1 v_1^2 \left[1 - \frac{\rho_1}{\rho_2}\right] = (\rho_2 - \rho_1)\left(\frac{\rho_1}{\rho_2}\right)v_1^2 \tag{6.34}$$

Therefore,

$$v_1^2 = \left(\frac{p_2 - p_1}{\rho_2 - \rho_1}\right)\left(\frac{\rho_2}{\rho_1}\right) = \frac{p_1\left[\frac{p_2}{p_1} - 1\right]}{\rho_1\left[\frac{\rho_2}{\rho_1} - 1\right]}\left(\frac{\rho_2}{\rho_1}\right) = \frac{\gamma - 1}{2}\left(\frac{p_1}{\rho_1}\right)\left[\frac{\gamma + 1}{\gamma - 1}\frac{p_2}{p_1} + 1\right]$$

69

Multiplying numerator and denominator by $\frac{\gamma+1}{\gamma-1}$ we have,

$$v_1 = \sqrt{\left(\frac{\gamma+1}{2}\right)\frac{p_1}{\rho_1}\left[\frac{p_2}{p_1} + \frac{\gamma-1}{\gamma+1}\right]} \qquad (6.35)$$

Similarly,

$$v_2^2 = \frac{p_2 - p_1}{\rho_2 - \rho_1}\left(\frac{\rho_1}{\rho_2}\right)$$

$$h_1 + \frac{V_1^2}{2} = h_2 + \frac{V_2^2}{2}$$

Therefore,

$$c_p(T_2 - T_1) = \frac{1}{2}(V_1^2 - V_2^2) \qquad (6.36)$$

Velocity triangles upstream and downstream of the shock gives

$$V_1^2 - V_2^2 = \left(v_1^2 + u_1^2\right) - \left(v_2^2 + u_2^2\right) = v_1^2 - v_2^2 \qquad (6.37)$$

Equation of state gives,

$$h = c_p T = \frac{\gamma}{\gamma - 1}RT = \frac{a^2}{\gamma - 1} = \frac{\gamma}{\gamma - 1}\frac{p}{\rho} \qquad (6.38)$$

Substituting Eqs. (6.37) and (6.38) into Eq. (6.35) we have,

$$\frac{\gamma}{\gamma - 1}\left(\frac{p_2}{\rho_2} - \frac{p_1}{\rho_1}\right) = \frac{1}{2}(v_1^2 - v_2^2) = \frac{1}{2}\left[\frac{p_2 - p_1}{\rho_2 - \rho_1}\right]\left[\frac{\rho_2}{\rho_1} - \frac{\rho_1}{\rho_2}\right] = \frac{1}{2}\frac{(p_2 - p_1)(\rho_2 - \rho_1)}{\rho_1\rho_2}$$

After rearranging we have,

$$2\gamma[\rho_1 p_2 - \rho_2 p_1] = (\gamma - 1)(p_2 - p_1)(\rho_2 - \rho_1) \qquad (6.39)$$

$$p_2\{(\gamma - 1)\rho_2 - (\gamma + 1)\rho_1\} = p_1\{(\gamma - 1)\rho_1 - (\gamma + 1)\rho_2\}$$

$$\frac{p_2}{p_1} = \frac{\frac{\gamma+1}{\gamma-1}\frac{\rho_2}{\rho_1} - 1}{\frac{\gamma+1}{\gamma-1} - \frac{\rho_2}{\rho_1}}$$

Equation (6.39) can also be written as

$$\rho_2\{-2\gamma p_1 - (\gamma - 1)(p_2 - p_1)\} = \rho_1\{(\gamma - 1)(p_2 - p_1) - 2\gamma p_2\}$$

70

$$\frac{\rho_2}{\rho_1} = \frac{(\gamma+1)p_2 + (\gamma-1)p_1}{(\gamma+1)p_1 + (\gamma-1)p_2}$$

$$\frac{\rho_2}{\rho_1} = \frac{\frac{\gamma+1}{\gamma-1}\frac{p_2}{p_1} + 1}{\frac{\gamma+1}{\gamma-1} + \frac{p_2}{p_1}} = \frac{\frac{p_2}{p_1} + \frac{\gamma-1}{\gamma+1}}{1 + \frac{\gamma-1}{\gamma+1}\frac{p_2}{p_1}} \tag{6.40}$$

Equations (6.24), (6.28), (6.29), (6.35) and (6.40) when written in the notations of the advanced time level in terms of the preceding time level can be written as

$$\overline{r_s^{n+1}} = r_s^n + \Delta t \, r_{s_t}^n \tag{6.41}$$

$$\overline{V_{nnx,j}^{n+1}} = \sqrt{\left(\frac{\gamma+1}{2}\right)\frac{p_\infty}{\rho_\infty}\left[\frac{\overline{p_{nnx,j}^{n+1}}}{p_\infty} + \frac{\gamma-1}{\gamma+1}\right]} \tag{6.42}$$

$$\frac{\overline{\rho_{nnx,j}^{n+1}}}{\rho_\infty} = \frac{\frac{\overline{p_{nnx,j}^{n+1}}}{p_\infty} + \frac{\gamma-1}{\gamma+1}}{1 + \frac{\gamma-1}{\gamma+1}\frac{\overline{p_{nnx,j}^{n+1}}}{p_\infty}} \tag{6.43}$$

$$\overline{u_{nnx,j}^{n+1}} = u_\infty - \left(1 - \frac{\rho_\infty}{\overline{\rho_{nnx,j}^{n+1}}}\right) \times \frac{\left[\overline{r_{s_{t(j)}}^{n+1}} - v_\infty + u_\infty\left(\frac{\overline{r_{s_{\theta(j)}}^{n+1}}}{r_{s_{(j)}}^{n+1}}\right)\right]\left(\frac{\overline{r_{s_{\theta(j)}}^{n+1}}}{r_{s_{(j)}}^{(n+1)}}\right)}{\left[1 + \left(\frac{\overline{r_{s_{\theta(j)}}^{n+1}}}{r_{s_{(j)}}^{(n+1)}}\right)^2\right]} \tag{6.44}$$

$$\overline{v_{nnx,j}^{n+1}} = v_\infty + \left(1 - \frac{\rho_\infty}{\overline{\rho_{nnx,j}^{n+1}}}\right) \times \frac{\left[\overline{r_{s_{t(j)}}^{n+1}} - v_\infty + u_\infty\left(\frac{\overline{r_{s_{\theta(j)}}^{n+1}}}{r_{s_{(j)}}^{n+1}}\right)\right]}{\left[1 + \left(\frac{\overline{r_{s_{\theta(j)}}^{n+1}}}{r_{s_{(j)}}^{n+1}}\right)^2\right]} \tag{6.45}$$

Note i is normal to the body and varies from $i = 1$ at the surface to $i = nnx$ at the shock. Also j is along to the body and varies from $j = 1$ at the stagnation line to $j = nny$ at the outflow boundary.

6.4 Solution Procedure

Solution procedures are followed in four steps as described below.

STEP 1 : Initial Solution

The initial conditions for this calculation are obtained by using an approximate

71

curve fit for the location and shape of the bow shock. Newtonian pressure distribution is used at the body. The approximate curve fit of Billig [46] is used to find r_s and $r_{s\theta}$ along the shock. To find the initial conditions immediately behind the shock, the radial shock velocity r_{s_t} is set equal to zero, and Eqs. (6.19) and (6.42)–(6.45) are used. The initial flow conditions on the wall are obtained by using the known wall temperature in conjunction with the pressure from the Newtonian pressure distribution. The initial flow conditions at the interior grid points are obtained by assuming a linear variation between the flow conditions immediately behind the bow shock and the wall conditions.

STEP 2 : Predictor Step

At the beginning of the predictor step, the shock-wave radial distance is computed from Eq. (6.41). The pressure immediately behind the shock $\left(\overline{p_{nnx,j}^{n+1}}\right)$ is computed with the MacCormack scheme

$$
\begin{aligned}
\overline{\mathbf{U}_{nnx,j}^{n+1}} = \mathbf{U}_{nnx,j}^n &- \frac{\Delta t}{\Delta y}\left(\mathbf{F}_{nnx,j+1}^n - \mathbf{F}_{nnx,j}^n\right) \\
&- \frac{\Delta t}{\Delta x}\left(\mathbf{G}_{nnx,j}^n - \mathbf{G}_{nnx-1,j}^n\right) - \Delta t \mathbf{H}_{nnx,j}^n
\end{aligned}
\tag{6.46}
$$

After the pressure behind the bow shock is obtained, $\overline{V_{nnx,j}^{n+1}}$ and $\overline{\rho_{nnx,j}^{n+1}}$ can be computed from normal shock relations given by Eqs. (6.42) and (6.43). Similarly, the components of the fluid velocity behind the bow shock can be found from the oblique-shock relations given by Eqs. (6.44) and (6.45). The remaining unknown $\overline{T_{nnx,j}^{n+1}}$ is calculated with the equation of state. This completes the predictor step.

STEP 3 : Corrector Step

The corrector step is similar to the predictor step, except that the shock-wave radial distance is evaluated with the modified Euler corrector, which is

$$
r_{s_{(j)}}^{n+1} = r_{s_{(j)}}^n + \frac{\Delta t}{2}\left(r_{s_{t(j)}}^n + \overline{r_{s_{t(j)}}^{n+1}}\right)
\tag{6.47}
$$

72

and Eq. (6.46) is replaced by the MacCormack corrector scheme, in which the usual

backward difference for $\partial G/\partial y$ is replaced by a forward difference given by

$$
\begin{aligned}
\mathbf{U}_{nnx,j}^{n+1} = \frac{1}{2} &\left[\mathbf{U}_{nnx,j}^{n} + \overline{\mathbf{U}_{nnx,j}^{n+1}} - \frac{\Delta t}{\Delta y}\left(\overline{\mathbf{F}_{nnx,j}^{n+1}} - \overline{\mathbf{F}_{nnx,j-1}^{n+1}} \right) \right] \\
&- \frac{1}{2}\left[\frac{\Delta t}{\Delta x}\left(\overline{\mathbf{G}_{nnx,j}^{n+1}} - \overline{\mathbf{G}_{nnx-1,j}^{n+1}} \right) + \Delta t \overline{\mathbf{H}_{nnx,j}^{n+1}} \right]
\end{aligned}
\tag{6.48}
$$

This completes the corrector step.

STEP 4 : Boundary Conditions

When the "shock-fitting" method is employed, the flow conditions at the outer compu-

tational boundary are those conditions which exist immediately downstream of the bow

shock as determined by the Rankine-Hugoniot relations. Consequently, it is necessary to

include logic which will permit this boundary to move with the bow shock as the latter

moves toward its "steady-state" position. After the calculation of the boundary condition

at $i = nnx$ (i.e., after the shock) has been performed by the shock-fitting method, the

predictor or the corrector steps are initiated at the interior grid points. All other boundary

conditions are calculated after the predictor or corrector step has been completed at all

interior grid points.

The flow conditions along the supersonic outflow boundary (i.e., at $j = nny$) are

determined by using a second-order extrapolation of the interior grid-point data.

Along the body surface, no-slip, zero-pressure-gradient, adiabatic, and noncatalytic

wall boundary conditions were used.

6.5 Artificial Viscosity

It is well known that central finite-difference schemes for non-linear convection

problems require the addition of artificial dissipation for stability and uniqueness. For

problems with boundaries, the boundary conditions for the dissipative operators are not

always obvious. In general case when no information about the field outside the boundary

is available the dissipative operators used must be supplied with suitable boundary
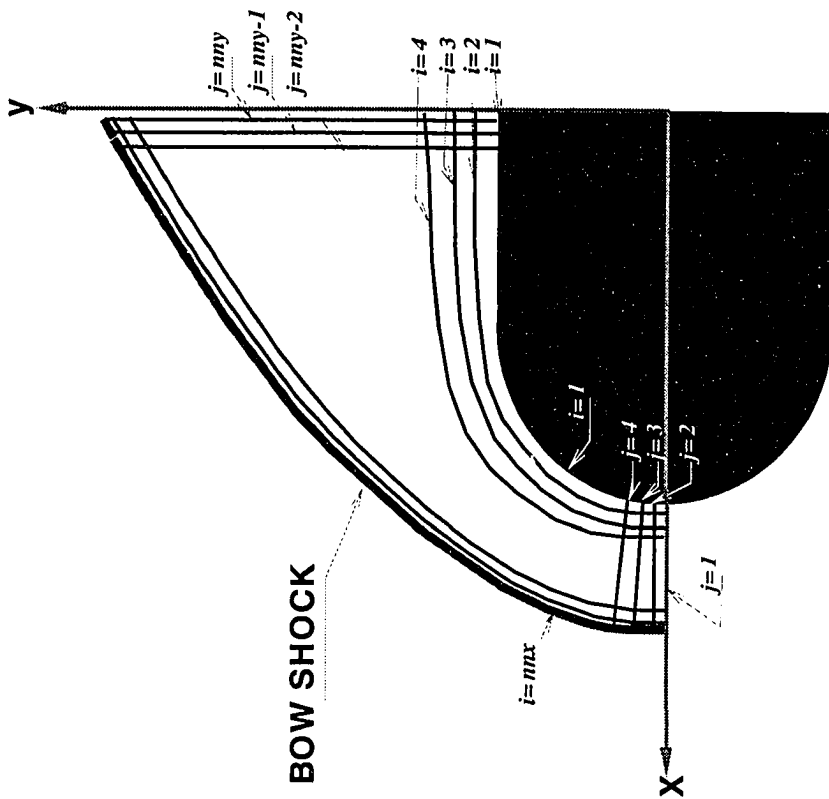
73

Figure 6.2 Notation used for artificial viscosity.

74

conditions. Such boundary conditions can be implemented either by extrapolating the field from interior grid points to the exterior grid points needed by the dissipative operators or by modifying the operators at the boundary so that no exterior grid points are addressed. For each extrapolation rule there is a corresponding boundary-modified operator and it is merely a matter of taste which representation is preferred. What is important is that the overall dissipative operator should be well behaved in the sense that it provides as much damping as possible without introducing unacceptable errors.

In most applications where artificial dissipation is used, the dissipative operators are based on either 2nd-differences or 4th-differences in the various coordinate directions. They are of either constant coefficients or variable coefficients type. Since in shock-fitting we need very little artificial dissipation, generally fourth order damping is sufficient. Fourth-order explicit dissipation term of the following form is used in this work

$$-\epsilon_c \left[(\Delta x)^4 \frac{\partial^4}{\partial x^4}(\mathbf{U}^i) + (\Delta y)^4 \frac{\partial^4}{\partial y^4}(\mathbf{U}^i) \right]$$

$$= -\epsilon_c \left[(\mathbf{U}^n_{i+2,j} - 4\mathbf{U}^n_{i+1,j} + 6\mathbf{U}^n_{i,j} - 4\mathbf{U}^n_{i-1,j} + \mathbf{U}^n_{i-2,j}) \right]$$

$$-\epsilon_c \left[(\mathbf{U}^n_{i,j+2} - 4\mathbf{U}^n_{i,j+1} + 6\mathbf{U}^n_{i,j} - 4\mathbf{U}^n_{i,j-1} + \mathbf{U}^n_{i,j-2}) \right]$$

The negative sign is required in front of the fourth-derivatives in order to produce positive damping. The smoothening coefficient ϵ_c should be less than $\frac{1}{16}$ for stability. The fourth derivative terms are evaluated using the finite-difference approximations shown on the right hand side of the above equation. The dissipative operators used are of the type

$$D\mathbf{U}_{i,j} = D_i \mathbf{U}_{i,j} + D_j \mathbf{U}_{i,j}$$

where D_i and D_j are the corresponding 1–D operators in i and j respectively. Referring to Fig. 6.2 for various notations we can write the following fourth order difference equation in the interior domain for the radial direction (i direction).

$$D_i \mathbf{U}_{i,j} = -\epsilon_c (\mathbf{U}_{i-2,j} - 4\mathbf{U}_{i-1,j} + 6\mathbf{U}_{i,j} - 4\mathbf{U}_{i+1,j} + \mathbf{U}_{i+2,j})$$

75

This we do from $i = 3$ to $i = nnx-2$. The points remained to be solved in the i direction are at $i = 1, 2$ and $i = nnx-1, nnx$. Hence,

$$D_i U_{1,j} = -\epsilon_e [U_{3,j} - 2U_{2,j} + U_{1,j}]$$

$$D_i U_{2,j} = -\epsilon_e [U_{4,j} - 4U_{3,j} + 5U_{2,j} - 2U_{1,j}]$$

$$D_i U_{nnx-1,j} = -\epsilon_e [-2U_{nnx,j} + 5U_{nnx-1,j} - 4U_{nnx-2,j} + U_{nnx-3,j}]$$

$$D_i U_{nnx,j} = -\epsilon_e [U_{nnx,j} - 2U_{nnx-1,j} + U_{nnx-2,j}]$$

Again in the j direction we have the following fourth-order differencing used in the interior domain.

$$D_j U_{i,j} = -\epsilon_e (U_{i,j-2} - 4U_{i,j-1} + 6U_{i,j} - 4U_{i,j+1} + U_{i,j+2})$$

This we do from $j = 3$ to $j = nny-2$ and $i = 1, nnx$ It needs to find out $U_{i,j}$ at $j = 1$, 2 and $j = nny-1, nny$ Therefore,

$$D_j U_{i,1} = -\epsilon_e [U_{i,3} - 2U_{i,2} + U_{i,1}]$$

$$D_j U_{i,2} = -\epsilon_e [U_{i,4} - 4U_{i,3} + 5U_{i,2} - 2U_{i,1}]$$

$$D_j U_{i,nny-1} = -\epsilon_e [-2U_{i,nny} + 5U_{i,nny-1} - 4U_{i,nny-2} + U_{i,nny-3}]$$

$$D_j U_{i,nny} = -\epsilon_e [U_{i,nny} - 2U_{i,nny-1} + U_{i,nny-2}]$$

Finally,

$$U_{i,j} = U_{i,j} - \epsilon_e [D_i U_{i,j} + D_j U_{i,j}]$$

6.5 Validation of Code

Before running the code with full chemistry and reactions, it was validated with two other existing sources. First it was validated with viscous shock layer code by Kumar and Graves [49] which also uses shock fitting method. Secondly, Bellig's [46] correlations

76

for sphere were used to find the shock profile and the shock stand-off distance was compared with the results of the current code. The free stream conditions used for this validation were

$$M_\infty = 5.11$$

$$p_\infty = 42732 \, \text{N/m}^2$$

$$T_\infty = 292\text{k}$$

$$\gamma = 1.4$$

The computational mesh consisted of 101 equally spaced points in the radial i direction and 91 points in the tangential (j) direction. Figure 6.3 shows a plot of radial shock velocity (r_{st}) as a function of time step number n. These velocities should approach zero as the steady-state solution is approached. The solution moves rapidly toward a steady state initially with large time-dependent oscillations appearing. In the final part of the solution, the convergence is very slow and has a monotonic behavior. As the computations proceeds the residuals or L_∞ norm of the flow field based on density variation drops by 6 orders of magnitude and then stays constant. This is shown in Fig. 6.4. At this point the flow field has attained a pseudo-steady state, i.e. the flow field keeps oscillating about a mean. Figure 6.5 shows a plot of the pressure distribution around the wall of the blunt projectile non-dimensionalized with respect to the stagnation line pressure. The solid curve is the current numerical result. The circles are the fairing of VSL code due to Kumar and Graves [49]. Both the results are in excellent agreement. A comparison of the numerically predicted shock shape with the empirical result of Billig is shown in Fig. 6.6. The circular symbol represent the emperical results, while the numerical result is shown as a solid curve. Again the two results match perfectly well. Figure 6.7 shows the line plot for pressure along various $j =$ constant lines and Figure 6.8 shows the line

77

plot for the density along various $j =$ constant lines. The circles are the result with the present calculations and the triangles are the results with VSL code. The results are in good agreement with each other. Figures 6.9–6.11 show the pressure, density and temperature contours respectively with the present calculations on the upper half of the plot whereas the lower half is plotted with VSL code by Kumar and Graves [49]. Both the shock profile as well as the shock stand-off distance matches well with the VSL code.

78
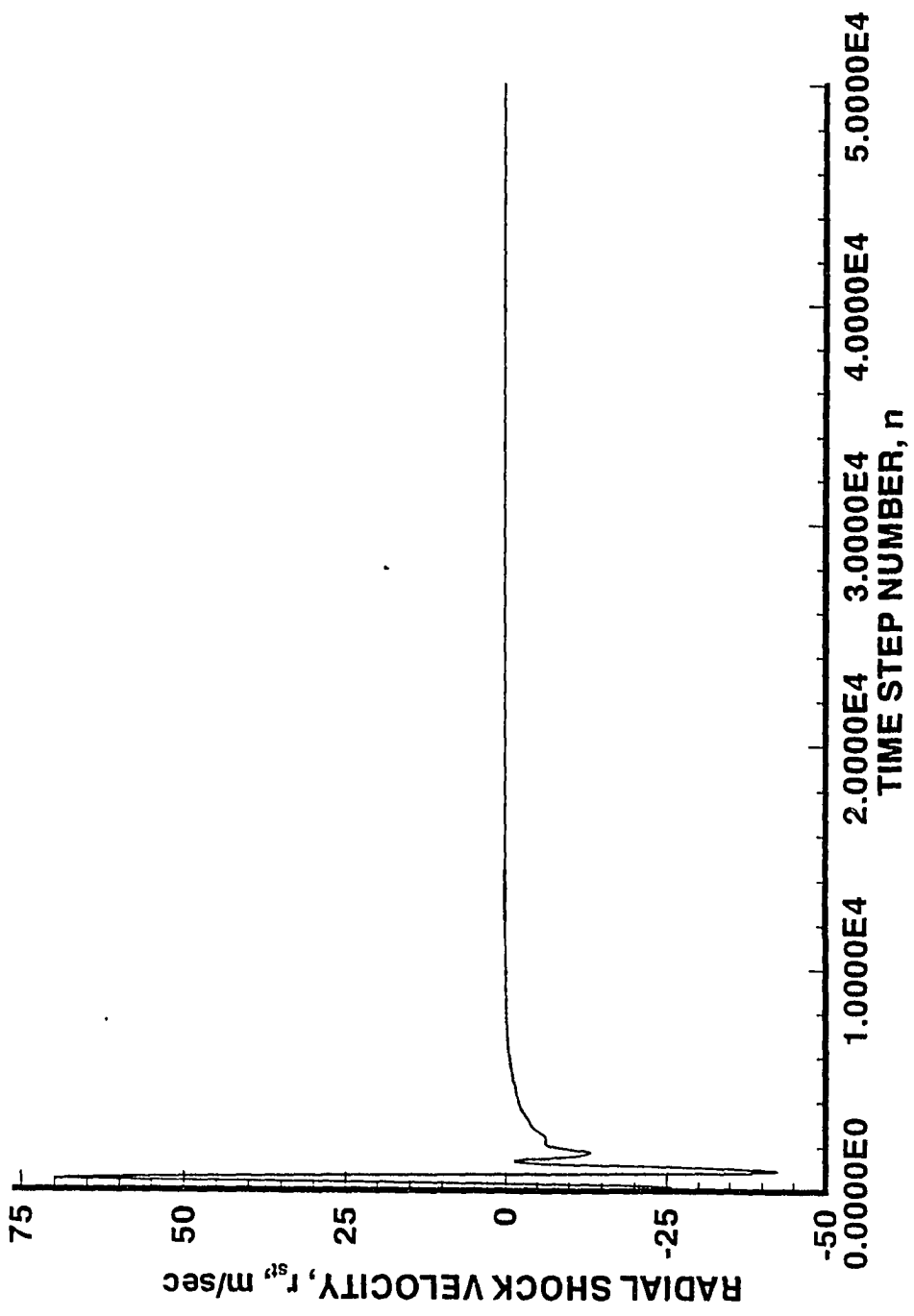
Figure 6.3 Plot of radial shock velocity (r_{st}) vs time step number n.

79

80
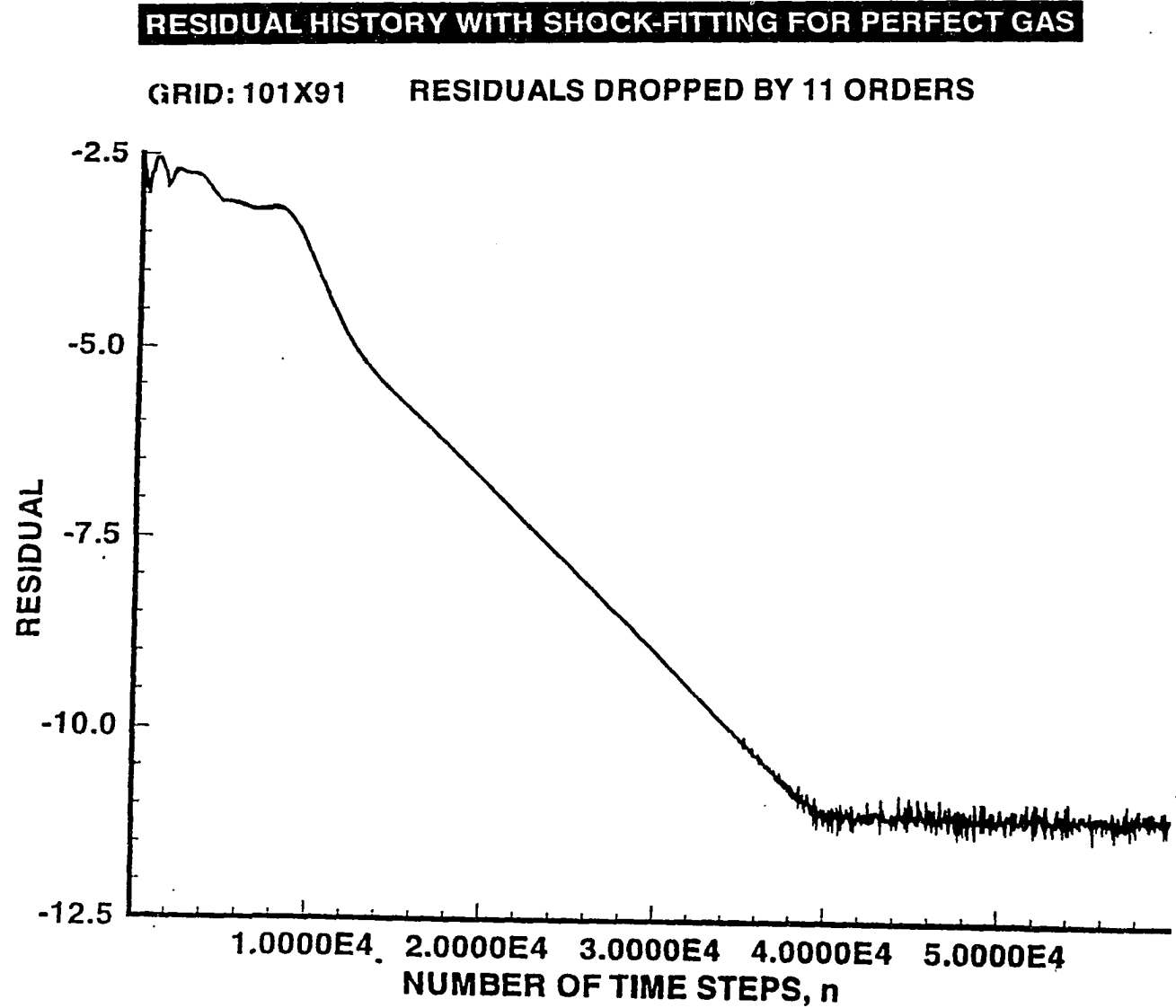
Figure 6.4   Residual history of computations.

○ ○ ○ ○   VSL CODE (KUMAR et al. AIAA PAPER # 77-172)

PRESENT CALCULATIONS

$M_\infty = 5.11$

$P_\infty = 42719 \ N/M^2$

$T_\infty = 292 \ K$

$\gamma = 1.4$
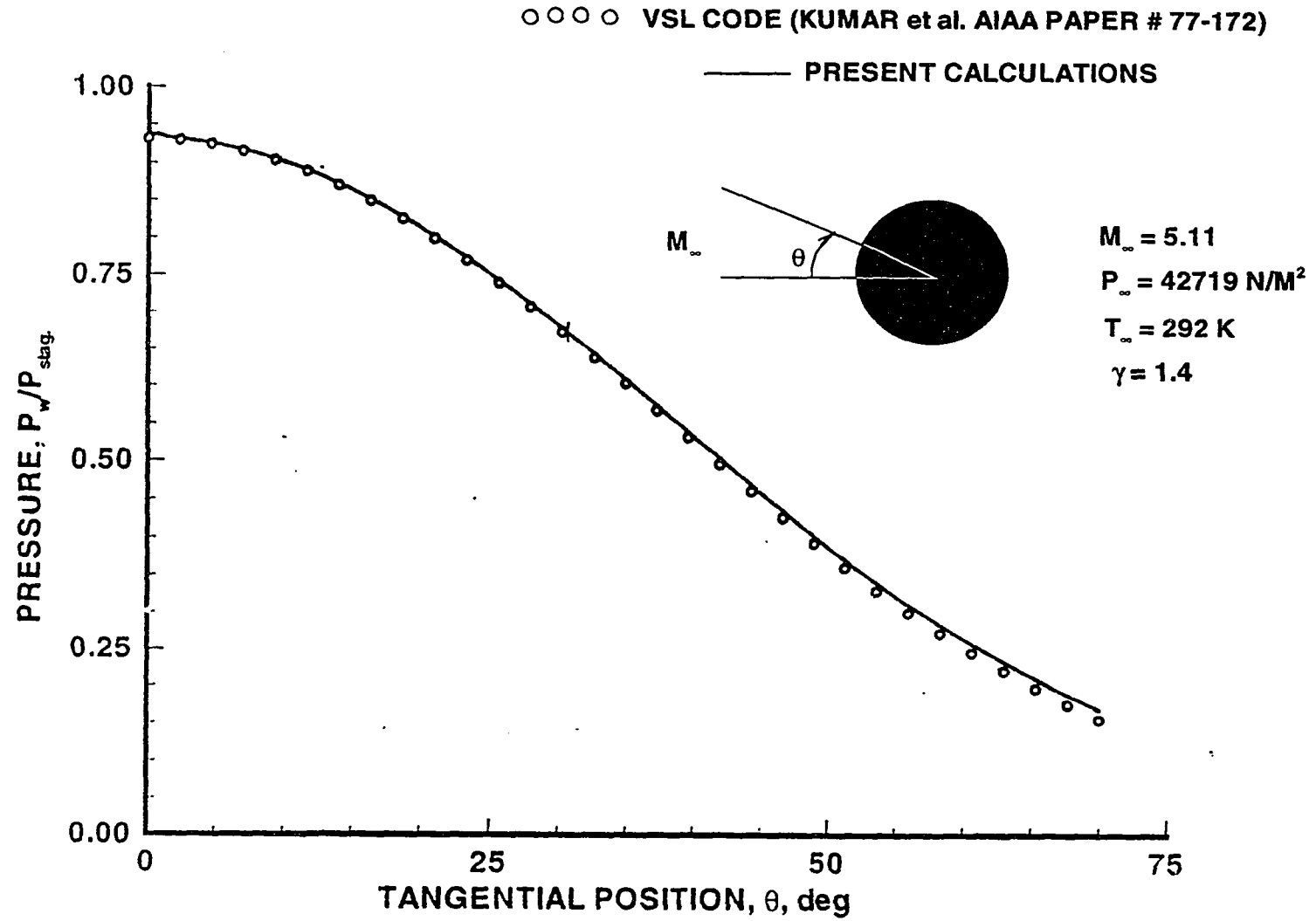
Figure 6.5   Pressure distribution around the wall, validated with viscous shock layer (VSL) code.
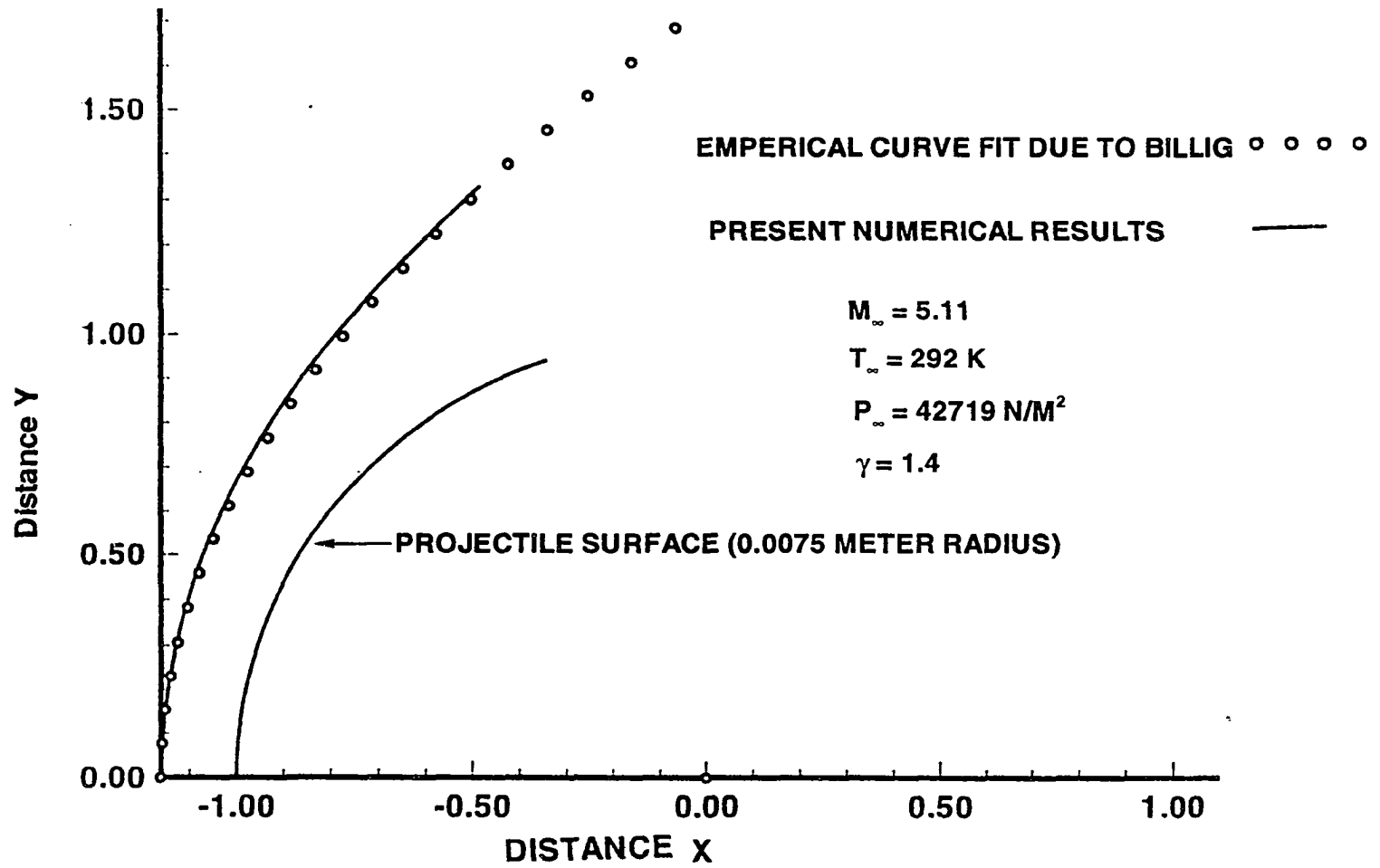
Figure 6.6 Comparison of numerically predicted shock shape with the emperical results of Billig.
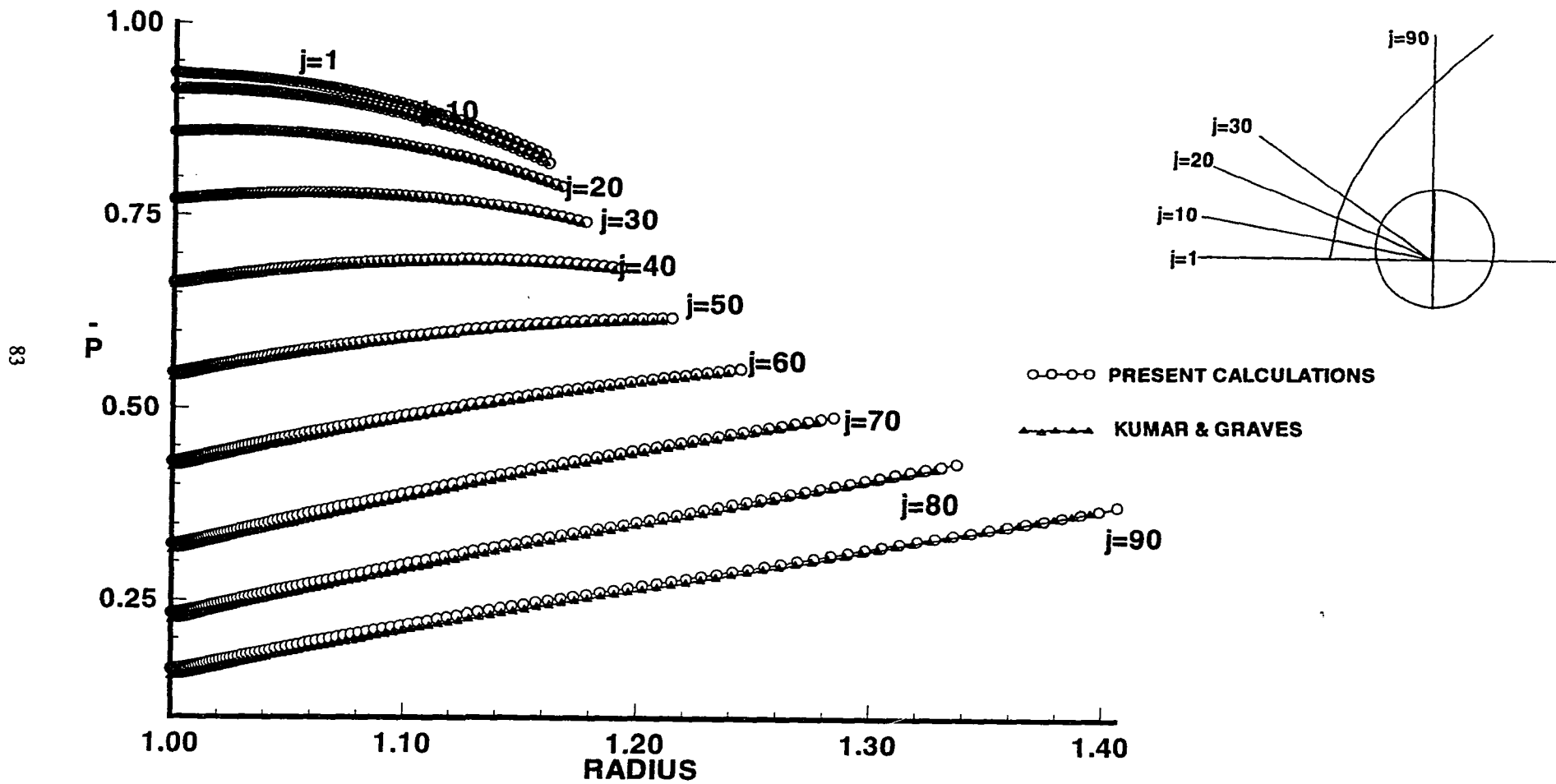
Figure 6.7   Line plot for pressure along various j = constant lines: circles with the present
computations and lines with VSL code.

84

LINE PLOT FOR DENSITY ALONG VARIOUS j = CONSTANT GRID LINES
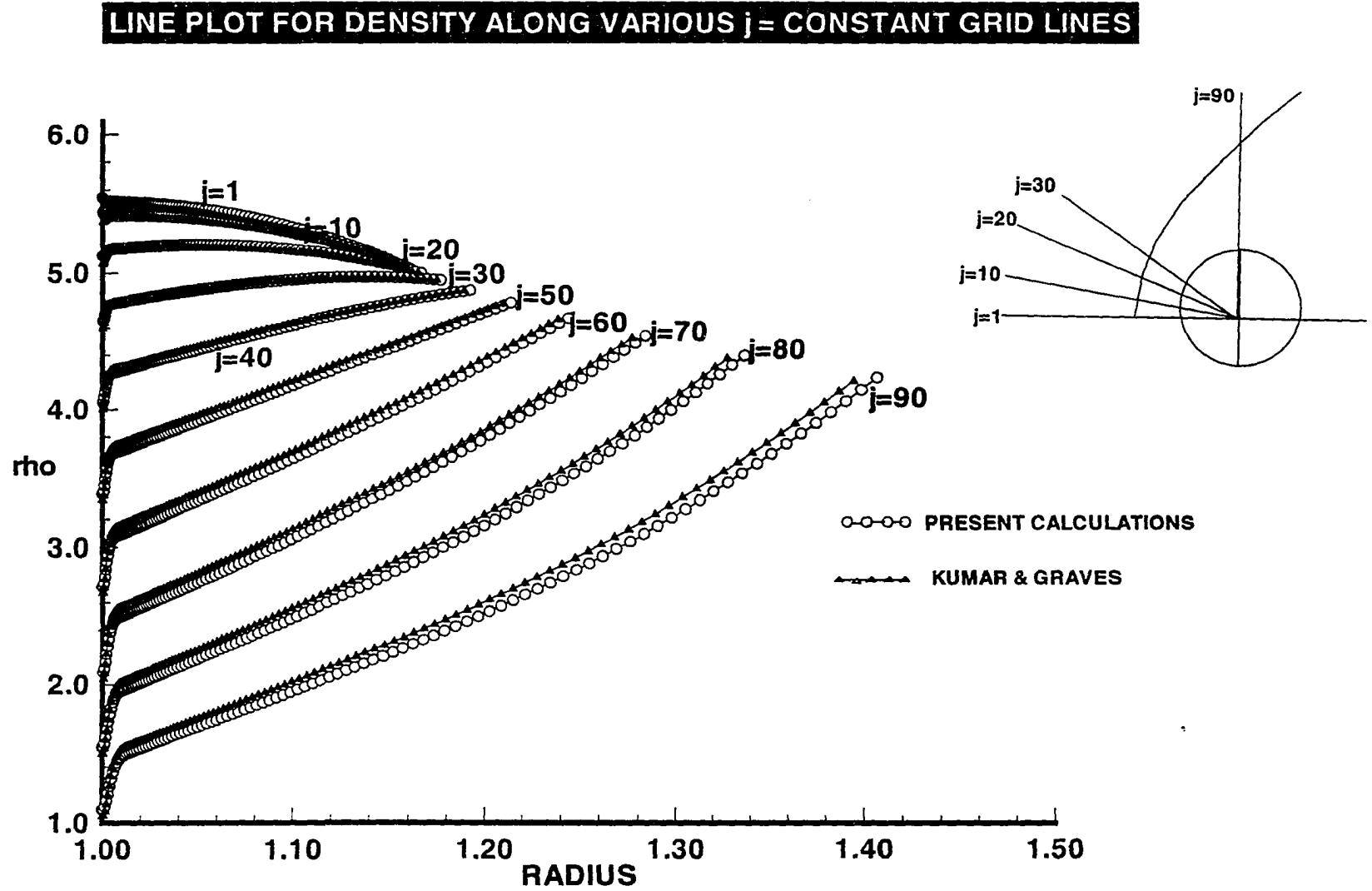
Figure 6.8   Line plot for density along various j = constant lines: circles with the present computations and lines with VSL code.

85

SPARK CODE VALIDATION FOR SHOCK-FITTING

GRID 101X91

$M_\infty = 5.11$

$P_\infty = 42719 \ N/M^2$

$T_\infty = 292 \ k$

$\gamma = 1.4$

$\leftarrow$————— PRESSURE CONTOURS WITH SPARK CODE

$\bar{P}$

$\leftarrow$————— PRESSURE CONTOURS WITH VSL CODE

(KUMAR et al. AIAA PAPER 77-172)

1.0

0.5

0.0

-0.5

-1.0

-1.0 -0.5 0.0 0.5 1.0 1.5 2.0

X
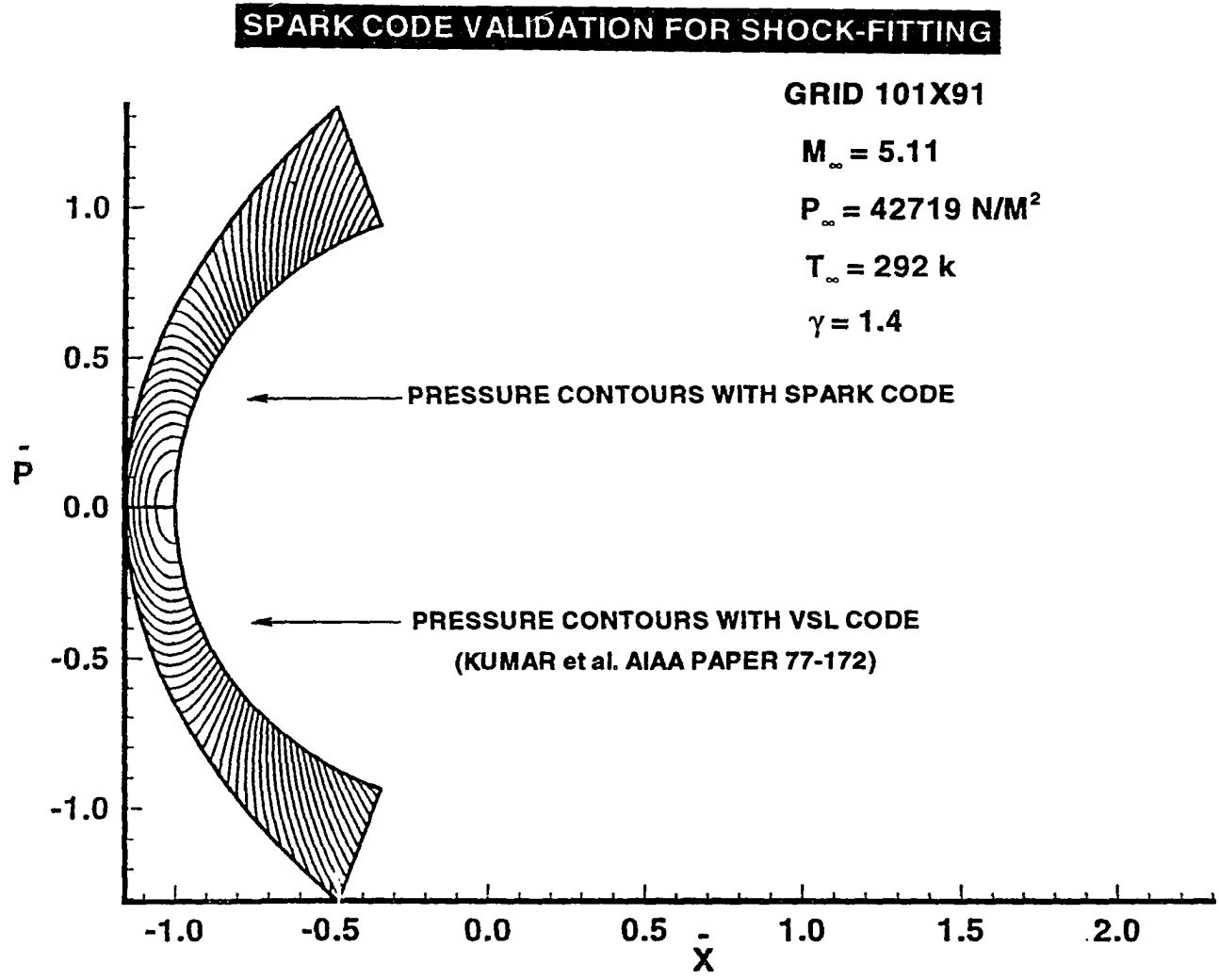
Figure 6.9   Comparison of current numerical results for pressure (upper half) with VSL code (lower half).

86

SPARK CODE VALIDATION FOR SHOCK-FITTING

GRID: 101X91

$M_\infty = 5.11$

$P_\infty = 42719 \ N/M^2$

$T_\infty = 292 \ K$

$\gamma = 1.4$

DENSITY CONTOURS WITH SPARK CODE

DENSITY CONTOURS WITH VSL CODE

(KUMAR et al. AIAA PAPER # 77-172)
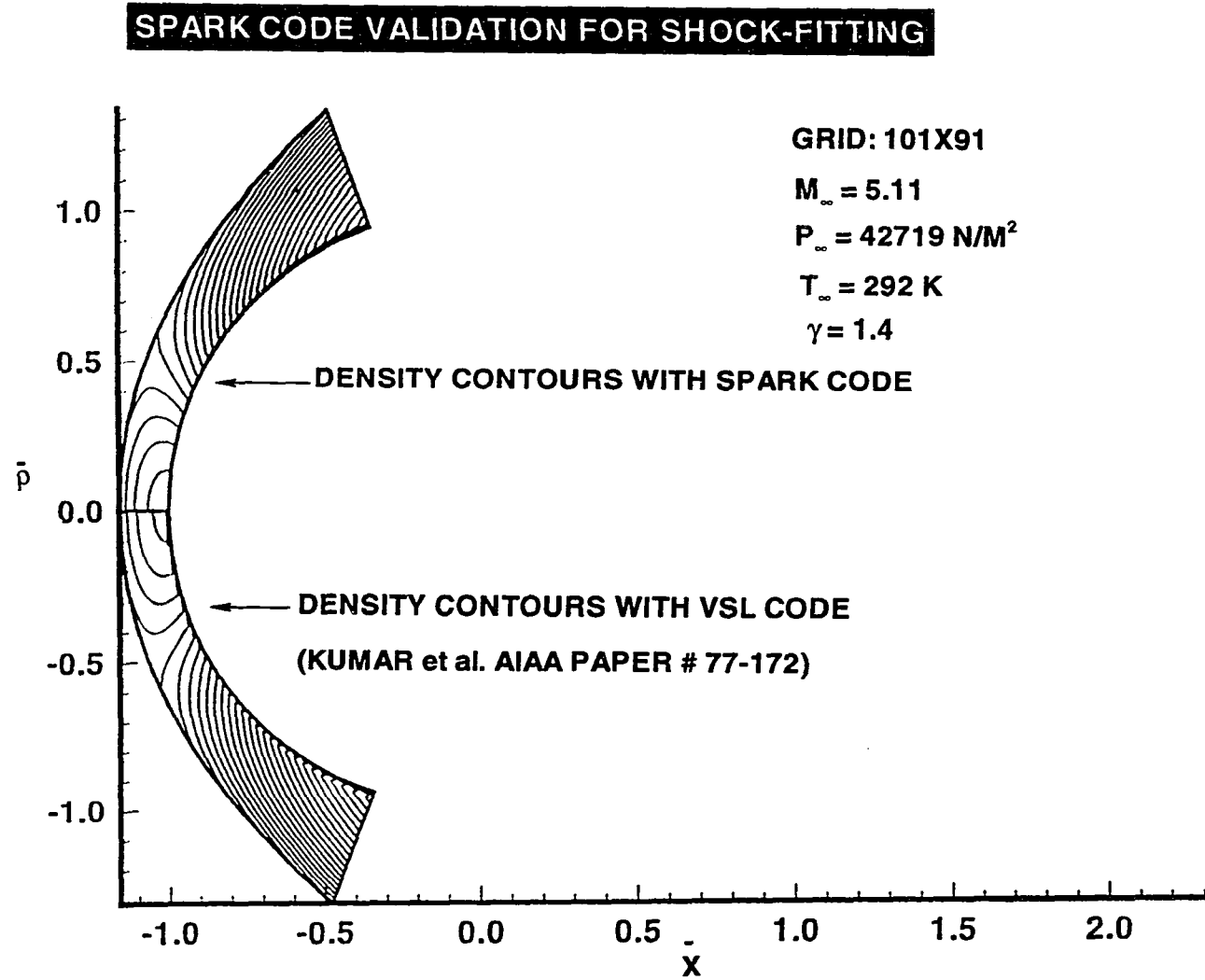
Figure 6.10   Comparison of current numerical results for density (upper half) with VSL code (lower half).

87

SPARK CODE VALIDATION FOR SHOCK-FITTING

GRID: 101X91

$M_\infty = 5.11$

$P_\infty = 42719 \ N/M^2$

$T_\infty = 292 \ K$

$\gamma = 1.4$

← TEMPERATURE CONTOURS WITH SPARK CODE

← TEMPERATURE CONTOURS WITH VSL CODE
(KUMAR et al. AIAA PAPER # 77-172)
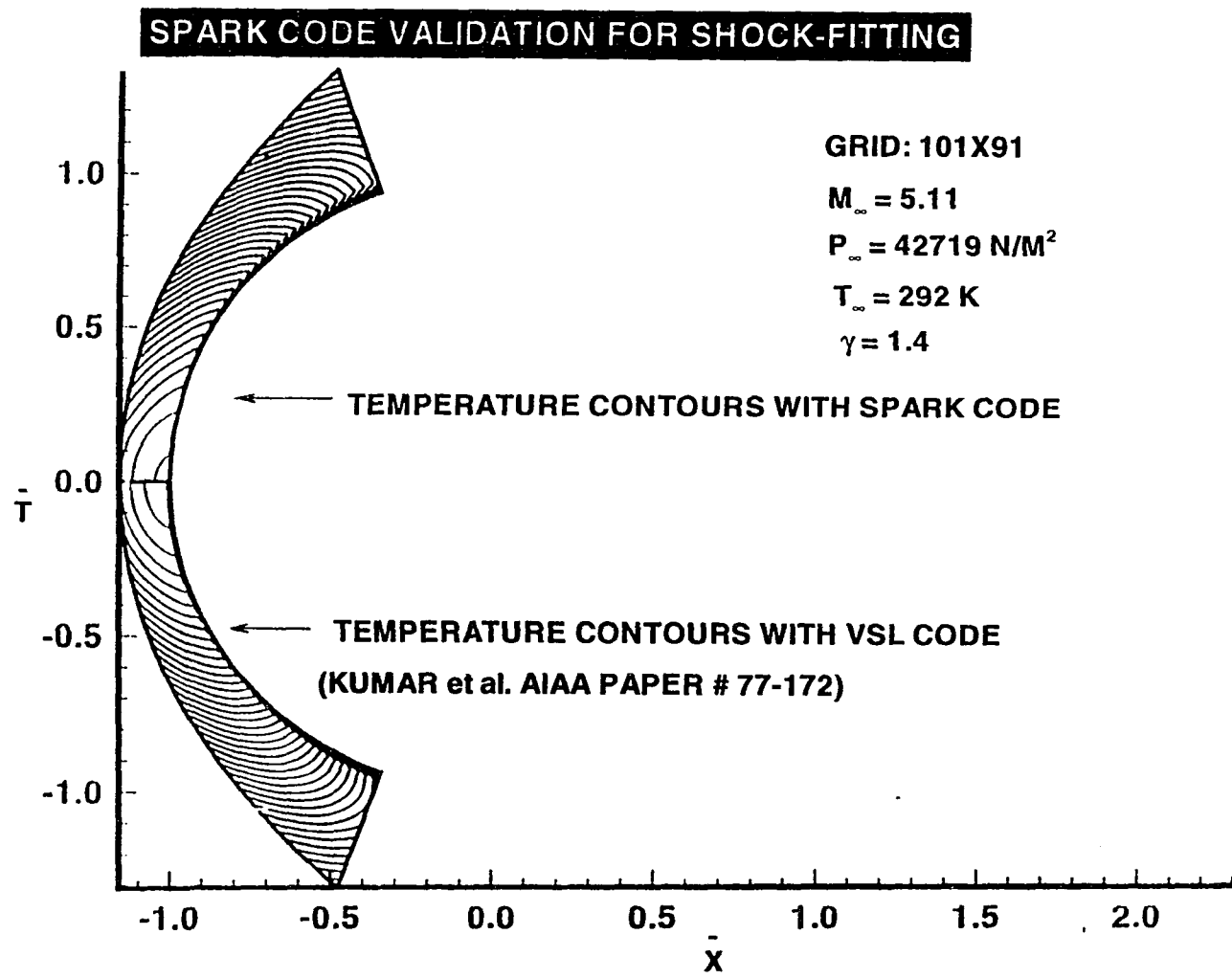
Figure 6.11   Comparison of current numerical results for temperature (upper half) with VSL code (lower half).

Chapter 7

RESULTS AND DISCUSSION USING SHOCK-CAPTURING METHOD

In this chapter we shall be discussing the numerical simulations results for Lehr's Mach 5.11 and 6.46 cases using shock-capturing method. Numerical simulations have been carried out for a 15 mm diameter spherical projectile and the following free-stream conditions:

M_∞ = 5.11 and 6.46

p_∞ = 42663.2 N/m^2 (320 mm of Hg)

T_∞ = 292 K, M_{CJ} = 5.11

The premixed fuel oxidizer mixture is taken as $2H_2 + O_2 + 3.76N_2$. For the spherically blunt projectile, a fluid particle approaching the body first encounters the bow shock thus raising its temperature, pressure and density while lowering the velocity. This fluid particle then travels a distance equal to the induction length at elevated temperature before it encounters the reaction front. Once the ignition starts, chemical energy is released and another discontinuity known as reaction front is formed. In the induction zone, the temperature and the pressure remain relatively constant at the post shock conditions, while the concentrations of radicals build up very rapidly. In the stagnation zone, due to large residence time, it attains equilibrium while away from it, flow is in non-equilibrium.

7.1 Mach 5.11 Case

The assumption of flow-field symmetry about the stagnation line is invoked and, therefore, only one half of the flow field is calculated. Calculations have been carried
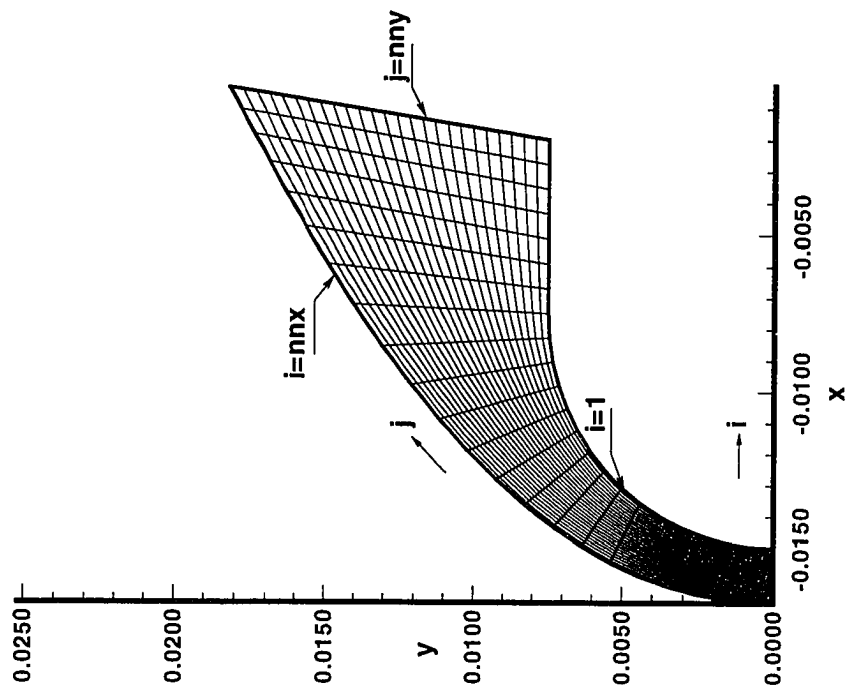
Figure 7.1 Typical grid used in the computation (every fourth point shown).

89

CONTOUR PLOT FOR PRESSURE

N/m^2

OUTER GRID BOUNDARY

BOW SHOCK

$M_\infty = 5.11$

I	1.98E6
H	1.87E6
G	1.76E6
F	1.65E6
E	1.54E6
D	1.43E6
C	1.32E6
B	1.21E6
A	1.09E6
9	9.83E5
8	8.72E5
7	7.61E5
6	6.50E5
5	5.39E5
4	4.28E5
3	3.17E5
2	2.06E5
1	9.55E4
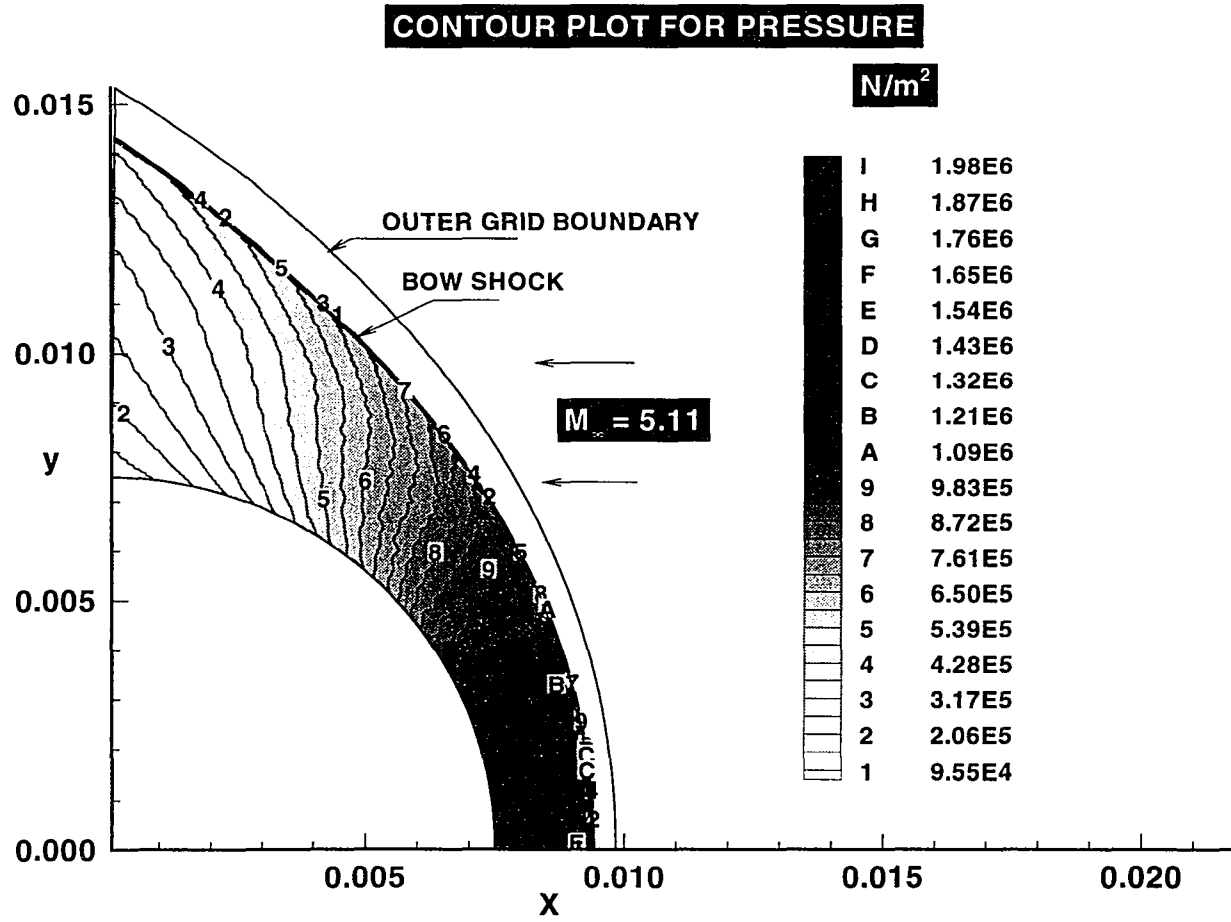
Figure 7.2 Contour plot of pressure for Mach 5.11 with shock-capturing.

out for a grid with 197 points in the circumferential direction and 152 points in the normal direction. Figure 7.1 shows the typical grid which contains 197×152 grid points (197 normal to the body and 152 along the body). For clarity, every fourth grid point is shown in the figure. This grid was chosen based on the earlier work by Ahuja et al. [25], where the flow field was shown to be adequately resolved with this grid. For the present case of stoichiometric hydrogen-air mixture, the Chapman-Jouget velocity is the same as the velocity of the projectile for the Mach 5.11 case. Unsteady flow phenomenon can occur if the free-stream velocity of the projectile is around the C-J detonation velocity of the mixture. The residuals dropped by three orders in 12,000 iterations and then remained constant.

Figure 7.2 shows the pressure contours. It shows the bow shock (similar to non-reacting flows) and the expansion waves as the flow expands over the body. The peak pressure occurs near the stagnation region where the shock is nearly normal and decreases away from it as the flow expands. The contours show some oscillations, which are caused by the fluctuating shock and reaction front and will be discussed later. The reaction front is not visible in this figure since the pressure stays constant across the reaction front. The shock standoff distance compares well with the Lehr's shadowgraph (Fig. 2.2).

The density contours (Fig. 7.3) show a very complex flow field with the presence of two discontinuities. The outer discontinuity is the bow shock and the inner discontinuity is the reaction front. These two fronts can be seen separated from each other by the induction distance. The separation (i.e., the induction distance) is minimum near the stagnation line and increased away from it. This is because near the stagnation line, bow shock is almost normal and, hence, the post shock temperature is maximum; thus, induction distance is minimum. Away from the stagnation line, the shock strength decreases, thereby decreasing the post-shock temperature and, hence, increasing the induction distance.

91

About one nose radius downstream, the induction length becomes infinite, i.e., infinite streamwise separation between shock and the reaction front. Therefore, it is not possible to form an oblique detonation wave under these circumstances. Also, the oscillations in the reaction front can be seen clearly. As the computations proceeds, the L_∞ norm of the flow field based on density variation drops by two orders of magnitude and then stays constant. At this point the flow field has attained a psuedo-steady state, i.e., the flow field keeps oscillating about a mean. As noticed earlier, the density increases just after the shock (peak value) and then decreases as the flow passes through the reaction front.

Figure 7.4 shows the temperature contours and the corresponding enlarged view. The bow shock and the reaction front can be seen clearly. Following a stream line into the stagnation zone, it is seen that temperature jumps across the shock and then stays constant in the induction zone. Past the induction zone, due to exothermic nature of H_2-air reaction mechanisms, the temperature increases almost instantaneously reaching about 11 times the free-stream value. The pulsation in the flow field can be vividly seen here.

Figures 7.5 shows the water mass fraction contours. The reaction front can be seen in this figure. To better show the instabilities, an enlarged view is also shown. At the end of the combustion zone, the temperature is high enough to start the combustion. As the reaction proceeds, the water mass fraction increases rapidly. The oscillations similar to temperature and density profiles can be seen here. The instability is characterized by an almost regular periodic wave motion having a constant frequency and amplitude. Similar instability has been observed experimentally in Lehr's work. The contour plots shown here show the spatial variation of instability at one point in time. It also shows that instabilities are not restricted to the reaction front only but are convected toward the body, thus affecting the entire flow field. Figure 7.6a shows the line plot for pressure along various j = constant grid lines. As the flow crosses the shock, it encounters the

92

pressure jump. The pressure decreases slightly after the shock. The Von Neumann spike, which is characteristic of reacting flows, is also visible. The post shock oscillations in pressure along stagnation line has also been observed in Ref. [14]. Figure 7.6b shows the temperature along various j = constant grid lines. The post shock stagnation point temperature is $3150°K$, which compares well with Ref. [15]. As the gas encounters the bow shock, the temperature increases abruptly. Immediately after the shock, the temperature stays constant for a short distance and then begins to increase due to exothermic reactions. The induction zone decreases with increasing temperature, as chemical energy release will be faster for higher temperatures.

To help understand the temporal nature of these instabilities, attention is now focussed on the time history of physical variables along the stagnation line only. The presentation of results in this form also allows comparison of the numerical results with the wave-interaction model originally proposed by McVey et al. [8] and further modified by Matsuo et al. [18]. This is a one-dimensional model which is used to explain the instability mechanism. The model successfully explains the main features of the flow field as identified in the numerical simulations as well as in schlieren pictures. The essential features of this model are shown in Fig. 7.7, which also shows the x-t plot for the computed water mass fraction along with an overlay of pressure. Also, one can see the unsteadiness in the reaction front. This unsteadiness originates from the induction zone near the stagnation line and then travels downstream. First, the contact discontinuity approaches the original reaction front. The hot gases behind the contact discontinuity begin to react. The resulting pulse of the energy release front generates two compression or pressure waves, one of which propagates upstream towards the bow shock and another downstream towards the body. The compression wave which propagates upstream interacts with the bow shock and produces a contact discontinuity behind the

93

bow shock. The bow shock is stronger after the interaction and, therefore, the gas is hotter on the upstream side of the contact discontinuity. The hot gases behind the contact discontinuity reduce the induction time and create a new reaction front thus generating another set of compression waves. The contact discontinuity then reaches the position of the original reaction front, extinguishing the reaction at this point because no more unreacted gas exists there. This reduces the rate of energy release thereby generating rarefaction waves. The reaction front begins to recede because of the increased induction time of the colder fluid. The other compression wave, travelling towards the body, gets reflected from the body to the bow shock, and interacts with it at about the same time that the most recently created compression wave arrives at the bow shock. The compression wave and the reflected compression wave from the body interact with the bow shock, thus providing a possible mechanism for the creation of another contact discontinuity i.e. secondary contact discontinuity. The gases being hotter on the upstream side of the contact discontinuity, start burning, again generating compression waves and the cycle is repeated. Matsuo et al. [18] also emphasized the importance of considering the reflection of the compression wave from the body in their calculations. The compression waves reflecting from the blunt body may not necessarily be in phase with the compression waves created by the new energy release front. Thus, once these reflected waves interact, they cause the flow to be not exactly periodic; however, the pulsating energy release front could still be nearly periodic. In some instances the original compression wave and the reflected compression wave may not hit the bow shock at the same time, thereby distorting some of the structure of the bow shock as clearly seen in Fig. 7.7.

If one observes these oscillations very closely, it is seen that in each cycle the water mass production rate, which is also a measure of energy release, at first increases and then eventually decreases to zero. This is the point of extinguishment of the reaction

94

front. The reaction almost comes to a standstill at this point. Since the new reaction front generated has high energy release (and, hence, high water mass production rate), it sends new sets of compression waves, which propagate both upstream and downstream, and the above cycle is repeated.

To further investigate the unsteady nature of the flow field, a Fourier analysis of the flow field was conducted. For this, data at various sample stations along the j = 61 grid line were stored for 30,000 iterations to get good temporal resolutions. The grid used was 101×78, and all calculations were time accurate. Figure 7.8 shows the amplitude versus frequency plot obtained by using a Fourier transform. The flow field spectrum is well resolved, and it clearly shows the fundamental frequency of 1.2 e+6 Hz and a peak amplitude of 0.004. It also shows subharmonics and high-frequency numerical noise. Experimental fundamental frequency, as given in Ref. [11], is 1.96e+6 Hz. The discrepancies between the experimental and the numerical value could be due to improper grid resolution. The calculations were repeated for a finer grid (131×101). The grid aspect ratio was kept the same in both the cases. Figure 7.9 shows the frequency spectrum for the flow field with finer grid. The sample stations have the same physical locations as in the previous case. The dominant frequency is 2.0e+6 Hz, and the amplitude is 0.004. This frequency is in close agreement with the experimental value of 1.96e+6 Hz. The above calculations were repeated once again for another finer grid of 197×152. The grid aspect ratio was kept the same and the sample stations have the same physical locations as in the previous cases. Figure 7.10 shows the frequency spectrum for this grid. The dominant frequency now is 2.1e+6 Hz., and the amplitude is 0.004. Thus, refining the grid has not changed the frequency and therefore, the oscillations in the reaction front are physical. The frequency prediction is very sensitive to not only the grid but also the

95

CONTOUR PLOT FOR DENSITY
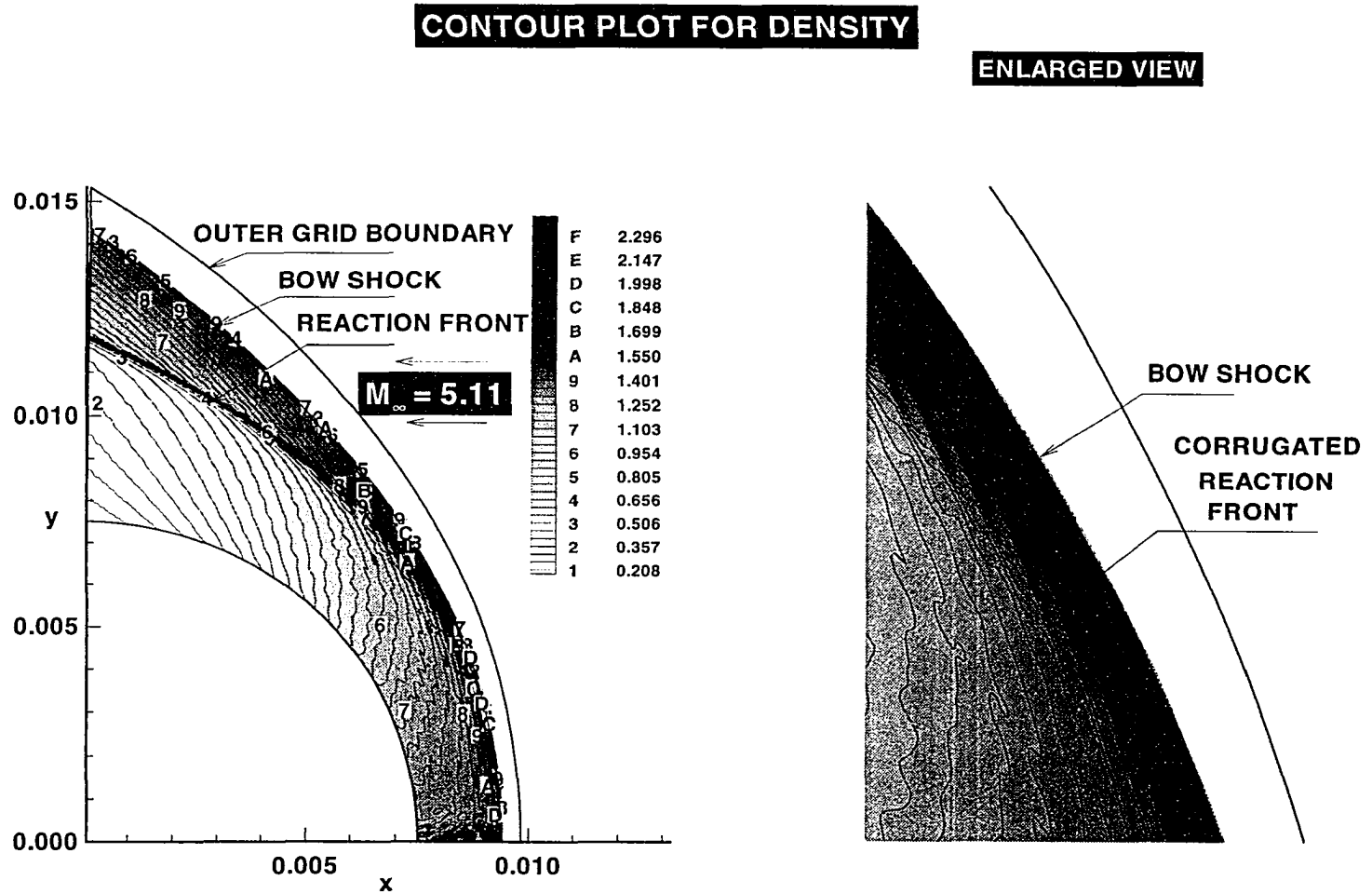
ENLARGED VIEW

Figure 7.3   Contour plot of density for Mach 5.11 with shock-capturing.

COTOUR PLOT FOR TEMPERATURE
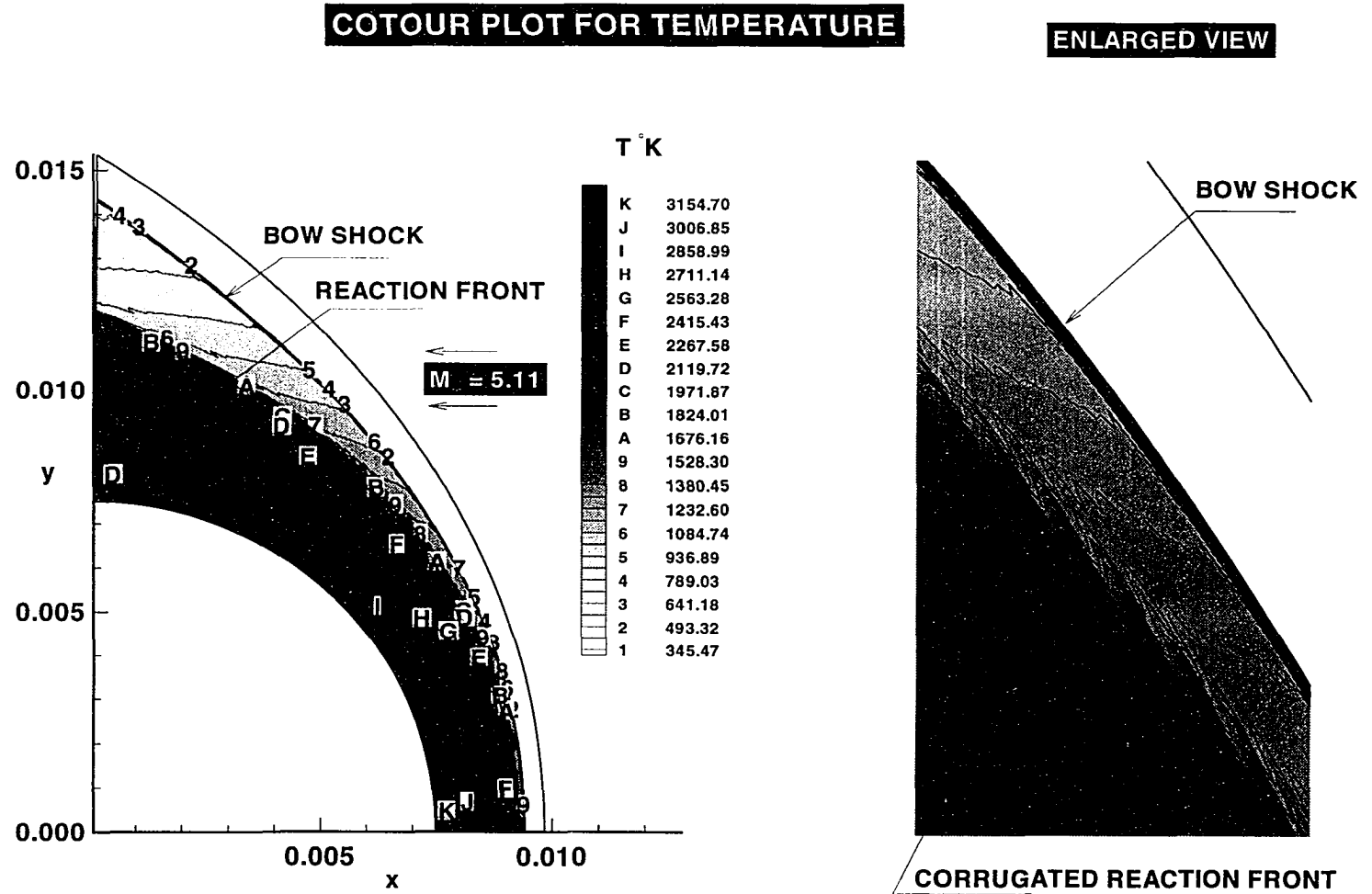
ENLARGED VIEW

Figure 7.4   Contour plot of temperature for Mach 5.11 with shock-capturing.

WATER MASS FRACTION CONTOURS

ENLARGED VIEW

REACTION FRONT

$M_\infty = 5.11$

0.209	
0.194	
0.180	
0.165	
0.151	
0.137	
0.122	
0.108	
0.094	
0.079	
0.065	
0.050	
0.036	
0.022	
0.007	

REACTION FRONT
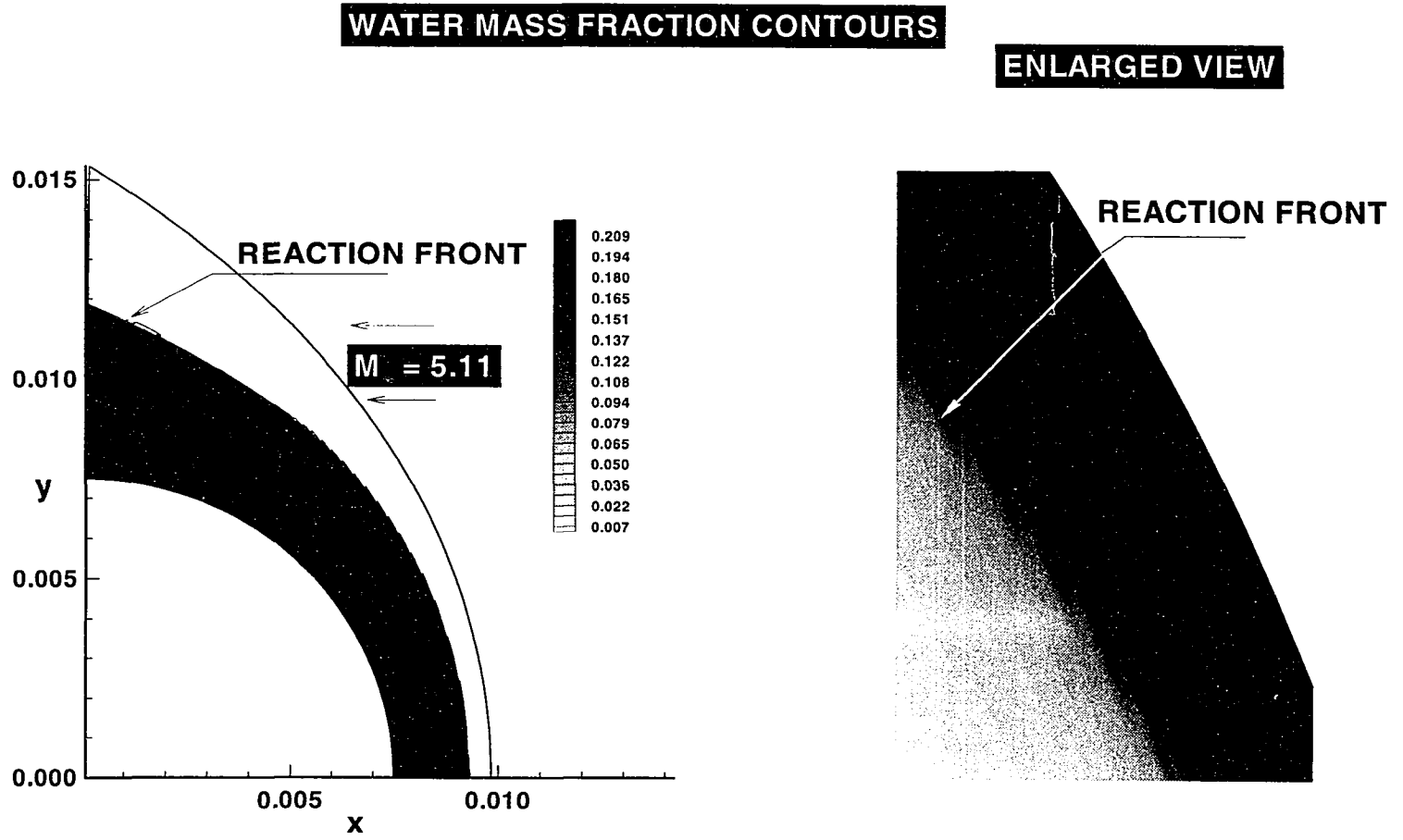
Figure 7.5   Contour plot of water mass fraction for Mach 5.11 and corresponding enlarged view.

LINE PLOTS FOR MACH 5.11
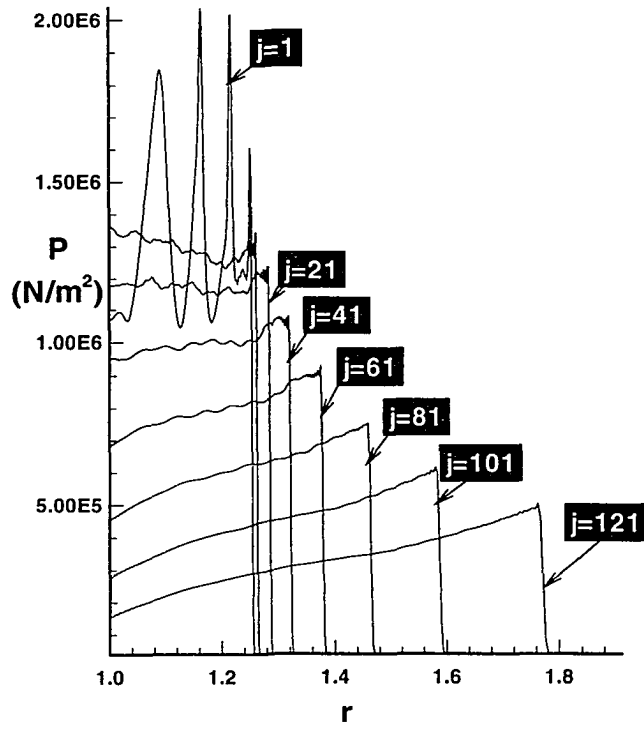
(a) PRESSURE VS RADIUS
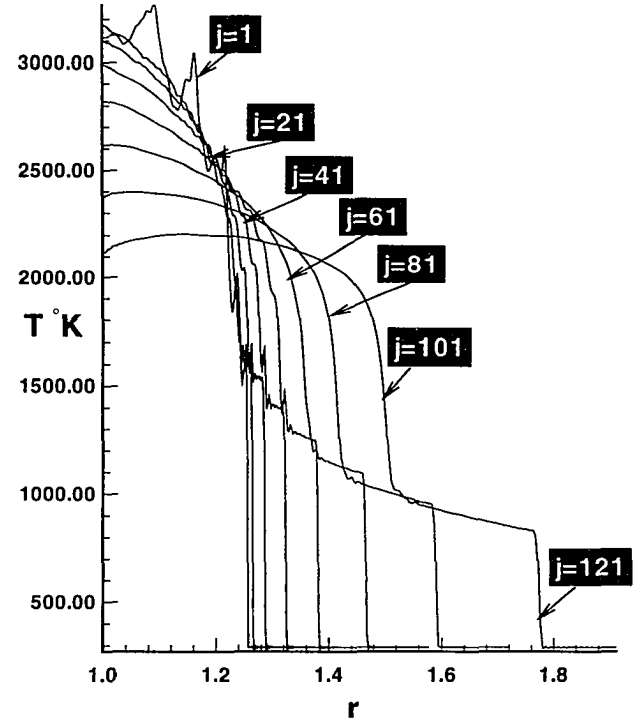
(b) TEMPERATURE VS RADIUS

Figure 7.6 Line plots for Mach 5.11 for (a) Pressure vs radius along various j = constant grid lines and (b) Temperature vs radius along various j = constant grid lines.

100
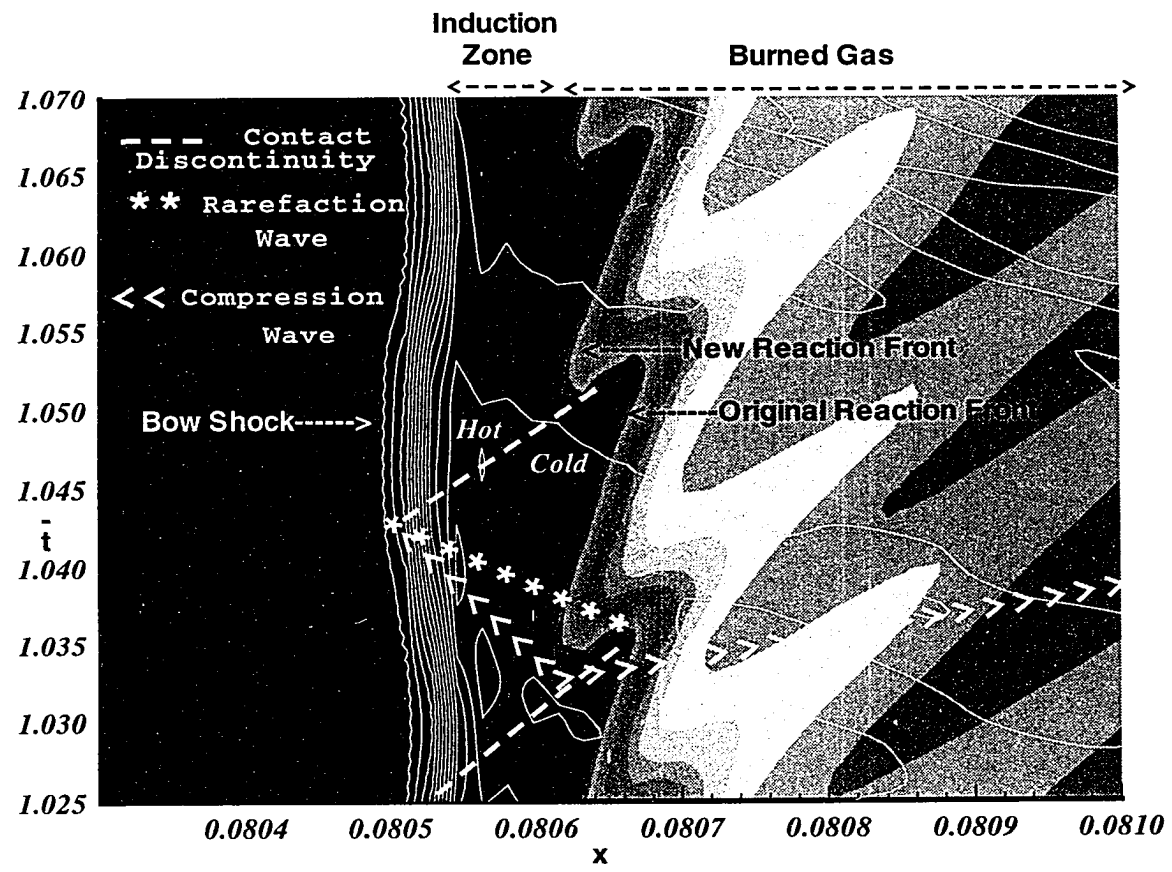
Figure 7.7 x-$\bar{t}$ plot of water mass fraction and pressure along the stagnation line showing proposed instability process.

101
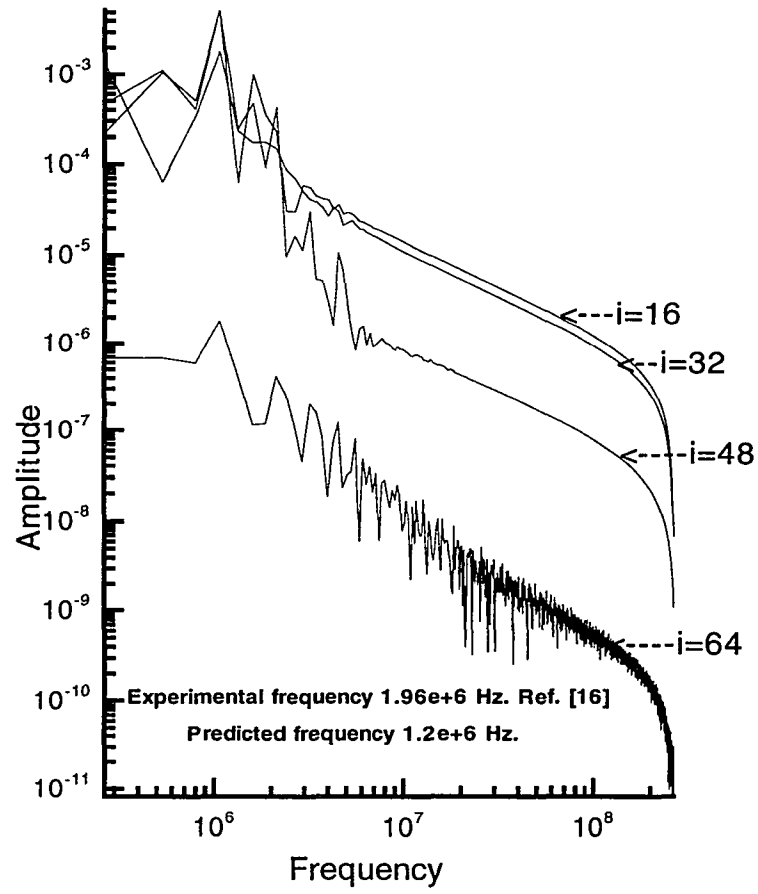
Figure 7.8   Temporal frequency spectrum of water mass fraction for Mach 5.11 for 101×78 grid.
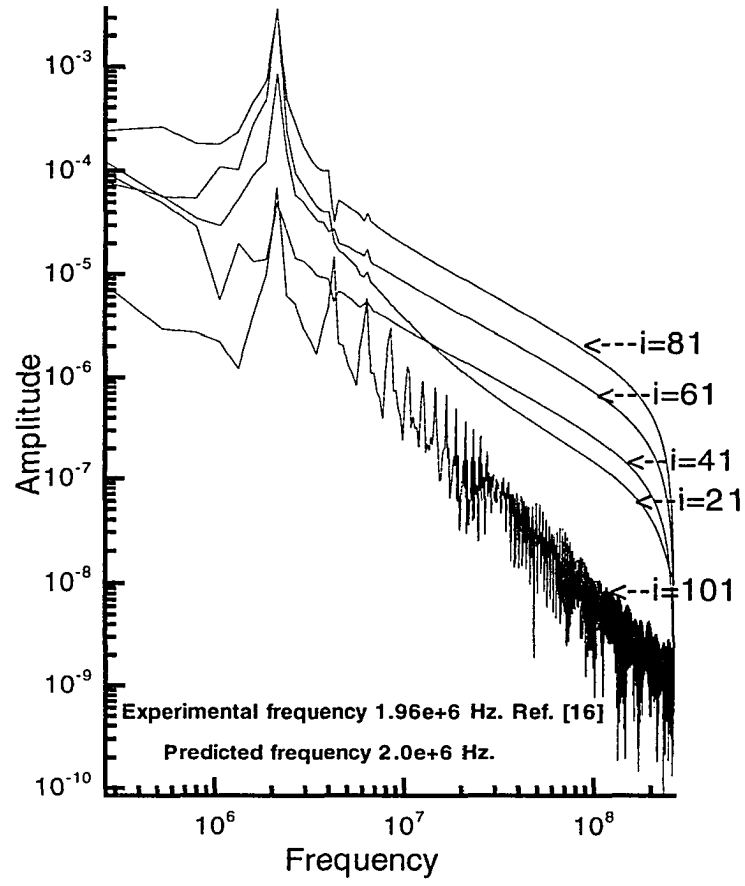
Figure 7.9 **Temporal frequency spectrum of water mass fraction for Mach 5.11 for 131×101 grid.**
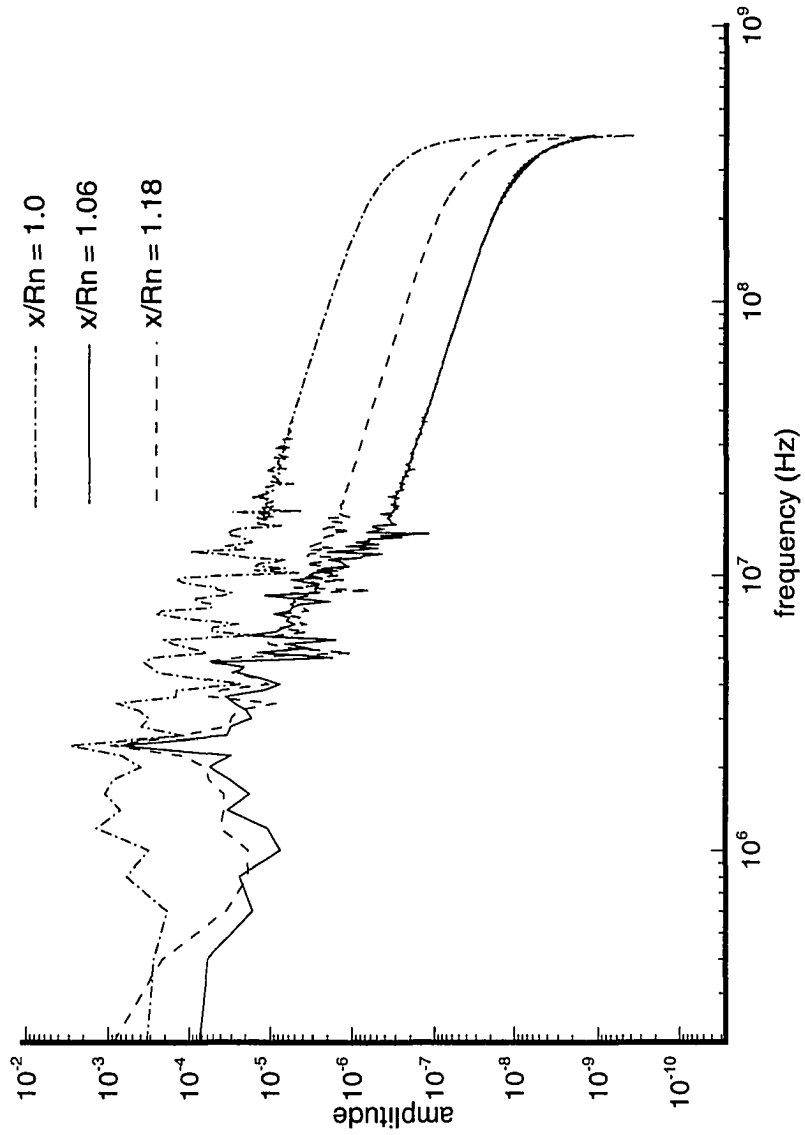
Figure 7.10 Temporal frequency spectrum of water mass fraction for Mach 5.11 for 197×152 grid.

103

chemical kinetics model. The frequency of oscillations depends very strongly on the ignition delay, which in turn depends on the rate constants. Wilson [15] in his investigation showed that, by changing the reaction rate constants for reaction (2) [Table 4.3] from Jachimowski [45] model to those recommended by Warnatz [47], the frequency of oscillations changed from 530 KHz to 820 KHz (55% change). This is because Jachimowski's model gives shorter ignition delay at higher temperature than Warnatz's model. Therefore, slight difference between the experimental and computed frequency can be attributed to the uncertainty in the reaction rate constants, among other factors such as grid resolution and the numerical damping.

7.2 Mach 6.46 Case

The results for the Mach 6.46 case will now be presented. For the present stoichiometric hydrogen-air mixture, the C-J velocity is Mach 5.11. Thus for the Mach 6.46 which is a superdetonative case, the projectile speed is significantly above the detonation velocity of the mixture. The numerical simulations is carried out for the following free-stream conditions:

$$M_\infty = 6.46$$

$$P_\infty = 42732 N/m^2$$

$$T_\infty = 292 K$$

Figure 7.11 shows the contour plot of temperature for the Mach 6.46 case. The bow shock and the reaction front can be clearly seen in the figure. They are coupled with each other near the stagnation line and up to about 60 degrees from the nose at which point they start decoupling from each other by the induction distance. This occurs because bow shock is almost normal near the stagnation line and the post-shock temperature is maximum. For Mach 6.46, a very small induction distance occurs as a result of the post shock temperature remaining significantly high up to some distance near the stagnation

104

zone. Away from the stagnation line, the induction distance is increased as a result of decreasing shock strength and post-shock temperature. A comparison with Fig. 2.3 shows that all the flow features are very well captured. The temperature further increases as the reaction proceeds due to the exothermic nature of the reaction. The peak temperature occurs at the stagnation point. Figure 7.12 shows the contour plot for density at Mach 6.46. The bow shock has a very crisp and smooth profile. The reaction front, which is smooth up to about 60–65 degree from the nose region, is wrinkled with very small amplitude waves downstream. The maximum density is seen to be just after the bow shock, and minimum density is after the reaction front. Figure 7.13 shows the pressure contours, the bow shock, and the expansion waves as the flow expands over the body. Peak pressure occurs near the stagnation region where the shock is nearly normal, and peak pressure decreases away from the stagnation region as the flow expands. Figure 7.14a shows the line plot for pressure along various j = constant grid lines. The flow encounters the pressure jump as it crosses the shock. The pressure decreases slightly after the shock. The post-shock oscillation in pressure along the stagnation line is also observed. Figure 7.14b shows the temperature along various j = constant grid lines. The post-shock stagnation point temperature is 3550°K. The temperature increases abruptly, as the gas encounters the bow shock. Immediately after the shock, the temperature stays constant for a short distance and then begins to increase due to exothermic reactions. The induction zone decreases with increasing temperature, as chemical energy release will be faster for higher temperatures. The contour plots for water mass fraction is shown in Fig. 7.15a. The temperature is high enough to start the combustion, at the end of the induction zone. The water mass fraction increases rapidly as the reaction proceeds. An enlarged view of the oscillations is presented in Fig. 7.15b and it shows the macroscopic behavior. The reaction front shows a smooth profile near the stagnation region, but

a corrugated pattern with extremely small amplitudes is observed 60–70 degrees away from the nose region.

A Fourier analysis of the flow field was conducted to further investigate the macroscopic steady nature of the flow field. Data at various sample stations along the stagnation line were stored for 40,000 iterations to get good temporal resolutions. The grid used was 197×152, and all calculations were time accurate. Figure 7.16 shows the amplitude versus frequency plot obtained by using Fourier transform. The flow-field spectrum is well resolved, and it clearly shows the fundamental frequency of 2.67e+6 Hz and a peak amplitude of 0.001. Harmonics and very high-frequency numerical noise are also shown. Experimental fundamental frequency for Mach 6.46 is not available.

7.3 Effect of Nose Radius on Stability of Reaction Front

The key parameters for the onset of periodic unsteadiness have been identified as (1) induction time, (2) reaction rate constant, (3) activation energy, (4) heat release rate and (5) projectile nose radius. In this study we shall be discussing the effect of nose radius on the stability of the reaction front while keeping the first four parameters constant by choosing a particular reaction model and by fixing the free-stream Mach number.

7.3.1 Mach 5.11 and Projectile Diameter of 2.5 mm

The diameter of the projectile was reduced to 2.5 mm while keeping the same free-stream Mach number of 5.11. Other free-stream conditions were also kept the same. Figure 7.17 shows the density contours and corresponding enlarged view. It clearly shows a very smooth bow shock and reaction front. Thus, reducing the projectile diameter caused the instabilities to disappear. Figure 7.18a shows the x-t plot of water mass fraction along stagnation line for the Mach 5.11 for a 15 mm projectile diameter. Figure 7.18b shows the x-t plot of water mass fraction along stagnation line for Mach 5.11, but with a projectile diameter of 2.5 mm. In the former case the reaction front

clearly shows periodic oscillations, whereas the later case shows a smooth reaction front. The instabilities for Mach numbers lower than the C-J Mach number are due to the ignition delay. What causes these instabilities to disappear for the same Mach number of 5.11 but lower projectile diameter can be explained now. Because the projectile speed is same in both the cases so the physical induction length are also the same. The difference is relative scale of the induction length and the shock stand-off distance. In the later case of small projectile diameter the physical length scale is small, reaction period is relatively large and temperature increase rather gradually within that small physical scale. Therefore, compression waves are created gradually rather abruptly. Thus the unsteadiness disappears for the small diameter projectile.

CONTOUR PLOT FOR TEMPERATURE

ENLARGED VIEW

K	3466.30
J	3300.41
I	3134.52
H	2968.63
G	2802.74
F	2636.85
E	2470.95
D	2305.06
C	2139.17
B	1973.28
A	1807.39
9	1641.49
8	1475.60
7	1309.71
6	1143.82
5	977.93
4	812.04
3	646.14
2	480.25
1	314.36

OUTER GRID BOUNDARY

BOW SHOCK

REACTION FRONT

$M_\infty = 6.46$

REACTION FRONT

BOW SHOCK
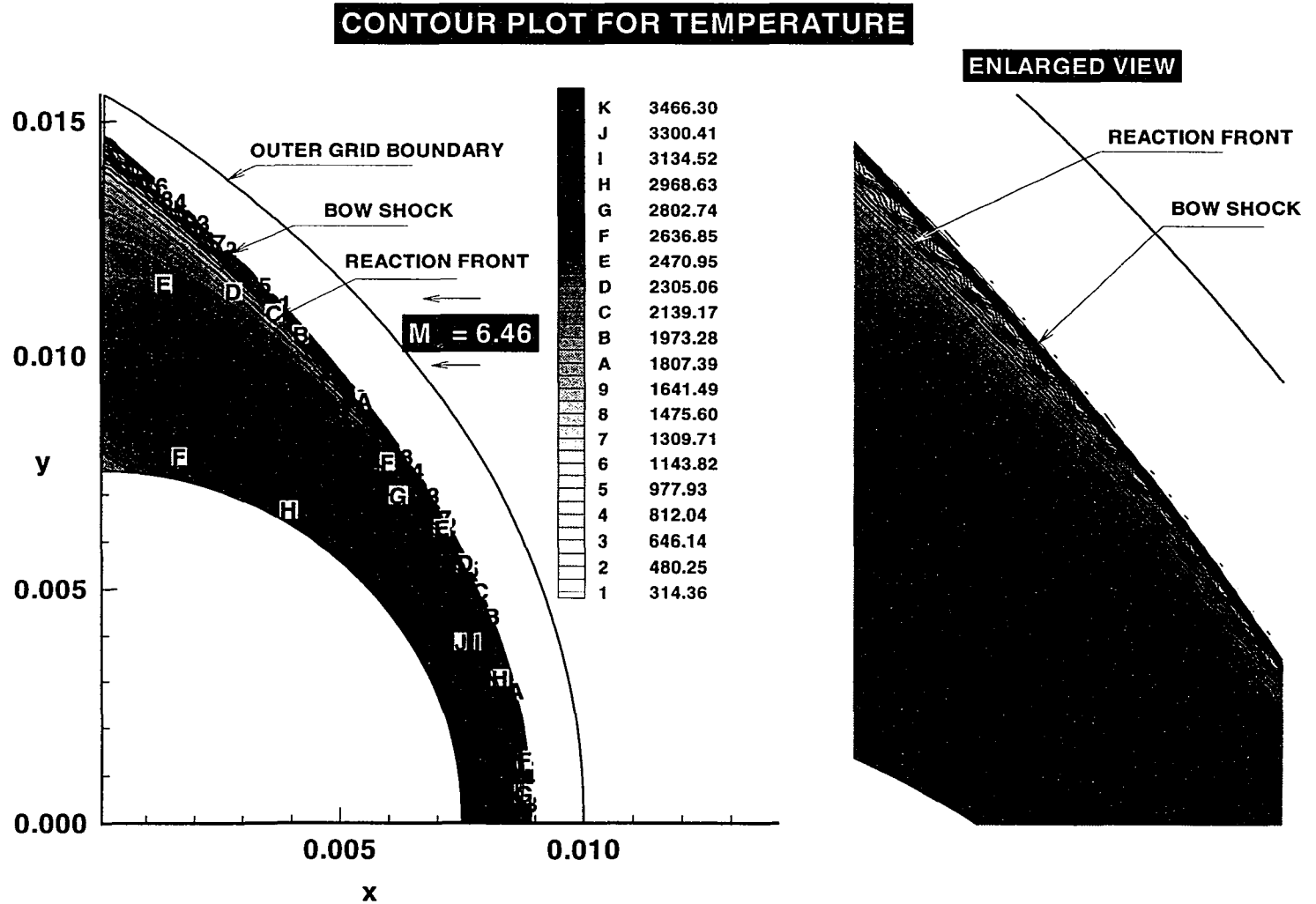
Figure 7.11 Contour plot of temperature for Mach 6.46 with corresponding enlarged view.

109

CONTOUR PLOT FOR DENSITY

ENLARGED VIEW

D	2.814
C	2.608
B	2.402
A	2.197
9	1.991
8	1.785
7	1.580
6	1.374
5	1.168
4	0.962
3	0.757
2	0.551
1	0.345

OUTER GRID BOUNDARY

REACTION FRONT

BOW SHOCK

BOW SHOCK

REACTION FRONT
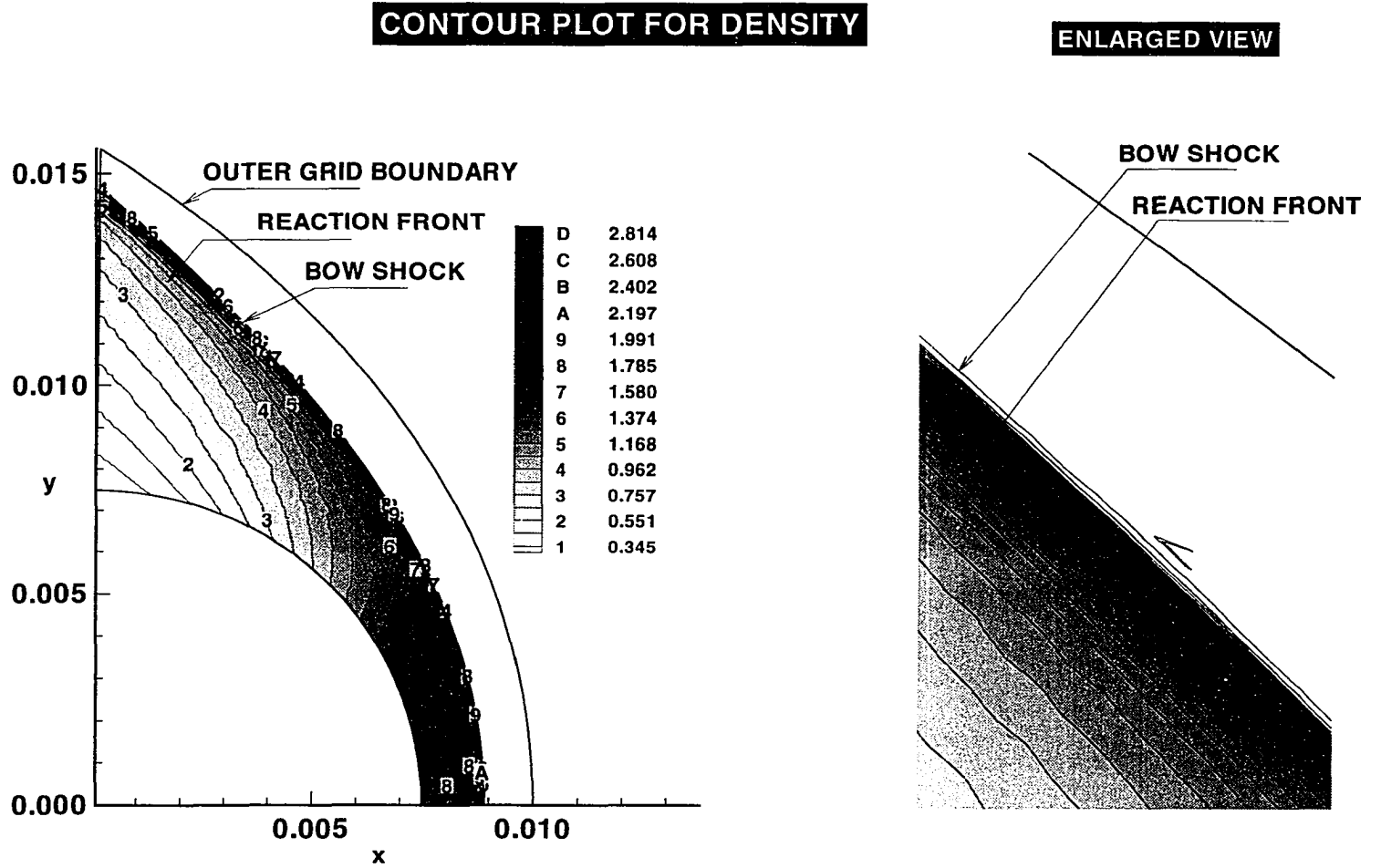
Figure 7.12   Contour plot of density for Mach 6.46 with corresponding enlarged view.

PRESSURE CONTOURS FOR MACH 6.46

N/m²

2.97E6
2.74E6
2.50E6
2.27E6
2.03E6
1.80E6
1.56E6
1.33E6
1.09E6
8.57E5
6.22E5
3.87E5
1.52E5

BOW SHOCK

M = 6.46
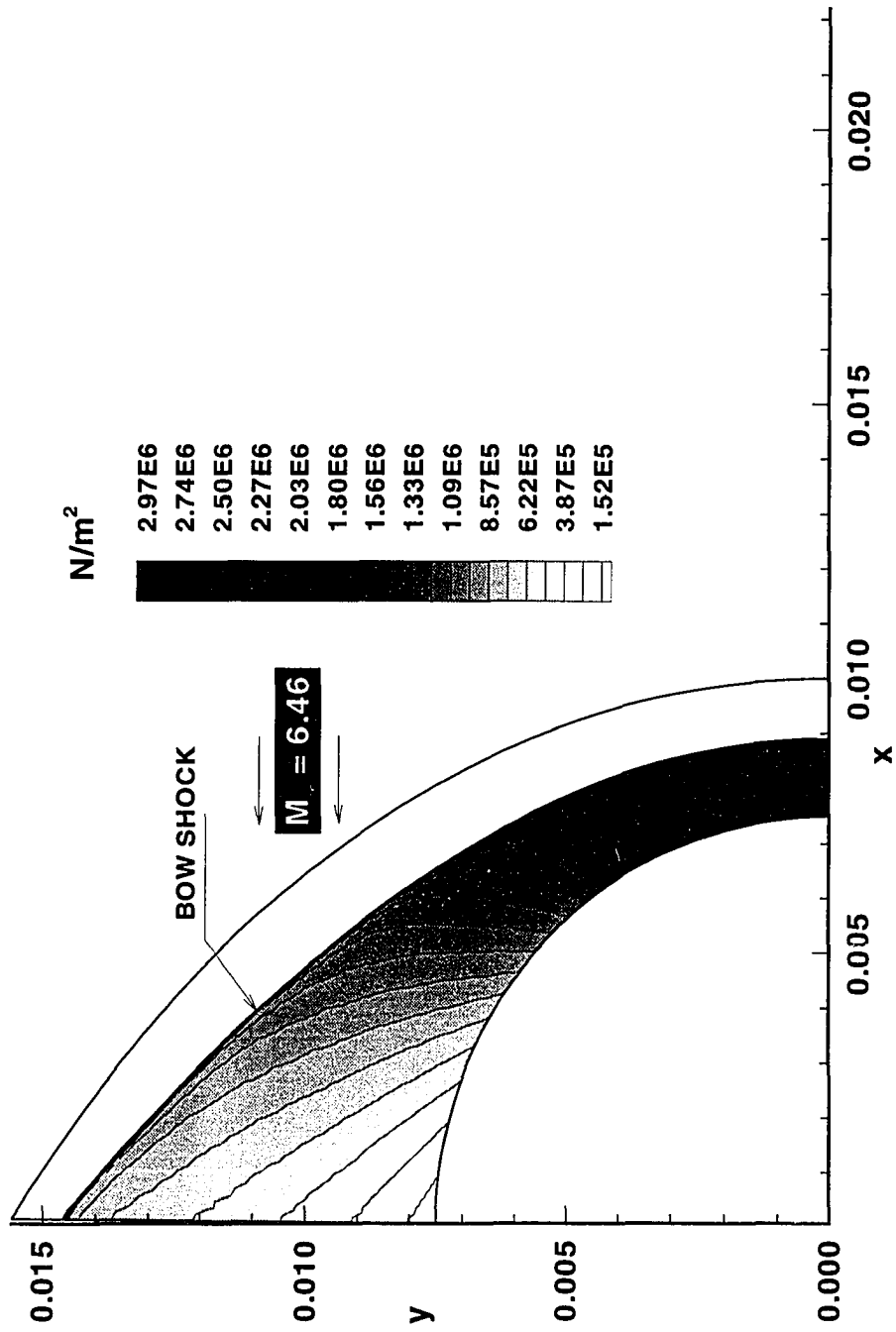
Figure 7.13   Contour plot of pressure for Mach 6.46.

111

LINE PLOTS FOR MACH 6.46
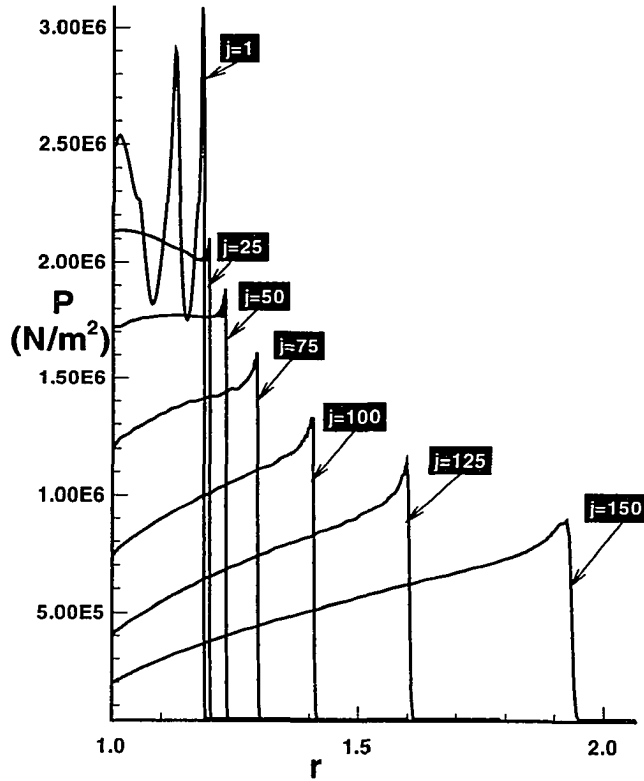
(a) PRESSURE VS RADIUS
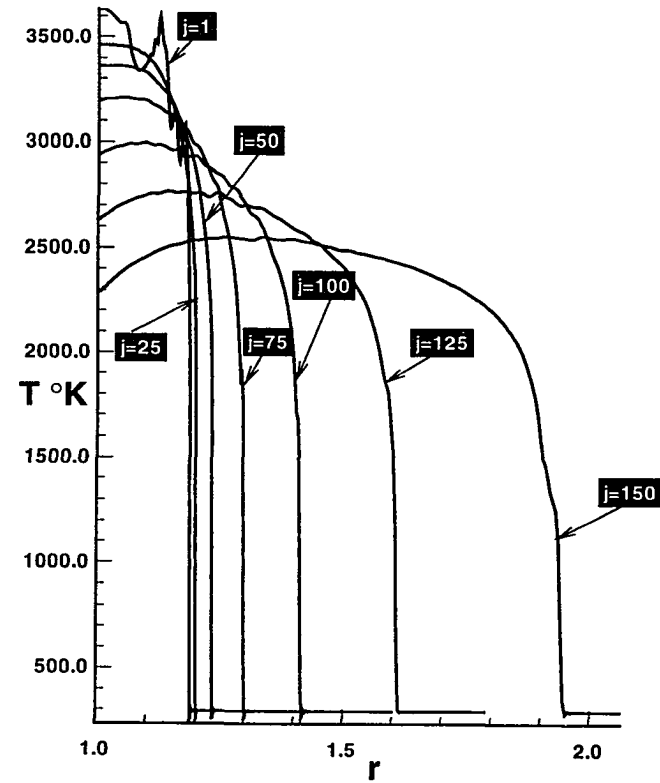
(b) TEMPERATURE VS RADIUS

Figure 7.14   Line plots for Mach 6.46 for (a) Pressure vs radius along various j = constant grid lines
and (b) Temperature vs radius along various j = constant grid lines.

WATER MASS FRACTION CONTOURS

ENLARGED VIEW

REACTION FRONT

$M_\infty = 6.46$

D	0.196
C	0.180
B	0.164
A	0.149
9	0.133
8	0.117
7	0.102
6	0.086
5	0.070
4	0.055
3	0.039
2	0.023
1	0.008

REACTION FRONT
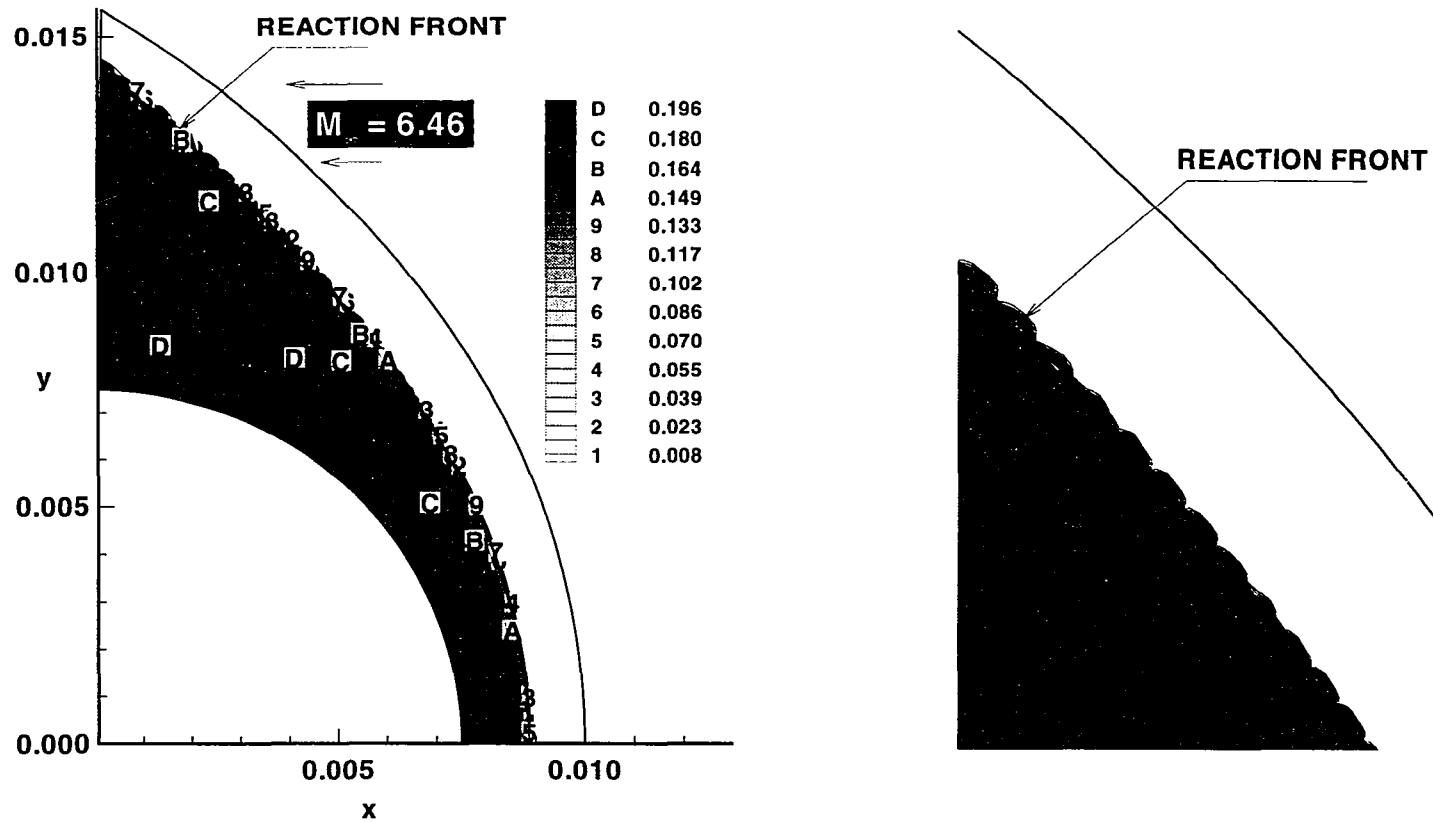
Figure 7.15 Contour plots of water mass fraction for Mach 6.46 and corresponding enlarged view.
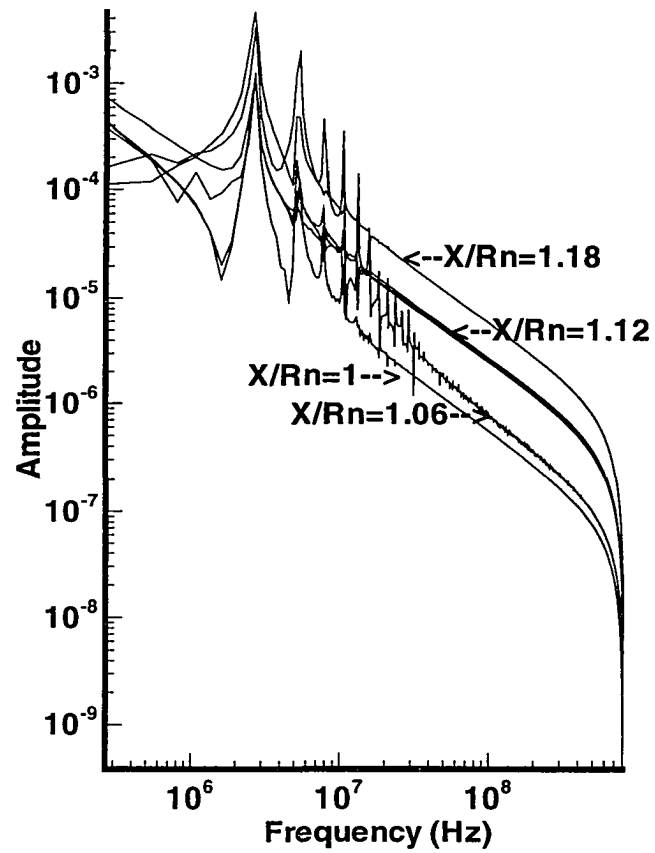
Figure 7.16   **Temporal frequency spectrum of water mass fraction for Mach 6.46 for 197×152 grid.**

CONTOUR PLOTS OF DENSITY FOR MACH 5.11 and PROJECTILE DIAMETER 2.5 mm

H	2.387
G	2.250
F	2.114
E	1.977
D	1.841
C	1.704
B	1.568
A	1.431
9	1.294
8	1.158
7	1.021
6	0.885
5	0.748
4	0.612
3	0.475
2	0.339
1	0.202

ENLARGED VIEW

BOW SHOCK

STEADY REACTION FRONT

STEADY REACTION FRONT

Figure 7.17   Contour plots of density for Mach 5.11 and projectile diameter 2.5 mm and corresponding enlarged view.
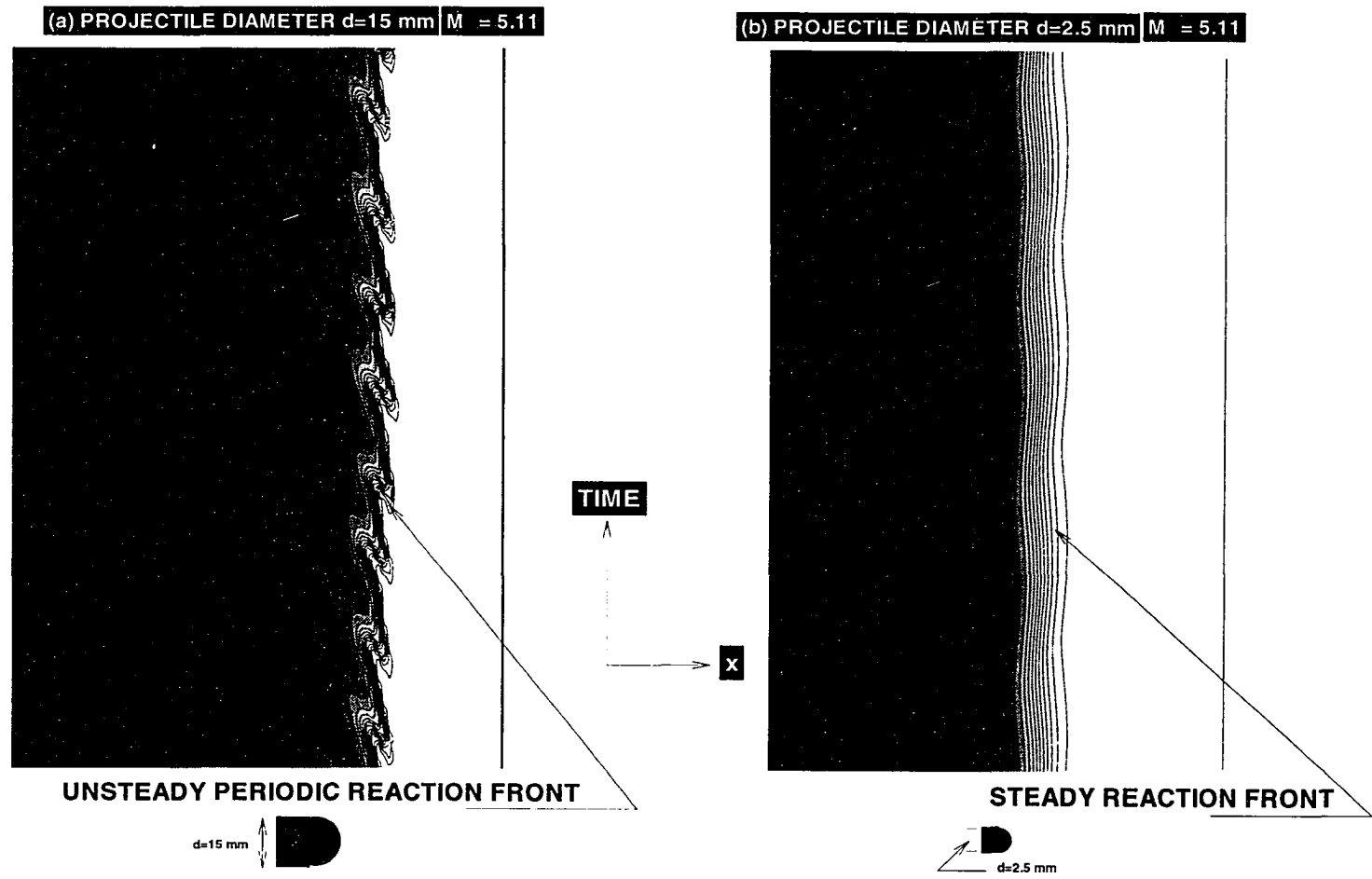
Figure 7.18   Time history plots of water mass fraction for (a) Projectile diameter 15 mm (Mach number 5.11) and (b) Projectile diameter 2.5 mm (Mach number 5.11).

Chapter 8

RESULTS AND DISCUSSION USING SHOCK-FITTING METHOD

In this chapter we shall be discussing the numerical simulations of Lehr's Mach 5.11 and Mach 6.46 cases using shock-fitting technique. A comparison of shock capturing method and shock-fitting method will clearly show the advantages of shock-fitting over shock capturing. Later we shall simulate Ruegg and Dorsey's experimental work using the same technique with emphasis to the large-disturbance regime.

The numerical simulations were conducted to simulate Lehr's [11, 38] experimental results. The physical and free-stream conditions used in the simulation were:

$$M_\infty = 5.11 \text{ and } 6.46$$

$$P_\infty = 42732 N/m^2$$

$$T_\infty = 292K$$

8.1 Mach 5.11 Case

For Mach 5.11 case, calculations were carried out on a grid of 101×101. Figure 8.1 shows the pressure contour plots for the Mach 5.11 case and Fig. 8.2 shows the corresponding enlarged view. The complicated wave pattern seen in Fig. 8.2 can be viewed as made up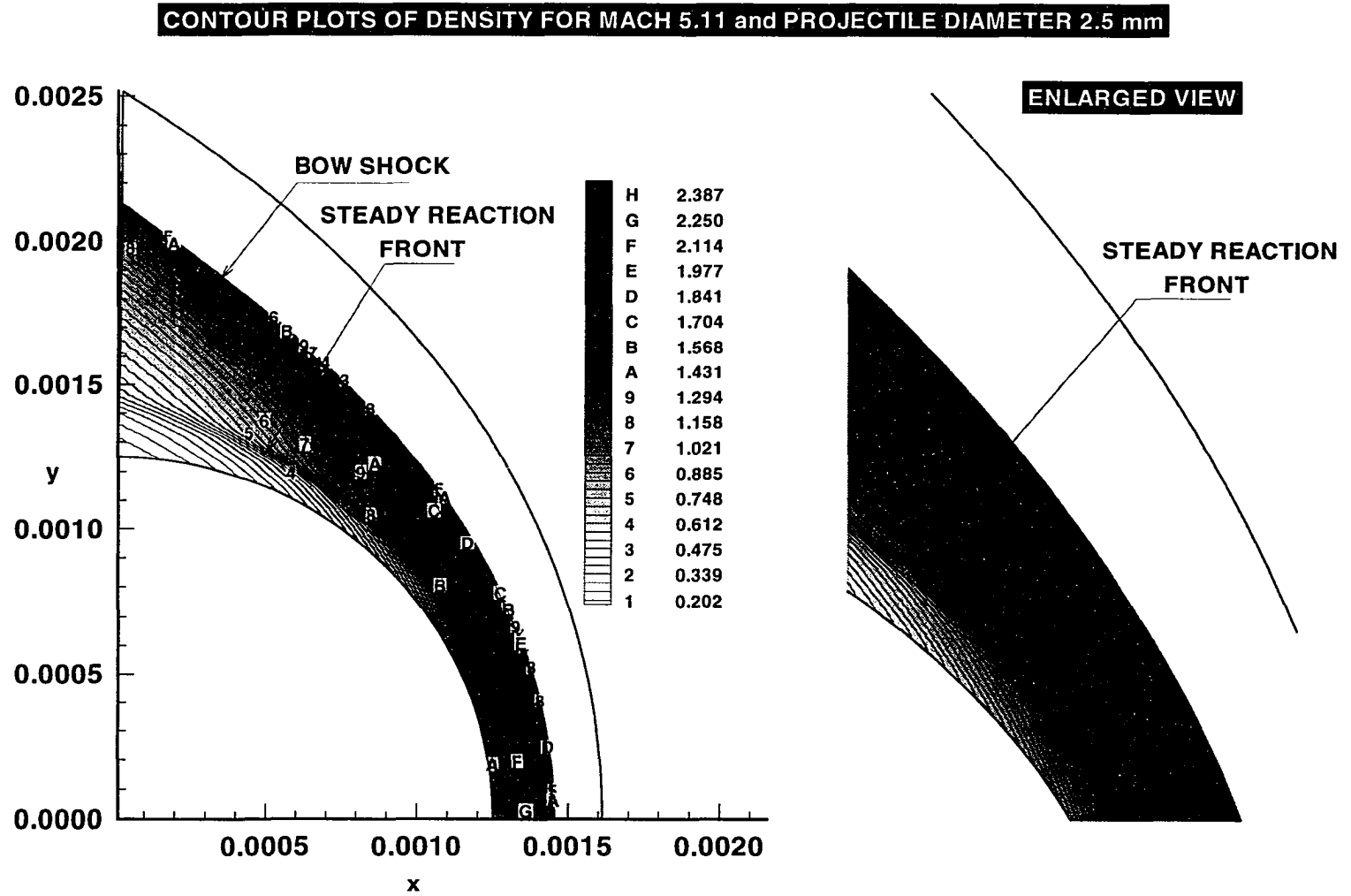 of two types of compression waves. One type of compression wave originates from the reaction front while the other has been reflected from the projectile body. The reflected compression wave interacts with the original compression wave and, at the point of interaction, two new waves are generated. This reflection produces the observed cell structure. The compression wave which moves towards the bow shock, overtakes it and causes the bow shock to move forward. Thus the kinks appearing

116

on the bow shock are due to some of its structure being distorted by the compression waves. Figure 8.2 also reveals that these pulsations in reaction front are strong near the nose region and dissipate near the shoulder regions of the projectile. This fact is further supported by Fig. 8.3, which shows the numerical value of pressure contours along the complete body. From the pressure values given, it is shown that the pulsation of compression waves that originate near the stagnation line are the strongest, and as one moves towards the shoulder region of the projectile, the pressure is reduced to almost atmospheric pressure.

Figure 8.4 shows the pressure distribution along the stagnation line. The pressure increases from free-stream pressure to 1.332 e+06 N/m^2 as the flow passes the normal shock along the stagnation line. The flow then encounters the pressure wave (see Fig. 8.2) which further raises the pressure to 1.375 e+06 N/m^2. The pressure then drops to 1.342 e+06 N/m^2 as it passes through the expansion wave. This pattern repeats itself as the flow encounters a series of compression and expansion waves.

To help understand the temporal nature of these instabilities, attention is now focused on the time history of physical variables along the stagnation line. Figure 8.5 shows the time history plot of water mass-fraction along the stagnation streamline. It shows two discontinuities. The outer discontinuity is the bow shock, which shows little kinks in the structure, and the inner discontinuity is the reaction front. The highly periodic oscillations in the reaction front that originate near the stagnation line and then spread downstream are clearly evident. The bow shock is at 0.009224 meter and the projectile surface is at 0.0075 meter (projectile surface is not shown in the figure) from the center of the blunt body. As seen from the figure, the frequency of oscillation (which is inverse of the time period) can be calculated directly from the plot. This frequency is 2.0 MHz, whereas the experimental frequency from Lehr's ballistic data for Mach 5.11 is 1.98

117

MHz. Also, the amplitude of the oscillations of reaction front is 8.0 e-05 meters. Figure 8.6 shows the water mass fraction contours. The reaction front can be seen in this figure. The instability is characterized by a regular periodic wave motion having a constant frequency and amplitude. The reaction is complete near the body where the maximum water mass production can be seen.

Density contours are shown in Fig. 8.7. It clearly shows the presence of two discontinuities. The outer discontinuity is the bow shock and the inner discontinuity is the reaction front. These two fronts can be seen separated from each other. Moving downstream the induction length increases because of lowering of post-shock temperature. The oscillations in the reaction front can be seen clearly. It is also seen that the density increases just after the shock and then decreases as the flow passes through the reaction front, in agreement with the experimental shadowgraph.

Figure 8.8 shows the temperature distribution along the stagnation streamline. Following a streamline into the stagnation zone, it is seen that the temperature jumps across the shock and then stays constant in the induction zone. Past the induction zone, due to the exothermic nature of the H_2-air reaction mechanism, the temperature increases rapidly reaching almost 11 times (3150 K) the free-stream value. To further compare the experimental data with the numerical data, Fig. 8.9a shows the computed shadowgraph of the Mach 5.11 case for the complete projectile and Fig. 8.9b is the corresponding enlarged view. It is seen that the bow shock and the reaction front are separated from each other near the stagnation line, and this separation keeps increasing downstream of the stagnation line. This is what was observed experimentally also. Also, the bow shock is quite smooth with very little waviness but the reaction front clearly shows a periodic behavior.

By means of time history plots, a comparison of the numerical results with the wave-interaction model originally proposed by McVey and Toong [8] and further modified by

118

Matsuo and Fujiwara [18], can be made. In order to understand how the wave interaction model fits with the numerical results, we shall have to consider Figs. (8.10-8.12) together.

Figure 8.10 shows the time history plot for the pressure along the stagnation streamline. Figure 8.11 shows the time history plot for temperature along the stagnation streamline. By comparing the actual model shown in Fig. 8.12b with the x-t diagrams of pressure and density shown in Figs. 8.12a and 8.12b, it is demonstrated below that the model proposed by McVey and Toong fits very well with the present numerical calculations.

As shown in Fig. 8.12b, a contact discontinuity first approaches the original reaction front. The gases are hot on the upstream side of the contact discontinuity and comparatively cold on the lower side, as clearly seen in Fig. 8.11. These hot gases behind the contact discontinuity begin to react, generating compression or pressure waves that propagate both upstream and downstream, as seen in Fig. 8.10. The compression wave which propagates upstream intersects with the bow shock and produces a contact discontinuity behind the bow shock (Figs. 8.12c and 8.11). The bow shock is stronger after the interaction and, therefore, the gas is hotter on the upstream side of the contact discontinuity. The hot gases behind the contact discontinuity reduce the induction time and create a new reaction front, thus generating another set of compression waves. At a somewhat later time, the contact discontinuity reaches the position of the original reaction front, extinguishing the reaction at this point because no more unreacted mixture exists there. The rate of energy release is effectively reduced, which generates rarefaction waves as shown in Fig. 8.10. The reaction front begins to recede because of increasing induction time of the colder fluid. The compression wave traveling towards the blunt body gets reflected from the body, travels back to the bow shock, and interacts with it at about the same time that the most recently created compression wave arrives at the bow

119

PRESSURE CONTOURS

BOW SHOCK

$M_\infty = 5.11$

PROJECTILE SURFACE

COMPRESSION WAVES
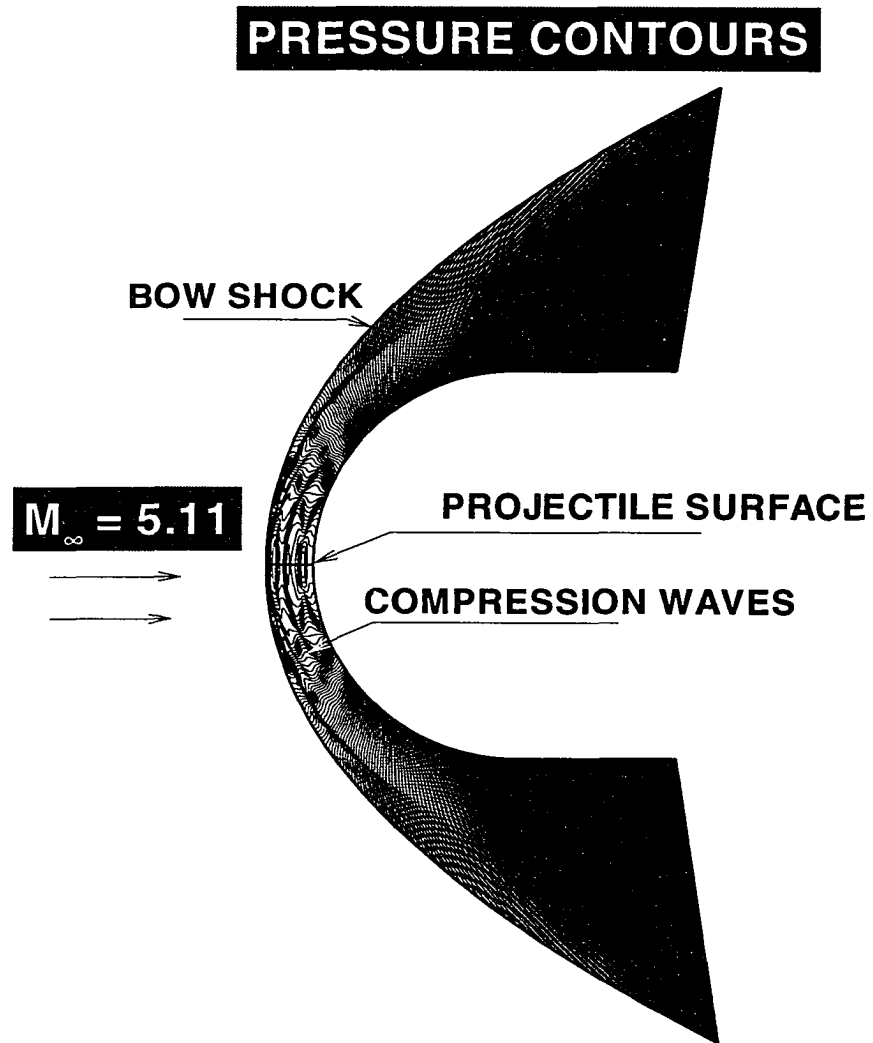
Figure 8.1   Pressure contours for Mach 5.11 over the complete blunt projectile.
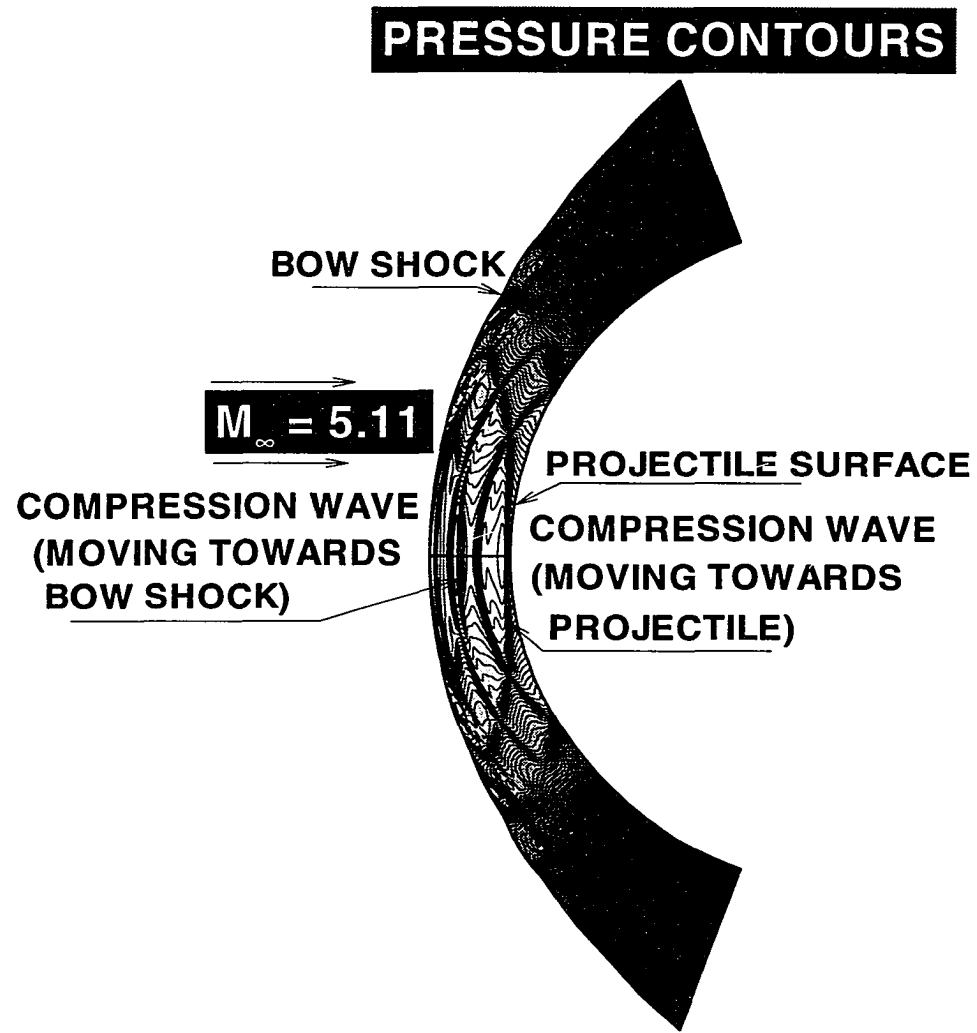
Figure 8.2   Enlarged view of pressure contours for Mach 5.11.

122

K	1.378E6
J	1.312E6
I	1.247E6
H	1.181E6
G	1.115E6
F	1.049E6
E	9.835E5
D	9.177E5
C	8.520E5
B	7.862E5
A	7.204E5
9	6.547E5
8	5.889E5
7	5.231E5
6	4.574E5
5	3.916E5
4	3.259E5
3	2.601E5
2	1.943E5
1	1.286E5
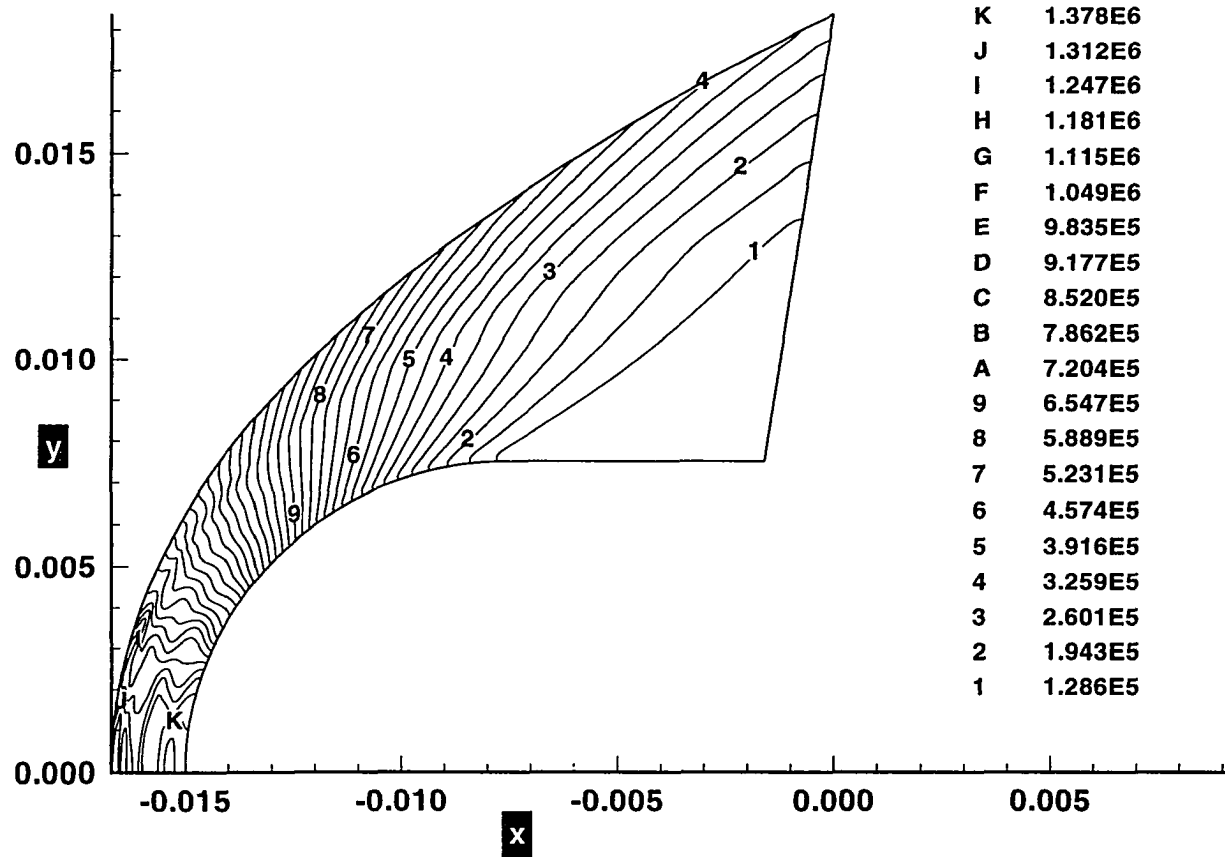
Figure 8.3 Pressure contours for Mach 5.11 showing numerical pressure distribution.

123
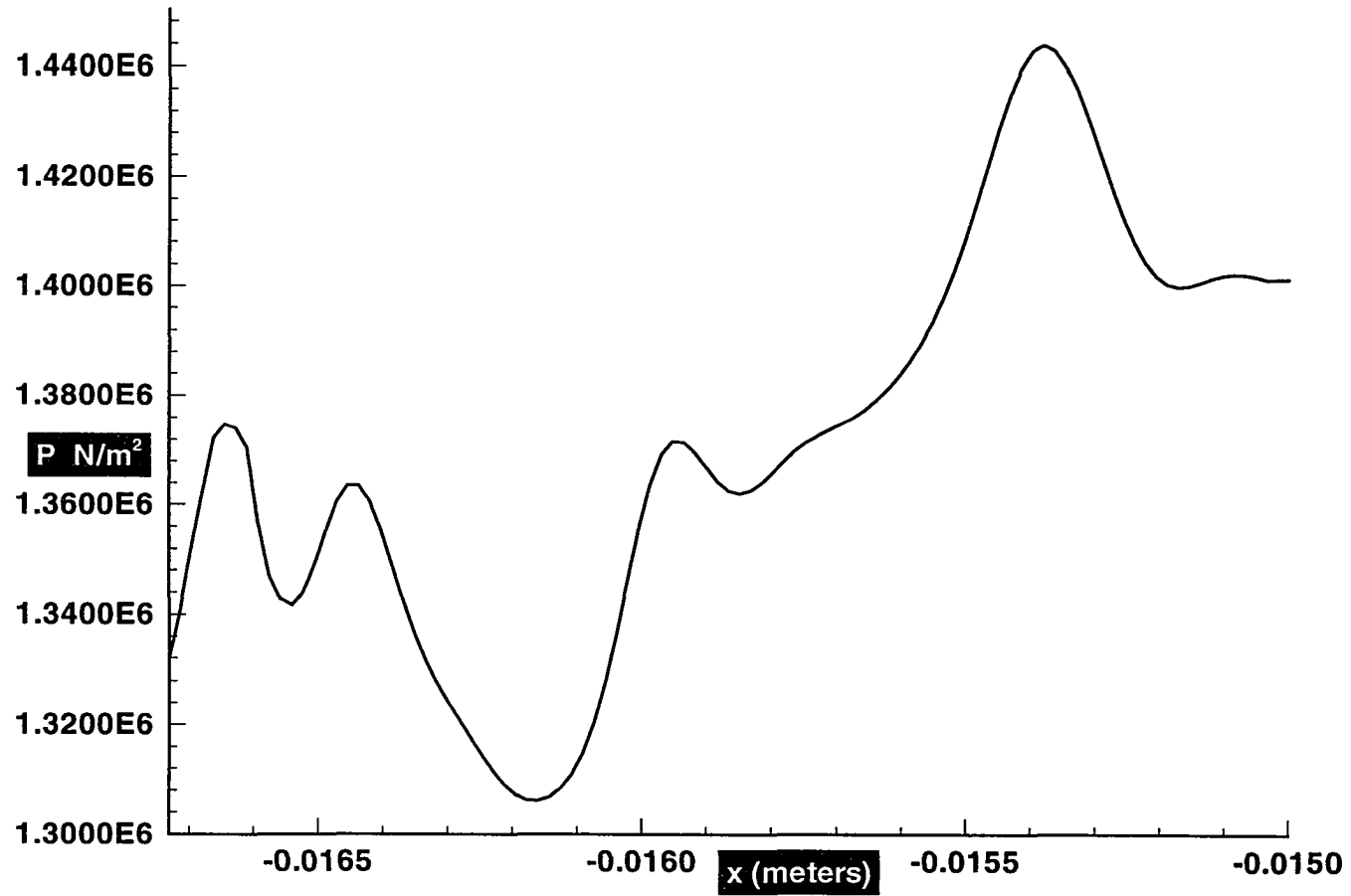
Figure 8.4   Pressure distribution along stagnation streamline for Mach 5.11.
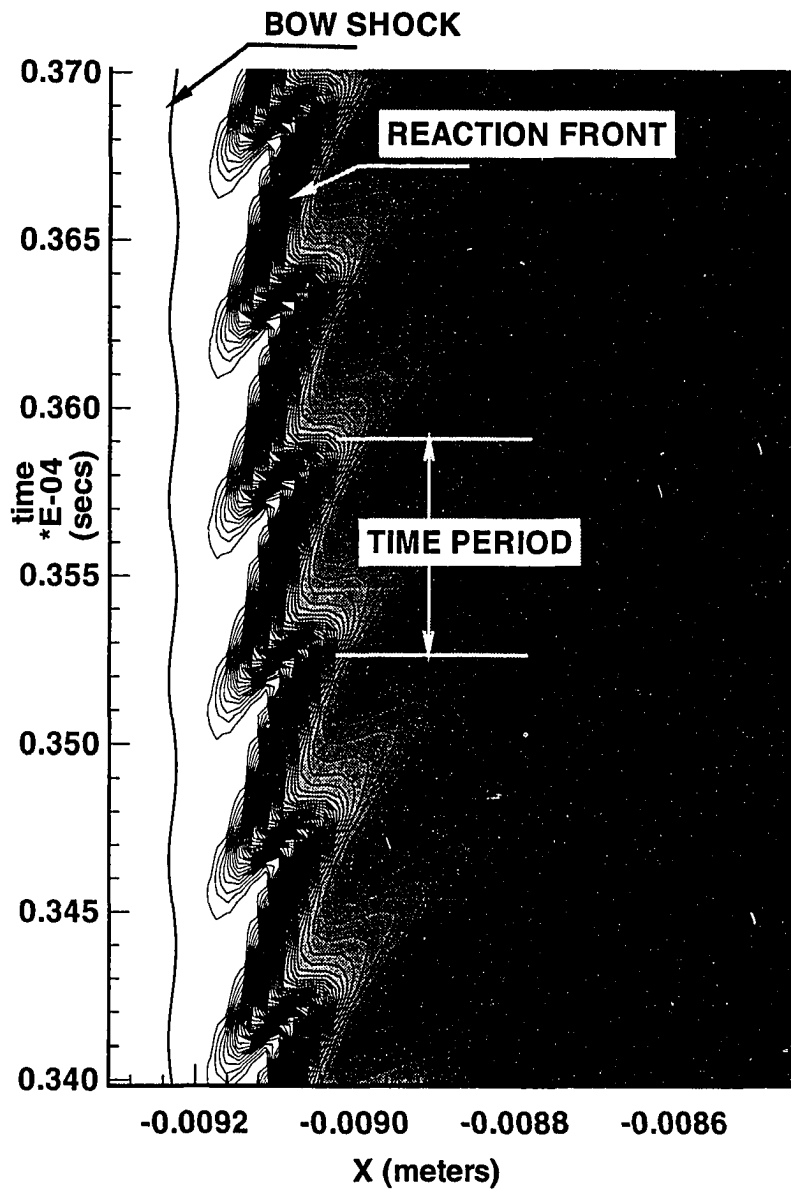
Figure 8.5 Time history plot of water mass fraction along stagnation streamline for Mach 5.11.

124

REACTION FRONT

BOW SHOCK

PROJECTILE SURFACE

	0.208
	0.197
	0.186
	0.176
	0.165
	0.154
	0.144
	0.133
	0.122
	0.112
	0.101
	0.091
	0.080
	0.069
	0.059
	0.048
	0.037
	0.027
	0.016
	0.005
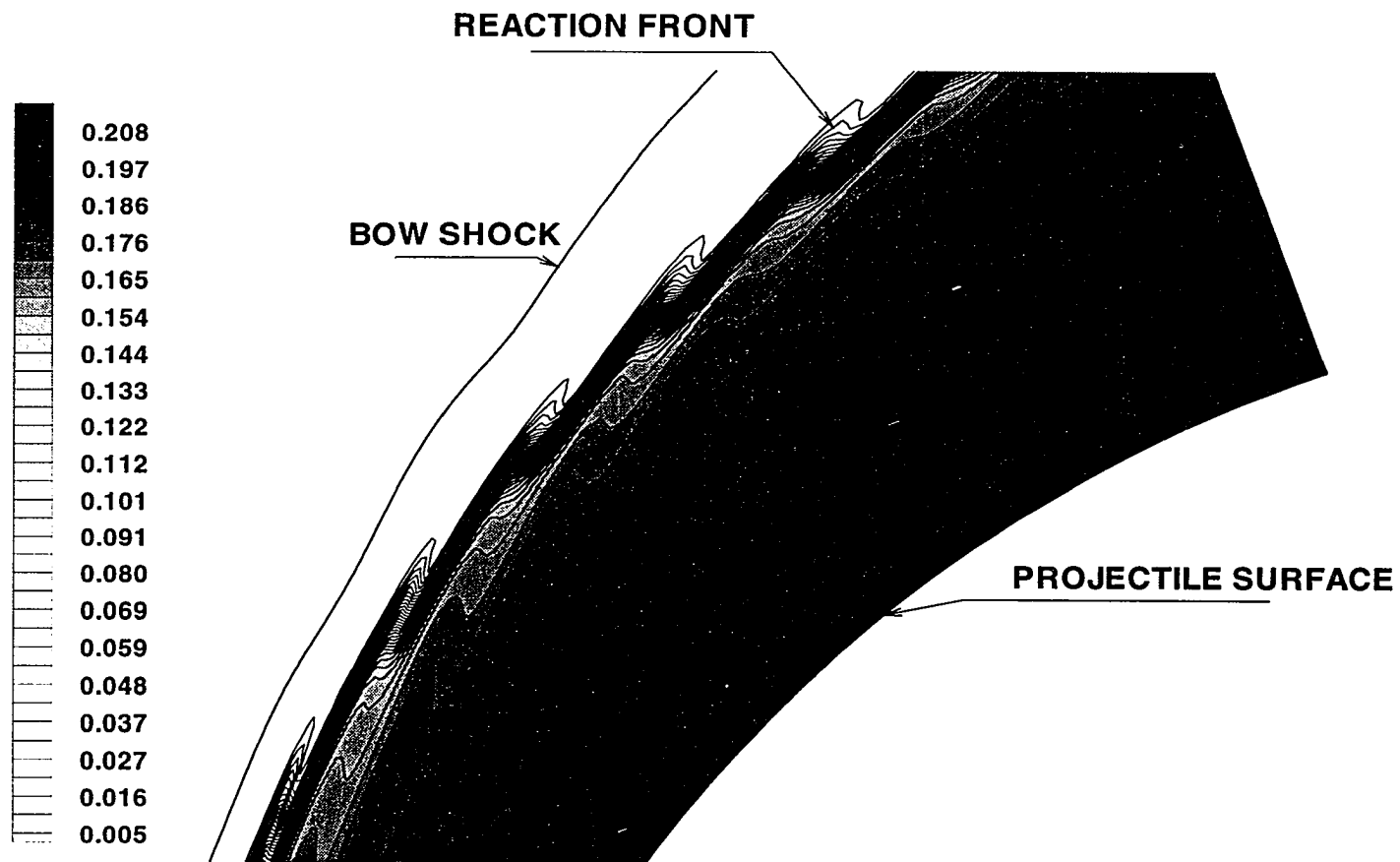
Figure 8.6   Enlarged view of water mass fraction contours for Mach 5.11.

DENSITY CONTOURS

BOW SHOCK

REACTION FRONT

K	2.1796
J	2.0804
I	1.9812
H	1.8821
G	1.7829
F	1.6837
E	1.5846
D	1.4854
C	1.3862
B	1.2871
A	1.1879
9	1.0887
8	0.9896
7	0.8904
6	0.7912
5	0.6921
4	0.5929
3	0.4937
2	0.3946
1	0.2954
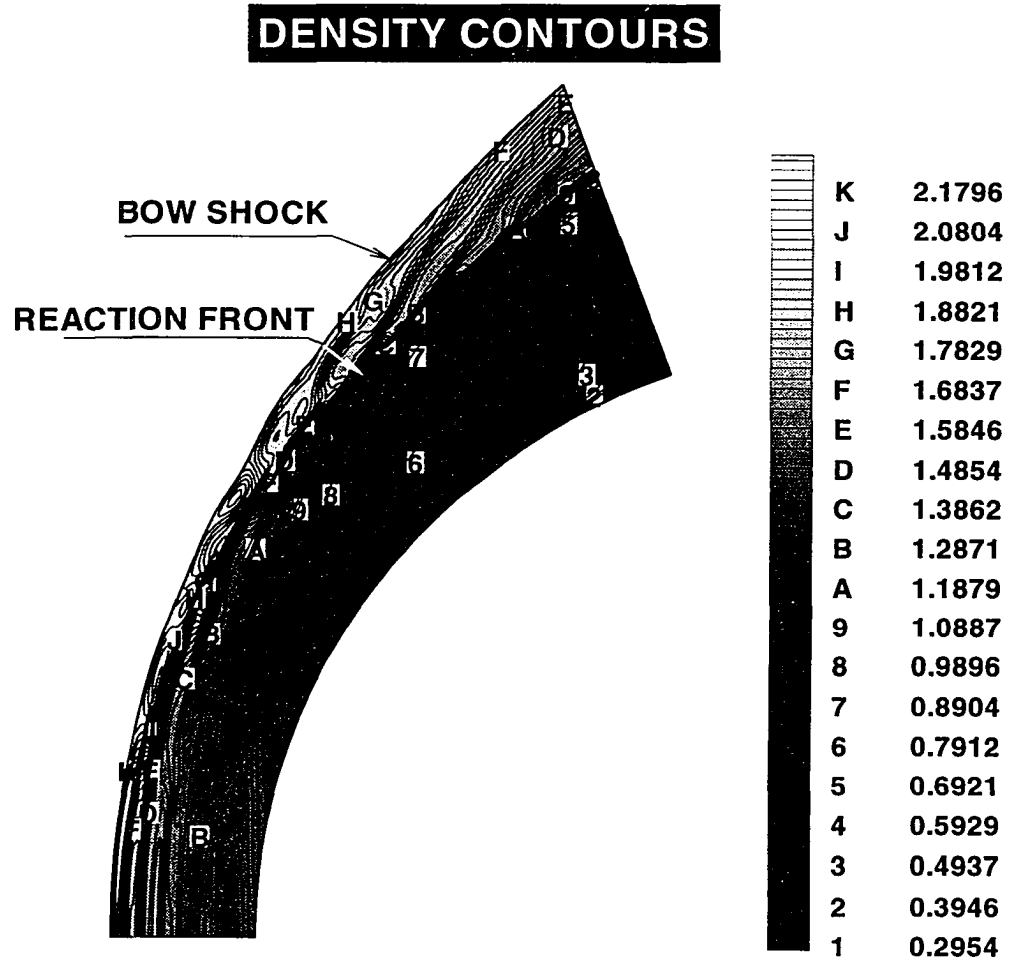
Figure 8.7   Density contours for Mach 5.11.

Figure 8.8   Temperature distribution along stagnation streamline for Mach 5.11.

127

COMPUTED SHADOWGRAPH

REACTION FRONT

CORRUGATED REACTION FRONT

BOW SHOCK

BOW SHOCK

$M_\infty = 5.11$

$M_\infty = 5.11$
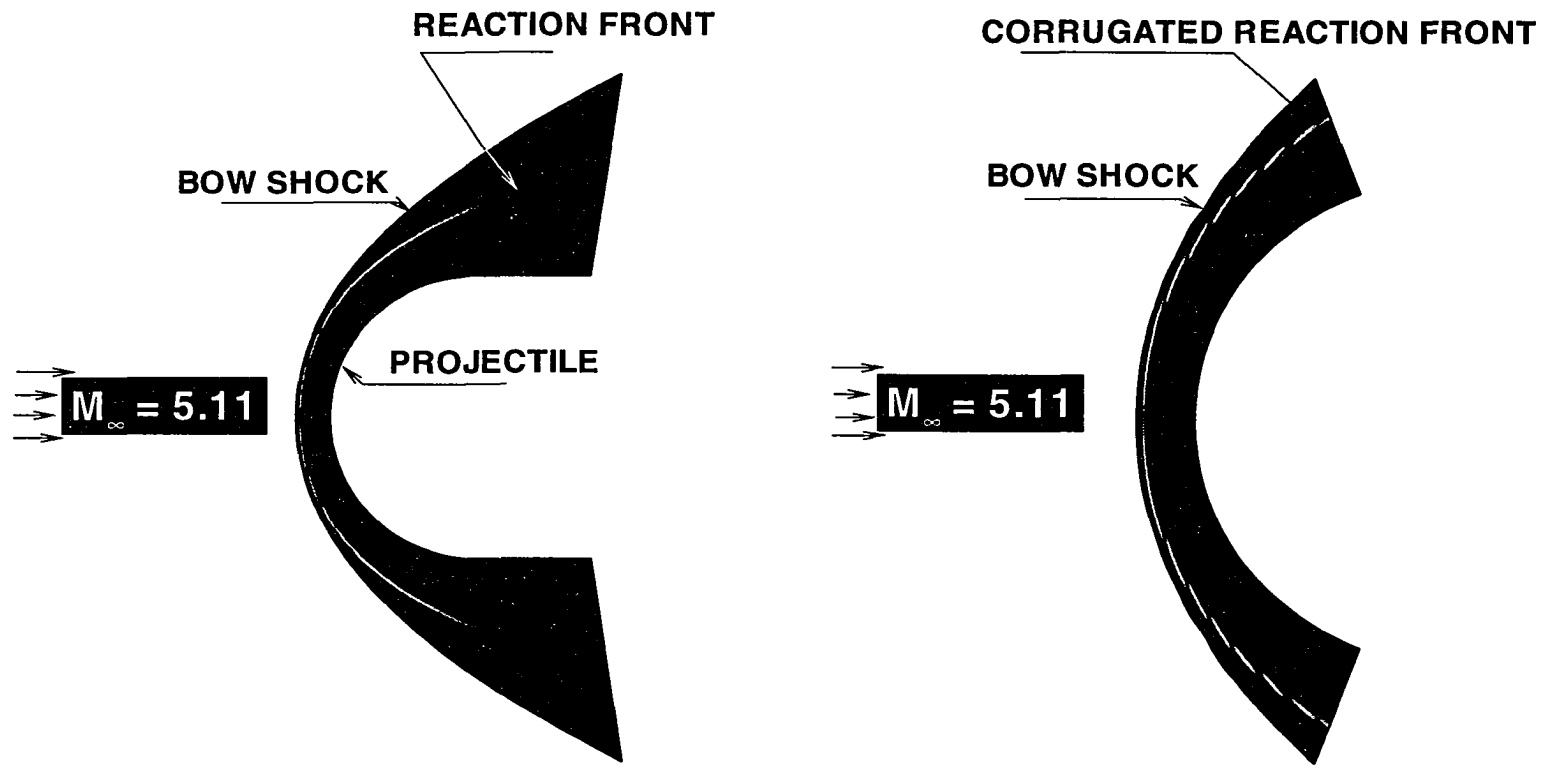
PROJECTILE

(a) COMPLETE PROJECTILE

(b) ENLARGED VIEW

Figure 8.9 Computed shadowgraphs for Mach 5.11 (a) Complete projectile and (b) Enlarged view.
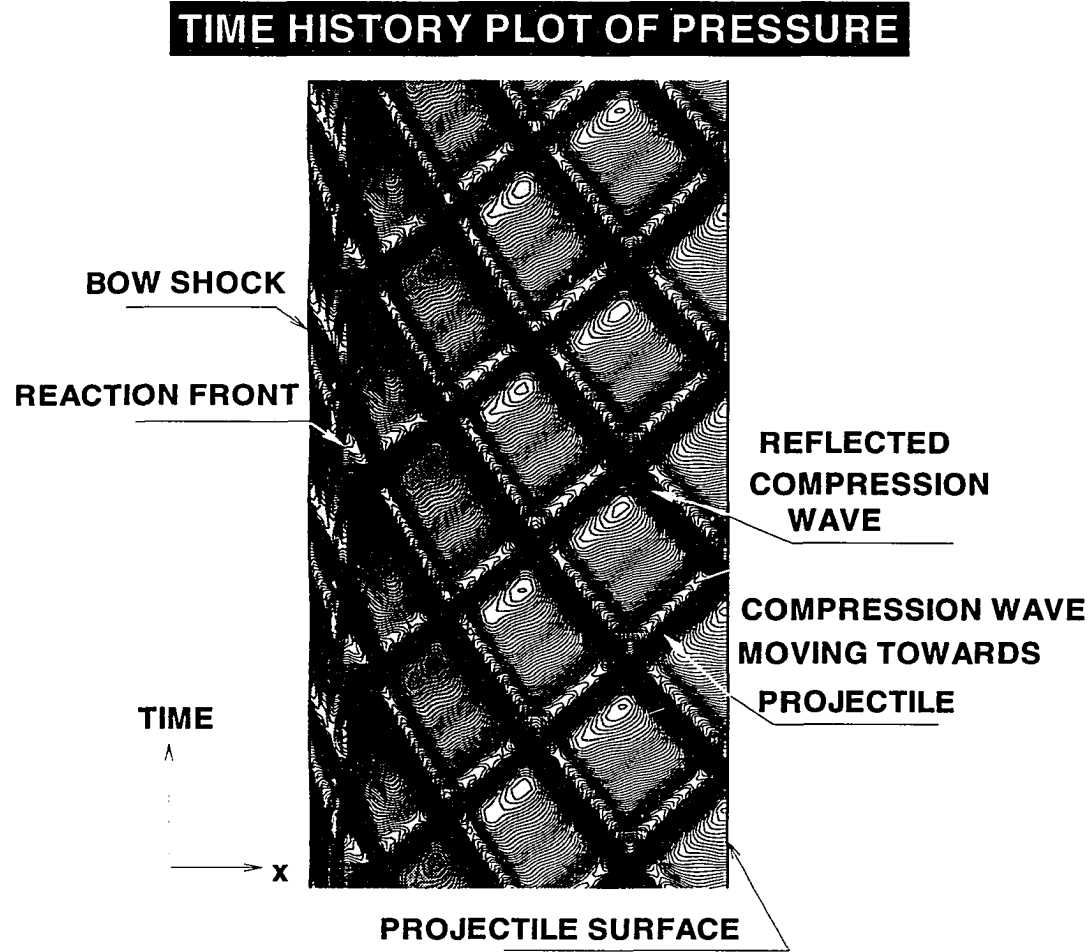
Figure 8.10   Time history plot for pressure along stagnation streamline for Mach 5.11.

130

TIME HISTORY PLOT OF TEMPERATURE

CONTACT DISCONTINUITY

BOW SHOCK

HOT SIDE

COLD SIDE

TIME

X

REACTION FRONT   PROJECTILE SURFACE

T (°K)	
F	3065.19
E	2954.36
D	2843.53
C	2732.7
B	2621.86
A	2511.03
9	2400.2
8	2289.37
7	2178.53
6	2067.7
5	1956.87
4	1846.04
3	1735.2
2	1624.37
1	1513.54

Figure 8.11   Time history plot for temperature along stagnation streamline for Mach 5.11.

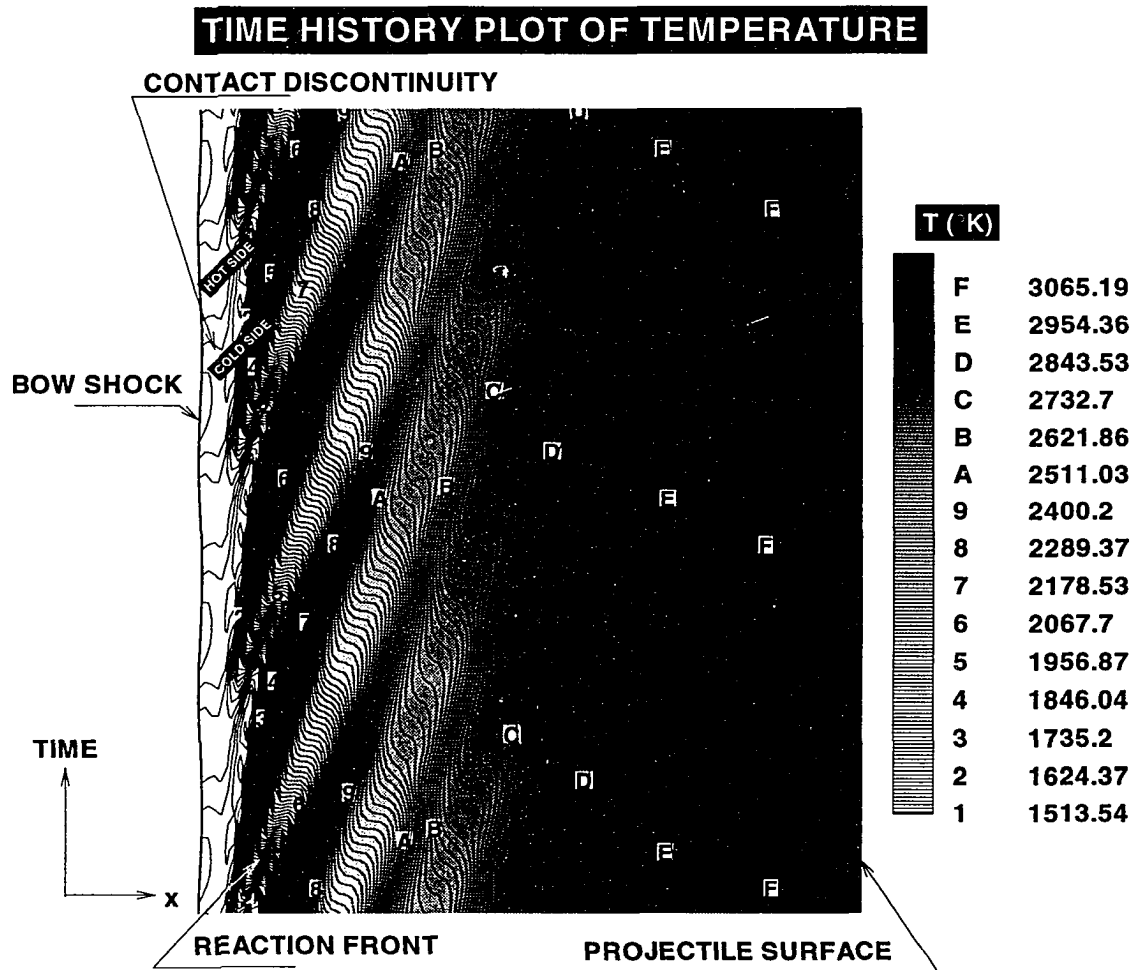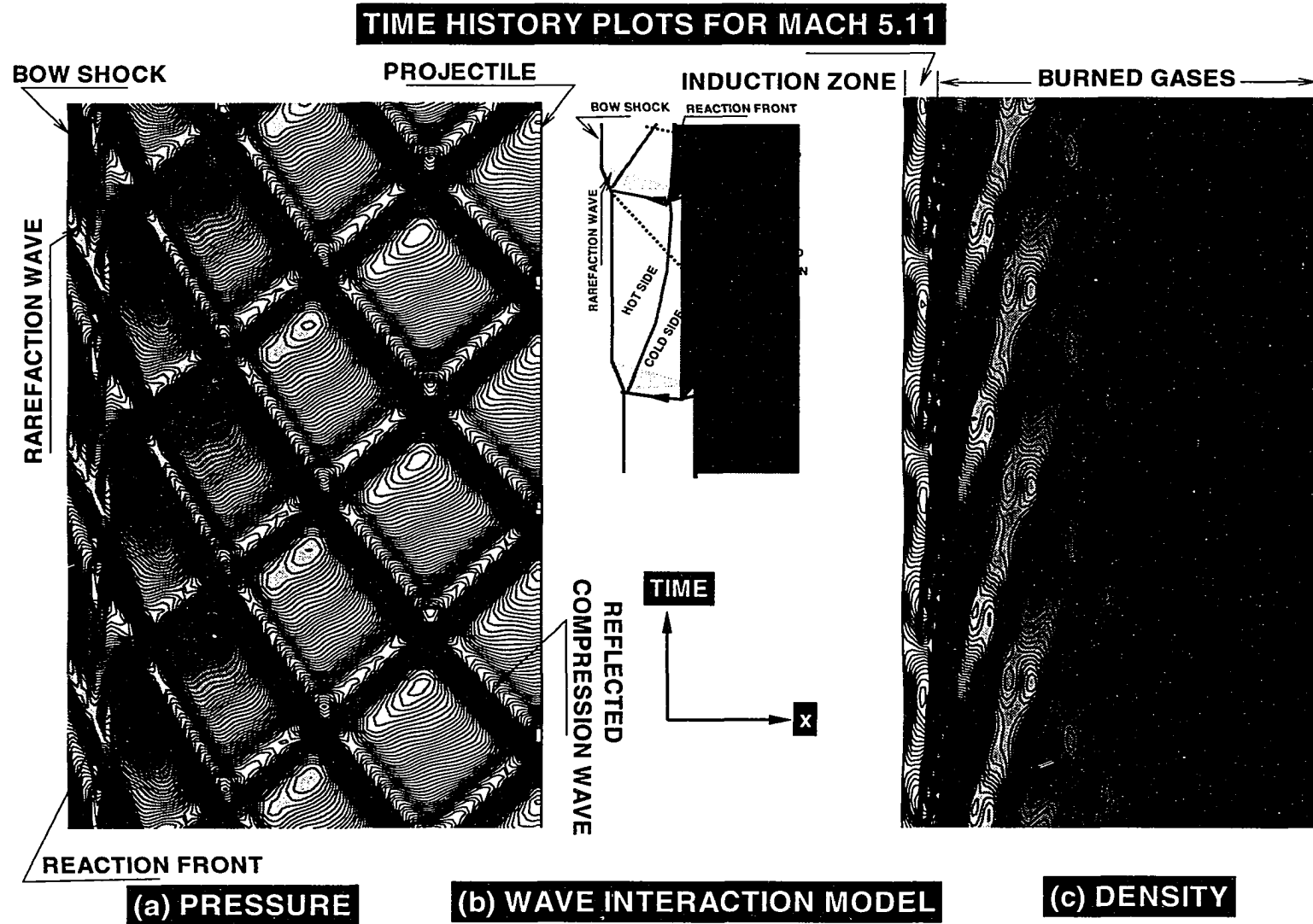Figure 8.12   Side-by-side comparison of time history plots for Mach 5.11 and the wave interaction model: (a) Pressure contours from simulation, (b) McVey and Toong wave interaction model, and (c) Density contours from simulation.

shock. The compression wave and the reflected compression wave from the body interact with the bow shock, thus providing a possible mechanism for the creation of another contact discontinuity, i.e., secondary contact discontinuity. The gases, being hotter on the upstream side of the contact discontinuity, start burning again generating compression waves; the cycle is then repeated as shown in Figs. 8.10.

8.2 Mach 6.46 Case

The results for the Mach 6.46 case are now presented. Due to close coupling of bow-shock and reaction front (i.e., small induction distance) at high Mach numbers, a finer grid was needed to resolve the flow field. Therefore, for Mach 6.46, a grid of 201×151 was used with 201 points in the circumferential direction and 151 points in the normal directions. This is a superdetonative case, i.e., the projectile velocity is higher than the C-J velocity of the mixture. Figure 8.13 shows the pressure contours as well as the wave pattern similar to Mach 5.11. When compared with Fig. 8.2, it is clear that the frequency of the compression waves moving towards the body and moving towards the bow shock is much higher. The bow shock and the reaction front are almost coupled with each other. Figure 8.14 shows the density contours. For this case, a very small induction distance occurs as a result of very high post-shock temperature. The features of the bow shock and reaction fronts appear to be the same like the simulations with shock-capturing. Figure 8.15 shows the pressure distribution along the stagnation streamline. There is a jump in pressure after the bow shock and then the pressure drops when the pressure wave meets a rarefaction wave. It increases again when it encounters another compression wave. After the energy release front, there is another jump in pressure. This pressure wave oscillates between a high value (when it encounters a compression wave) to a low value (when it encounter a rarefaction wave). Also, when compared with Fig. 8.4 for Mach 5.11, we see that there are more numerous oscillations in pressure for the Mach 6.46 case because

132

133
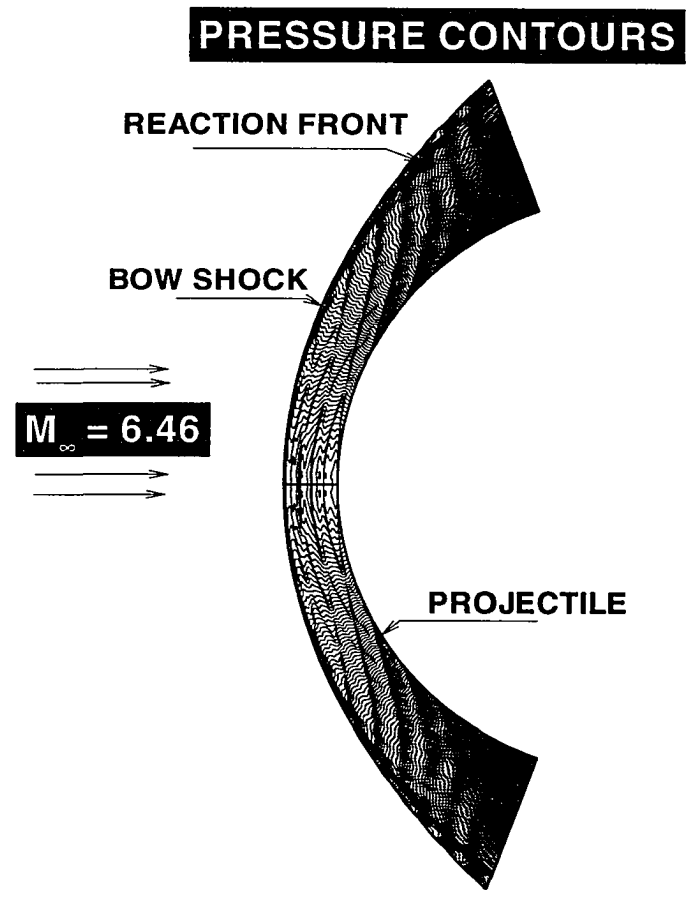
Figure 8.13   Pressure contours for Mach 6.46.
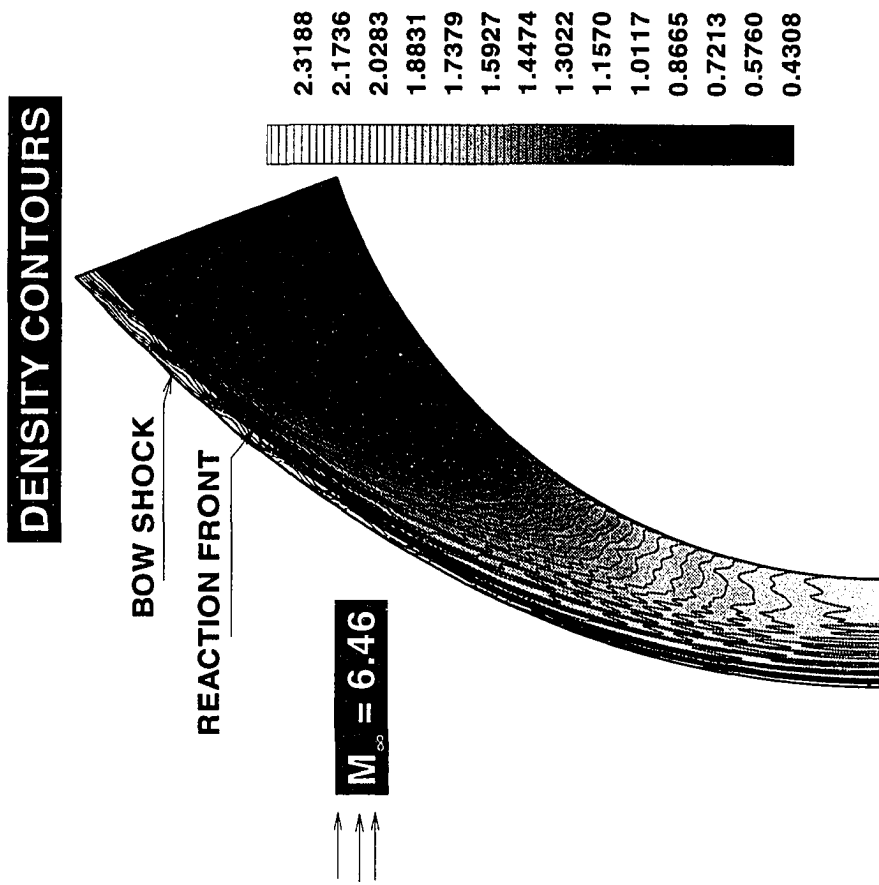
Figure 8.14 Density contours for Mach 6.46.

134
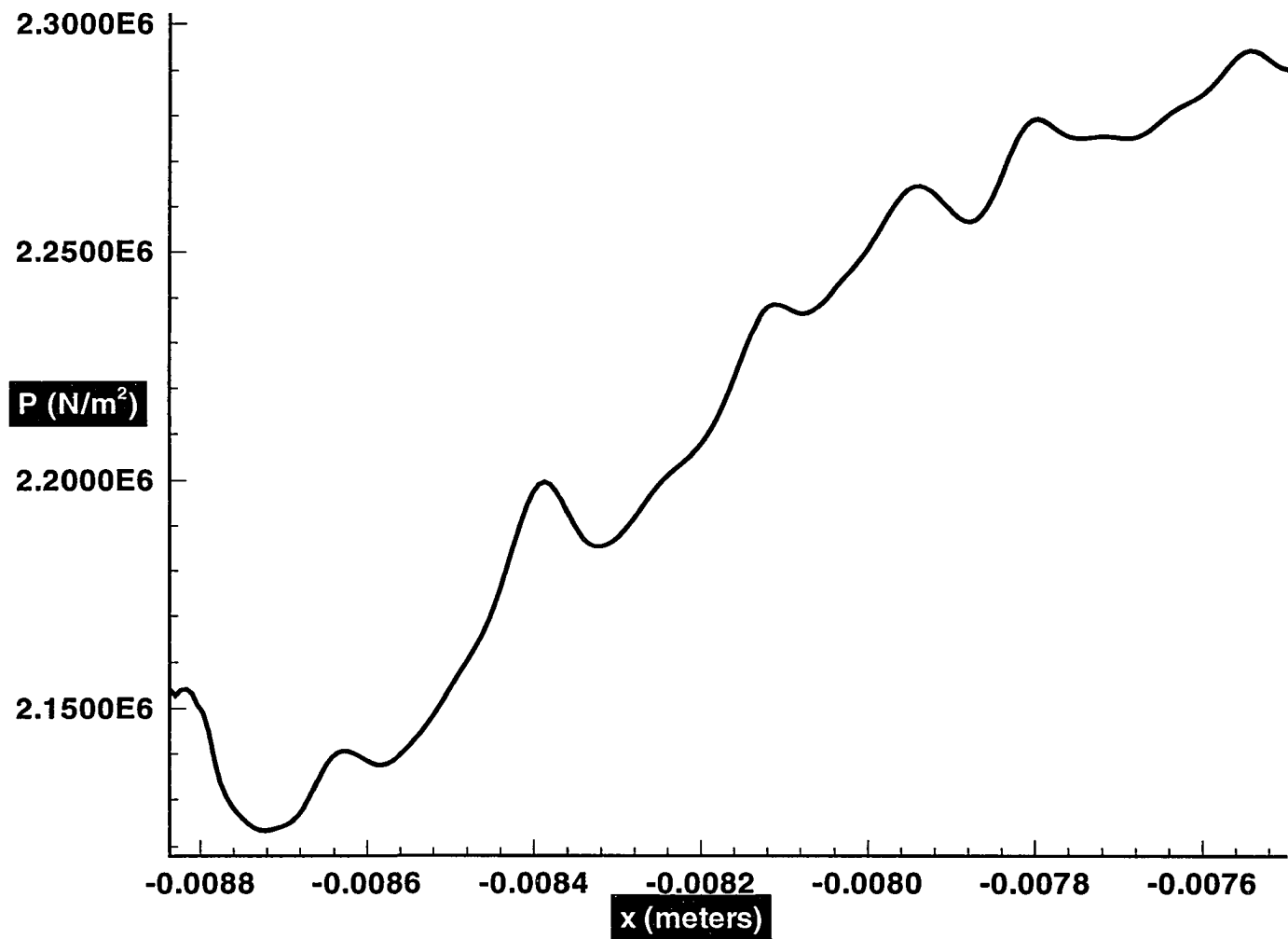
Figure 8.15   Pressure distribution along stagnation streamline for Mach 6.46.
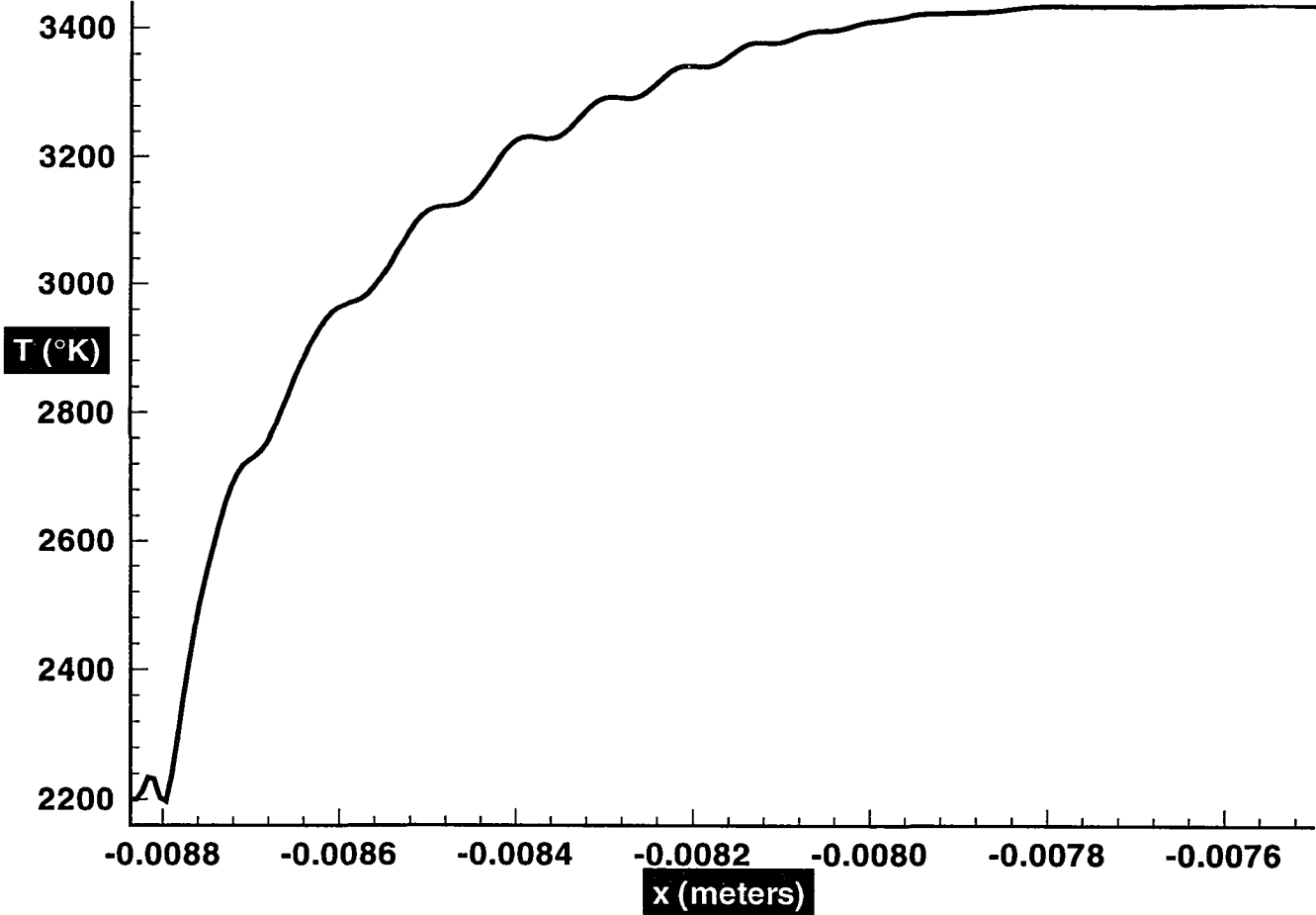
Figure 8.16   Temperature distribution along stagnation streamline for Mach 6.46.

137

COMPUTED SHADOWGRAPH

BOW SHOCK

REACTION FRONT

$M_\infty = 6.46$

PROJECTILE

(a) EXPERIMENTAL SCALE

(c) HIGHLY ENLARGED VIEW
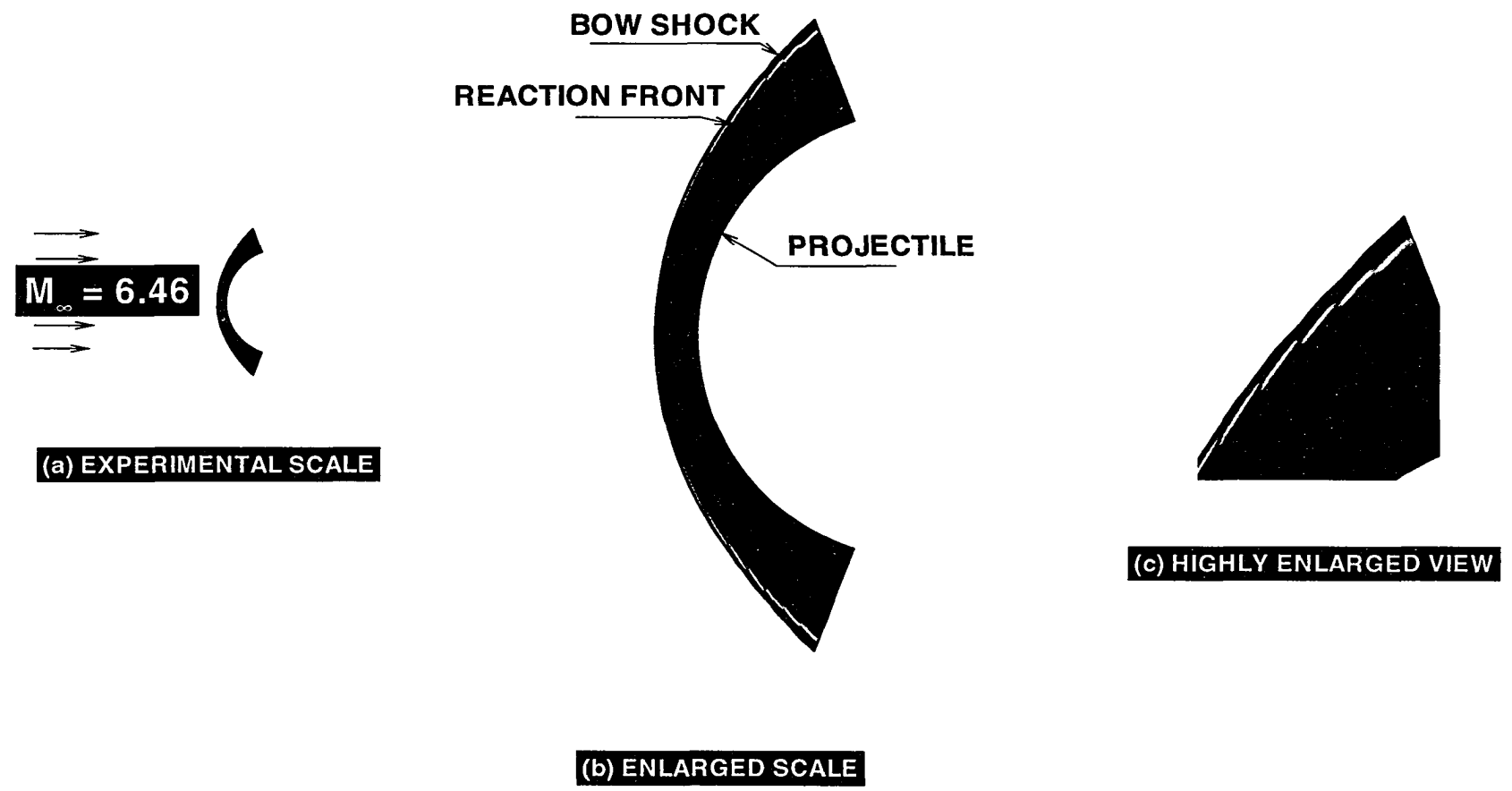
(b) ENLARGED SCALE

Figure 8.17   Computed shadowgraphs for Mach 6.46: (a) Experimental scale, (b) Enlarged scale, and (c) Highly enlarged view.
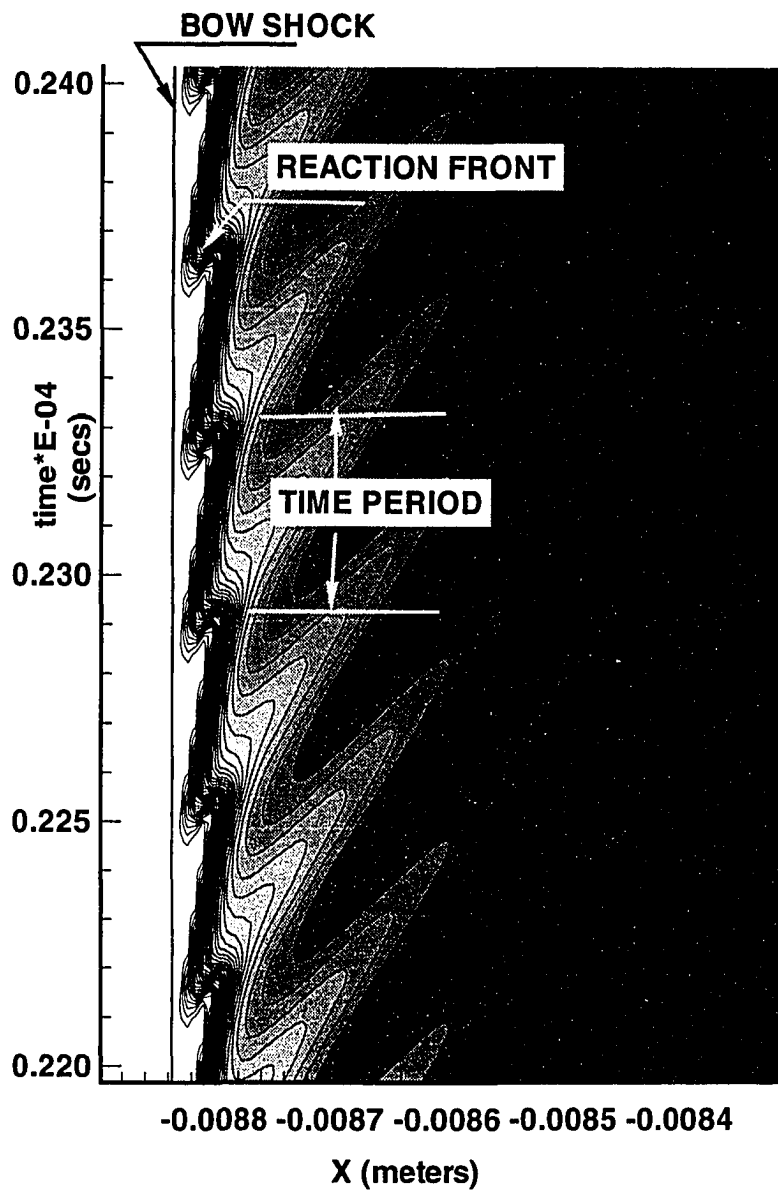
Figure 8.18 Time history plot of water mass fraction along stagnation streamline for Mach 6.46.

138

139

Grid 197X152

M$_\infty$ = 5.11

Grid 101X101

Bow Shock

Reaction Front

Projectile Surface

Bow Shock

Projectile Surface

Reflected Compression Wave

Time

X
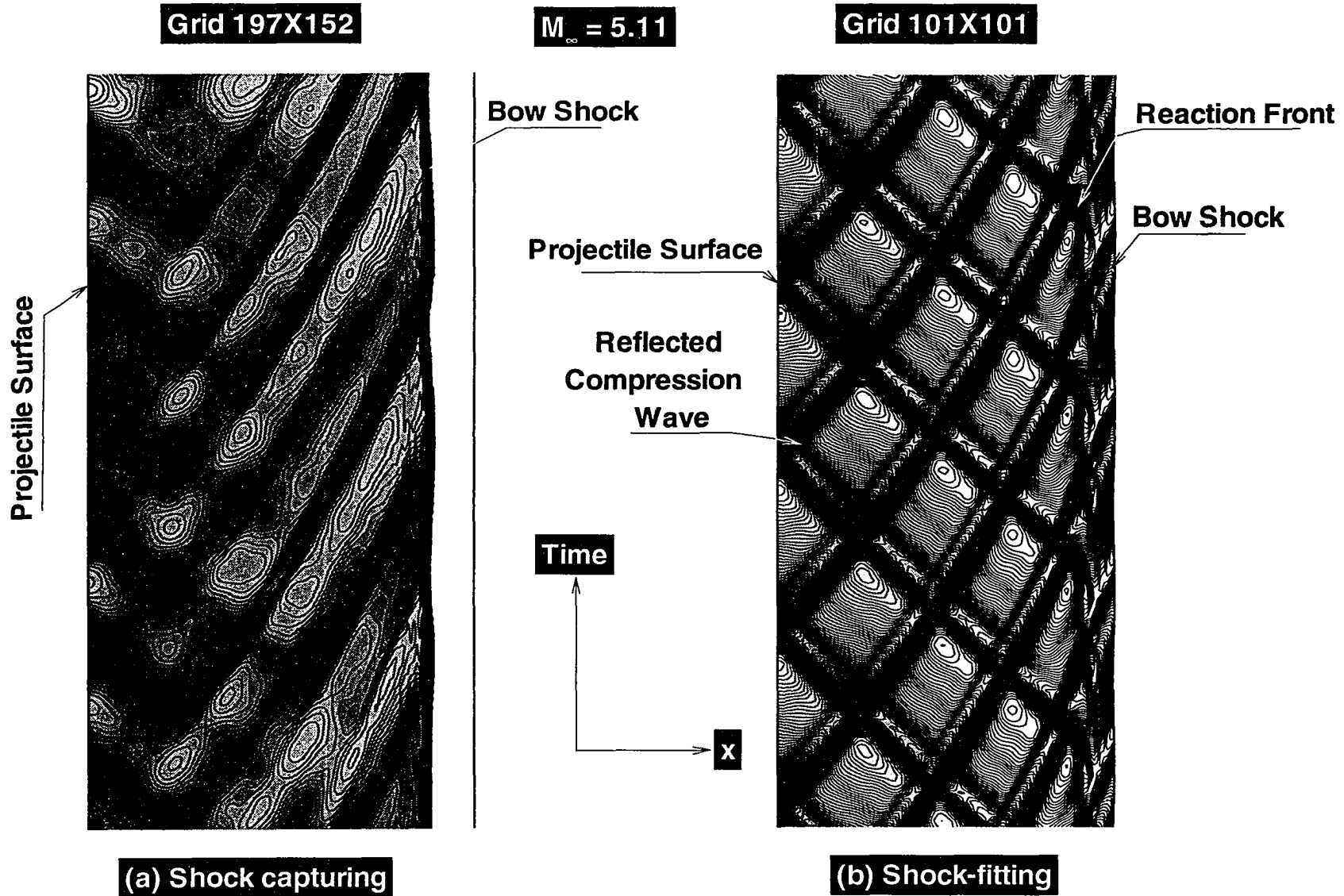
(a) Shock capturing

(b) Shock-fitting

Figure 8.19 Comparison of shock-capturing vs shock-fitting: Time history plots of pressure for Mach 5.11 along stagnation streamline (a) with shock-capturing method and (b) with shock-fitting method.

of higher frequency compression waves generated. Figure 8.16 shows the temperature distribution along the stagnation streamline. The stagnation point temperature is 3550 K. The temperature increases abruptly as the gas encounters the bow shock. Immediately after the shock, the temperature stays constant for a short distance and then begins to increase due to exothermic reaction. Figure 8.17 shows the computed shadowgraph for density. Figure 8.17b and 8.17c shows the corresponding enlarged view. The bow shock and the reaction front remain coupled with each other up to about 60–65 degrees from the stagnation streamline, as observed experimentally, and then start decoupling. Also, the reaction front shows slight oscillations of very low amplitude. Figure 8.18 shows the time history plot for water mass fraction. The bow shock is at 0.00884 meters from the center of the blunt body. The distance between the bow shock and the reaction front is very small. Also, as is clear from the figure, the amplitude of oscillations of the reaction front is 2.5 e-05 meters which is quite small as compared with the Mach 5.11 case. The frequency of oscillations can be computed directly from this figure and it is found to be 2.85 MHz, which is comparable with the earlier work [26]. Thus, Mach 6.46 case is a very high frequency but very low amplitude phenomena.

8.3 Comparison of Shock Capturing vs Shock-Fitting

As mentioned earlier that shock-fitting requires very small dissipation which does not smear the important flow features and therefore the intricate details of the flow field can be reproduced. This is clearly shown in Fig. 8.19 which is the x-t plot for water mass fraction contours. Figure 8.19a shows the x-t plot for water mass fraction for Mach 5.11 using shock capturing method whereas Fig. 819b shows the same using shock-fitting method. It is clear from Fig. 8.19b that almost all the intricate details of the flow field has been simulated very clearly whereas in Fig. 8.19a all the flow features are smeared. The cellular structure of the detonation wave phenomenon is clearly evident in Fig. 819b. It

must be emphasized that the number of grid points used in shock capturing were almost three times more than that in shock-fitting, yet the resolution of the flow field was much better in shock-fitting method.

8.4 Ruegg and Dorsey's Simulation

In the present study Ruegg and Dorsey's [6] three cases of ballistic data were simulated with the free-stream conditions given in Table 2.2. The grid used in the calculations was with 101 grid points in the x direction and 91 points in the y direction. This grid was selected based on our previous work [25], in which an extensive grid-refinement study was done to determine the grid most suited to this type of study and to give a grid-independent solution.

Figure 8.20a shows the contour plot for pressure for the steady case. The detailed mechanism of detonation-wave development depends primarily on the action of pressure waves that are generated in the course of combustion. This point has been given special attention by earlier researchers [12]. Under the current free-stream conditions, nearly no pressure waves are generated between the bow shock and the blunt body because of the weak reaction wave. As we move to Fig. 8.20b, which corresponds to the regular-regime free-stream conditions with p = 0.25 atm, we can see the pressure waves that are generated by the combustion between the bow shock and the body. Figure 8.20c shows the pressure contours for the large-disturbance-regime case, where p = 0.5 atm. The compression waves for this case are much more intense and the bow shock is distorted significantly. Inspection of Figs. 8.20a-c shows that the combustion moves the shock wave away from the body; this effect increases as the pressure increases.

Figures 8.21a-c show the density contours for the three cases. The flow has an outer bow shock, followed by an induction zone and a reaction front. The induction zone (i.e., the separation between the bow shock and the reaction front) is maximum for the

141

steady-regime case when p = 0.1 atm. Both the bow shock and the reaction fronts are very smooth in structure. If the pressure rises to 0.25 atm, then periodic instabilities arise near the stagnation line and spread downstream, as shown in Fig. 8.21b. Furthermore, the induction zone is considerably shorter than the previous case. A jump occurs in the density after the bow shock, followed by a drop in density after the reaction front due to the increase in temperature. Figure 8.21c shows the density contours when the pressure is increased further to 0.5 atm. The induction zone is further decreased as the combustion becomes more intense which causes the bow shock to distort.

Figures 8.22a-c show the computed shadowgraphs for the three cases. In Fig. 8.22a both the bow shock and the reaction front are separated considerably, and both fronts are smooth. The combustion front is quite weak, as has been observed experimentally. Figure 8.22b clearly shows the regular pattern of the instabilities of the reaction front. The instabilities are almost periodic in nature. The computed shadowgraph for the large-disturbance-regime case is shown in Fig. 8.22c. The distorted bow shock and an irregular, unsteady reaction front are clearly evident. A side-by-side comparison of Figs. 8.22b and 8.22c clearly shows that almost four to five periods of oscillation of the regular regime are equivalent to one period of oscillation for the large-disturbance regime. This result was reported in Ruegg and Dorsey's work also [6]. Thus, the large-disturbance regime consists of long period oscillations as compared with the regular regime.

Figures 8.23a-c show a schematic of an oblique detonation wave-engine and three possible time history plots of pressure depending upon the various free stream conditions. Since this phenomenon has been observed in detonations in tubes as well as in external flows, therefore, considering that the same free stream conditions can also be encountered in the combustors of an oblique detonation wave engine, and, therefore, similar flow features can be expected in the combustors of an oblique detonation wave engine. Figure

142

8.23a shows the x-t plot for pressure when the free stream pressure is 0.1 atm. It shows a very smooth bow shock and reaction front. Figure 8.23b shows the x-t plot for pressure when the free stream pressure is 0.25 atm. Now the same smooth reaction front has turned into a highly periodic reaction front. Compression waves generated between the reaction front and the blunt projectile starts interacting with each other and this interaction of the compression waves sustains the instability. Moving to Fig. 8.23c where the free stream pressure is now 0.5 atm, we notice that the regular periodicity of the reaction front disappears and its place is taken over by bumps in the reaction front and the bow shock. Both the reaction front and the bow shock are highly distorted. This is the large-disturbance regime.

Figure 8.24a-c show the time history plots for the three cases for water mass fraction along the stagnation streamline. Figure 8.24a shows a smooth and steady bow shock and reaction front. The maximum water production after the reaction front shows that the reaction is nearly completed after the reaction front. As the pressure is increased to 0.25 atm and Mach number is increased to 4.9, a highly periodic unsteady reaction front develops (Fig. 8.24b). The induction zone has reduced considerably. Although the reaction front is unsteady, the bow shock is quite smooth. This effect has been observed experimentally also. Figure 8.24c shows the large-disturbance-regime case, in which the combustion becomes so intense that the bow shock is completely distorted. Highly pronounced combustion surges cause a completely different profile of the reaction front than for the regular regime. The induction zone is much shorter than for the previous two cases.

In order to validate the present numerical results, we compare the wave-detachment distance (both for the shock wave and the combustion wave) for the three cases with the experimental results of Ruegg and Dorsey. Figure 8.25 shows the plot of wave detachment

143

versus Mach number for p = 0.1 and 0.5 atm. For both cases, the numerical shock stand-off distance and the reaction-front stand-off distance closely match the experimental data. Figure 8.26 shows the same plot for p = 0.25 atm. In this case, the numerical reaction front closely matches the experimental value, but the shock stand-off distance is underpredicted by about 8–9 percent. This discrepancy has not been resolved at present.

Figure 8.27a shows the time history plot for pressure, and Fig. 8.27c shows the time history plot for density for the regular-regime case (i.e, when p = 0.25 atm). This pattern of instabilities (which has also been observed in Lehr's work [11] has been explained in the past by many researchers with McVey and Toong's one-dimensional wave-interaction model. A brief description of this model and a discussion of regular-regime results in regard to the model has already been explained in the earlier sections. It need only to be emphasized here that the results presented in Fig. 8.27a-c are very similar to Lehr's Mach 5.11 case.

Now we concentrate our attention on the large-disturbance regime (i.e the free-stream pressure is increased to 0.5 atm). Figure 8.28a shows the time history plot along the stagnation streamline for pressure. Figure 8.28b shows the one-dimensional wave-interaction model due to Matsuo et al. [24], and Fig. 8.28c shows the time history plot for density. To understand the instabilities for the large-disturbance regime, we must consider Figs. 8.28a-c together. The concepts developed in Ref. [12] and used in the model by Matsuo et al. [24] are shown in these figures. As shown in Fig. 8.28b, the cycle begins when an "explosion within an explosion" occurs on the reaction front; then, the reaction shocks propagate upstream and downstream. The forward shock which has been referred to as "superdetonation", moves into the unburned gases. The backward shock, referred to as "retonation", moves into the burned gases. At a later time, the detonation wave overtakes and penetrates the bow shock. Then, the bow shock and

144

the detonation wave create a triple point and generate a reflected shock and a contact discontinuity. The bow shock is accelerated by this penetration, and the gas behind the bow shock is further compressed. At a later time, the bow shock is decelerated, and the bow shock and reaction front become separated. The retonation wave and the reflected shock reach the body surface, and the reflected compression wave goes to the bow shock. The reflected compression wave interacts with the bow shock, and another contact discontinuity is generated. Finally, the contact discontinuity reaches the original reaction front, the explosion within an explosion occurs on reaction front, and the cycle of events is repeated.

By comparing the model (Fig. 8.28b) with the numerical results (Figs. 8.28a and 8.28c), we see that the model developed by Matsuo et al. [24] agrees well with the current numerical results. As the pressure is increased to 0.5 atm, the strong exothermicity on the reaction front generates strong reaction shocks, which move toward the bow shock and the body. The exothermic reaction accelerates the reaction shock. As mentioned earlier, this phenomenon is called the explosion within an explosion and has also been observed in detonations in tubes [12]. Both Figs. 8.28a and 8.28c clearly show this phenomenon. At this point explosion, two strong shocks are produced one that moves into the unburned medium, which we refer to as "superdetonation," and the other that moves into the burned gases and is known as "retonation." Both superdetonation and retonation are seen in the numerical results of Fig. 8.28a and Fig. 8.28c.

So that we could better examine the series of wave interactions and the many point explosions and penetrations, the large-disturbance case was run longer. Figures 8.29a and 8.29b show the time history plots for pressure and density for an extended period of time. Two penetrations are evident (i.e, transitions from deflagration to detonation and vice versa).

145

Figures 8.30a and 8.30b show enlarged views of the history plots for pressure and density. As shown in Fig. 8.31a, the superdetonation causes the reaction front to accelerate, which in turn causes the bulging, or penetration, of the bow shock. This case is a typical example of deflagration-to-detonation (DDT) transition and also has been observed in detonations in tubes. Because of the accelerating reaction front and the eventual merging of the bow shock with the reaction front, a self-sustained detonation wave exists in front of the projectile body. The point of intersection of the bow shock and reaction front is termed as "triple point". A reflected shock is necessary to satisfy the continuity of the pressure and flow direction across the point of intersection of the bow shock and reaction front. This reflected shock is clearly shown in the numerical results. Thus, the triple point is the point at which the bow shock, the reaction front and the reflected shock meet. Of the three phenomena, the reflected shock is the weakest. Next, the bow shock wave begins to decelerate. Thus, the merged bow shock and reaction front begin to separate, as shown in Fig. 8.30b. This separation stage is the transition from detonation to deflagration; thus, it is known as the ordinary shock-induced combustion. The reflected shock (after reflecting from the body) reaches the bow shock and generates a contact discontinuity (as shown in Fig. 8.30b), and the entire process is repeated.

146

Figure 8.20 **Pressure contours for (a) Stable case, (b) Unstable regular regime, and (c) Unstable large-disturbance regime.**

BOW SHOCK

REACTION FRONT

(a)

BOW SHOCK

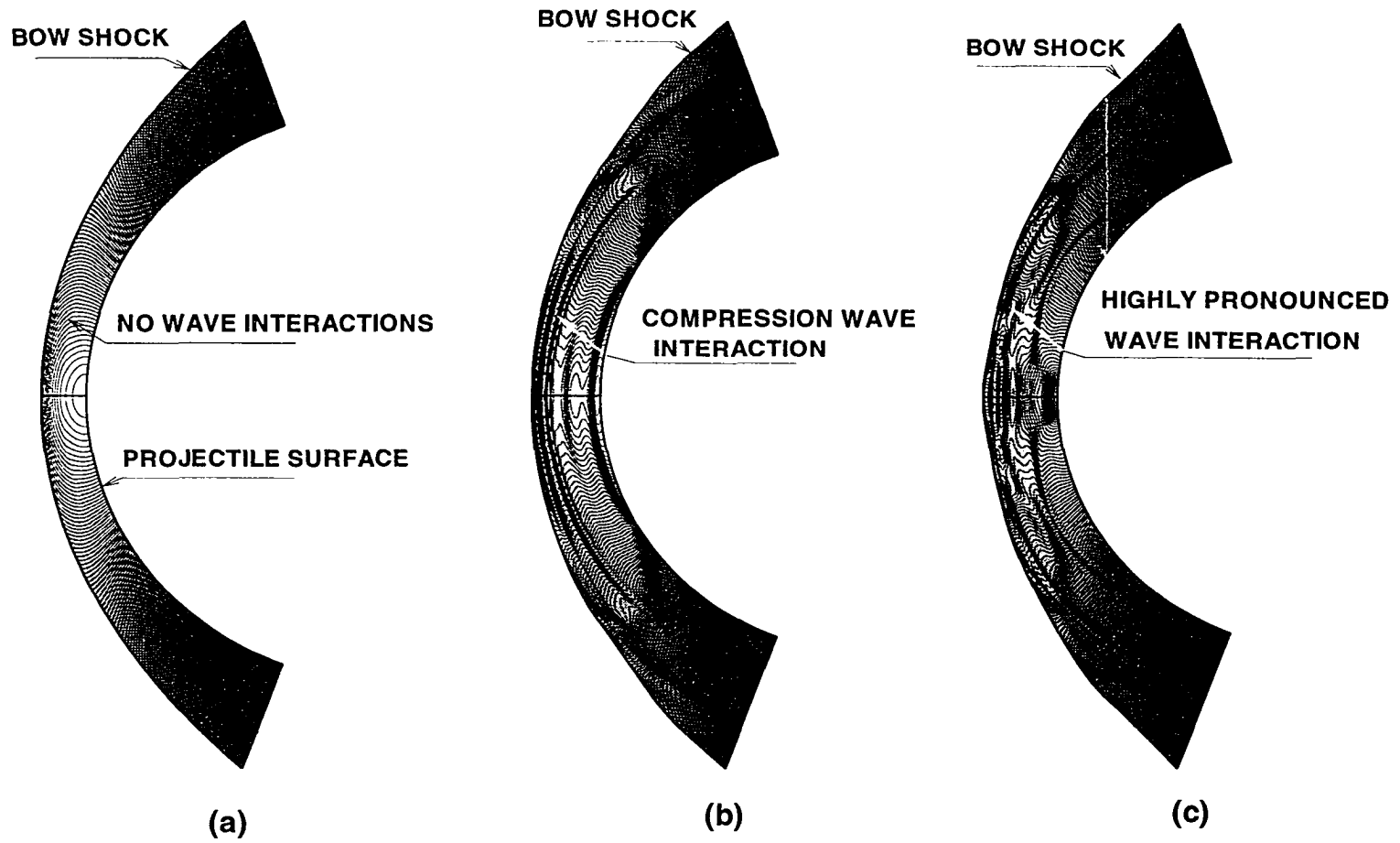**REACTION FRONT**

(b)

BOW SHOCK

REACTION FRONT

(c)

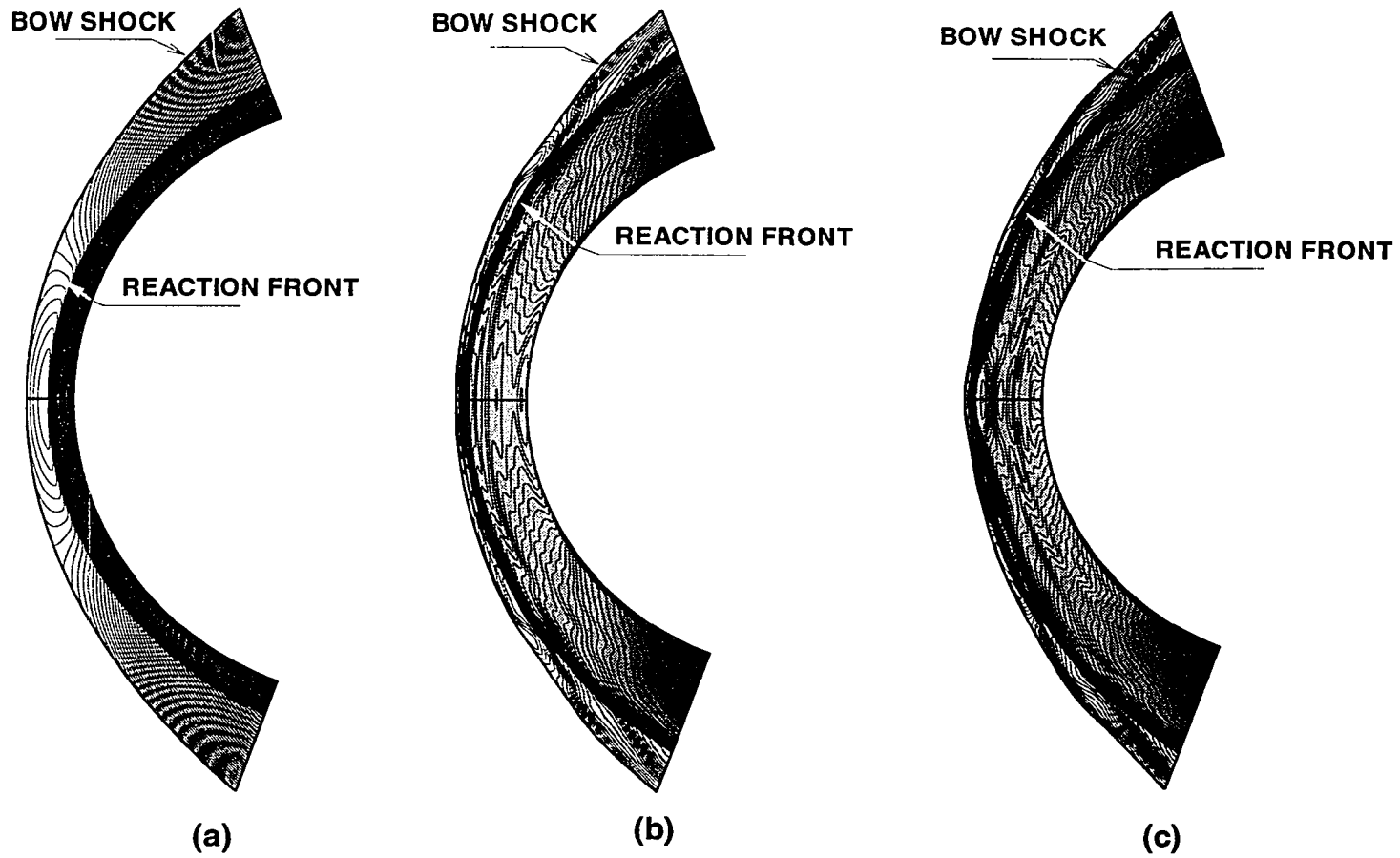Figure 8.21   Density contours for (a) Stable case, (b) Unstable regular regime, and (c) Unstable large-disturbance regime.
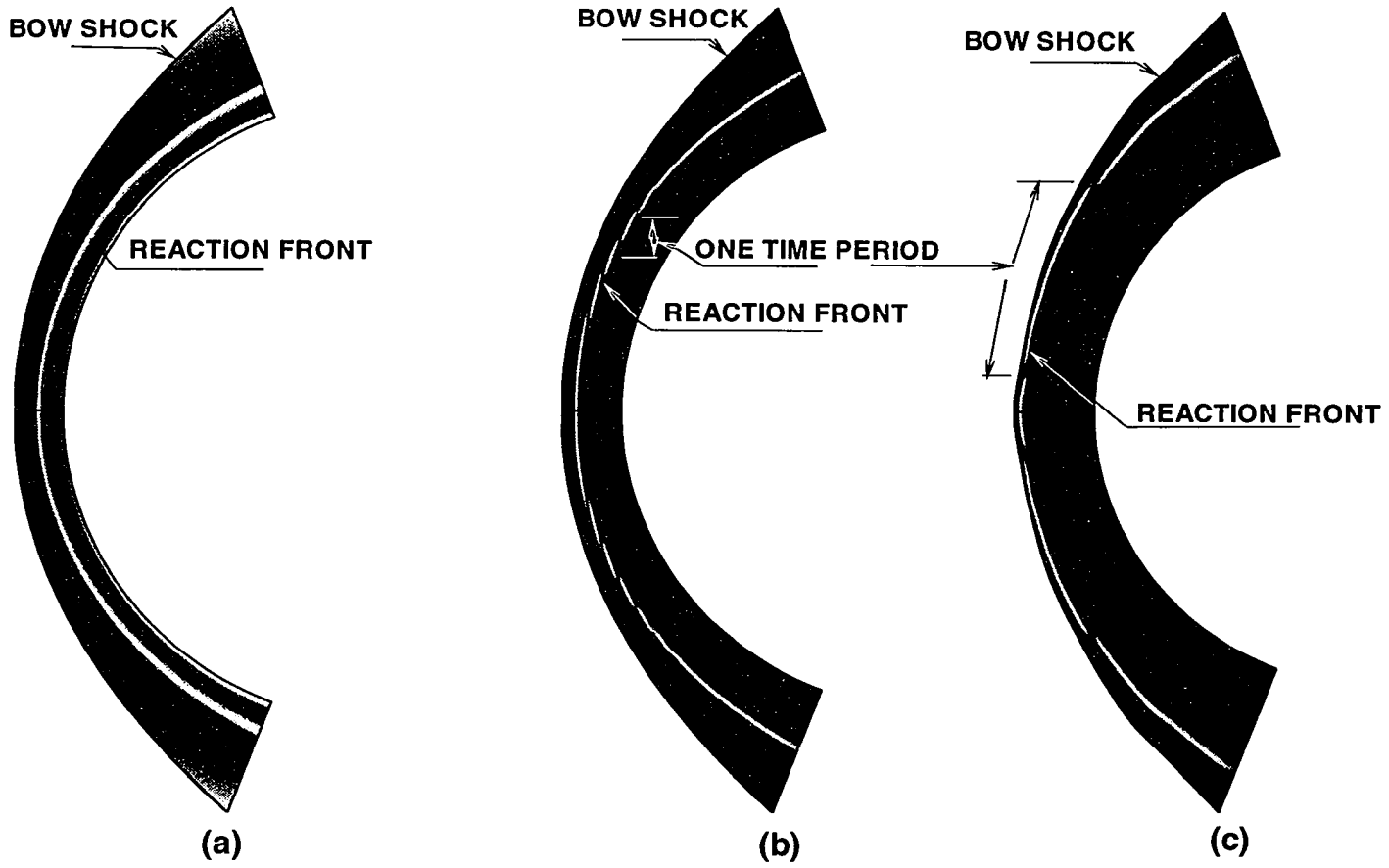
Figure 8.22 Computed shadowgraphs for (a) Stable case, (b) Unstable regular regime, and (c) Unstable large-disturbance regime.

149

Figure 8.23 Time history plots of pressure along stagnation line for (a) Stable case, (b) Unstable regular regime, and (c) Unstable large-disturbance regime.

TIME HISTORY PLOTS OF WATER MASS FRACTION
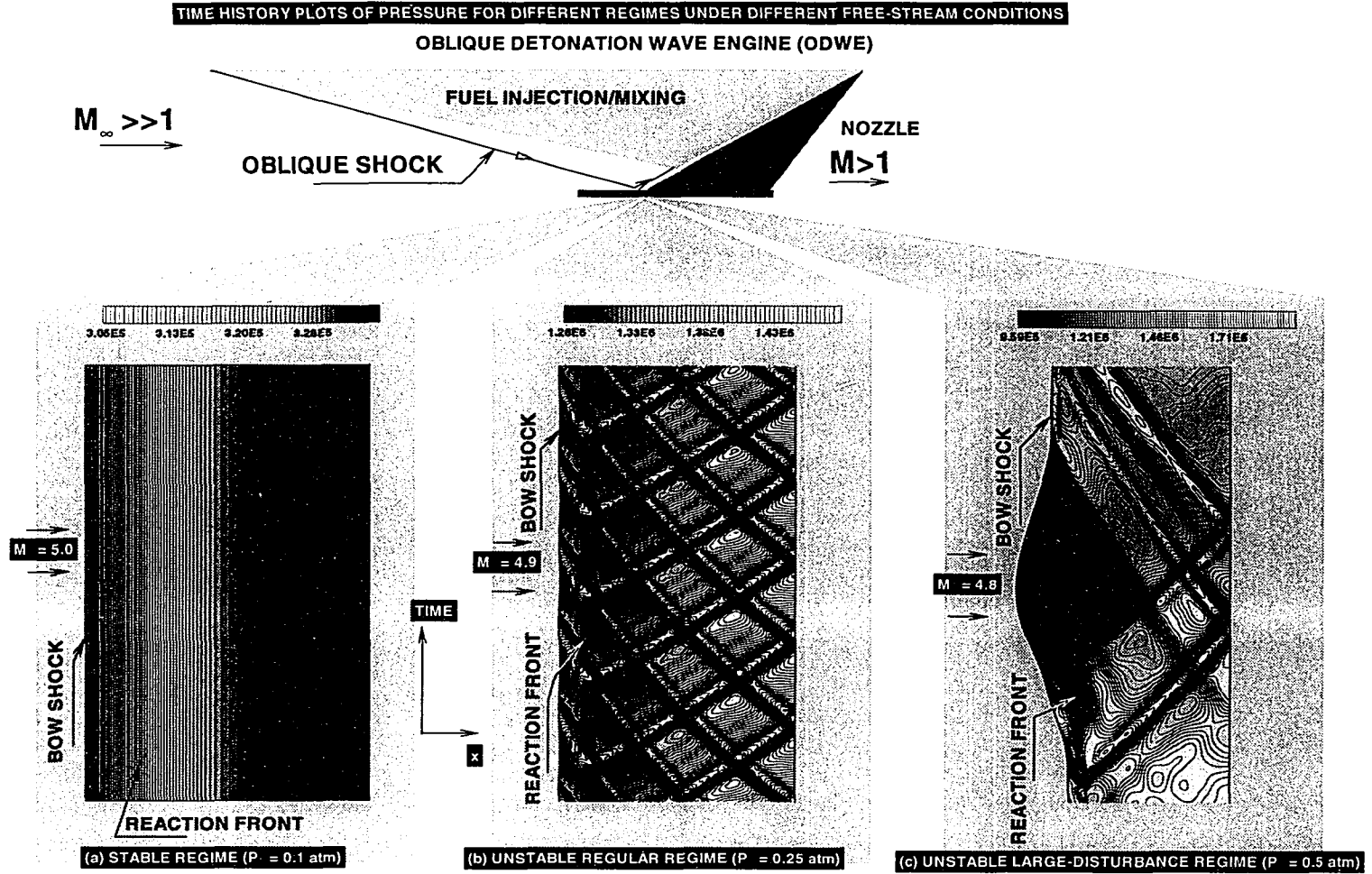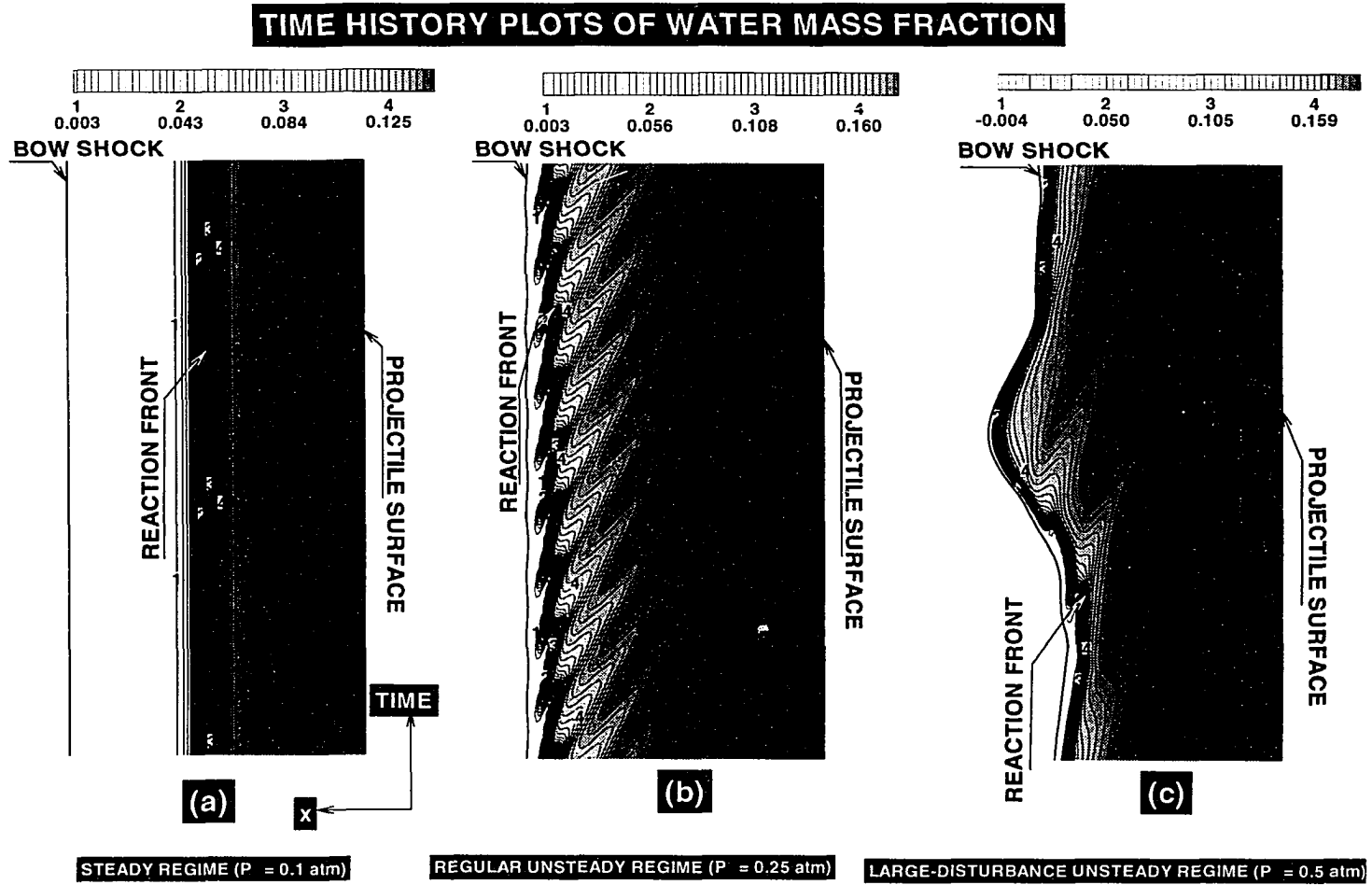
Figure 8.24 Time history plots of water mass fraction along stagnation line for (a) Stable case, (b) Unstable regular regime, and (c) Unstable large-disturbance regime.

152
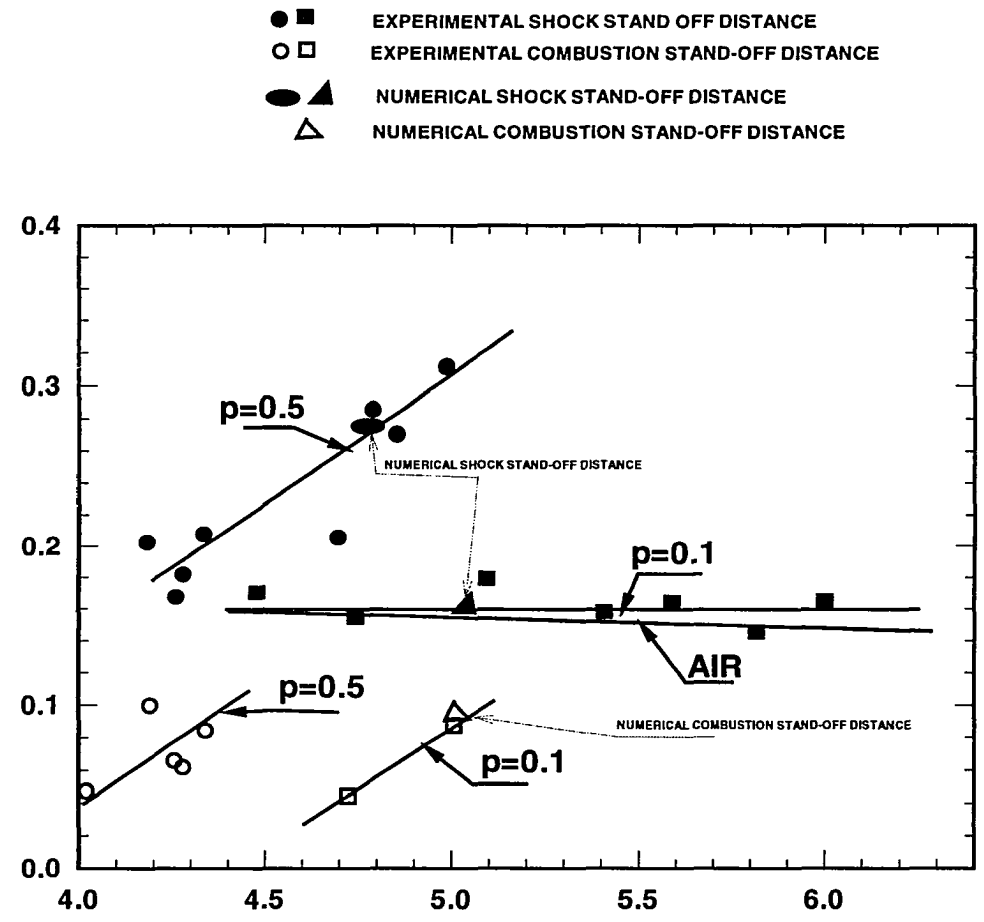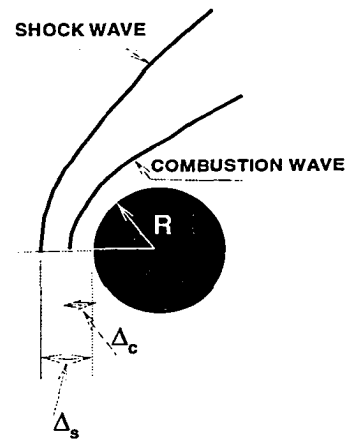
Figure 8.25   Comparison of wave detachment distance from experiments of Ruegg and Dorsey, and the current numerical work for pressure of 0.1 atm and 0.5 atm.

153
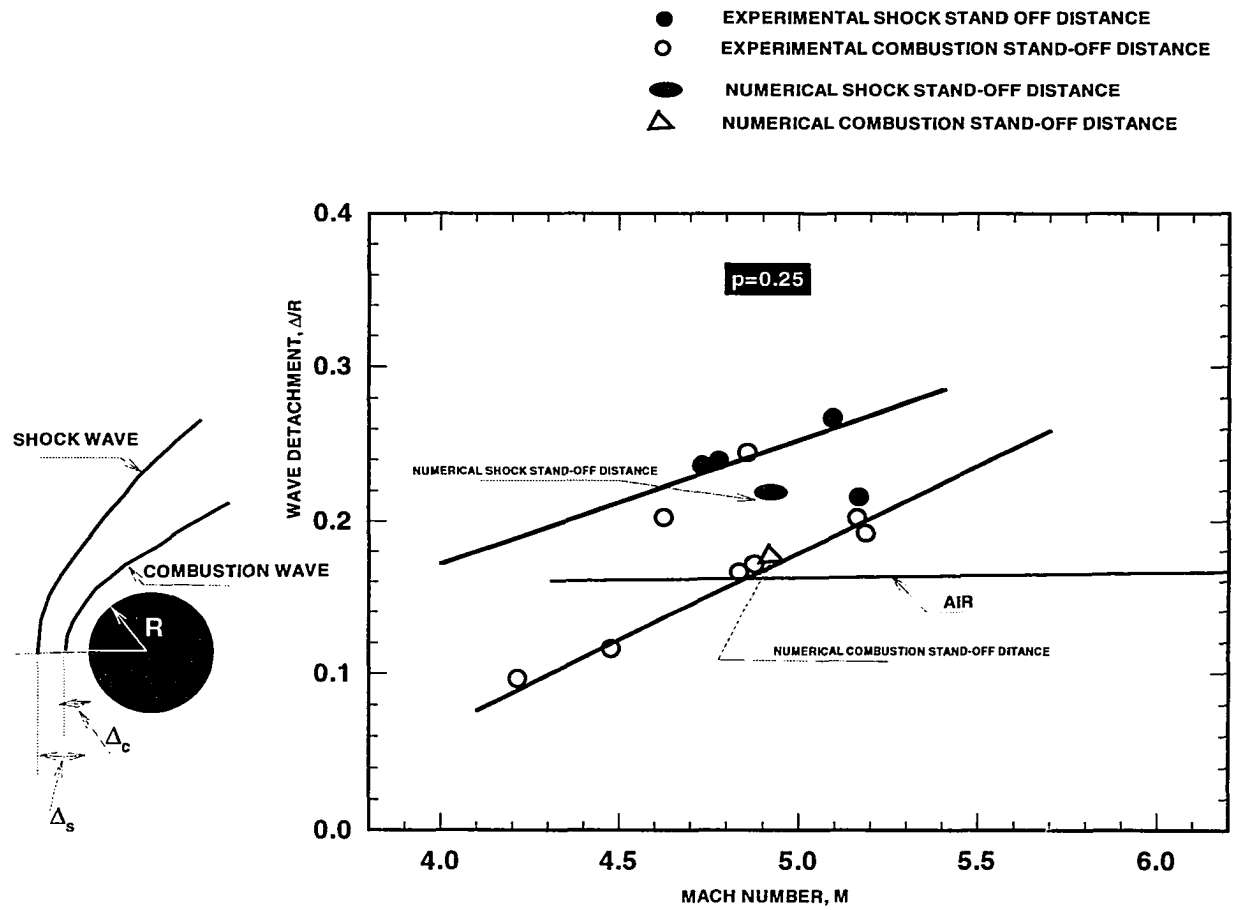
Figure 8.26 Comparison of wave detachment distance from experiments of Ruegg and Dorsey, and the current numerical work for pressure of 0.25 atm.

154

TIME HISTORY PLOTS FOR REGULAR REGIME

COMPRESSION WAVE

BOW SHOCK

REACTION FRONT

BOW SHOCK

CONTACT DISCONTINUITY

BOW SHOCK

ED COMPRESSION
AVE

SION WAVE
OWARDS BODY)

RAREFACTION WAVE

REACTION FRONT

RAREFACTION WAVE

TIME

REACTION FRONT

X

(a) PRESSURE   (b) WAVE INTERACTION MODEL   (c) DENSITY
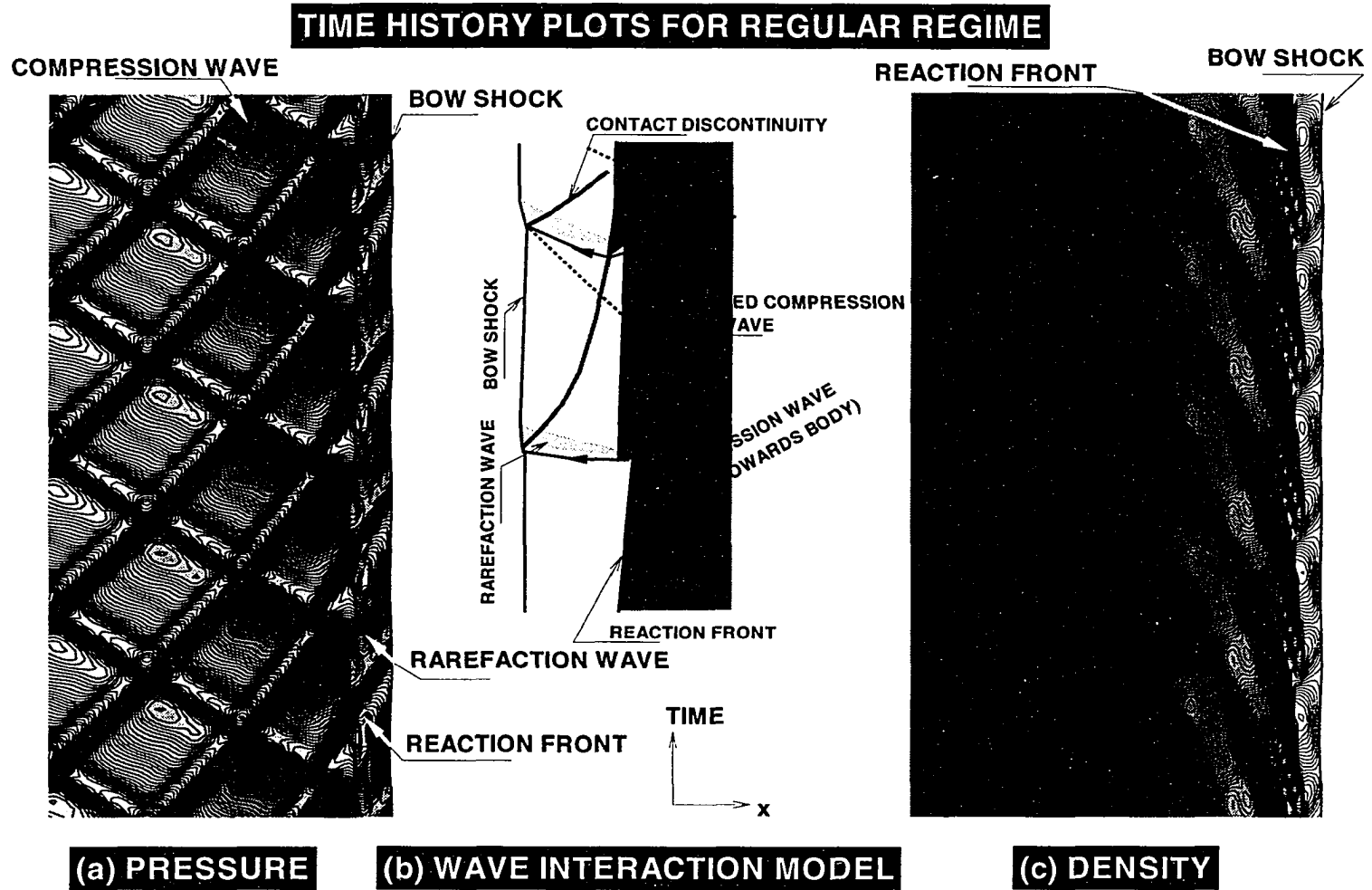
Figure 8.27   Side-by-side comparison of time history plots for regular regime and the wave interaction model: (a) Pressure contours from simulation, (b) McVey and Toong wave interaction model, and (c) Density contours from simulation.

155
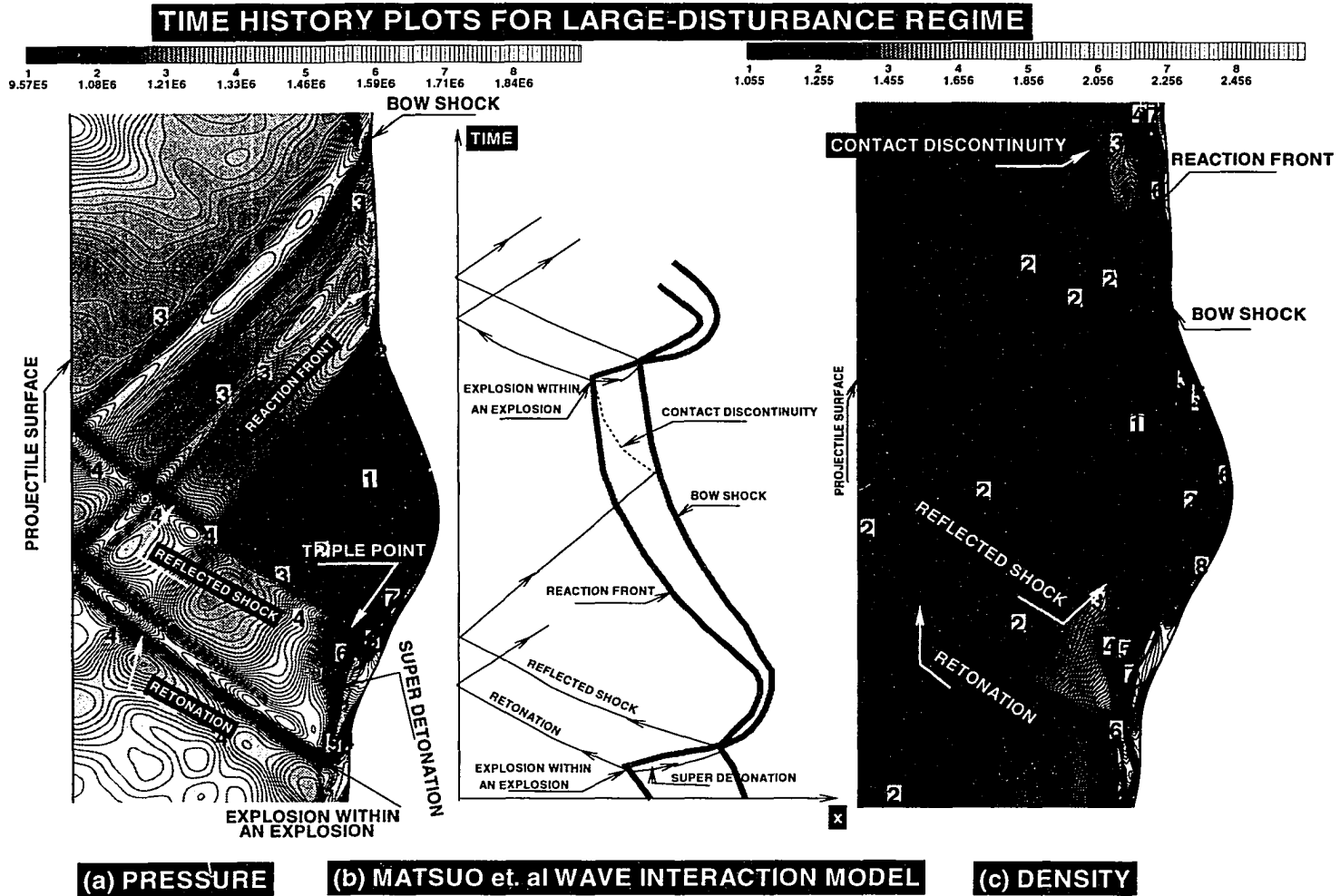
Figure 8.28   Side-by-side comparison of time history plots for large-disturbance regime and the wave interaction model: (a) Pressure contours from simulation, (b) Matsuo et al. wave interaction model, and (c) Density contours from simulation.

156

Figure 8.29   Time history plots for large-disturbance regime for an extended period of time: (a) Pressure contours from simulation and (b) Density contours from simulation.

157

Figure 8.30   Enlarged view of x-t plots for large-disturbance regime showing DDT: (a) Pressure contours from simulation and (b) Density contours from simulation.
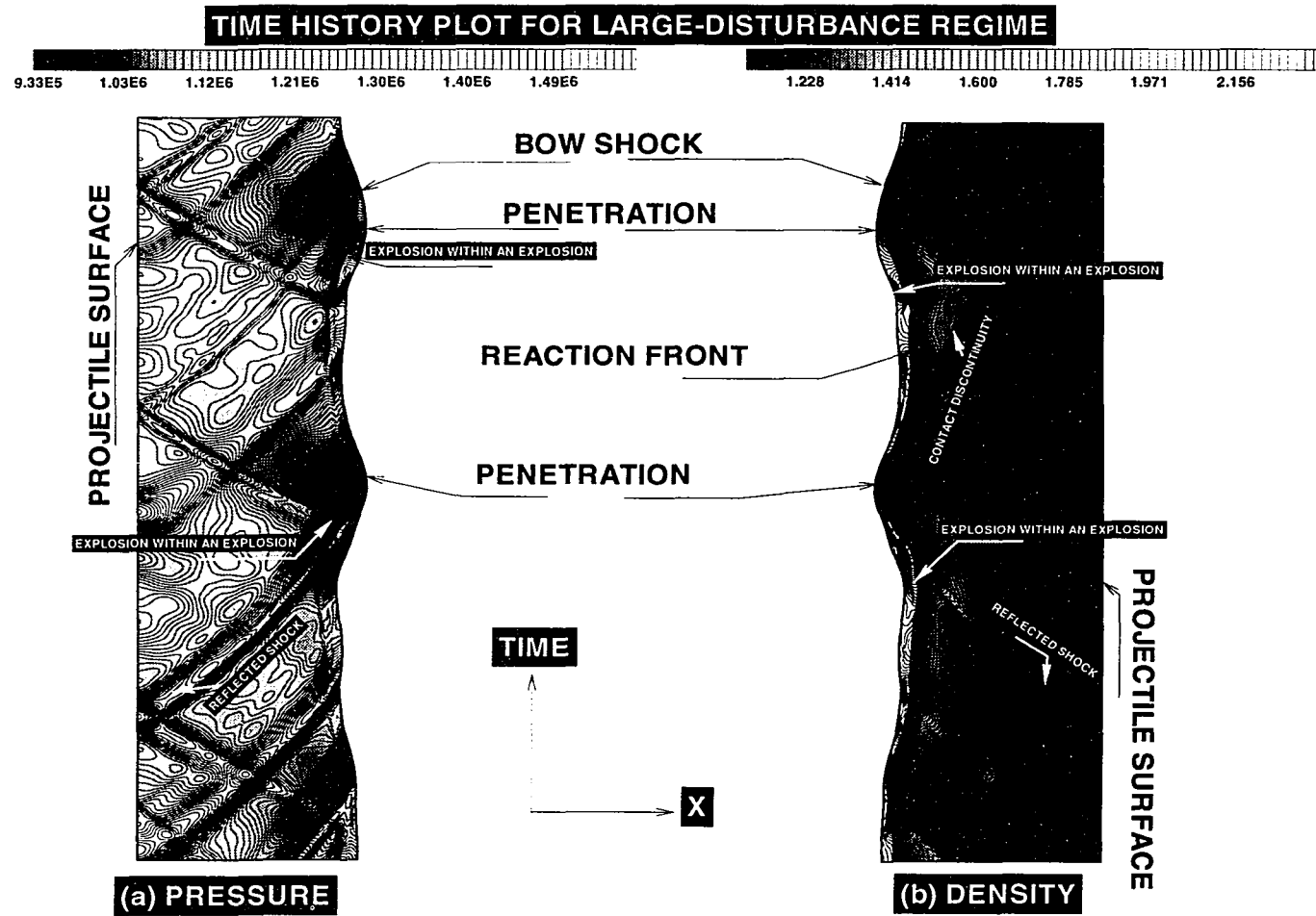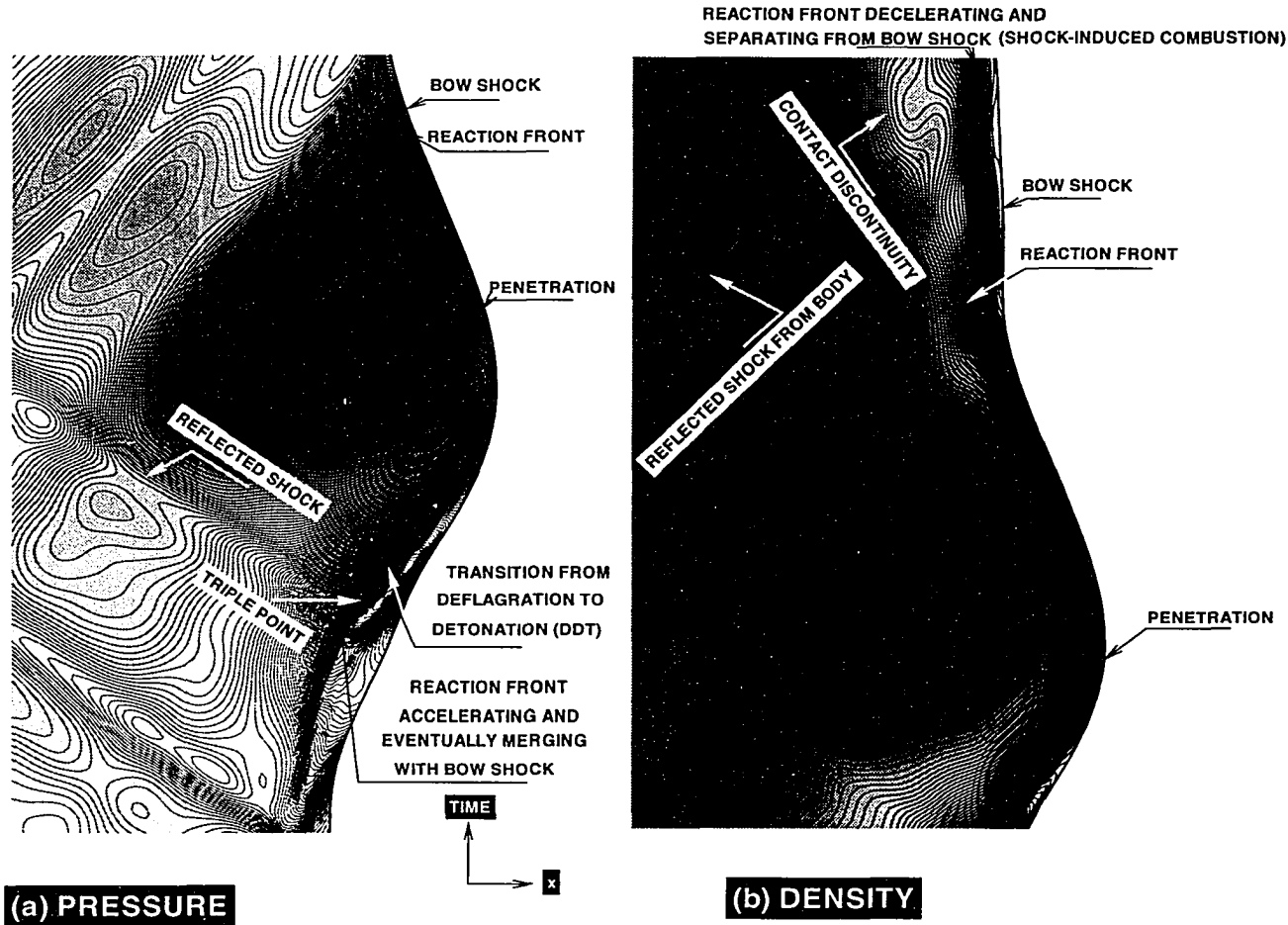
Chapter 9

CONCLUSIONS

A numerical study is presented to demonstrate the capabilities of modern CFD techniques for complex reacting flow-field predictions. Unsteady and steady ballistic-range experiments are successfully simulated. The calculations have been carried out for Mach 5.11 and 6.46. The Mach 5.11 case was found to be unsteady with periodic oscillations. The frequency of oscillations was calculated and was found to be in good agreement with the experimentally observed frequency. The Mach 6.46 case was found to be macroscopically stable, thus supporting the existing view that it is possible to stabilize the shock-induced combustion phenomena with sufficient level of overdrive. All the experimentally observed flow features are captured, and the frequency of the combustion instabilities is found to be in good agreement with the experimentally observed frequency.

Study also included simulations of three cases of Ruegg and Dorsey's ballistic-range experiments. Results show that an increase in the free-stream pressure can drive a stable reaction front to a regular, periodic unstable regime and again to a large-disturbance regime, as observed experimentally. The flow features of the regular regime have been successfully described with the one-dimensional wave-interaction model of McVey and Toong. The flow features of the large-disturbance regime have been described by the one-dimensional model of Matsuo et al. The shock stand-off and combustion stand-off distances agree well with the experimental results of Ruegg and Dorsey.

The current study used both shock-capturing and shock-fitting techniques to simulate the shock-induced combustion past blunt projectiles. In such problems which involve

158

instabilities, the shock-fitting technique gives much better resolution of the flow features than the shock-capturing technique. The observed flow features have been successfully correlated with the one-dimensional wave-interaction models, and the frequency of oscillations has been matched with the experimental data as well as with earlier investigations.

REFERENCES

1. Cambier, J. L. and Adelman H., "Numerical Simulations of an Oblique Detonation Wave Engine," AIAA Paper 88–0063, January 1988.

2. White, M. E., Drummond, J. P., and Kumar, Ajay, "Evolution and Status of CFD Techniques for Scramjet Applications," AIAA Paper 86–0160, January 1986.

3. Atamanchuk, T. and Sislian J., "On-And-Off Design Performance Analysis of Hypersonic Detonation Wave Ramjets," AIAA Paper 90–2473, July 1990.

4. Hertzberg, A., Brucker, A. P., and Bagdanoff, D. W., (1988), "Ram Accelerator; A New Chemical Method for Accelerating Projectiles to Ultrahigh Velocities," AIAA Journal, Vol. 26, 1988, pp. 195–203.

5. Zeldovich, Y. B. and Shlyapintokh, I. Y., "Ignition of Explosive Gaseous Mixtures in Shock Waves," Office of Technical Services, U.S. Department of Commerce, Washington, D.C., OTS:60–41, 553, 1960.

6. Ruegg, F. W. and Dorsey, W. W., "A Missile Technique for the Study of Detonation Waves,"Journal of Research, National Bureau of Standards, Vol. 66c, No. 1, January-March 1962, pp. 51–58.

7. Behrens, H., Struth, W., and Wecken F., "Studies of Hypervelocity Firings into Mixtures of Hydrogen with Air or with Oxygen," Tenth Symposium (International) on Combustion, 1965, pp. 245–252.

8. McVey, J. B. and Toong, T. Y., "Mechanism of Instabilities of Exothermic Hypersonic Blunt-Body Flows,"Combustion Science and Technology, Vol. 3, 1971, pp. 63–76.

9. Alpert, L. R. and Toong, T. Y., "Periodicity in Exothermic Hypersonic Flows about Blunt Projectiles,"Acta Astronautica, Vol. 17, September 1972, pp. 539–560.

10. Toong T. Y., "Instabilities in Reacting Flows,"Acta Astronautica, Vol. 1, 1974, pp. 317–344.

11. Lehr, H. F., "Experiments on Shock-Induced Combustion,"Acta Astronautica, Vol. 17, September 1972, pp. 589–586.

12. Oppenheim, A. K., Manson, N., and Wagner, H. G., "Recent Progress in Detonation Research," AIAA Journal, Vol. 1, 1963, pp. 2243–2252.

160

13. Youngster, S., Eberhardt, S., and Bruckner, A. P., "Numerical Simulation of Shock-Induced Combustion by High-Speed Projectiles in Detonable Gas Mixtures," AIAA Paper 89–0673, July 1989.

14. Lee, S. and Deiwert, G. S., " Calculation of Non-equilibrium Hydrogen-Air Reaction with an Implicit Flux Vector Splitting Method," AIAA Paper 89–1700, 1989.

15. Wilson, G. J. and MacCormack R. W., "Modelling Supersonic Combustion Using a Fully-Implicit Numerical Method," AIAA Journal, Vol. 30, No. 4, 1992, pp. 1008–1015.

16. Sussman, M. A., "Source Term Evaluation for Combustion Modelling," AIAA Paper 93–0239, January 1993.

17. Wilson, G. J. and Sussman, M. A., "Computation of Unsteady Shock-Induced Combustion Using Logarithmic Species Conservation Equations," AIAA Journal, Vol. 31, 1993, pp. 294–301.

18. Matsuo, A. and Fujiwara T., "Numerical Simulations of Shock-Induced Combustion around an Axisymmetric Blunt Body," AIAA Paper 91–1414, June 1991.

19. Matsuo, A. and Fujiwara, T., "Numerical Investigation of Oscillatory Instability in Shock-Induced Combustion around a Blunt Body," AIAA Journal, Vol. 31, 1993, pp. 1835–1841.

20. Matsuo, A., Fujiwara, T., and Fujii, K., "Flow Features of Shock-Induced Combustion around Projectiles Travelling at Hypervelocities," AIAA Paper 93–0451, January 1993.

21. Ahuja, J. K. and Tiwari, S. N., "A Parametric Study of Shock-Induced Combustion in a Hydrogen-Air System," AIAA Paper 94–0674, January 1994.

22. Kumar, A. and Singh, D. J., "Unsteady Shock-Induced Combustion Past Blunt Bodies," Proceedings of the ICASE/LaRC Workshop on Transition, Turbulence, and Combustion.

23. Tivanov, G. and Rom, J., "Analysis of the Stability Characteristics of Hypersonic Flow of a Detonable Gas Mixture in the Stagnation Region of a Blunt Body," AIAA Paper 93–1918, June 1993.

24. Matsuo, A., Fujii, K., and Fujiwara, T., "Computational Study of Unsteady Combustion around Projectiles with Emphasis on the Large-Disturbance Oscillation," AIAA Paper 94–0764, January 1994.

25. Ahuja, J. K. and Tiwari, S. N., "Investigation of Hypersonic Shock-Induced Combustion in a Hydrogen-Air System," AIAA Paper 92–0339, January 1992.

26. Ahuja, J. K. and Tiwari, S. N., "Numerical Simulation of Shock-Induced Combustion in a Superdetonative Hydrogen-Air System," AIAA Paper 93–0242, January 1993.

27. Singh, D. J., Ahuja, J. K., and Carpenter, M. H., "Numerical Simulations of Shock-Induced Combustion/Detonation," Computing Systems in Engineering, Vol. 3, 1992, pp. 201–215.

28. Ahuja, J. K., Tiwari, S. N., and Singh, D. J., "Hypersonic Shock-Induced Combustion in a Hydrogen-Air System," AIAA Journal, Vol. 33, No. 1, January 1995, pp. 173–176.

29. Ahuja, J. K., Kumar, A., Singh, D. J., and Tiwari, S. N., "Numerical Simulation of Shock-Induced Combustion Past Blunt Bodies Using Shock-Fitting Technique," AIAA Paper 94–3100, June 1994.

30. Ahuja, J. K., Kumar, A., and Tiwari, S. N., "Numerical Investigation of Shock-Induced Combustion Past Blunt Projectiles in Regular and Large-Disturbance Regimes," AIAA Paper 95–0153, January 1995.

31. Gross, R. A. and Chinitz, W., "A Study of Supersonic Combustion,"Journal of the Aerospace Sciences, Vol. 27, July 1960, pp. 517–524.

32. Pratt, D. T., Humphery, J. W. and Glenn, D. E., "Morphology of a Standing Oblique Detonation Wave," AIAA Paper 87–1785, July 1987.

33. Adelman, H. G., Cambier, J. L., Menees, G. P., and Balboni, J. A., "Analytical and Experimental Validation of the Oblique Detonation Wave Engine Concept," AIAA Paper 88–0097, January 1988.

34. Fort, J. and Pratt, D., "Supersonic Flameholding by Attached Oblique Shock Waves," AIAA Paper 90–0735, January 1990.

35. Singh, D. J., Carpenter, M. H., and Kumar, A., "Numerical Simulation of Shock-Induced Combustion/Detonation in a Premixed H_2-Air Mixture Using Navier-Stokes Equations," AIAA Paper 91–3358, June 1991.

36. Li, C., Kailasanath, K., and Oran, E. S., "Stability of Oblique Detonations in Ram Accelerators," AIAA Paper 92–0089, January 1992.

37. Drummond, J. P., Rogers, R. C., and Hussaini, M. Y., "A Detailed Numerical Model of a Supersonic Reacting Mixing Layer," AIAA Paper 86–1427, June 1986.

38 Anonymous, Rapport-Bericht CO 7/73, Institut Franco-Allenmand De Recherches De Saint-Louis, Kolloquium Uber Gasdetonationen, obgehalten im ISL am 22.10.1973, ISL-Beitrage.

39. McBridge, B. J., Heimel, S., Ehlers, J. G., and Gordon, S., "Thermodynamic Properties to 6000°K for 210 Substances Involving the First 18 Elements," NASA SP-3001, 1963.

40. White, F. M., Viscous Fluid Flow, McGraw-Hill, Inc, 1974.

41. Svehla, R. A., Estimated Viscosities and Thermal Conductivities of Gases at High Temperatures, NASA TR R-132, 1962.

42. Wilke, C. R., "A Viscosity Equation For Gases Mixtures.", Chem. Phys., Vol. 18, No. 4, April 1950, pp. 517–519.

43. Berman, H. A., Anderson, J. D., Jr., and Drummond, J. P., "Supersonic Flow over a Rearward Facing Step with Transverse Nonreacting Hydrogen Injection," AIAA Journal, Vol. 21, No. 12, December 1983, pp. 1707–1713.

44. Williams, F. A., Combustion Theory, Anderson-Wesley Pub. Co., Inc., 1965.

45. Jachimowski, C. J., "An Analytical Study of the Hydrogen-Air Reaction Mechanism with Application to Scramjet Combustion," NASA TP-2791, 1988.

46. Billig, S. F., "Shock-Wave Shapes around Spherical and Cyndrical-Nosed Bodies," Journal of Spacecraft, Vol. 4, No. 6, 1967, pp. 822–823.

47. Warnatz, J., "Rate Coefficients in the C/H/O System,"Combustion Chemistry, Chapter 5, Gardiner, Jr., W. C., Editor, Springer-Verlag, New York, 1984.

48. MacCormack, R. W., "The Effect of Viscosity in Hypervelocity Impact Cratering," AIAA Paper 69-354, April-May 1969.

49. Kumar, A. and Graves, R. A., "Numerical Solution of the Viscous Hypersonic Flow Past Blunted Cones at Angle of Attack," AIAA Paper 77-172, January 1977.

APPENDIX A

SOLUTION OF GOVERNING EQUATIONS ALONG STAGNATION LINE FOR AXISYMMETRIC FLOWS USING L'HOPITAL'S RULE

L'hopital rule says that if the function $f(x)$ and $\phi(x)$ vanish at the point $x = a$, that is $f(a) = \phi(a) = 0$, then if the ratio $\frac{f'(x)}{\phi'(x)}$ has a limit as $x \rightarrow a$ there also exists a limit $\lim_{x \rightarrow a} \frac{f(x)}{\phi(x)}$ and $\lim_{x \rightarrow a} \frac{f(x)}{\phi(x)} = \lim_{x \rightarrow a} \frac{f'(x)}{\phi'(x)}$. Since for axisymmmetric problems we have a coordinate singularity at the symmetry axis, $y = 0$, in the source term, therefore, to remove the singularity we use L'Hopital's rule and make the following replacements in the equations:

$$\frac{v}{y} = \frac{\frac{\partial v}{\partial y}}{\frac{\partial y}{\partial y}} = \frac{v_y}{1} = v_y$$

$$\frac{v_x}{y} = \frac{\frac{\partial v_x}{\partial y}}{\frac{\partial y}{\partial y}} = \frac{v_{xy}}{1} = v_{xy}$$

$$\frac{u_y}{y} = \frac{\frac{\partial u_y}{\partial y}}{\frac{\partial y}{\partial y}} = \frac{u_{yy}}{1} = u_{yy}$$

$$\frac{2\mu}{y}\left(v_y - \frac{v}{y}\right) = 2\mu\left(\frac{yv_y - v}{y^2}\right) = 2\mu\left[\frac{\frac{\partial(yv_y - v)}{\partial y}}{\frac{\partial(y^2)}{\partial y}}\right] = 2\mu\left(\frac{yv_{yy} + v_y - v_y}{2y}\right) = \mu v_{yy}$$

and

$$\frac{k}{y}\frac{\partial T}{\partial y} = \frac{kT_y}{y} = \frac{k\frac{\partial T_y}{\partial y}}{\frac{\partial y}{\partial y}} = kT_{yy}$$

With these changes the governing equations at the axis of symmetry reduces to:

164

$$U = \begin{bmatrix} \rho \\ \rho u \\ \rho v \\ \rho E \end{bmatrix}$$

$$F = \begin{bmatrix} \rho u \\ \rho u^2 + p + \tau_{xx} \\ \rho u v + \tau_{yx} \\ (\rho E + p + \tau_{xx})u + \tau_{yx}v + q_x \end{bmatrix}$$

$$G = \begin{bmatrix} \rho v \\ \rho v u + \tau_{yx} \\ \rho v^2 + p + \tau_{yy} \\ (\rho E + p + \tau_{yy})v + \tau_{yx}u + q_y \end{bmatrix}$$

$$H = \begin{bmatrix} \rho v_y \\ \rho u v_y - \mu[v_{xy} + u_{yy}] \\ 2\rho v v_y - \mu v_{yy} \\ \rho E v_y + p v_y - \underbrace{\frac{2}{3}\mu[2v_y^2 - v_y - v_y u_x]}_{\text{(See Below)}} - \mu[v_{xy}u + u u_{yy}] + kT_{yy} \end{bmatrix}$$

$$\frac{\tau_{yy}\cdot v}{y} = \frac{v}{y}\left[-\frac{2}{3}\mu\left\{ 2\frac{\partial v}{\partial y} - \frac{v}{y} - \frac{\partial u}{\partial x} \right\} \right]$$

$$= -\frac{2}{3}\mu\left[2v\frac{\partial v}{\partial y} - \frac{v^2}{y} - v\frac{\partial u}{\partial x} \right]\frac{1}{y}$$

$$= -\frac{2}{3}\mu\left[2\frac{v}{y}\frac{\partial v}{\partial y} - \frac{v^2}{y^2} - \frac{v}{y}\frac{\partial u}{\partial x} \right]$$

$$= -\frac{2}{3}\mu\left[2v_y v_y - \frac{v}{y}v_y - v_y u_x \right]$$

$$= -\frac{2}{3}\mu\left[2v_y^2 - v_y^2 - v_y u_x \right]$$

Also the following terms to be replaced with their final values given on the R.H.S.

$$\tau_{xx} = -\frac{2}{3}\mu\left(2\frac{\partial u}{\partial x} - \frac{\partial v}{\partial y} - \frac{v}{y} \right)$$

$$= -\frac{2}{3}\mu\left(2\frac{\partial u}{\partial x} - \frac{\partial v}{\partial y} - \frac{\partial v}{\partial y} \right)$$

$$= -\frac{2}{3}\mu\left(2\frac{\partial u}{\partial x} - 2\frac{\partial v}{\partial y} \right)$$

$$\tau_{xx} = -\frac{4}{3}\mu\left(\frac{\partial u}{\partial x} - \frac{\partial v}{\partial y} \right)$$

165

$$\tau_{yy} = -\frac{2}{3}\mu\left(2\frac{\partial v}{\partial y} - \frac{v}{y} - \frac{\partial u}{\partial x}\right)$$

$$= -\frac{2}{3}\mu\left(2\frac{\partial v}{\partial y} - \frac{\partial v}{\partial y} - \frac{\partial u}{\partial x}\right)$$

Hence,

$$\tau_{yy} = -\frac{2}{3}\mu\left(\frac{\partial v}{\partial y} - \frac{\partial u}{\partial x}\right)$$

and

$$\tau_{\theta\theta} = -\frac{2}{3}\mu\left(2\frac{v}{y} - \frac{\partial v}{\partial y} - \frac{\partial u}{\partial x}\right)$$

$$= -\frac{2}{3}\mu\left(2\frac{\partial v}{\partial y} - \frac{\partial v}{\partial y} - \frac{\partial u}{\partial x}\right)$$

$$\tau_{\theta\theta} = -\frac{2}{3}\mu\left(\frac{\partial v}{\partial y} - \frac{\partial u}{\partial x}\right)$$

Though the governing equations changes at the axis of symmetry as shown above, but we would still like to use the same set of governing equations everywhere (including at the axis of symmetry) with only a slight modifications at the axis of symmetry to take care of the above changes. The only term needs to be taken care of at the axis of symmetry is the term $\frac{v}{y}$

As $y \rightarrow 0$ and $v \rightarrow 0$ at the axis of symmetry we get $\frac{v}{y} = \frac{0}{0}$ = indeterminate.

Therefore, using L'Hopital's rule we have

$$\frac{v}{y} = \frac{\frac{\partial v}{\partial y}}{\frac{\partial y}{\partial y}} = \frac{\partial v}{\partial y}$$

$$= \frac{v(2) - v(1)}{y(2) - y(1)} = \frac{v(2) - 0}{y(2) - 0} = \frac{v(2)}{y(2)}$$

(Values inside the brackets denote grid points along the body)

Hence,

$$\frac{v}{y} = \frac{v(2)}{y(2)}$$

166

This is because both the normal velocity and value of y is zero at the stagnation line. Therefore, at the axis of symmetry simply replace $\frac{v}{y}$ terms by $\frac{v(2)}{y(2)}$ terms. Also if absolute values of $y(i,1)$ is $\geq 10^{-10}$ (machine zero) then use the general expression for $\frac{v}{y}$ i.e., at the stagnation line it will be $\frac{v(1)}{y(1)}$.

But if the absolute value of $y(i,1)$ is $< 10^{-10}$ which means zero, then L'Hopital's rule is used for $\frac{v}{y}$ i.e., $\frac{v}{y} = \frac{v(2)}{y(2)}$ i.e., the value at the second grid point is used at the stagnation line.

167

APPENDIX B

CALCULATION OF THE CHEMICAL JACOBIAN MATRIX

We shall be discussing the calculations of the chemical jacobian matric for the species

O_2, H_2O, H_2, OH

Applying the law of mass action to the global model $2H_2 + O_2 \rightleftarrows 2H_2O$ we have

$$\dot{C_{O_2}} = -k_{f_2} C_{H_2} C_{o_2} + k_{b_1} C_{OH}^2 \tag{B1}$$

$$\dot{C_{H_2O}} = 2\left[k_{f_2} C_{OH}^2 C_{H_2} - k_{b_2} C_{H_2O}^2 \right] \tag{B2}$$

$$\dot{C_{H_2}} = \dot{C_{O_2}} - \frac{1}{2}\dot{C_{H_2O}} \tag{B3}$$

$$\dot{C_{OH}} = -\left(2\dot{C_{O_2}} + \dot{C_{H_2O}} \right) \tag{B4}$$

$$\mathbf{U} = \begin{bmatrix} \rho \\ \rho u \\ \rho v \\ \rho E \\ \rho f_1 \\ \rho f_2 \\ \rho f_3 \\ \rho f_4 \end{bmatrix} = \begin{bmatrix} U_1 \\ U_2 \\ U_3 \\ U_4 \\ U_5 \\ U_6 \\ U_7 \\ U_8 \end{bmatrix}$$

$$\mathbf{H} = \begin{bmatrix} 0 \\ 0 \\ 0 \\ 0 \\ \dot{\omega}_1 \\ \dot{\omega}_2 \\ \dot{\omega}_3 \\ \dot{\omega}_4 \end{bmatrix} = \begin{bmatrix} H_1 \\ H_2 \\ H_3 \\ H_4 \\ H_5 \\ H_6 \\ H_7 \\ H_8 \end{bmatrix}$$

Species :

$$1 \rightarrow H_2$$

168

$$2 \rightarrow O_2$$

$$3 \rightarrow OH$$

$$4 \rightarrow H_2O$$

Derivation of $\dot{\omega}_i$ terms in terms of U Variables

Note: This is required before we carry out differentiation i.e. $\frac{\partial H(H_1, H_2, \ldots H_8)}{\partial U(U_1, U_2, \ldots U_8)}$.

Now,

$$\dot{\omega}_1 = \dot{\omega}_{H_2} = \frac{kg}{m^3 - sec}$$

$$= \dot{C}_{H_2} \frac{kg - moles}{m^3 - Sec} M_{H_2} \frac{Kg}{Kg - moles}$$

$$= \dot{C}_{H_2} M_{H_2} \frac{Kg}{m^3 - Sec}$$

(If $\dot{C}_{H_2}$ is in $\frac{Kg-moles}{m^3-sec}$ and M_{H_2} is in $\frac{Kg}{Kg-moles}$)

$$\dot{\omega}_1 = \dot{\omega}_{H_2} = \dot{C}_{H_2} \left[\frac{gram - moles}{cm^3 - sec} \right] [2.016] \left[\frac{gram}{gram - mole} \right]$$

$$= \dot{C}_{H_2} \left[\frac{1}{10^{-6} m^3 - sec} \right] \left[\frac{1}{1000} kg \right] [2.016]$$

$$2.016 \times 10^3 \dot{C}_{H_2}$$

(if $\dot{C}_{H_2}$ is in $\frac{gram-moles}{cm^3-sec}$ and M_{H_2} is in $\frac{gram}{gram-moles}$)

Since, C_i = Concentration of species i = $\frac{gram-mole}{cm^3}$

$$= \frac{\rho_i}{M_i} = \frac{\frac{gram}{cm^3}}{\frac{gram}{gram-mole}} = \frac{gram - mole}{cm^3}$$

Therefore,

$$C_i = \frac{\rho_i}{M_i} = \frac{\rho \left[\frac{\rho_i}{\rho} \right]}{M_i} = \frac{\rho f_i}{M_i} = \frac{gram - mole}{cm^3}$$

169

if density is given in $\frac{kg}{m^3}$ and molecular weight in $\frac{gram}{gram-mole}$

Therefore,

$$C_i \left(\frac{gram - mole}{cm^3} \right) = \frac{\rho_i \frac{1000gram}{10^6 cm^3}}{M_i \frac{gram}{gram-mole}}$$

$$= 10^{-3} \frac{\rho_i}{M_i} \frac{gram - mole}{cm^3}$$

Hence,

$$C_i = 10^{-3} \frac{\rho f_i}{M_i} \frac{gram - mole}{cm^3}$$

Therefore,

$$C_{H_2} = \frac{10^{-3}}{2.016} \rho f_{H_2}$$

$$C_{O_2} = \frac{10^{-3}}{32} \rho f_{O_2}$$

$$C_{OH} = \frac{10^{-3}}{17.008} \rho f_{OH}$$

$$C_{H_2O} = \frac{10^{-3}}{18.016} \rho f_{H_2O}$$

From Eq. (B1) we have

$$\dot{C}_{O_2} = -k_{f_1} C_{H_2} C_{O_2} + k_{b_1} C_{OH}^2$$

$$= -k_{f_1} \frac{10^{-3}}{32} \rho f_{O_2} \frac{10^{-3}}{2.016} \rho f_{H_2} + k_{b_1} \left(\frac{10^{-3}}{17.008} \right)^2 \rho^2 f_{OH}^2$$

Therefore,

$$\dot{\omega}_{O_2} = \dot{C}_{O_2} \times M_{O_2} \times 10^3$$

$$= -\frac{10^{-3}}{2.016} k_{f_1} \rho^2 f_{H_2} f_{O_2} + \frac{32 \times 10^{-3}}{(17.008)^2} \rho^2 f_{OH}^2 k_{b_1}$$

$$\dot{\omega}_{O_2} = -\frac{10^{-3}}{2.016} k_{f_1} \underbrace{[\rho f_{H_2}]}_{U_5} \underbrace{[\rho f_{O_2}]}_{U_6} + \frac{32 \times 10^{-3}}{(17.008)^2} k_{b_1} \underbrace{[\rho f_{OH}]^2}_{U_7}$$

Therefore,

$$\dot{\omega}_{O_2} = -\frac{10^{-3}}{2.016} k_{f_1} U_5 U_6 + \frac{32 \times 10^{-3}}{(17.008)^2} k_{b_1} U_7^2$$

170

Similarly, from Eq. (B2) we have,

$$\dot{C}_{H_2O} = 2\left[k_{f_2} C_{OH}^2 C_{H_2} - k_{b_2} C_{H_2O}^2\right]$$

$$= 2\left[k_{f_2}\left(\frac{10^{-3}}{17.008}\right)^2 (\rho f_{OH})^2 \left(\frac{10^{-3}}{2.016}\right)\rho f_{H_2} - k_{b_2}\left(\frac{10^{-3}}{18.016}\right)^2 (\rho f_{H_2O})^2\right]$$

Therefore,

$$\dot{\omega}_{H_2O} = \dot{C}_{H_2O} \times M_{H_2O} \times 10^3$$

$$= 2\left[k_{f_2}\frac{10^{-6}}{(17.008)^2(2.016)}\rho^3 f_{OH}^2 f_{H_2} - k_{b_2}\frac{10^{-3}}{(18.016)^2}\rho^2 f_{H_2O}^2\right] M_{H_2O}$$

$$= 2\left[\frac{18.016 \times 10^{-6}}{(17.008)^2(2.016)}k_{f_2}\rho^3 f_{OH}^2 f_{H_2} - \frac{10^{-3}}{(18.016)}k_{b_2}\rho^2 f_{H_2O}^2\right]$$

Hence,

$$\dot{\omega}_{H_2O} = 2\left[\frac{18.016 \times 10^{-6}}{(17.008)^2(2.016)}k_{f_2} U_7^2 U_5 - \frac{10^{-3}}{(18.016)}k_{b_2} U_8^2\right]$$

From Eq. (B3) we have

$$\dot{C}_{H_2} = \dot{C}_{O_2} - \frac{1}{2}\dot{C}_{H_2O}$$

$$= -k_{f_1}\left(\frac{10^{-6}}{32 \times 2.016}\right)(\rho f_{O_2})(\rho f_{H_2}) + k_{b_1}\left(\frac{10^{-3}}{17.008}\right)^2 \rho^2 f_{OH}^2$$

$$- \left[k_{f_2}\frac{10^{-9}}{(17.008)^2(2.016)}(\rho f_{OH})^2 (\rho f_{H_2}) - k_{b_2}\frac{10^{-6}}{(18.016)^2}(\rho f_{H_2O})^2\right]$$

$$\dot{\omega}_{H_2} = \dot{C}_{H_2} \times M_{H_2} \times 10^3$$

$$= -\left(\frac{10^{-3}}{32}\right)k_{f_1} U_5 U_6 + \frac{10^{-3} \times 2.016}{(17.008)^2}k_{b_1}(U_7)^2$$

$$- \frac{10^{-6}}{(17.008)^2}k_{f_2} U_7^2 U_5 + \frac{10^{-3} \times 2.016}{(18.016)^2}k_{b_2} U_8^2$$

$$\dot{\omega}_{H_2} = -\left(\frac{10^{-3}}{32}\right)k_{f_1} U_5 U_6 + \frac{2.016 \times 10^{-3}}{(17.008^2)}k_{b_1} U_7^2 - \frac{10^{-6}}{(17.008)^2}k_{f_2} U_7^2 U_5 + \frac{10^{-3} \times 2.016}{(18.016)^2}k_{b_2} U_8^2$$

171

From Eq. (B4) we have

$$\dot{C}_{OH} = -\left(2\dot{C}_{O_2} + \dot{C}_{H_2O}\right)$$

$$= -\left[2\left\{-k_{f_1}\frac{10^{-3}}{32}\rho f_{O_2}\frac{10^{-3}}{2.016}\rho f_{H_2} + k_{b_1}\left(\frac{10^{-3}}{17.008}\right)^2\rho^2 f_{OH}^2\right\}\right]$$

$$-2\left[k_{f_2}\left(\frac{10^{-3}}{17.008}\right)^2(\rho f_{OH})^2\left(\frac{10^{-3}}{2.016}\right)\rho f_{H_2} - k_{b_2}\left(\frac{10^{-3}}{18.016}\right)^2(\rho f_{H_2O})^2\right]$$

and

$$\dot{\omega}_{OH} = \dot{C}_{OH} \times M_{OH} \times 10^3$$

$$= -2\left\{-\frac{10^{-3}\times 17.008}{32\times 2.016}k_{f_1}U_6 U_5 + \left(\frac{10^{-3}}{17.008}\right)k_{b_1}U_7^2\right\}$$

$$-2\left\{\left(\frac{10^{-6}}{17.008\times 2.016}\right)k_{f_2}U_7^2 U_5 - \left(\frac{10^{-3}}{[18.016]^2}\times 17.008\right)k_{b_2}U_8^2\right\}$$

Hence we get

$$\dot{\omega}_{OH} = 2\left[\left(\frac{17.008\times 10^{-3}}{32\times 2.016}\right)k_{f_1}U_6 U_5 - \left(\frac{10^{-3}}{17.008}\right)k_{b_1}U_7^2 - \left(\frac{10^{-6}}{17.008\times 2.016}\right)k_{f_2}U_7^2 U_5\right]$$

$$+2\left[\frac{10^{-3}\times 17.008}{(18.016)^2}k_{b_2}U_8^2\right]$$

172

Therefore, Chemical Jacobian Matrix $\frac{\partial H}{\partial U} = \frac{\partial H(H_1,H_2,H_3,\ldots\ldots\ldots H_8)}{\partial U(U_1,U_2,U_3,\ldots\ldots\ldots U_8)}$

$$
= \begin{bmatrix}
\frac{\partial H_1}{\partial U_1} & \frac{\partial H_1}{\partial U_2} & \frac{\partial H_1}{\partial U_3} & \frac{\partial H_1}{\partial U_4} & \frac{\partial H_1}{\partial U_5} & \frac{\partial H_1}{\partial U_6} & \frac{\partial H_1}{\partial U_7} & \frac{\partial H_1}{\partial U_8} \\
\frac{\partial H_2}{\partial U_1} & \frac{\partial H_2}{\partial U_2} & \frac{\partial H_2}{\partial U_3} & \frac{\partial H_2}{\partial U_4} & \frac{\partial H_2}{\partial U_5} & \frac{\partial H_2}{\partial U_6} & \frac{\partial H_2}{\partial U_7} & \frac{\partial H_2}{\partial U_8} \\
\frac{\partial H_3}{\partial U_1} & \frac{\partial H_3}{\partial U_2} & \frac{\partial H_3}{\partial U_3} & \frac{\partial H_3}{\partial U_4} & \frac{\partial H_3}{\partial U_5} & \frac{\partial H_3}{\partial U_6} & \frac{\partial H_3}{\partial U_7} & \frac{\partial H_3}{\partial U_8} \\
\frac{\partial H_4}{\partial U_1} & \frac{\partial H_4}{\partial U_2} & \frac{\partial H_4}{\partial U_3} & \frac{\partial H_4}{\partial U_4} & \frac{\partial H_4}{\partial U_5} & \frac{\partial H_4}{\partial U_6} & \frac{\partial H_4}{\partial U_7} & \frac{\partial H_4}{\partial U_8} \\
\cdot & \cdot & \cdot & \cdot & \cdot & \cdot & \cdot & \cdot \\
\cdot & \cdot & \cdot & \cdot & \cdot & \cdot & \cdot & \cdot \\
\frac{\partial H_8}{\partial U_1} & \frac{\partial H_8}{\partial U_2} & \cdot & \cdot & \cdot & \cdot & \cdot & \frac{\partial H_8}{\partial U_8}
\end{bmatrix}
$$

173

$$\frac{\partial H}{\partial U} =$$

	(1)	(2)	(3)	(4)	(5)	(6)	(7)	(8)
(1)	0	0	0	0	0	0	0	0
(2)	0	0	0	0	0	0	0	0
(3)	0	0	0	0	0	0	0	0
(4)	0	0	0	0	0	0	0	0
(5)	0	0	0	0	$-(10^{-3}/32)k_{f1}U_6 + \dfrac{-10^{-6}}{(17.008)^2}k_{f2}U_7^2$	$-\dfrac{10^{-3}}{32}\,k_{f1}U_5$	$\dfrac{2*2.016*10^{-3}}{(17.008)^2}\,k_{b1}U_7 - \dfrac{2*10^{-6}}{(17.008)^2}\,k_{f2}U_7U_5$	$\dfrac{2*10^{-3}*2.016}{(18.016)^2}\,k_{b2}U_8$
(6)	0	0	0	0	$-10^{-3}/2.016\,k_{f1}U_6$	$-\dfrac{10^{-3}}{2.016}\,k_{f1}U_5$	$\dfrac{2*32*10^{-3}}{(17.008)^2}\,k_{b1}U_7$	0
(7)	0	0	0	0	$\dfrac{2*17.008*10^{-3}}{32*2.016}\,k_{f1}U_6 - \dfrac{10^{-6}}{(17.008*2.016)}\,k_{f2}U_7^2$	$\dfrac{2*17.008*10^{-3}}{32*2.016}\,k_{f1}U_5$	$-\dfrac{2*10^{-3}}{17.008}\,k_{b1}U_7*2 - \dfrac{2*2*10^{-6}}{17.008*2.016}\,k_{f2}U_7U_5$	$\dfrac{2*2*10^{-3}*17.008}{(18.016)^2}\,k_{b2}U_8$
(8)	0	0	0	0	$\dfrac{2*18.016*10^{-6}}{(17.008)^2(2.016)}\,k_{f2}U_7^2$	0	$\dfrac{2*18.016*10^{-6}*2}{(17.008)^2(2.016)}\,U_7U_5$	$-\dfrac{2*10^{-3}}{(18.016)^2}\,k_{b2}U_8*2$